An Investigation into the Human Upper Airways Humidification

Sandra Grau Bartual

A thesis submitted to Auckland University of Technology in fulfilment of the requirements for the degree of Doctor of Philosophy in Biomedical Engineering

Primary Supervisor: Professor Ahmed M. Al-Jumaily

Faculty of Design and Creative Technologies

Auckland, New Zealand

December, 2018

Borrowers Page

The Auckland University of Technology requires the signatures of all the people using or photocopying this thesis. Accordingly all borrowers are required to fill out this page.

Date	Name	Address	Signature

Abstract

This research focuses on the analysis of the human upper airway humidification looking on one hand at the natural humidification or air conditioning process and on the other hand at the external humidification. Lung supportive devices are widely used to restore the breathing cycle and provide proper ventilation to patients. These devices introduce compressed room air into the respiratory system and generate a positive pressure inside the respiratory system and a turbulent effect to keep the airways open which distorts the natural lubrication and humidification. Hence, lung supportive devices incorporate a convective heated humidifier which provides external humidification to the patients to alleviate the upper airway dryness produced by the compressed airflow. However, the humidifier makes the devices bulky and patients are still reporting side effects after the therapy. Therefore, the purpose of this research is to investigate the effect of the positive airway pressure on the human upper airway epithelium, extrapolate the results to the entire human upper airways and develop a miniaturized, eco-friendly and affordable self-humidifying device able to overcome the dryness side effect and replace the actual convective heated humidifier.

Table of Contents

Attestation of Authorship

"I hereby declare that this submission is my own work and that, to the best of my knowledge and belief, it contains no material previously published or written by other person (except where explicitly defined in the acknowledgements), nor material which to a substantial extent has been submitted for the award of any other degree or diploma of a university or other institution of higher learning."

Sandra Grau Bartual

List of Figures

List of Tables

List of Abbreviations and Nomenclature

Abbreviations

1D	One-dimensional
2D	Two-dimensional
3D	Three-dimensional
AC	Alternating current
AH	Absolute humidity
ALI	Air-liquid interface
APAP	Auto-adjusting positive airway pressure
ARDS	Adult respiratory distress syndrome
ASL	Airway surface liquid
ATRP	Atom transfer radical polymerization
BiB	Bromoisobutyrate
C	Capacitance
CAD	Computer aided design
CCS	Coconut shell
CFD	Computational fluid dynamics
COPD	Chronic obstructive pulmonary disease
CPAP	Continuous positive airway pressure
CSA	Central sleep apnoea
CuBr	Copper(I)bromide
DMAP	4-(dimethylamino) pyridine
DMF	Dimethylformamide
DSC	Differential scanning calorimetry
E	Epithelium
EBMA	Ethyl 2-(bromomethyl) acrylate
ECIS	Electric cell-substrate impedance sensing system
EDS	Energy dispersive X-Ray spectroscopy
e.g.	For example
ELISA	Enzyme-linked immunosorbent assay
FBS	Fetal bovine serum

Flu-Na	Fluorescein sodium
FOT	Forced oscillation technique
FTIR	Fourier transform infrared spectroscopy
HBSS	Hank’s balanced salt solution
HEPES	Hydroxyethyl piperazine ethane sulfonic acid
HIPPV	Positive-pressure ventilation with high inflation pressure
HMEs	Heat and moisture exchangers
I	Current
ICU	Intensive care unit
i.e.	In other words
IL-6	Interleukin-6
IL-8	Interleukin-8
ISB	Isothermal saturation boundary
LCST	Lower critical solution temperature
LSD	Lung supportive devices
MW	Molecular weight
NaOH	Sodium hydroxide
NAR	Nasal airway resistance
NIPAM	N-isopropylacrylamide
NMR	Nuclear magnetic resonance
OH	Alcohol
OSA	Obstructive sleep apnoea
PAP	Positive airway pressure
PBS	Phosphate buffered saline
PMDETA	Pentamethyldiethylenetriamine
PNIPAM	Poly(N-isopropylacrylamide)
ppm	Parts per milion
PVA	Polyvinyl alcohol
R	Resistance
RC	Resistor and capacitor
RGB_B	Intensity of blue colour
RGB_G	Intensity of green colour
RGB_R	Intensity of red colour
RH	Relative humidity
SAP	Super absorbent polymers
SD	Standard deviation

SEM	Scanning electron microscopy
SPAP	Superimposed positive airway pressure
SPO	Sinusoidal pressure oscillations
STA	Simultaneous thermal analysis
T	Temperature
TEA	Triethylamine
TEER	Trans-epithelial electrical resistance
TGA	Thermal gravimetric analysis
THF	Tetrahydrofuran
TMS	Tetramethylsilane
TNF-α	Tumour necrosis factor alpha
UCST	Upper critical solution temperature
V	Voltage
Z	Impedance

Symbols

α	Fraction of the cilia period during stroke
β	Fraction of the cilia period during mucus penetration
δ	Chemical shift
ρ	Density of moist air
μ	Dynamic viscosity of moist air
ν	Cilia beat frequency
τ	Dominant relaxation time of the mucus

A	Tidal volume
A_k	Local cross-sectional area
$A_{Membrane}$	Area of the inserts membrane
B	Bulk modulus of respiratory epithelium
C	Capacitance
C_{A_k}	Local airflow water vapour concentration
C_{Apical}	Initial Flu-Na concentration
C_{M_k}	Local saturation water vapour concentration at the ASL outer Surface

C_{pA}	Moist air heat capacity at constant pressure
C_{pW}	Water heat capacity at constant pressure
$D_0(k)$	UA diameter vector at ΔP=0
dC/dt	Flux of Flu-Na
Dif	Diffusivity of water vapour in air
f	Frequency
h_{C_k}	Local heat transfer coefficient
h_{fg}	Latent heat of vaporization
J	Coupling constant
k_A	Moist air thermal conductivity
k_{C_k}	Local mass transfer coefficient
k_M	Epithelial and ASL thermal conductivity
L	Length/thickness between the electrodes
$L(k)$	UA length vector
M_W	Water molecular weight
N_k	Local water transfer rate from the ASL outer surface to the airflow
Nu_k	Local dimensionless Nusselt number
P	Pressure
p	Period of the signal
P_{app}	Apparent permeability
P_{sat_k}	Tetens saturation pressure
Q_0	Airflow rate at ΔP=0 cmH_2O
Q_5	Airflow rate at ΔP=5 cmH_2O
Q_{10}	Airflow rate at ΔP=10 cmH_2O
Q_{15}	Airflow rate at ΔP=15 cmH_2O
Q_{20}	Airflow rate at ΔP=20 cmH_2O
Q_{BC}	Breathing airflow rate
R	Ideal gas constant
Re_k	Local dimensionless Reynolds number
rH_k	Relative humidity
Sh_k	Local dimensionless Sherwood number
t	Time
T_{A_k}	Local airflow temperature
T_{B_k}	Local blood temperature at the basement capillary membrane
T_{M_k}	Local mucus temperature at the ASL outer surface

V	Volume
V_{Basal}	Basal volume
v_k	Local airflow velocity
X_C	Reactive part
y	Thickness
y_0	Epithelium thickness at ΔP=0
Z	Impedance

Acknowledgements

I would like to acknowledge my deepest and sincere gratitude to Professor Ahmed M. Al-Jumaily, professor of mechanical engineering at Auckland University of Technology for his kind supervision, suggestion to the problems raised, constructive guidance, pointing out the mistakes, critical reading , looking out for me over these years, valuable suggestions, and for his continuous support.

I would also like to express my cordial thanks and deep appreciation to Dr. Jack Chen, lecturer of chemistry, school of science at Auckland university of Technology, for his kind supervision and continuous support.

Many thanks to the Institution of Biomedical Technology (IBTec) for providing all facilities to help me bring the best performance and outcome. Thanks as well to everyone at IBTec and chemistry lab for providing a friendly and nice working atmosphere.

Thanks to the Auckland University of Technology for supporting me financially over three years through the Vice Chancellor's Doctoral Scholarship. Also, thanks to the ethics committee for approving the ethical application (18/139 An investigation into the upper airway humidification).

I would also like to express my deepest thanks and appreciation to Dr. Maliheh Ghadiri, postdoctoral fellow at Woolcock Institute of Medical Research, Professor Paul Young, professor of respiratory technology at the University of Sydney, and Professor Daniela Traini, professor in respiratory science at the University of Sydney, for providing all facilities, valuable suggestions and support.

At last but not the least, I would like to convey special thanks to my lovely friends and family, Juan Ramón and Beatriz, for their continuous support, encouragement and comprehension until this work has reached completion.

Moltíssimes gràcies a totes i tots.

Chapter 1

Background

1.1 Introduction

This chapter provides the information needed to contextualize this research and understand what is involved in the human upper airways humidification. The physiology of the respiratory system is explained in section 1.2. The mucus properties and ciliary activity is explained in section 1.3. A description of the respiratory diseases affecting New Zealand including sleep apnoea syndrome is provided in section 1.4. The therapies used to treat these diseases such as lung supportive devices including continuous positive airway pressure (CPAP) therapy followed by a closure of the chapter are explained in section 1.5 and 1.6 respectively.

1.2 Physiology of the respiratory system

Respiration is an automatic and semi-involuntary vital process driven by the demand of energy from cells. This energy is given in the form of ATP (Adenosine Triphosphate), which requires oxygen and produces carbon dioxide to form it. The respiration process consists of two steps. The first step is the inspiration, where the diaphragm and the rib muscles are contracted producing a large and flat thorax cavity, which enables the introduction of air flow into the lungs allowing the oxygen absorption to the blood flow. The second one is the expiration, where the diaphragm and the rib muscles press the lungs expelling the air, which contains carbon dioxide taken from blood, out of the body.

The respiratory system is responsible for a broad range of functions, as it is already explained, allows the oxygen and carbon dioxide exchange between the blood and air, but also helps to regulate blood pressure and control the pH of the body fluids. The last one is possible by removing the carbon dioxide, because an excess reacts with water producing hydrogen ions which decrease pH in body fluids. In addition, respiration makes possible the speech and other vocalizations such as laughing or crying, and provides the sense of smell [1].

The principal organs of the respiratory system can be divided in two parts. Nose, pharynx, and larynx, which are located at head and neck, are called the upper respiratory tract. And the lower respiratory tract is composed by trachea, bronchi, and lungs, which are located in the thorax [1]. A schematic representation of the respiratory system is outlined in Figure 1.1.

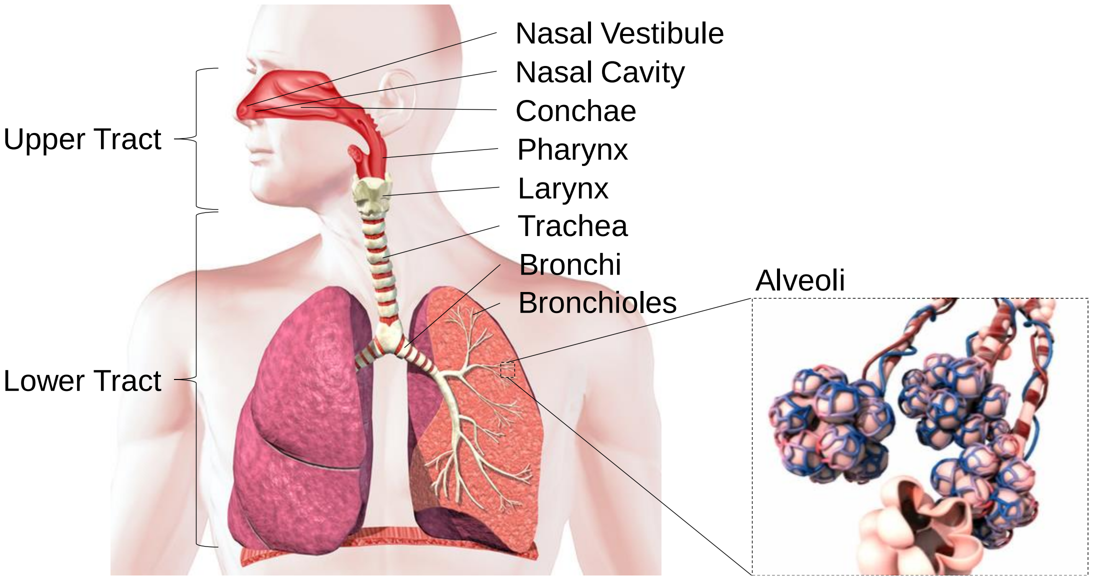

Figure 1.1. Schematic representation of the principal organs of the upper and lower human respiratory system [1].

Focussing on the upper respiratory tract, the hard palate divides the nasal cavity and the oral cavity allowing breathing while chewing food. Nasal cavity starts with a small chamber called the nasal vestibule. This space is lined with stratified squamous epithelium which has stiff guard hairs used to block insects and large particles from the airflow. Then the narrowness of the following passage and the turbulence caused by the conchae allow that most air contacts the mucous membrane, where most dust in the air sticks to the mucus, and the air picks up moisture and heat from the mucosa. The rest of the nasal cavity is lined with respiratory epithelium which is mobile ciliated pseudostratified columnar epithelia. The goblet cells secrete mucus moved by ciliated cells toward the pharynx. The nasal mucosa also contains mucous glands in the lamina propria, which is the connective tissue layer next to the epithelium. They deliver the mucus generated in the goblet cells allowing the stick of foreign matter which will be passed through the digestive tract instead of contaminating the lungs. The lamina propria also contains lymphocytes used against inhaled pathogens, plasma cells that secrete antibodies, and large blood vessels to warm the air. The pharynx is a muscular funnel of 13 cm long from the conchae to the larynx, which is divided by three regions: the nasopharynx, oropharynx, and laryngopharynx. Finally, the larynx is a 4 cm cartilaginous chamber whose primary function is to produce sounds and keep food and drink out of the airway. The superior opening of the larynx is protected by the epiglottis which closes the airway and directs food and drink into the oesophagus during swallowing [1].

Regarding lower respiratory tract, the trachea is a tube of 12 cm long and 2.5 cm in diameter supported by 16 to 20 C-shaped hyaline cartilage rings. The open part of the C faces allows oesophagus to expand as food passes by. The trachea epithelium is composed of ciliated cells, mucus-secreting goblet cells, and short basal stem cells, which makes possible the mucociliary escalator, where the debris-laden mucus is moved toward the pharynx to be swallowed. At the level of the sternum the trachea forks into right and left bronchi. The lungs, which are not symmetric, are conical organs with a concave base resting on the diaphragm, the top part is projected above the clavicle, and the costal surface is pressed against the rib cage. This surface exhibits a slit through which the lung receives the bronchi, blood vessels, lymphatic vessels, and nerves. Each lung contains a bronchial tree from the main bronchus to the terminal bronchioles. Each respiratory bronchiole divides into alveolar ducts, which have alveoli along their walls. The ducts end in alveolar sacs, which are grape like clusters of alveoli located around a central space. Branches of the bronchial arteries supply the blood to the bronchi, bronchioles, and pulmonary tissues, and follow the bronchial tree to capillaries surrounding the alveoli where gas exchange occurs [1]. A schematic representation of the human respiratory epithelium is outlined in Figure 1.2.

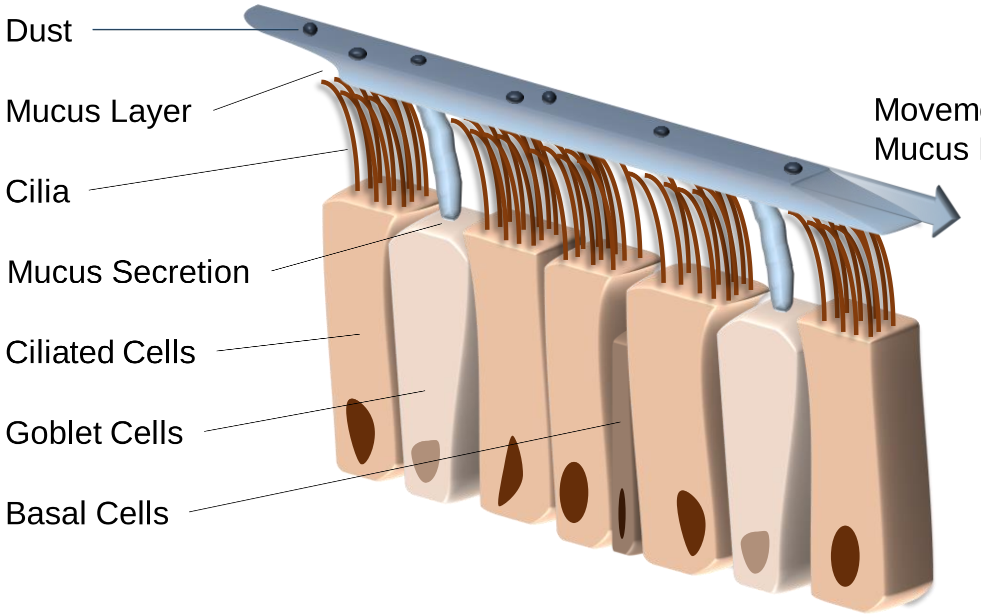

Figure 1.2. Schematic representation of the human respiratory epithelium including epithelial cells and mucus layer.

1.3 Mucus Properties and Ciliary Activity

Mucociliary transport is the movement of the mucus covering the respiratory epithelium which relies on coordinated ciliary activity and on mucus specific rheological properties [1]. In the nose the mucus is moved towards the pharynx, and in the tracheobronchial tree the mucus is moved toward and through the larynx and swallowed. Mucus is a non-Newtonian fluid with heterogeneous viscoelastic properties which are determined by its complex polymeric structure and degree of hydration. An alteration in mucus rheology, which can be caused by a range of pathophysiological conditions, can affect the mechanical coupling of the cilia with the overlying mucus called airway surface liquid (ASL) layer [2]. The ciliary beat consists of two steps the rapid forward/effective and the slow return/recovery stroke. On the effective stroke, the cilium is perpendicular to the cell surface and its tip is in contact with the mucus. The mucus layer acts as a coupler transferring momentum from the tips of the cilia to the load. When the cilia contacts the mucus they bend backwards, but if the mucus is too viscous or elastic, the ciliary bend is too great and the system does not work effectively ceasing mucociliary transport. The cilia beats efficiently at 10.8 Hz, although this frequency is regulated differently in the distal and tracheal airway epithelium [3, 4]. To achieve a good interaction between cilium and mucus, the distance (length of the cilium minus thickness of ciliary fluid layer) must be large enough to generate an adequate force to be transferred to the mucus layer with minimum loss. The time of contact is defined by $(1/\nu)\alpha$ where α

represents the fraction of the period during stroke. Then, cilium will require a time $(1/\nu)\beta$ first to penetrate and then to disengage itself from the mucus layer. This time must be enough for mechanical relaxation otherwise no penetration could occur. Hence the dominant relaxation time of the viscoelastic mucus τ is represented by equation 1.1, having optimum values between 0.1 to 1 second [5].

$$(1/\beta)\alpha \leq \tau \leq (1/\nu)\beta \qquad 1.1$$

Healthy nasal secretions consist of 2-3% proteins and glycoproteins, 1% lipids, 1% ions, and 0.02% DNA in 95% water [4]. Goblet and glandular mucus cells secrete acidic glycoproteins (sialomucins and sulphomucins) and serous cells secrete neutral glycoproteins (fucomucins), enzymes (lysozymes and lactoferrin) and IgA immunoglobulins. The water and ions are produced mainly by the serous glands from the capillary network as plasma transudate. This last mechanism is characterized by vascular exudation caused by an increase of subepithelial hydrostatic pressure to 5 cmH_2O which increases epithelial hydraulic conductivity allowing water transudation to airway. It is important to note that water is also removed from the airway by active Na^+ transport across the epithelium [6]. Both the goblet cells and the serous glands produce mucins which are secreted in vesicles derived from the Golgi apparatus and are released by exocytosis as 1-2 μm droplets. Then they absorb water and increase in volume by several hundred times in about 3 s [7]. The mucins are high molecular weight polydisperse glycoproteins consisting of approximately 80% carbohydrate with molecular masses ranging from a few hundred thousand to more than 1 million Daltons. They are up to 5 μm long and consist of sialic acid residues and random coils of carbohydrate chains linked by O-glycoside to a protein core. Mucins contain a large amount of sugar residues *i.e.* sugar side chain linked covalently to a polypeptide chain polymerised by disulphide bonds. The proportion of hydroxylated amino acids in the protein core is 70%, and the common sugars in the glycosylated regions are fructose, galactose N-acetylglucosamine, N-acetylgalactosamine, and N-acetylneuraminic acid. The carbohydrate residues are attached by N-acetylglucosamine linked to serine or threonine, and there are 25-30 carbohydrate chains per 100 amino acid residues. Mucins can bond between them by weak covalent or non-covalent bonds forming dimers and polymers. The structure is outlined in Figure 1.3. This hydroscopic three dimensional polymer interacts with water and ions forming a gel, which determines the viscoelastic properties of mucus [7]. Thereby, mucus properties can be altered chemically introducing extra cross-links between the glycoproteins to increase the elastic modulus or breaking mechanically some existing cross-links in order to decrease it [8, 9].

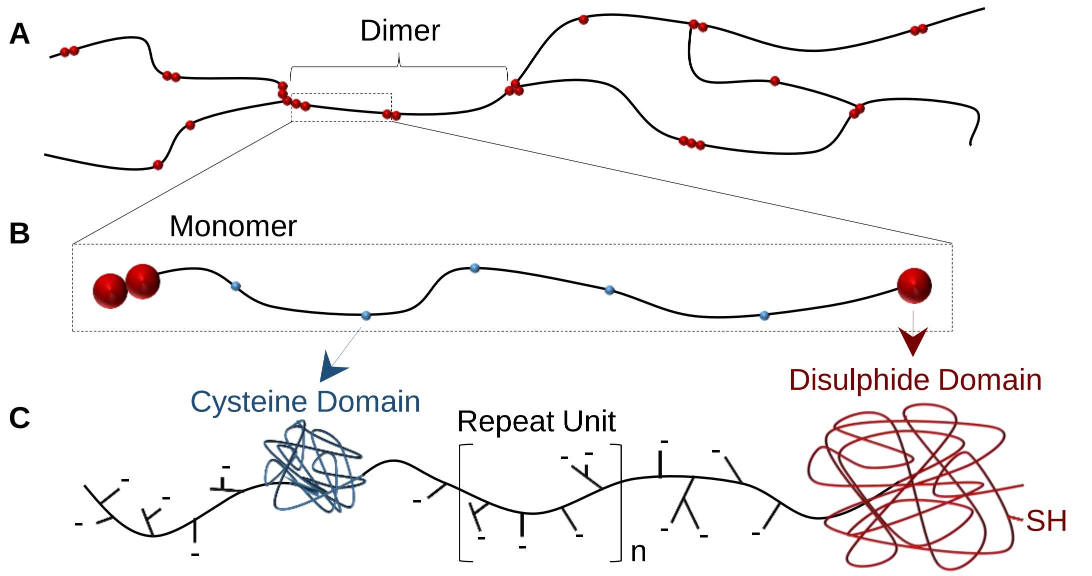

Figure 1.3. Mucin structure. A) Mucin polymer composed by secreted mucin monomer units linked end-to-end by disulphide bonds forming a long thread-like mature mucin molecules. B) Mucin monomer, approximately 500 nm in length, composed by an amino acid backbone with high glycosylated domains and folded regions stabilized via disulphide bonds with O-glycosylation links. C) Zoom in monomer part where it is possible to identify cysteine and disulphide domains.

The viscoelastic properties of the mucus are mainly derived from the molecular structure and amount of glycoproteins, and the proportion of water [10]. It means that mucus have some of the properties of a liquid and some of a solid. Liquids normally flow instantaneously when a force is applied because they do not store energy, also their flow rate is proportional to the amount of force applied according to their viscosity. On the other hand, solids do not flow, but they are deformed when force is applied because they are able to store energy according to their modulus of elasticity. Mucus rheological properties are not determined only considering both elastic and viscoelastic properties, it is also important to study the bio-rheological matching based on the mucus capacity to support a load and not distort the ciliary tips, the formation of a continuous mucus blanket able to overcome gravity, the spinnability based on the mucus ability to be drawn into long threads under the effect of traction, or adhesiveness between bacteria and inhaled particles and mucus [11]. Some optimum values can be quantified using the Ostwald viscometer, cone-plate viscometer, magnetic micro-rheometer, oscillating sphere magnetic rheometer, or the controlled stress technique. The spinnability of normal respiratory mucus ranges from 40 to 100 mm and mucus transport increases when this decreases [4]. Girod, S. *et at.* [12] quantified the viscosity and the elastic modulus close to 12 Pa·s and 1 Pa respectively to achieve efficient mucociliary transport, and suggested that low adhesivity of 70 $mN \cdot m^{-1}$ and wettability corresponding to a contact angle lower than 20°, represents the optimal conditions for the protective and lubricant properties of the mucus [13-17].

1.4 Respiratory diseases and sleep apnoea syndrome

According to the New Zealand ministry of health, respiratory diseases are the third most common cause of death in New Zealand. One in six (over 700,000) people live with a respiratory condition and a respiratory disease accounts for one in eight of all hospital stays, which cost more than $5.5 billion every year. Respiratory diseases can be classified as restrictive or obstructive disorders, which includes asthma, lung cancer, chronic obstructive pulmonary disease (COPD), obstructive sleep apnoea (OSA), bronchiectasis, bronchiolitis and pneumonia.

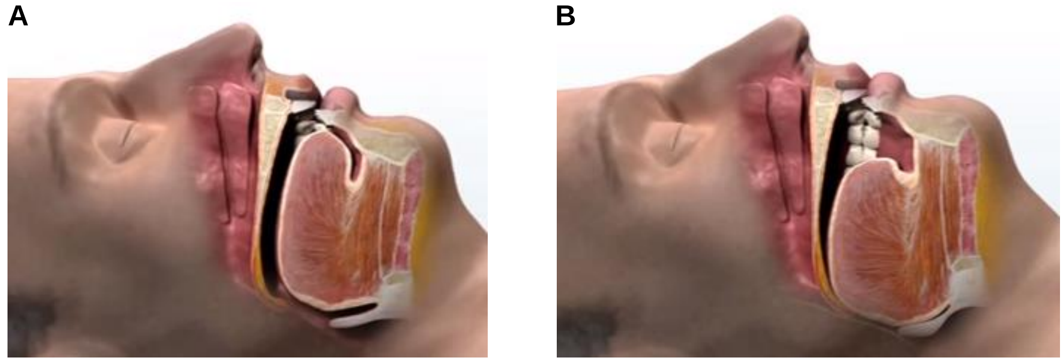

Figure 1.4. Representation of the human upper airways during rest. A- Normal breathing pathway. B- Blocked breathing pathways occurred during an apnoea episode.

Sleep apnoea syndrome is characterized by pauses in breathing during sleep. Each pause is called an apnoea, and can take from seconds to minutes occurring several times in an hour [18]. This dysfunction can be divided in two forms, central sleep apnoea (CSA), where breathing is interrupted by a lack of respiratory effort, and obstructive sleep apnoea (OSA), where breathing is interrupted by an airflow physical block. OSA is the most common disease between people, although an individual with sleep apnoea is rarely aware of having difficulties in breathing [19]. Sleep apnoea problem is usually recognized by others witnessing the individual during episodes since snoring is common. The collapse of the airway can be produced because throat muscles and tongue are more relaxed than normal or are large compared with the trachea dimensions. The shape of the head and neck can be related to small airway size, or in overweight conditions, soft fat tissue can thicken the tracheal wall which is harder to keep open during rest. Also aging slows brain signal ability to maintain throat muscles stiff during sleep as the airway is more likely to narrow or collapse [20, 21]. Figure 1.4 shows a normal breathing pathway (A) and a blocked breathing pathways occurred during an apnoea episode (B).

The problem, when breathing is paused, is that carbon dioxide builds up in the blood flow. As a body response, chemoreceptors detect this high carbon dioxide levels, and the brain sends a signal to wake up the person in order to breathe. The result is that by breathing normally the oxygen levels are restored and the person falls asleep again. However, this produces several side effects such as daytime fatigue causing behavioural effects such as moodiness, slow reaction time, insomnia, depression, and vision problems which increases the risk for driving and work-related accidents. If OSA is not treated, other health problems will appear such as diabetes, liver function impairment and fatty liver diseases, or even death due to a lack of oxygen [22]. Sleep apnoea syndrome is diagnosed by checking mouth, nose and throat looking for extra or large tissues in a physical exam, or on a sleep study such as polysomnogram where brain activity, eye movements, heart rate and blood pressure are recorded. There are several possible treatments to avoid airway collapse and restore regular breathing during sleep by using lung supportive devices, plastic mouthpieces or surgery. However, it can be achieved by changing lifestyle avoiding alcohol and tobacco, losing weight, side sleeping, using nasal sprays to keep nasal passages open or doing oropharyngeal exercises daily [23-25].

1.5 Lung supportive devices (LSD) and continuous positive airway pressure (CPAP) therapy

LSD devices, such as asthma nebulizers, positive airway pressure devices or respirators are used to restore or provide a proper respiration cycle in some patients. Continuous positive airway pressure (CPAP) is the most effective long-term treatment for obstructive sleep apnoea [26]. CPAP device is composed by an air pump connected to a mask used to cover only the nose or nose and mouth (face mask). Their principal function is to introduce air from the atmosphere at specific pressure into the respiratory system in order to maintain the airway open and avoid blockage during sleep. In order to achieve the effectiveness of the treatment the pressure inside the mask has to remain constant, which is solved by an automatic feed forward compensation control [26, 27]. There are two basic types of pumps used on CPAP, the oldest one is characterized by a specific fixed pressure used in a ramp function, so the system increases the pressure until it is achieve [28]. Recent CPAP pumps track the airflow and adjust the pressure required to maintain the airway open at each stage. They are able to cope with changes in pressure requirements such as temporary nasal congestion or weight change [29, 30]. Several nasal symptoms such as dryness, sneezing, rhinorrhoea, post-nasal drip, nasal congestion or epistaxis are reported by patients receiving CPAP treatment. They describe the symptoms as similar to an upper respiratory tract infection, *i.e.* like having a cold [31].

Drying on the airways produced as a side effect of CPAP might be the consequence of troubles in air conditioning. This is a transport process which controls the temperature and the humidity of the air during respiration. During inspiration, air is in contact with the warm and moist nasal mucosa and is rapidly warmed and humidified. This heat and mass transfer process is produced because there is a driving force created by the difference in temperature and water concentration between the inspired air, which is at room temperature and humidity [32] and the airway surface liquid layer, which is at body temperature and composed by 95% water and 5% of carbohydrate, protein, lipid and inorganic material [11]. During expiration air loses heat and water towards the outside. A healthy individual consumes 350 kcal of heat and 400 mL of water in one day in order to condition the inspired air considering moderate environmental conditions at about 25°C and 50% of relative humidity, and only one third is recovered during expiration [33]. However, under CPAP there is an increase in turbulent effect during inspiration and the air introduced on the respiratory system has higher pressure than in normal breathing (where the inspiratory linear velocity is between 6 and 18 m/s in the nasal valve, 2 m/s in the main passage, and 3 m/s in the nasopharynx during inspiration, and between 1 and 2 m/s, and 3 and 6 m/s at the nasal valve during expiration [34-38], in order to maintain the airway open. The problem is during the application of these high pressures the respiratory tissue is temporary deformed, so secreting cells may be closed blocking mucus secretion and hindering natural lubrication and normal air-conditioning on the airway. Toremalm, N.G. [39] and Roessler, F. *et at.* [40] explain in their work that the increase in turbulent effect causes drying and trauma of the mucosa which means squamous metaplasia appears and ciliated cells are inactivated and reduced. Nevertheless, there are no further studies or experiments which analyse the response on the respiratory tissue or mucociliary activity under CPAP therapy.

1.6 Closure

This chapter presented background information on the physiology of the respiratory system, mucus properties, sleep apnoea syndrome and CPAP therapy, which is the main treatment for OSA due to is non-invasive nature. This chapter also showed the disadvantages and side effects reported by CPAP patients after the therapy. In order to investigate what is causing this side effects and improve acceptance and comfort of the therapy, it is necessary to understand the effect of positive airway pressure (PAP) on the human respiratory epithelium, the improvements of the CPAP device such as oscillations and humidification, and the humidification alternatives.

Chapter 2

Literature Survey

2.1 Introduction

The analysis of the literature for the review has grown out of the studies and experiments done in different areas or themes such as alterations on the human respiratory epithelium, modelling of the air-conditioning process, improvements of the continuous positive airway pressure therapy including humidification and pressure oscillations, and the humidification alternatives.

The studies have been collected via searches on scholarly databases intended to direct us towards significant material, specifically PubMed, ATS Journals, Science Direct, or Chest Journal, using key words and combinations of terms. In addition, important works were searched through papers and books cited in reference lists of relevant papers. The review reflects contemporarily findings and methodologies, so a 25 year period was applied for literature used, with the majority of these published within the past 10 years. Older references are included only when providing appropriate information.

2.2 Human respiratory epithelium: alterations and models

Many research lines have been focused on finding a representative model of the human respiratory system. The best representation is found according to the application and what is desired to be measured. The most used models are developed with live animals, animal tissue, which is the most accessible material for research, human tissue or human epithelial cells cultures in air liquid interface to stimulate cell differentiation and mucus secretion, which required a good practice and knowledge in cell culture methodology, equipment and techniques [41-69].

Dreyfuss, D. *et at.* [70] investigated the mechanisms by which intermittent positive-pressure ventilation with high inflation pressure (HIPPV) induced pulmonary edema. They investigated the physiologic and anatomic changes related to HIPPV at 45

cmH_2O peak inspiratory pressure in rats. They found that after 5 min of HIPPV, there was a significant increase in Na space, dry lung weight, and fractional albumin uptake when compared with that in control rats mechanically ventilated at 7 cmH_2O peak inspiratory pressure.

Meduri, G.U. *et at.* [71] investigated the effect of the CPAP treatment in asthmatic patients with acute respiratory failure and Chronic obstructive pulmonary disease (COPD) patients since the medical intensive care unit (ICU) provides non-invasive positive pressure ventilation with the CPAP device. They found that CPAP ventilation in asthmatic patients was highly effective in correcting gas exchange abnormalities using a low inspiratory pressure (< 25 cm H_2O).

Oka, S. *et at.* [72] investigated the effect of fluid pressure on the expression of interleukin-1α, matrix metalloproteinases, and prostaglandin E2 in odontogenic keratocystis to determine whether this pressure stimulated inflammatory cytokine production and signalling of osteoclastogenic events. They found that positive fluid pressure play a crucial role in odontogenic keratocyst growth via stimulating the expression of interleukin-1α in epithelial cells.

Finally, Zhu, Y. *et at.* [73] investigated the effect of gas concentrations, exposure time, biophysical stress, and biological agents on human airway Calu-3 cell line as a respiratory model. They concluded that Calu-3 air-liquid interface cell culture was a sensitive and efficient model to e study human respiratory diseases, airway injury related to oxygen toxicity, and positive mechanical ventilation, and the evaluation of novel therapies. Also, they found that positive airway pressure triggered airway epithelial cells to secrete more proinflammatory mediators and showed more swollen nuclei and intracellular vacuoles. However, the effect of positive airway pressure by itself on the respiratory epithelium has not been investigated in any of the respiratory models previously described.

2.3 Modelling of the air-conditioning process

Air-conditioning is a natural transport process which controls the temperature and the humidity of the air during respiration process. During inspiration, air is in contact with the warm and moist nasal mucosa and is rapidly warmed and humidified [33]. This heat and mass transfer process is produced because a driving force is created by the difference in temperature and water concentration between the inspired air, which is at room temperature and humidity [36], and the mucus layer, which is at body temperature. The mucus layer is composed of 95% water and 5% of carbohydrate, protein, lipid and inorganic material [11, 33, 36].

Optimal gas exchange occurs when air reaches the lungs at 37°C with 100% relative humidity which corresponds to 44 mgH_2O/L. This is known as isothermal saturation boundary (ISB). Under this condition the physical properties of the mucus layer are optimized and the mucociliary transport is maximum. This process is a self-clearing mechanism of the respiratory system. The mucus covering the respiratory epithelium traps particulate material and pathogens, and the coordinated ciliary activity moves the layer and removes the particles trapped. In the nose the mucus is moved towards the pharynx, and in the tracheobronchial tree the mucus is moved towards and through the larynx and swallowed. An alteration in mucus rheology, which can be caused by a range of pathophysiological conditions, can affect the mechanical coupling of the cilia with the overlying mucus called airway surface liquid layer [2, 32].

One-dimensional (1D), two-dimensional (2D) and three-dimensional (3D) computational models for temperature and water vapour concentration have previously been developed to study air conditioning characteristics in the human respiratory tract. 1D and 2D models are the most popular methods due to their simplicity and efficiency, where air temperature and water vapour concentration are obtained by solving scalar transport equations and energy balance equations based on control volume analysis [33, 74]. 3D models are computationally more demanding because they provide detailed air distributions of velocities, temperature and water vapour concentration, but the computational time and model size is greater compared to 1D models [33, 74-79]. However, these models does not consider possible physiological changes in the respiratory epithelium such as alterations in mucus secretions, rheological properties, temperature variations or water content on the airway surface liquid (ASL) layer. They assume constant ASL properties from a healthy respiratory tract to perform the modelling and solve the equations.

2.4 Pressure Oscillations coupled with Continuous Positive Airway Pressure Therapy

To reduce tissue deformation, some research lines are focused on the possibility that many afferent neural receptors are stimulated by the vibration occurring during snoring. Plowman, L. *et at.* [80] developed their study to examine the arousal responses that high-frequency oscillating pressures have on upper airway muscles of awake and sleeping dogs focussing on the genioglossus, which is the muscle able to avoid the tong to relax and close the upper airways. They found that application of oscillating pressure waves at frequencies similar to those found during snoring but at less magnitude order (30 Hz and ± 3 cmH_2O), produced reflex responses that help maintain upper airway patency during sleep. Posteriorly, Zhang, S. *et at.* [81], Brancatisano, A. *et at.* [82], and Eastwood, P.R. *et at.* [83] arrived to similar conclusions. Their experiments were also carried out with dogs at 30 Hz and ± 2.5 cmH_2O, finding that the vast majority of laryngeal mechanoreceptors are activated in these conditions, and that the reflex augmentation of soft palate muscle activity may serve to dilate the retropalatal airway.

A further step was achieved performing these experiments on humans. Henke, K.G. *et at.* [84] applied high-frequency (30 Hz) and low-pressure oscillations (4 cmH_2O) to the upper airway, via a nose mask, on genioglossus, sternomastoid, and diaphragm activity measured by electromyogram in sleeping humans. An important finding was that 46% of the trials in the patients with sleep apnea, the genioglossus activity was increased producing a partial or complete reversal of the upper airway obstruction. However it is seen that using lower oscillations (1 cmH_2O), there was not any change in the upper airway muscle activity [85-91].

Following these scientific advances, an alternative to conventional CPAP is studied applying superimposed oscillation pressures in order to maintain the airway open [92-96]. The forced oscillation technique (FOT) is a non-invasive method which employs small-amplitude pressure oscillations superimposed on the normal breathing being a suitable tool for the monitoring of respiratory mechanics during mechanical ventilation and sleep. Randerath, W.J. *et at.* [97], Ficker, J.H. *et at.* [98], and Konermann, M. *et at.* [99], developed an auto-adjusting positive airway pressure based on forced oscillation technique (APAP-FOT) device able to match more accurately the pressure required from patients based on the measurement of upper airway impedance. These results show that APAP-FOT is as efficient as constant CPAP in the treatment of OSA, but as the pressure applied can be highly reduced, patients prefer APAP-FOT for home treatment. However, these studies do not show the relation between the pressure applied and the dryness effect if there is any.

2.5 Heated Humidifier coupled with Continuous Positive Airway Pressure Therapy

An intense research is done to solve the dryness side effect focussing on humidification because it is seen that dryness is alleviated with a rise in humidity on inspired air [100]. During quiet breathing at room temperature the nasal cavity heats the inspired air to 34°C and the air is humidified from 10 mgH_2O/L to 38 mgH_2O/L, and reaches 37°C and 44 mgH_2O/L in the main bronchi. During expiration it is found 36°C and 40 mgH_2O/L on the larynx, and 32-34°C and 27-34 mgH_2O/L on the nares [36, 101]. So a hypothetic failure in air-conditioning under CPAP therapy could be corrected introducing the inspired air close to 37°C and 44 mgH_2O/L [102].

Regarding the ability to increase the absolute humidity in the inspired air during CPAP, heated, non-heated and no-humidifiers are studied on healthy individuals at pressures of 5 mbar and 10 mbar measuring relative humidity and temperature of the air at the junction between CPAP tube and nose mask. The results, obtained under laboratory conditions, show that heated humidifiers are clearly superior to the others obtaining an absolute humidity of 30 mgH_2O/L, so 100% relative humidity at 30°C [103]. These results can be compared with those obtained by Randerath, W.J. *et at.* [104], where the relative humidity of the inspired air and the water loss during respiration between cold passover, heated humidifiers and without humidification under CPAP are compared. They also conclude that the best results are obtained with heated humidification, where water loss is reduced by 38% compared to cold humidification, and absolute humidity during inspiration is 21.3 ± 5.1 mgH_2O/L and 33.6 ± 3.5 mgH_2O/L during expiration. Also a comparison between two heated humidifiers adapted to CPAP is done between Somnowave®, Weinmann GmbH, Hamburg, Germany; and Fischer & Paykel, Inc., Auckland, New Zealand; showing that there is no significant difference between both, so they are suitable for the treatment of dry upper airways under CPAP therapy [105].

Another point of view is studied by Martins de Araújo, M.T. *et at.* [106] focussing on face mask instead of using the common nasal CPAP to avoid the effect of mouth leaks during CPAP therapy. Mouth leaks are particularly important because they cause unidirectional inspiratory nasal airflow and progressive drying of the nasal mucosa, due to air from the lungs not passing over the nasal mucosa. This by-pass promotes the release of inflammatory mediators, reduces efficiency of CPAP treatment, and increases nasal airway resistance (NAR). Then, an increase of NAR causes mouth leaks, which in turn, aggravates the problem by contributing to increase NAR setting up a cycle. Also, nasal inspiration is important for the defence against infiltrating particles and conditioning of the inspired air to alveolar conditions (saturated with water vapour at body temperature) in order to maintain the internal milieu of the lung by the time it reaches the pharynx [32]. Their results show that heated humidification reduces side effects such as NAR or dryness during therapy, but can be totally prevented by using a face mask. This becomes an alternative to cases when CPAP therapy using heated humidification does not correct dryness caused by mouth leaks in OSA patients.

It is important to consider that humidifier performance is very sensitive to ambient conditions, so all humidifiers coupled with CPAP have to be calibrated for each environmental situation [107, 108]. Also, it is seen that all these data agree with the minimum standards set for breathing machines in the UK which is 33 mg H_2O/L [109] and in USA is 30 mg H_2O/L [110], but the minimum humidity required to avoid dryness during CPAP therapy still unknown. Finally, as it is discussed during this section, heated humidification during continuous positive airway pressure is the treatment of excellence for obstructive sleep apnoea because it is able to avoid dryness as a side effect in most of the patients. However it fails to improve both the comfort and the acceptance of patients [111], so a further research to reduce the size should be investigated.

2.6 Hydrophobic and Hydrophilic Eco-Friendly Polymers

Focussing on alternatives to the humidifier coupled to CPAP therapy in order to reduce its size is reviewed in this section. It is important to analyse all previous work involved in eco-friendly materials able to absorb or retain only vapour or liquid water from a mixture [112-123].

Islam, M.R. *et at.* [124] evaluated the effectiveness of different rates of super absorbent polymers (SAP) as water-retaining materials in horticultural and agricultural fields due to these materials are able to retain large quantities of water and nutrients when incorporated with soil, and then the stored water and nutrients are released slowly as required by the plant in order to improve growth when limited water is supplied. They show on their results the optimum amounts of SAP and fertilizer needed for an appropriate corn production, but the amount of water absorbed and released is not evaluated and relevant to their work.

Then, Lin, N. *et at.* [125] developed crosslinked polysaccharide sponges prepared by freeze-drying of amorphous alginate−oxidized nanocellulose with Ca^{2+} ionic as a crosslinking agent improving the capacity of water absorption and retention. Although the water absorption is extended up to 1300%, their results show that after absorbing−discharging water for 10 times the structure of the sponge is disrupted. So a further research should be done in order to improve the reliability. Also a sodium carboxymethyl cellulose/graphene oxide nanocomposite film is synthesised and characterized by Yadav, M. *et at.* [126]. They report that the numerous hydroxyl and carboxylic groups in this material enable water binding and moisture sorption properties, but there is no experimental data provided.

Additionally, the polyvinyl alcohol (PVA) is studied by different research groups due to its biocompatibility, absence of toxicity, hydrophilicity, mechanical strength and flexibility, thermal stability, availability, and cheapness [127-129]. Polyvinyl alcohol composites with coconut shell (CCS) powder are tested for physicomechanical properties including moisture analysis. The PVA/CCS powder composite films show enhancement moisture resistance, but there is a decrease in the moisture content for plain PVA (12.07%) to PVA with 50 wt % CCS powder (9.38%), because PVA is more hydrophilic than that of CCS powder [130]. Karimi, A. *et at.* [131] report on their work that there is a lack of sufficient data on the mechanical properties of PVA sponges, so they provide an experimental analysis for swelling ratio of a custom-made PVA sponge (P-sponge) compared with two commercially available PVA sponges (CENEFOM and EYETEC). The results indicate that the swelling ratio of the P-sponge is 26.78% higher than that of the CENEFOM and EYETEC sponges, which is 1300%, 14 times its original weight. Also nanocomposite sponges are fabricated from starch and PVA reinforced with cellulose whiskers by Wang, Y. *et at.* [132]. The results revealed that the repeated freezing/thawing cycles induced larger pores and tougher walls emerged in the sponges, leading to a high swelling degree up to 1231% after water immersion. Finally, PVA/gelatin scaffolds in different concentrations are prepared and blended to evaluate the polymer concentration effects on the architecture of the scaffold by Choi, S.M. *et at.* [133]. Results indicate PVA/gelatin with gelatin concentration of 4% has the highest water adsorption, the sponge swell up to 1500% of its original weight in 1 minute, and reached equilibrium in 3 minute.

It is important to note that none of this water-absorbent and eco-friendly materials reviewed provide specific data related to water absorption, desorption or retention in a humid environment, only under water immersion. These experimental data are only found on works involving temperature-sensitive or thermo-responsive polymers.

2.7 Thermo-responsive polymers

Temperature-responsive polymers exhibit a volume phase transition at a certain temperature, which causes a sudden change in the solvation state. Polymers, which become hydrophobic upon heating, have a so-called Lower Critical Solution Temperature (LCST). Systems, which become hydrophilic upon heating, have an Upper Critical Solution Temperature (UCST). LCST and UCST systems are not restricted to an aqueous solvent environment, but only the aqueous systems are of interest for biomedical applications [134].

Typical LCST polymers are based on N-isopropylacrylamide (NIPAM), N,N-diethylacrylamide, methyl vinyl ether, and N-vinylcaprolactam as monomers. A typical UCST system is based on a combination of acrylamide and acrylic acid and its corresponding co-polymers [134].

Poly(N-vinyl caprolactam) possesses very interesting properties for medical and biotechnological applications, since it is soluble in water and organic solvents, biocompatible, has high absorption ability and a transition temperature of 33 °C. Poly(oxazoline)s suchas Poly(2ethyl2oxazoline) or Poly(2isopropyl2oxazoline), have a transition temperature around 62°C, which is too high for any drug delivery application. Poly(methyl vinyl ether) has a transition temperature at exactly 37°C, which makes it very interesting for biomedical application. Poly(acrylic acid-co-acrylamide) such as polyacrylic acid or polyacrylamide are examples of a system with UCST behaviour within the biomedical setting. The transition temperature is at 25°C. The UCST behaviour is caused by the cooperative effects coming from the hydrogen bonding between acrylic acid and acrylamide units. Elastin-like oligo- and polypeptides such us Poly(GVGVP)poly(pentapeptide) of elastin (G: Glycine, V: Valine, and P: Proline) can also show LCST behaviour, when hydrophilic and hydrophobic residues are well balanced. A polymer based on the pentapeptide GVGVP as repeating unit shows a volume phase transition at 30 °C, which is the hydrophobic folding and assembling transition. Below the phase transition, water molecules surround the polymer molecule, and the attractive forces weaken upon heating and go into the bulk phase [134].

Poly(N-alkylacrylamide)s such as poly(N-isopropylacrylamide) (PNIPAM), is the most prominent candidate as thermos-responsive polymer for our application. Poly n-isopropylacrylamide may be abbreviated as PNIPAM, PNIPAm, pNIPAm, PNIPA, pNIPA, PNIPAAm, pNIPAAm, PNIPAA, pNIPAA. PNIPAM is an eco-friendly and biocompatible polymer which undergoes a coil-to-globule transition (hydrophilic-to-hydrophobic) in aqueous solution at a specific temperature of 32°C (LCST). Below the LCST and in the presence of water, the PNIPAM structure is predominantly hydrophilic and the amide groups tend to form inter-molecular hydrogen bonds with the surrounding water molecules. Above the LCST, intramolecular hydrogen bonds between neighbouring amide groups within the PNIPAM polymer are formed, which are energetically more favourable at higher temperatures. This transition is accompanied with a change from coil-to-globule configuration [135]. PNIPAM is commonly used as copolymer in stimuli-responsive membranes, which change their physicochemical properties in response to changes in their environment such as temperature [136-139], and for the oral delivery of calcitonin and insulin. The peptide or hormone is immobilised in polymeric beads, which stay stable while passing through the stomach. Then in the alkaline intestine the beads disintegrate and the drug is released [134].

However, the structural changes of a temperature-responsive polymer combined with the highly rough surface of a fabric, leads to reversible and repeatable switching between two extreme wettability states, superhydrophobic and superhydrophilic, which were founded by Yang, H. *et at.* [140]. They covered the hydrophilic surface of a cotton fabric with the PNIPAM polymer layer whose chains will grow from the fibres surface with a concentric orientation creating a highly rough surface at the micrometre level. Their results show that this new material is able to absorb water from a humid environment, below the LCST (lower critical solution temperature) and release it upon a temperature change at constant humid air flow. At 23°C and ~96% of relative humidity, the PNIPAM-cotton showed a water uptake of approximately 340%, and at 34°C and ~96% of relative humidity, a minimal water uptake of 24% was registered. It is shown that this PNIPAM-cotton fabric is able to collect a substantial amount of water (~3.4 L/kg material) from a humid environment, however it should be further developed in order to evaluate the time response according to specific applications.

2.8 Research gaps and Objectives

The analysis of the past research has shown some limitations that have to be completed or further studied. During the review of the CPAP therapy it is seen that there is a lack of knowledge about how the respiratory epithelium, ASL layer water content and mucus secretion change under high pressures and turbulent effect provided by CPAP therapy or pressure oscillations. Regarding pressure oscillations coupled with continuous positive airway pressure therapy to prevent high tissue deformations, it is seen that it is as efficient as the constant CPAP therapy and the pressure applied is highly reduced, so it becomes the preferred treatment for OSAS patients. However, the studies reviewed do not show the relation between the pressure applied and the dryness effect if there is any. Focussing on the review on heated humidifiers coupled to CPAP therapy to prevent dryness as a side effect, it is observed that there are no minimum humidity standards set for CPAP machines, which would be very useful to provide the specific humidification that the patient needs. Also it is manifest that increasing the amount of water in inspired air dryness is prevented, but there is a discomfort and unacceptance from the patients that could be palliate reducing the size of the humidifier. Finally, some hydrophilic, hydrophobic and thermos-responsive eco-friendly and biocompatible polymers have been examined in order to explore an alternative to the commercial heated humidifier. The experiments reviewed show that PNIPAM is able to absorb and desorb water from the environment, but specific data related to amount of water absorbed and desorbed as a function of time should be experimentally quantified to develop a new device.

Therefore, the project is divided in two main parts, analyse the behaviour of the human respiratory epithelium under CPAP therapy and quantify the minimum humidity needed to avoid dryness side effect, and design a new alternative to the commercial heated humidifier used with the CPAP therapy to avoid dryness. Hence, the main objectives of this research are listed as follows:

1) Analyse the human respiratory epithelium deformation and inflammation, quantify the mucus secretion rate and quantify the minimum humidity needed to avoid dryness under CPAP therapy and pressure oscillations. To achieve the objective formulated, human airway epithelial Calu-3 cells and nasal RPMI 2650 cells grown in air-liquid interface (ALI) on permeable supports are used as *in-vitro* respiratory models. To simulate positive airway pressure (PAP) scenarios and human respiratory conditions, different setups will be used. The cell layer permeability and ASL thickness are measured to investigate cell integrity, compression and quantify the amount of water over-evaporated from the ASL after PAP application. Cell surface staining for mucus detection is evaluated to determine the mucus secretion rate. Finally, an enzyme-linked immunosorbent assay is performed to investigate the cell inflammation response after each experiment.

2) Formulate a simple, efficient, fast computing and realistic 1D human upper airway model to extrapolate the results obtained from the *in-vitro* respiratory models to the entire human upper airways. The model will be validated and optimized to predict the heat and water transfer variation between normal breathing and PAP conditions. Hence, water transfer will be measured comparing changes in temperature and relative humidity on the airflow under three PAP scenarios. At the end of this part, the results achieved will confirm or not the respiratory cell dysfunction and will quantify the minimum humidification needed to avoid dryness under CPAP therapy (temperature and relative humidity of the compressed airflow).

3) Develop a material able to uptake water from expiration and release it to the inspiration airflow using PNIPAM according to the literature review. The polymerization process and material properties will be optimized to achieve the maximum amount of water vapour uptake and release in the shortest time. The water desorbed will be in agreement with the minimum humidification needed to avoid dryness under CPAP therapy quantified on the previous objective.

4) Design a new alternative to the commercial heated humidifier used with the CPAP therapy to avoid dryness using the PNIPAM material optimized in the previous objective. A prototype able to absorb moisture from the expiration and desorb it on the inspiration airflow will be built and optimized. The device will be characterized and validated under clinical trials to confirm that it is able to overcome dryness with the moisture reintroduced from the expiration airflow and replace the commercial convective heated humidified.

2.9 Closure

In summary, the literature review has shown some lack of knowledge in each area studied such as how the respiratory epithelium, ASL layer water content and mucus secretion change under high pressures and turbulent effect provided by CPAP therapy or pressure oscillations. Also, it is observed that there are no minimum humidity standards set for CPAP machines, which would be very useful to provide the specific humidification that the patient needs or to reduce the size of the humidifier. Finally, PNIPAM properties are reviewed, but further experiments have to be developed to design a new device.

The research gaps detected in this study and hence the objectives of this research are addressed and accomplished in the next chapters of the thesis. The deformation and inflammation of the human respiratory epithelium, the quantification of the minimum humidity needed to avoid dryness and mucus secretion rate under CPAP therapy and pressure oscillations are analysed in chapter 3. Then, a simple, efficient, fast computing and realistic 1D human upper airway model is formulated, validated and optimized in chapter 4 to predict the heat and water transfer variation between normal breathing and PAP conditions to extrapolate the results obtained from the *in-vitro* models to the entire human upper airways and quantify the minimum humidification needed to avoid dryness under CPAP therapy. The structure, synthesis and properties of the PNIPAM are optimized in chapter 5 in order to achieve the maximum amount of water vapour uptake and release in the shortest time. In chapter 6, a miniaturized, affordable and eco-friendly self-humidifying device using the PNIPAM material able to humidify the inspired airflow up to the humidity levels required by using recovered moisture from expiration, warm the air and adjust the water delivered into the respiratory system is developed and its performance validated with 21 volunteers. Finally, the discussion of the results, conclusions and future work make up the last chapter 7 of the thesis.

Chapter 3

Respiratory epithelial cell behaviour under positive airway pressure

3.1 Introduction

Chapter 1 and 2 stated that the use of LSD devices normally results in dryness, sneezing, rhinorrhea, post-nasal drip, nasal congestion or epistaxis in the upper airways. It was hypothesized that the application of positive pressure may inhibit the natural air conditioning process and deform the respiratory epithelium, leading to disruption of the natural lubrication. This change could be elicited by an over-evaporation of the ASL water content due to the increase in volume to keep the airways opened or a blockage of goblet cells or mucus secretion glands due to the effect of the pressure on the airway epithelium. This may avoid the natural mechanism to restore the ASL layer properties such as mucus/water ratio concentration.

The purpose of this chapter is to test this hypothesis and analyse the human respiratory epithelium response under positive pressure. Human airway epithelial Calu-3 cells and nasal RPMI 2650 cells grown in air-liquid interface (ALI) on permeable supports are used as *in-vitro* respiratory models. To simulate positive pressure scenarios and human respiratory conditions, different setups have been used.

In the course of this investigation, trans-epithelial electrical resistance and apparent permeability coefficient have been calculated to analyse the cell barrier integrity and permeability. The cell layer and ASL thickness have been measured to investigate cell compression and quantify the amount of water over-evaporated from the ASL after PAP application. Cell surface staining for mucus detection has been evaluated to determine the mucus secretion rate. Finally, enzyme-linked immunosorbent assay

(ELISA) tests have been performed to investigate the cell inflammation response after each experiment.

The experiments were undertaken at Woolcock, Institute of Medical Research, University of Sydney, Sydney, Australia as part of the Respiratory Technology Group.

The materials and methodology used to grow Calu-3 and RPMI 2650 cells in ALI are discussed in section 3.2. Then, the 3D cell insert holder designs and experimental setups to generate different airflow trajectories under different pressure scenarios are detailed in sections 3.3 and 3.4. The methodology followed to perform the cells experiments is explained in section 3.5, followed by the statistical analysis in section 3.6. The analysis of the effect of the airflow trajectories and positive pressure profiles on the epithelial cells is explained in section 3.7. Finally, the discussion of the results and closure of the chapter are discussed in sections 3.8 and 3.9 respectively.

3.2 Cell Preparation

As stated before, in this part of the chapter the materials used and methodology followed for cell culture and preparation to develop two *in-vitro* human upper airway cell models are explained in detail.

3.2.1 Materials

The chemical products, reagents and materials used for cell preparation and experiments are listed below with their corresponding manufacturers, city and country of purchase.

Minimum Essential Medium and Dulbecco's Modified Eagle's medium/F-12 (x100) were purchased from Life Technologies (Sydney, Australia). Trypan blue solution (0.4%, w/v) and L-glutamine (200 mM) were obtained from Sigma-Aldrich (Sydney, Australia). Fluorescein-sodium (flu-Na) was purchased from May & Baker Ltd. (Dagenham, England). Fetal bovine serum (FBS), Hank's balanced salt solution (HBSS), and phosphate buffered saline (PBS) were from Gibco, Invitrogen (Sydney, Australia). Alcian blue 1% (pH 2.5) in 3% acetic acid was purchased from Fronine laboratory (Sydney, Australia). Transwell® cell culture inserts (0.33 cm^2 polyester, 0.4 μm pore size) and black 96-well plates were from Corning Costar (Lowell, MA, USA). ELISA enzyme immunoassay kit was purchased from BD Bioscience (Sydney, Australia). All other culture plastics were from Sarstedt (Adelaide, Australia). All chemicals and reagents were of the highest analytical grade.

3.2.2 Cell culture

Two *in-vitro* cell lines, human nasal and airway epithelial cells (RPMI 2650 and Calu-3 respectively), were used to simulate human upper airway conditions, as validated previously in the literature [141]. RPMI 2650 cells and Calu-3 cells were both purchased from ATCC (USA) and cultured in a microbiological safety cabinet using an aseptic technique to ensure the sterility.

- They were grown in 75 cm^2 flasks in a Minimum Essential Medium for Calu-3 cells and Dulbecco's Modified Eagle's medium/F-12 for RPMI 2650 cells, according to the manufacturer's protocol. Both mediums contained 10% (v/v) fetal bovine serum, 1% (v/v) non-essential amino acid solution, and 2 mM L-glutamine. Cells were incubated in a humidified atmosphere of 95% air and 5% CO_2 at 37°C and the medium was replaced three times a week. Cells were checked microscopically daily to ensure they were mainly attached to the bottom of the flask, healthy and growing as expected.

- When the 80% of the surface of the flask is covered by the cell monolayer (80% confluent), a sub-culturing is required. In this step, the confluent cell solution is divided or diluted according to the manufacturer's recommendations. In this case cells were passaged at a ratio of 1:3 (split ratio). This process is used to ensure that cells are ready for the experiment or to keep the cell culture running, otherwise cells become over confluent and start to die off. It is important to note that a high split ratio, more than 1:10, should not be used since the seeding density will be too low for the cells to survive. The media from the flask was carefully poured off and replaced with pre-warmed fresh culture media. A cell scraper was used to gently suspend all the cells attached to the bottom of the flask into the media. 1/3 (split ratio) of the cell suspension was taken into a new flask, topped up with pre-warmed fresh culture media and incubated in a humidified atmosphere of 95% air and 5% CO_2 at 37°C. Cells were ready for the experiments in 2-3 days.

- To grow RPMI 2650 cell on polyester transwells, 200 μL of 1 μg/mL collagen solution in PBS was added to the inserts, incubated and aspirated after 24 hours in order to coat the membranes before seeding. Then, 200 μL of each corresponding cell suspension at an initial density of 1.65 x 10^5 cells/insert was added into the transwell inserts (apical part) and incubated in a humidified atmosphere of 95% air and 5% CO_2 at 37°C. After 24 hours, the cells were attached to the transwell permeable membrane and an air-liquid interface (ALI) model [50, 57] was created by aspirating the apical medium and leaving the cells attached in contact to the environmental air. Cells were maintained with 0.5 ml of culture medium in the basolateral chamber. ALI process and transwell parts are described in Figure 3.1. The ALI conditions stimulated differentiation of the cell line. It is a process where a cell becomes more specialized, in this case to form a tight epithelial layer and develop goblet cells able to produce mucus. Cells were completely differentiated and ready for the experiments after 11 days [50, 57].

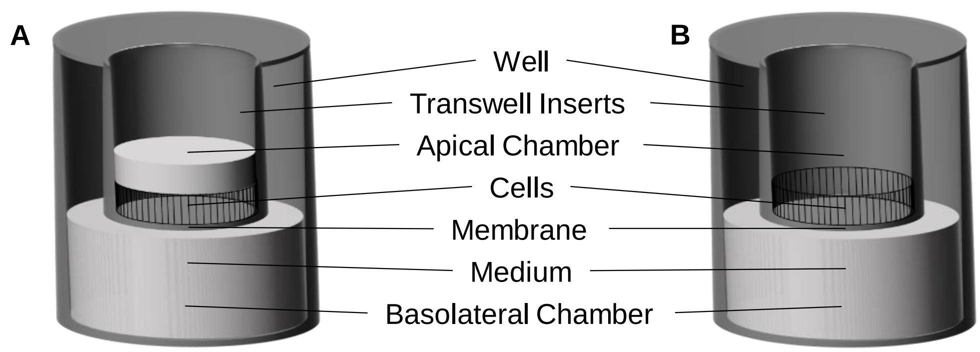

Figure 3.1. Description of ALI formation. A- 24 h after addition of cell-medium solution into the apical chamber for seeding, cells attach to the membrane. B- Apical medium is aspirated leaving the cells attached to the membrane to stimulate layer differentiation.

3.2.3 Cell viability assay

First, cell viability assay after PAP application was performed using trypan blue exclusion analysis to confirm cells could tolerate the pressure within the experimental times. This is an essential process in this protocol to ensure the validity of the results.

- Cells grown on transwells were exposed to 5, 10, 15 and 20 cmH_2O PAP for 8 hours, the longest experimental time.

- Subsequently, the cells were rinsed with PBS, detached from the membrane with trypsin, centrifuged and suspended in 1 ml medium.

- A 100 μl trypan blue (0.4%) and 500 μl cell solution were then added to a centrifuge tube and mixed thoroughly. The solution was allowed to incubate at room temperature for 5 min.

- Viable and non-viable cells were counted using a hemocytometer, a counting-chamber cell device. Cells exposed to 0 cmH_2O PAP (no-pressure applied) were used as control samples.

3.3 Cell holder design

Aiming to investigate the effect of the PAP on the upper airway human epithelial cells, two cell insert holders were designed, optimized and 3D printed to achieve the desired positive pressure application at specific airflow conditions on the cell lines. Computational fluid dynamics (CFD) flow simulations were performed on the two cell insert holder designs to ensure that the final geometry does not affect the achievement of the desired positive airway pressure inside the main cell insert chamber.

3.3.1 Geometrical modelling of 3D cell holders

The geometries of the two cell insert holders were reconstructed as 3D CAD models (Computer Aided Design) using a commercially available CAD software (SolidWorks® 2017, SolidWorks Corporation, Concord, USA). The basis for the reconstruction was to generate a simple smooth wall geometry based on the transwells and air compressor PAP device geometries. The main objective of the cell holder designs was to keep the desired positive pressure on the cell inserts under two compressed airflow conditions, static and dynamic flows. The holder designs are outlined in Figure 3.2.

The holder A is a closed-flow holder designed to generate a static positive pressure flow. It is made of a 600 cm^3 main chamber which includes a 24 well plate, two openings to allow sensor connections, one airflow inlet junction and a cover to seal it.

The holder B is a continuous-flow holder designed to simulate two dynamic flow trajectories. It is made of a 520 cm^3 main chamber which includes 8 wells, two openings to allow sensor connections, two airflow inlet junctions, one airflow outlet, whose geometry is optimized to generate the desired positive pressure, and a cover to seal the chamber. This holder also has an S-shape chamber or serpentine shape to connect a warm water recirculating bath for an extra temperature control and keep the transwells constant at 37°C hence avoid that changes in environmental temperature affect the behaviour of the cells.

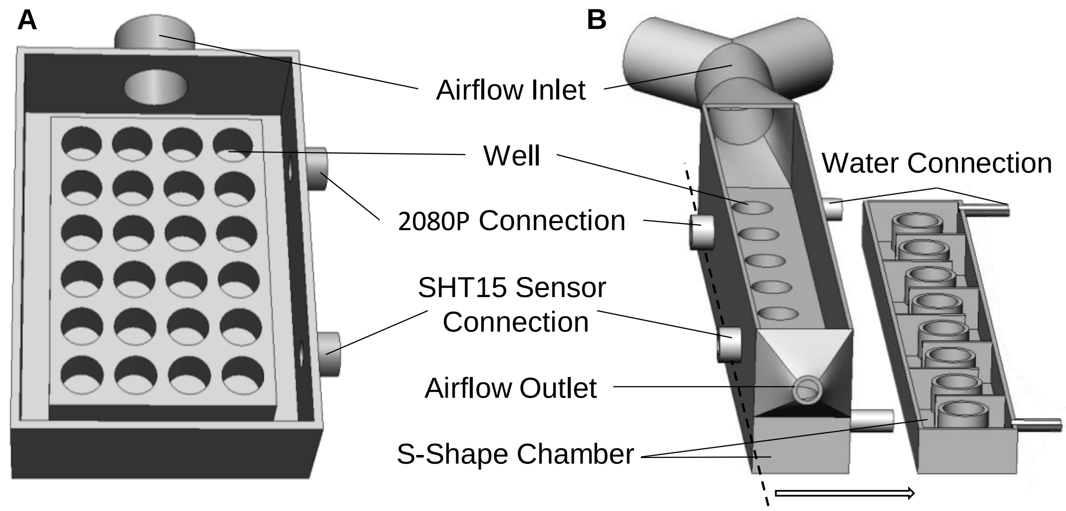

Figure 3.2. Sealed well holder designs, cover not included (not to scale). A- Closed-flow holder with one inlet connection to generate positive pressure onto the transwell inserts. B- Continuous-flow holder with two inlet connections and one outlet optimized to generate the same positive pressure as holder A. Contains an S-shape chamber to connect a water bath for an extra temperature control.

3.3.2 Computational airflow simulations of 3D cell insert holders

A commercially available computational fluid dynamics (CFD) software package, SolidWorks® Flow Simulation, was chosen to perform the 3D cell insert holder flow simulations and hence ensure that the final geometry does not affect the achievement of the desired positive airway pressure inside the main chamber.

A *k-epsilon* ($k - \varepsilon$) turbulence model was used to solve the steady-state momentum and conservation of mass equations. A hexahedral mesh was used to model the control volume and an advanced refinement was performed on the cell inserts surface area.

The CPAP airflow was assumed pure, dry, incompressible and isothermal airflow for physical modelling. The inlet flow was defined as a constant volume flow rate. According the CPAP device specifications, volume flow rates of 48.47, 53.95, 59.42 and 64.91 L/min to generate 5, 10, 15 and 20 cmH_2O respectively were simulated. The outflow condition of an environmental pressure, 10332.27 mmH_2O, was applied at the location corresponding to the outlet opening of the holder.

The static positive pressure flow was simulated using the holder A. At time 0 seconds, the airflow inlet is considered to be connected to the PAP device in order to introduce the compressed air into the main chamber, which accommodate the transwell inserts, until the selected pressure is reached. Then, the openings are considered sealed while the pressure profile is maintained on the cell inserts.

The first dynamic airflow trajectory was simulated using holder B. The PAP device was considered to be connected to one airflow inlet while the second one was considered closed and sealed. The desired PAP was reached on the transwell inserts while the compressed air was continuously flowing through the main cavity constantly over time.

The second dynamic airflow trajectory was simulated using holder B, and it is an extension of the previous one. The objective is to superimpose the PAP generated to the human breathing cycle. Hence, the second inlet is now considered to be connected to a lung simulator to generate a breathing cycle flow through the transwell inserts. A simple sinusoidal function, described in equation 3.1, was considered to simulate the breathing volume as a function of time ($Q_{BC}(t)$), where A corresponds to the tidal volume, volume of air inhaled and exhaled, which is assumed 500 ml + 500 ml = 1000 ml. The period of the signal (p) corresponds to the time needed to complete a single cycle and it was set at 6 seconds, and the residual human lung capacity, remaining volume of air in the lungs after a breath, was set at 2200 ml, therefore, the phase shift (y_0) corresponds to 2200 ml + 500 ml = 2700 ml [75].

$$Q_{BC}(t) = \left.\frac{A}{2}\right) \sin\left(\frac{2\pi}{p}\cdot t\right) + y_0 \tag{3.1}$$

Exemplary simulations of the three previously explained airflow trajectories are displayed in Figure 3.3. Flowrates of 48.47 and 53.95 L/min were used as input values to generate 5 and 10 cmH_2O, respectively. The pressure profile obtained in the main chamber with the three airflow trajectories (A, B and C) is in agreement with the theoretical targets (5 and 10 cmH_2O) and proves the validity of the geometrical design to achieve the desired positive airway pressure using the CPAP device.

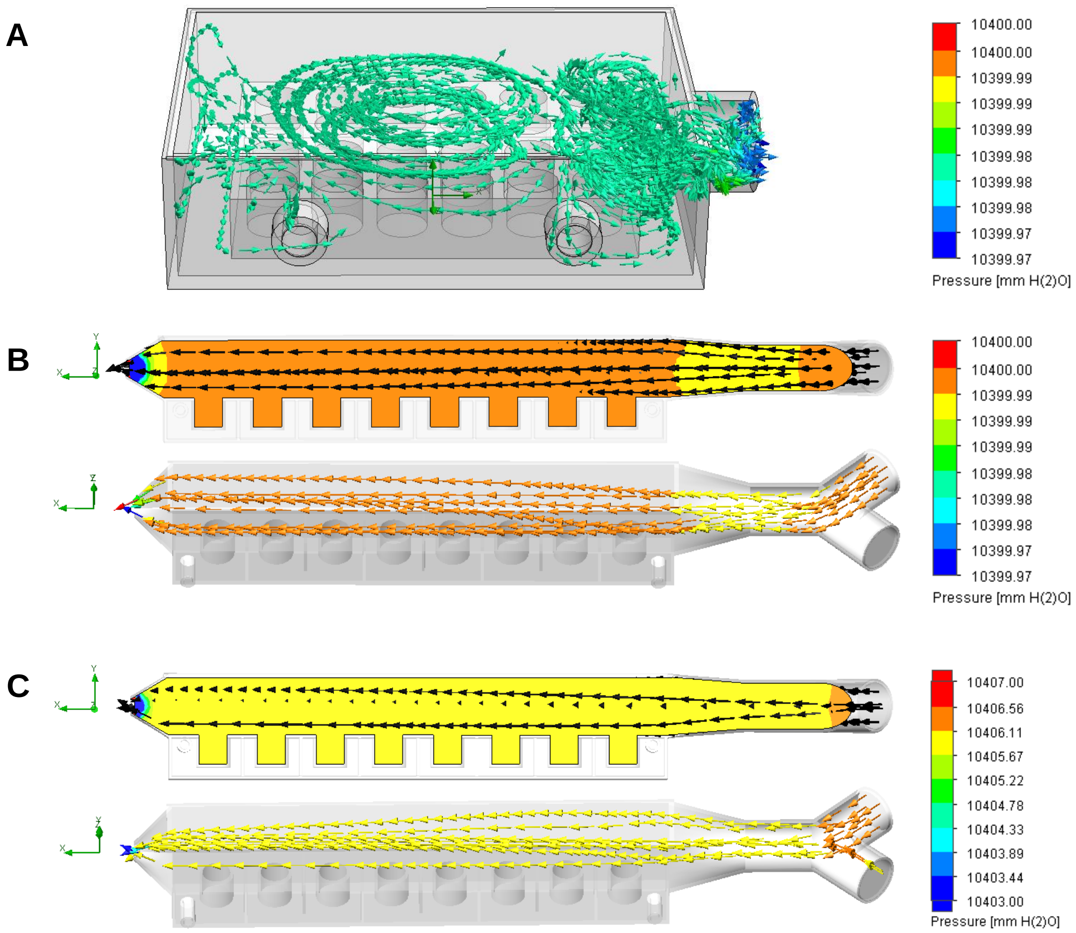

Figure 3.3. 5-10 cmH_2O SolidWorks flow simulations. A- CPAP Static flow simulation on holder A at time 0-1 seconds (filling the main chamber with compressed air). B- CPAP Dynamic flow simulation on Holder B where black arrows indicate the flow direction. C- CPAP and breathing cycle simulation (expiration part of the cycle) on holder B where black arrows indicate the flow direction. Absolute pressure values are displayed in mmH_2O. Ambient pressure is considered at 10332.27 mmH_2O.

3.3.3 Cell insert holder 3D printing and validation

Both cell insert holder 3D CAD files were saved in STL format and modelled with the EOS RP (Eos, Germany) software tools for 3D printing using the Formiga P 100

(Eos, Germany) plastic laser-sintering system. The 3D cell holders were printed in 5 hours at 5 m/s from polyamide.

The previously explained three airflow trajectories and 3D printed cell insert holders were validated using a 2080P digital manometer (Digitron, UK). The static positive pressure flow was validated using the holder A. Empty transwells were placed inside the holder, a commercial CPAP device (FP Healthcare, New Zealand) was connected to the inlet and the digital manometer was placed into the corresponding sensor inlet. Then, the main cavity was sealed and the CPAP device was set to generate 5, 10, 15 and 20 cmH_2O pressures. Pressure readings from the cell holder cavity were acquired as a function of time, up to 8 hours. Results showed that the previously set pressure from the CPAP device was maintained constantly for 8 hours, no leaks were found on the holder A.

The first dynamic airflow trajectory was validated using holder B. The CPAP device was connected to one airflow inlet while the second one was completely sealed leaving the outlet open. Empty transwells were placed inside the holder, the digital manometer was placed into the corresponding sensor inlet and the main chamber was carefully sealed. Then, the CPAP device was set to generate 5, 10, 15 and 20 cmH_2O pressures. Pressure readings from the cell holder cavity were acquired as a function of time, up to 8 hours. Results showed that the previously set pressure from the CPAP device was maintained constantly for 8 hours on the holder B while the compressed air was continuously flowing through the main cavity.

The second dynamic airflow trajectory was validated also using holder B. The CPAP device was connected to one airflow inlet and a commercial lung simulator (Hans Rudolph, USA) was connected to the second airflow inlet. The lung simulator was programed through the Hans Rudolph software to provide the flow rate specified in equation 3.1, where the tidal volume A was 1000 ml, the period of the signal p was set at 6 seconds and the residual human lung capacity y_0 was 2700 ml. Then, empty transwells were placed inside the holder, the digital manometer was placed into the corresponding sensor inlet and the main chamber was carefully sealed. The CPAP device was set to generate 5, 10, 15 and 20 cmH_2O pressures. Pressure readings from the cell holder cavity were acquired as a function of time, up to 8 hours. Results showed that the simulated values were maintained constant for 8 hours on the holder B while the compressed air was flowing through the main cavity.

3.4 Experimental setup

To investigate the effect of the PAP on the upper airway human epithelial cells, three experimental setups were designed to generate three gauge or relative (PAP) positive airway pressure scenarios on the cell lines. The three setups were placed inside an incubator at 37°C in all the experiments. As control, cells under the same experimental setting with ΔP = 0 cmH_2O pressure were used. The CPAP humidifier was used to set the desired airflow conditions and provide the specific temperature and humidity in each experiment. The experimental environmental conditions were monitored with the SHT15 temperature and humidity sensor (Sensirion AG, Switzerland) and the 2080P digital manometer (Digitron, UK). All experiments were performed in triplicate and the PAP exposure time was adjusted for each experiment.

3.4.1 Continuous positive pressure setup

The generation of continuous positive airway pressure (CPAP) was achieved using a CPAP device (FP Healthcare, New Zealand) connected to the custom-made cell holder A or B to maintain the desired pressure on the cells during the experiments. The PAP generated by the CPAP device to prevent airway collapse during an apnea episode ranges from 4 - 20 cmH_2O, hence 5, 10, 15 and 20 cmH_2O pressures were selected for the cells experiments. The setup is outlined in Figure 3.4.

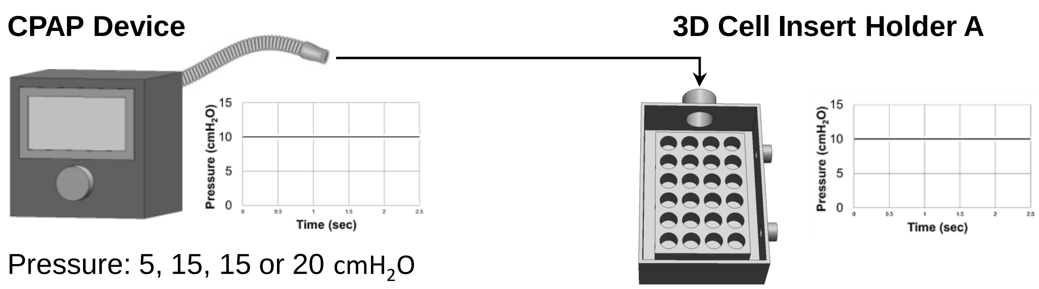

Figure 3.4. Schematic diagram to describe the process and set up to generate 5, 10, 15 or 20 cmH_2O continuous positive pressures on the cell lines. Pressure readings as a function of time were measured with the 2080P digital manometer. As an example, holder A and 10 cmH_2O continuous pressure are used in the diagram.

3.4.2 Superimposed pressure oscillations setup

To reduce tissue deformation, some research lines are focused on the possibility that many afferent neural receptors are stimulated by the vibration occurring during snoring [85-88]. Hence, the second scenario is an amplification of the first one, where a function generator AFG3120C (Tektronix, SW, USA) was connected to an electrodynamic vibration shaker (The Modal Shop, OH, USA) and a 125.66 cm^3 custom-made piston to produce a sinusoidal pressure variation superimposed to the 5, 10, 15 and 20 cmH_2O CPAP pressures, process described in Figure 3.5. According to previous literature findings on human genioglossus stimulation [85-88], a signal amplitude of ± 1 cmH_2O amplitude and three frequencies, 10, 20 and 30 Hz, were selected for the cell experiments.

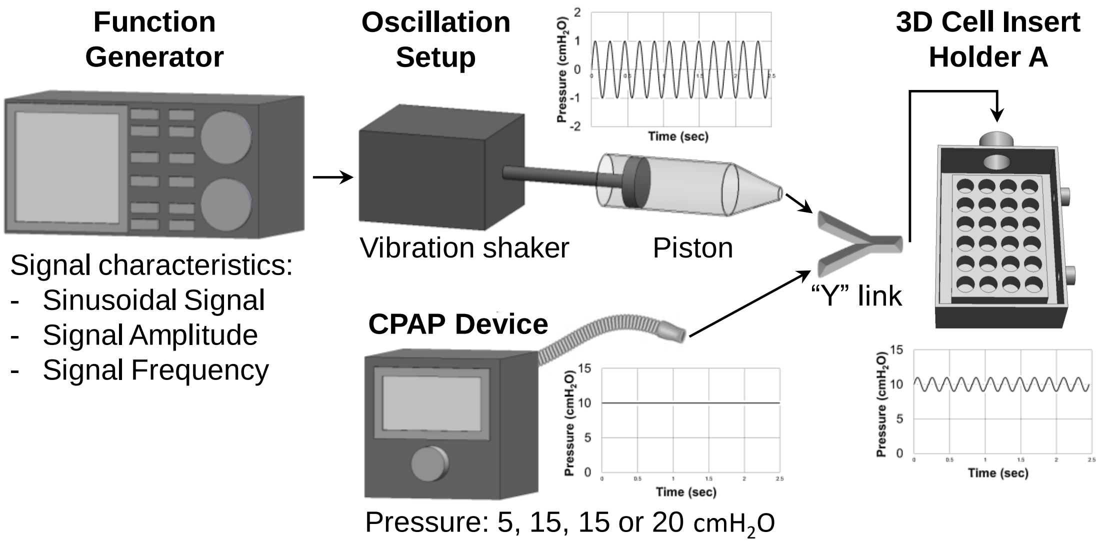

Figure 3.5. Schematic diagram to describe the process and set up to generate ± 1 cmH_2O sinusoidal pressure oscillation superimposed to 10 cmH_2O continuous pressures on the cell lines. Pressure readings as a function of time were measured with the 2080P digital manometer. As an example, holder A and 1 ± 10 cmH_2O continuous pressure at 10 Hz are used in the diagram.

3.4.3 Sinusoidal pressure oscillations setup

On the third scenario, the sinusoidal positive pressure oscillation by itself is generated using the function generator, the electrodynamic vibration shaker and the 125.66 cm^3 custom-made piston directly connected to the cell holder. An amplitude of 5 cmH_2O is selected to generate an intermittent pressure (from 0 to 5 cmH_2O) on the cells and compare the results with the 5 cmH_2O CPAP and the same three frequencies (10, 20 and 30 Hz) were selected for the cell experiments. The setup is outlined in Figure 3.6.

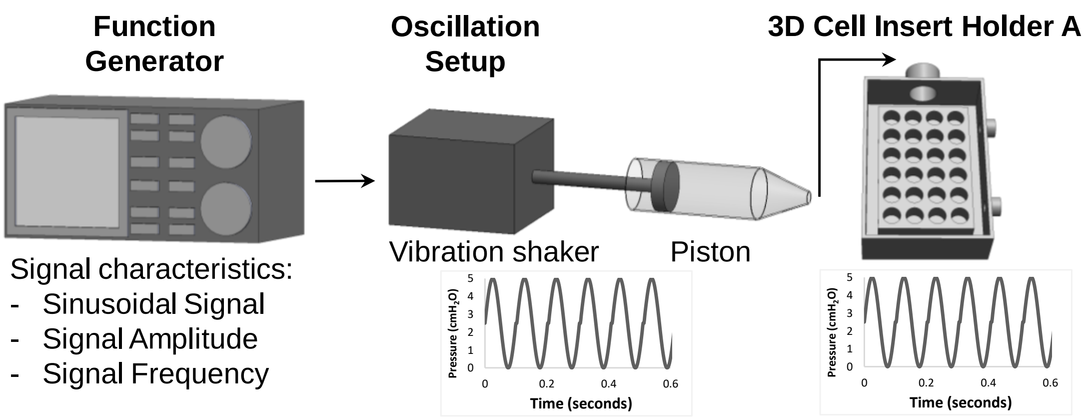

Figure 3.6. Schematic diagram to describe the process and set up to generate a sinusoidal pressure oscillation signal with 5 cmH_2O amplitude at 10, 20 or 30 Hz on the cell lines. Pressure readings as a function of time were measured with the 2080P digital manometer. As an example, holder A and sinusoidal pressure oscillation signal with 5 cmH_2O amplitude at 10 Hz are used in the diagram.

3.5 Experimental protocols

As stated at the beginning of this chapter, in this section of the methodology followed to carry on each experiment to investigate the effect of the PAP on the human upper airways is explained in detail.

3.5.1 Measurement of trans-epithelial electrical resistance (TEER)

To assess cell layer integrity and permeability, trans-epithelial electrical resistance (TEER) measurements were performed in real-time without cell damage using the electric cell-substrate impedance sensing system (ECIS®; Applied BioPhysics, Troy, NY). TEER values are based on measuring ohmic resistance or impedance across a wide spectrum of frequencies [142]. The amount of electrical current which flows is restricted by the amount of resistance (R) present, *i.e.*, the voltage incite the current to flow, but it is resistance that dampens it.

ECIS measurements use an alternating current (AC) signal, where the applied current (I) oscillates in a sinusoidal manner at determined frequencies through the electrodes. The resulting voltage (V) is measured and the impedance (Z) is given by the AC equivalent of Ohm's law: $Z = V/I$. Impedance can be written as a simple resistor and capacitor (RC) circuit, function of the pure resistance (R) and the reactive part (X_C), $Z = (R^2 + X_C^2)/2$. The last part is associated with the phase of the voltage relative to the current, $X_C = 1/(2\pi f C)$, which depends on the AC frequency (f) and the capacitance (C). Hence, ECIS measures changes in the total impedance (Z), pure resistance (R) and capacitance (C) of the cell layer over the time [143].

TEER was measured on the cells grown on transwells using an 8W ECIS filter adaptor, with a dipping electrode in the apical chamber and large electrodes at the base of the wells as shown in Figure 3.7.

- The ECIS device was placed inside an incubator at 37°C with 95% RH and 5% CO_2. Subsequently, 100 µl and 800 µl of PBS were added to the apical and basolateral chamber, respectively, as electrolyte solution to allow the transmission between the electrodes.

- Data was recorded every 5 minutes. TEER was measured for one hour before applying the pressure to collect the baseline resistance.
- Then, apical PBS was aspirated from all inserts, and PAP was applied on the cells for different times inside the incubator. Followed by adding 100 µl of PBS to the apical chamber and the resistance was measured consequently.

- Data was normalized by subtracting the resistance values from cell-free inserts and multiplied by the surface area of insert (0.34 cm^2) to obtain the TEER ($\Omega \cdot cm^2$) across the cells and ASL layer [143]. Data was analysed using ECIS software.

Since TEER values are strong indicators of the integrity of the cellular barriers, this measurement was used to evaluate the effect of the airflow trajectories on the cell layers and the effect of PAP on cell layer integrity and permeability, and airway surface liquid layer (ASL) thickness. A multi frequency analysis was performed to determine the best frequency to measure the most representative TEER values in each experiment. A low frequency of 1000 Hz, to allow the current pathway passing only through the cell junctions [144], was chosen to analyse cell layer integrity and permeability. A medium frequency of 4000 Hz, to allow the current pathway passing through the cell membrane and cell junctions [144], was chosen to analyse the effect of the airflow trajectories and the ASL thickness.

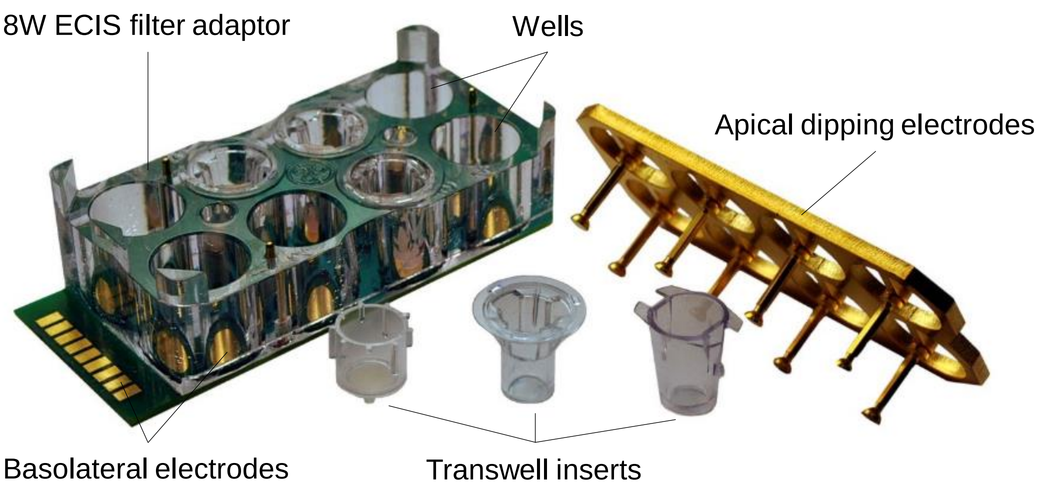

Figure 3.7. Commercial 8W ECIS filter adaptor from Applied BioPhysics to measure TEER as a function of time.

3.5.2 Measurement of Apparent Permeability (P_{app})

Experimental diffusion studies of the movement of molecules across biological cell lines are used to assess the barrier properties. Mathematically, molecular transport across a barrier is normally measured by fluxes, where the flux of a solute is defined as the mass or number of molecules moving through a defined cross-sectional area during a specific period of time.

Hence, paracellular fluorescein sodium (Flu-Na) transport across epithelial layer was conducted in apical to basolateral direction (A-B) to assess the barrier integrity and permeability of epithelia cell layers after PAP application.

- Followed by PAP application, 200 µL of 2.5 mg/mL Flu-Na solution was added on the apical chamber (donor), while the basal chamber (acceptor) was filled with 600 µL of PBS.

- At pre-determined time points up to 4 hours, 200 µL samples were taken from the basal chamber and replaced with fresh buffers to maintain sink conditions.

- Fluorescence reading of samples and standards were measured using a black 96-well Spectromax M2 plate reader with excitation/emission wavelengths of 485/520 nm. The calibration coefficient of determination was 0.999, with standards prepared between 1.25 and 0.0125 µg/ml. Cells exposed to 0 cmH_2O PAP (no-pressure applied) were used as a control.

The molecular transport across the cell barrier is caused by diffusion, a net transport of molecules in the presence of a concentration gradient, described by the Fick's first law. Samples were analysed and the apparent permeability coefficient (P_{app}) of flu-Na across the epithelial cell layer was calculated according to the simplified diffusion equation 3.2. Where V_{Basal} is the basal volume, $A_{Membrane}$ is area of the inserts membrane, C_{Apical} is the initial Flu-Na concentration and dC/dt is the flux of Flu-Na.

$$P_{app} = \left(\frac{V_{Basal}}{A_{Membrane}\ C_{Apical}}\right)\left(\frac{dC}{dt}\right) \tag{3.2}$$

3.5.3 Measurement of cell layer thickness

Total cell layer thickness (epithelial cell layer plus ASL layer) before and after PAP application was measured using the Nikon Eclipse Ti Time-Lapse Inverted Microscope (Nikon Instruments, NY, USA) in a humidified atmosphere of 95% air and 5% CO_2 at 37°C to avoid cell and ASL dryness.

- Transwell inserts were placed in the microscope and the height (z axis) from above the insert membrane to the top of the ASL layer was measured by choosing 14 points selected from cross-sectional surface on the XY plane.

- Then, PAP was applied in a humidified atmosphere of 95% air and 5% CO_2 at 37°C to keep the same environmental conditions and the total height was measured from each of the 14 points previously selected.

- The total height at 0 (measured before PAP application), 5 and 20 cmH_2O PAP was measured.

3.5.4 Pro-inflammatory marker expressions

The expression of cytokine proteins Interleukin-6 (IL-6), Interleukin 8 (IL-8) and Tumour necrosis factor alpha (TNF-α) after PAP application were evaluated only in

Calu-3 cells because RPMI 2650 cells do not express these pro-inflammatory cytokines [145]. IL-6 is produced in response to infections and tissue injuries and contributes to defence immune reactions [146]. IL-8 is a pro-inflammatory CXC chemokine linked to the promotion of degranulation and neutrophil chemotaxis, which is implicated in the pathogenesis of the adult respiratory distress syndrome (ARDS) [147]. TNF-α is involved in the regulation of immune cells and the inflammation in chronic obstructive pulmonary disease (COPD) [148].

- After PAP application on Calu-3 cells, 200 µl of medium was added into the apical part of the transwells and cells were incubated for 2 hours at 37°C with 95% RH and 5% CO_2.

- Then, 100 µl of the apical medium was collected and kept at -20°C until cytokine assays were conducted. Cells exposed to 0 cmH_2O PAP (no-pressure applied) were used as a control.

- Finally, IL-8, IL-6 and TNF-α markers were measured using ELISA enzyme immunoassay kits according to the manufacturer's protocol as detailed below.

- To prepare the standards and working detectors, after warming lyophilized standard to room temperature, the vial was carefully opened to avoid loss of material.

- The lyophilized standard was reconstituted with 1.0 mL of deionized water to yield a stock standard. The standard was equilibrated for 15 minutes and gently mixed before making dilutions. The standard was stored in polypropylene vials at 50 µl per vial and frozen at -80°C.

- A standard solution at 300 pg/mL was prepared from the stock solution. 300 µL assay diluent, which served as the zero standard (0 pg/mL), was added to 6 tubes previously labelled as 150 pg/mL, 75 pg/mL, 37.5 pg/mL, 18.8 pg/mL, 9.4 pg/mL, and 4.7 pg/mL. Serial dilutions were performed by adding 300 µL of each standard to the next tube and vortexing between each transfer.

- The detection antibody was added to the assay diluent and the enzyme reagent was added after 15 minutes mixing the solution properly.

The assay procedure to measure the concentration of cytokine proteins IL-6, IL-8 and TNF-α after PAP application is described below step by step:

- Microwells were coated with 100 μL per well of capture antibody previously diluted in coating buffer. Then the plate was sealed and incubated overnight at 4°C.

- The wells were aspirated and washed 3 times with 300 μL/well wash buffer. After last wash, the plate was inverted and blotted on absorbent paper to remove any residual buffer.

- The plates were blocked with 200 μL/well assay diluent and incubated at room temperature for 1 hour.

- The wells were again aspirated and washed 3 times with 300 μL/well wash buffer and blotted on absorbent paper to remove any residual buffer.
- Standards and sample dilutions in assay diluent were prepared. 100 μL of each standard, sample, and control were pipetted into appropriate wells. Then, the plate was sealed and incubated for 2 hours at room temperature.

- The wells were aspirated and washed 5 times with 300 μL/well wash buffer and blotted on absorbent paper to remove any residual buffer.

- 100 μL of working detector solution were added to each well and the plate was sealed and incubated for 1 hour at room temperature.

- The wells were aspirated and washed 7 times. Wells were soaked in wash buffer for 30 seconds to 1 minute for each wash and blotted on absorbent paper to remove any residual buffer.

- 100 μL of substrate solution was added to each well and the plate was incubated (without plate sealer) for 30 minutes at room temperature in the dark.

- 50 μL of stop solution was added to each well. Absorbance at 450 nm was read within 30 minutes of stopping reaction.

To calculate the results, the mean absorbance for each set of duplicate standards, controls and samples were calculated. The mean zero standard absorbance from each was subtracted. The standard curve on log-log graph was plotted, with IL-6, IL-8 or TNF-α concentration on the x-axis and absorbance on the y-axis. The best fit curve through the standard points was drawn. To determine the IL-6, IL-8 or TNF-α concentration of the unknowns, the unknown's mean absorbance value was found on the y-axis and a horizontal line to the standard curve was drawn. At the point of intersection, a vertical line to the x-axis was drawn and the IL-6, IL-8 or TNF-α concentration was read.

3.5.5 Cell surface staining for mucus detection

To evaluate the effect of pressure on the mucus secretion of both epithelial cells, alcian blue staining was performed. Alcian blue stains mucus glycoproteins allowing the visualization of mucus production [149].

- Already secreted mucus on the cells was removed by washing them three times with HEPES (hydroxyethyl piperazine ethane sulfonic acid)/PBS (50:50) [46, 53].

- Then pressure was applied for different times and the amount of secreted mucus was assessed by alcian blue staining.

- Cells were washed twice with 100 µL PBS and fixed using 2.5% w/v glutaraldehyde for 10 minutes.

- The cells were washed again with PBS and stained using 100 µL alcian blue (1% w/v in acetic acid, 3% v/v pH 2.5) for 1 hour.

- Cells were rinsed multiple times with PBS and air-dried overnight. The filter membrane was cut with a sharp point scalpel, mounted and sealed on glass slides.

Images were taken using an Olympus BX60 microscope equipped with an Olympus DP71 camera and analysed using Image J software (v1.42q, NIH). A three-dimensional colour space was produced representing the 8-bit red-green-blue (RGB) value of each image. The ratio of blue (RGB_B ratio) was calculated according to equation 3.3, where RGB_R, RGB_G and RGB_B correspond to the intensity of red, green and blue colour, respectively. The mean RGB_B ratio of ten images was used as a semi-quantitatively indication of the amount of mucus produced.

$$RGB_B\ Ratio = \frac{RGB_B}{RGB_R + RGB_G + RGB_B} \qquad 3.3$$

3.6 Statistical analysis

Statistical analysis was performed using GraphPad Prism software (GraphPad, San Diego, CA, USA) version 6.07 for windows using one-way and two-way analysis of variance (ANOVA), followed by Tukey post hoc analysis for multiple comparisons. Results are presented as mean ± standard deviation (SD) of three independent experiments (n = 3). To determine the significance of the results, a probability value (p value) between 0 and 1 is used to test the validity of a claim made about the parameter measured, which is called null hypothesis. Therefore, a small p value ($p < 0.05$) indicates strong evidence against the null hypothesis, which means that the null hypothesis is rejected and there is a significant difference on the parameter measured hence on the results (* $p < 0.05$, ** $p < 0.01$, *** $p < 0.001$ and **** $p < 0.0001$) [150, 151].

3.7 Results

To investigate the effect of the PAP on the cultured human epithelial cells, cell viability assay was firstly performed to prove that Calu-3 and RPMI 2650 cell lines were able to survive the positive pressure application within the experimental times. Then, the effect of the three airflow trajectories and three pressure scenarios was investigated.

3.7.1 Cell viability

Cell viability assay showed that applying 5, 10, 15 and 20 cmH_2O CPAP (continuous positive airway pressure) for 8 hours, maximum experimental time considered to avoid a bacterial contamination risk based on previous literature [46], to both cell lines did not cause significant cell death (p values of 0.9171, 0.4768, 0.9995 and 0.9986 for Calu-3 cells and 0.9525, 0.9761, 0.9526 and 0.9729 for RPMI 2650 cells, at 5, 10, 15 and 20 cmH_2O respectively). The percentage of viable cells after PAP application was compared to the control (no-pressure applied) in both cell lines as shown in Figure 3.8. Cell viability data indicates that both cell lines could survive the positive pressure application for 8 hours, the longest experimental time.

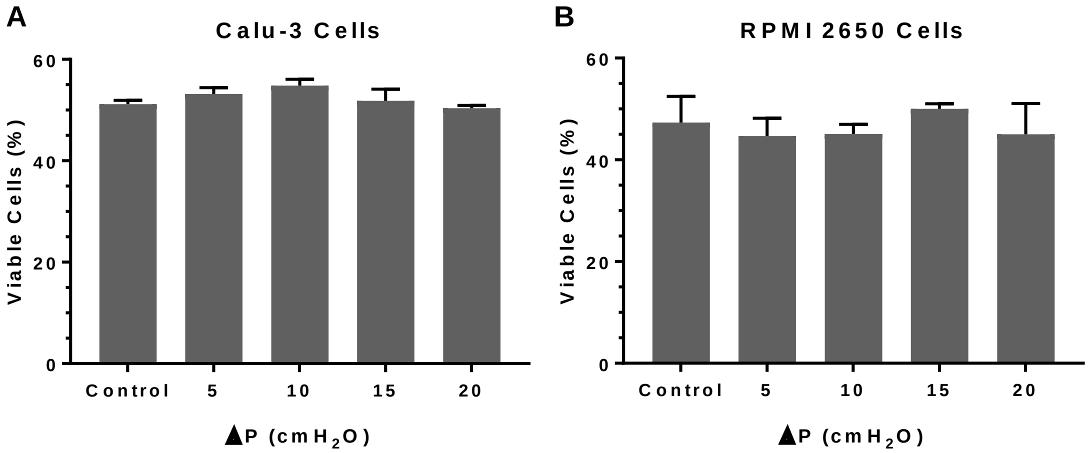

Figure 3.8. Viability of Calu-3 (A) and RPMI 2650 (B) cells after 5, 10, 15 and 20 cmH_2O of PAP application for 8 hours with trypan blue exclusion test. The percentage of viable cells after PAP application are not significantly different compared to the control in both cells lines.

3.7.2 Effect of airflow trajectories on upper airway cell lines

The effect of the three airflow trajectories previously described on both cell lines has been studied using both holder designs, the closed-flow holder A to simulate the PAP static flow and the continuous-flow holder B to simulate the continuous PAP dynamic flow and the superimposed human breathing cycle to the PAP dynamic flow.

Calu-3 and RPMI 2650 transwells were placed inside the corresponding holder and 20 cmH_2O of PAP (maximum pressure selected) was applied for 8 hours, maximum experimental time considered. The effect of the three airflow trajectories on the cell lines was investigated by measuring the TEER at 4000Hz using the ECIS apparatus after PAP application.

The results show that the TEER values increased significantly after PAP application compared to the control at ΔP of 0 cmH_2O in both holders and cell lines. However, no significant difference is found in TEER values at ΔP of 20 cmH_2O between the three airflow trajectories in both cell lines as shown in Figure 3.9 ($p \geq 0.9927$ for Calu-3 cells and $p \geq 0.9249$ for RPMI 2650 cells). This demonstrates that the airflow trajectory does not have any effect on the results in the experimental time frame considered. Hence, the static flow achieved with holder A (closed-flow holder) was chosen to generate the pressure on the transwells in the subsequent experiments.

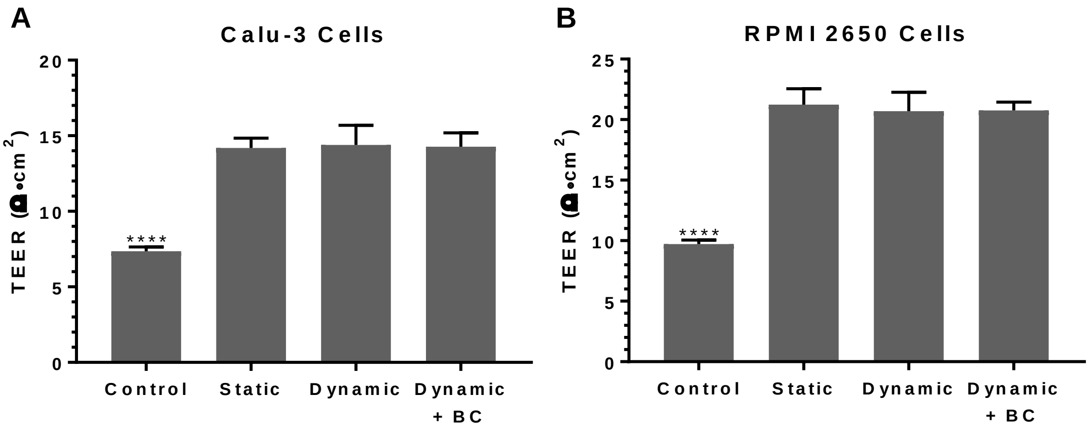

Figure 3.9. TEER measurements at ΔP=0 cmH_2O (Control) and ΔP=20 cmH_2O at 4000 Hz using the holder A to generate a static flow (Static) and B to generate the continuous PAP dynamic flow (Dynamic) and the superimposed human breathing cycle to the PAP dynamic flow (Dynamic + BC). A- TEER measurements for Calu-3 cells. B- TEER measurements for RPMI 2650 cells.

3.7.3 Effect of continuous positive pressure on human upper airway cell lines

3.7.3.1 Optimization of PAP application time to measure cell layer characteristics

The pressure application time is an important parameter to be considered for optimization in order to investigate the effect of PAP on the cell layer physiological characteristics. According to previous literature results, the time frame can vary from 5 minute to 72 hours depending on the experiment performed, the parameters selected for measuring or the methodology followed [46]. Hence, aiming to investigate the effect of the PAP on the cell layer integrity, permeability, thickness and inflammation, the minimum significant pressure application time is desired in order to avoid a bacterial contamination risk and avoid mucus secretion which would interfere in the parameter reading.

Calu-3 and RPMI 2650 transwells were placed inside the holder A and 20 cmH_2O of PAP (maximum pressure selected) was applied for four different times: 0 minutes (before pressure application and considered as a control), 10 minutes, 1 hour and 8 hours, according to previous literature results [46]. The effect of the PAP as a function of time on the cell lines was investigated by measuring the TEER at 4000Hz using the ECIS apparatus after each PAP application.

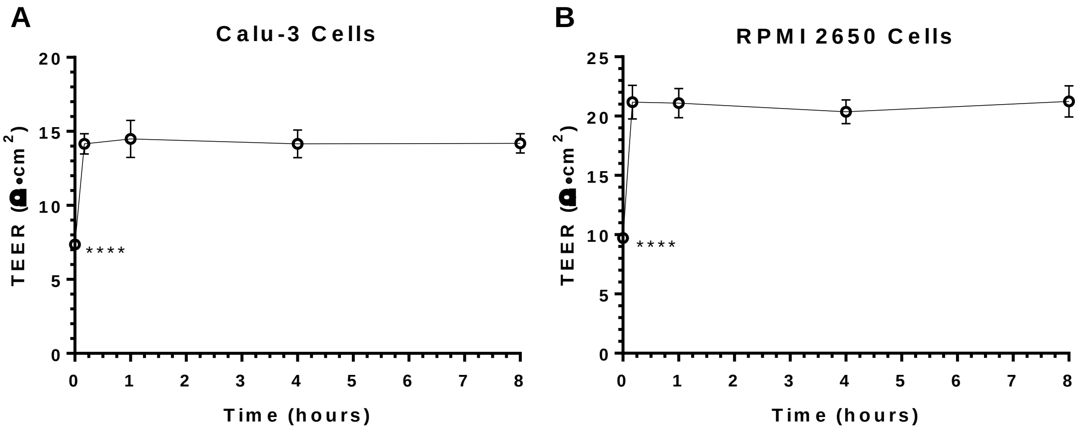

Figure 3.10. TEER measurements as a function of time cells at ΔP=20 cmH_2O and 4000Hz using the holder A. A- TEER measurements for Calu-3 cells. B- TEER measurements for RPMI 2650 cells.

The results showed that the TEER values increased significantly after 10 minutes of pressure application compared to the control at 0 minutes (no-pressure applied) in both cell lines. However, no significant difference is found in TEER values from 10 minutes to 8 hours of 20 cmH_2O PAP application in both cell lines as shown in Figure 3.10 ($p \geq 0.9871$ for Calu-3 cells and $p \geq 0.8683$ for RPMI 2650 cells). This demonstrates that 20 cmH_2O PAP applied for longer than 10 minutes does not have any effect on the TEER values in both cell lines. Hence, a PAP application time of 10 minutes was chosen to investigate the effect of the positive pressure scenarios on the cell layer integrity and permeability, and also cell layer thickness, ASL thickness and pro-inflammatory markers, in order to obtain all the parameters selected for measuring in the same time frame.

3.7.3.2 Measurement of trans-epithelial electrical resistance (TEER)

Cell layer integrity and electrical permeability on both cell lines after 5, 10, 15 and 20 cmH_2O CPAP (continuous positive airway pressure) for 10 minutes on holder A measured using the ECIS apparatus at 1000 Hz of frequency was evaluated and compared with no pressure controls (Figure 3.11). In both cell models, ECIS results showed a significant increase of TEER values after PAP application, which means that the electrons have a higher resistance to pass through the cell layer after 10 minutes of pressure application compared to the control where no pressure was applied. These results indicate that cell integrity is not affected, otherwise if the cell layer was damaged, lower TEER values compare to the control were expected.

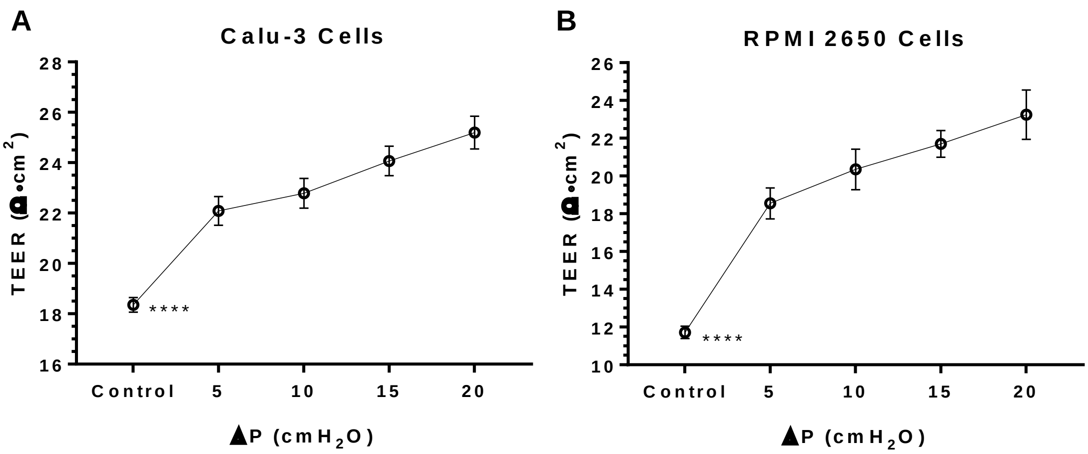

Figure 3.11. TEER measurements at Control ($\Delta P=0$ cmH_2O) and $\Delta P=$ 5, 10 15 and 20 cmH_2O at 1000 Hz using holder A. A- TEER measurements for Calu-3 cells. B- TEER measurements for RPMI 2650 cells.

3.7.3.3 Measurement of Apparent Permeability (P_{app})

Cell layer integrity and paracellular permeability on both cell lines after 5, 10, 15 and 20 cmH_2O CPAP (continuous positive airway pressure) for 10 minutes on holder A measured by Na-flu transport was evaluated and compared with no pressure controls (Figure 3.12). In both cell models, flu-Na transport across cell layer demonstrated a significant decrease of apparent permeability after PAP application, which means that both cell layers are less permeable to the paracellular markers after 10 minutes of pressure application compared to the control where no pressure was applied. These results indicate that cell integrity is not affected, otherwise if the cell layer was damaged, higher P_{app} values compared to the control were expected.

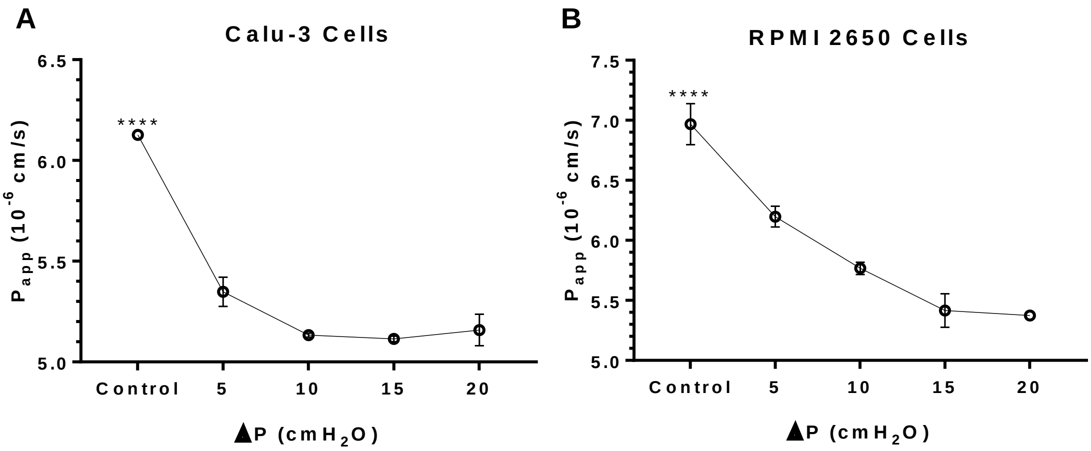

Figure 3.12. Apparent permeability coefficient (P_{app}) at Control (ΔP=0 cmH_2O) and ΔP= 5, 10 15 and 20 cmH_2O using holder A. A- P_{app} values for Calu-3 cells. B- P_{app} values for RPMI 2650 cells.

3.7.3.4 Measurement of cell layer thickness

Total cell layer thickness (y_{cell}, epithelial cell layer plus ASL layer) before and after 5 and 20 cmH_2O CPAP application for 10 minutes using holder A was measured using the Nikon Eclipse Ti Time-Lapse Inverted Microscope (Nikon Instruments, NY, USA) in a humidified atmosphere of 95% air and 5% CO2 at 37°C to avoid cell and ASL dryness. The Calu-3 and RPMI 2650 thickness results are shown in Figure 3.13.

Results show a significant thickness reduction after both pressure applications, which means that the PAP is able to compress significantly both cell lines while they are alive (see cell viability results in section 3.7.1).

This finding proves that the epithelial cell layer can be considered as a compressible material, and hence the elastic properties of Calu-3 and RPMI 2650 cell lines under pressure can be determined with the bulk modulus. Bulk modulus (B) is the measure of the ability to resist changes in volume under compression, and is equal to the quotient of the applied pressure divided by the relative deformation, strain or volume reduction. Therefore, a material easy to compress has a low bulk modulus and high compressibility [152, 153]. The bulk numerical constant is calculated mathematically according to equation 3.4, where ΔP and ΔV correspond to the relative positive pressure and epithelial cell volume decreases respectively from the control to 5 and 20 cmH_2O CPAP application. The volume variation is substituted with the thickness variation (y_0 and y_1, the total thickness measured before and after pressure application respectively) because the transwell cell insert surface area ($A, 0.34\ cm^2$) is not affected by the positive pressure.

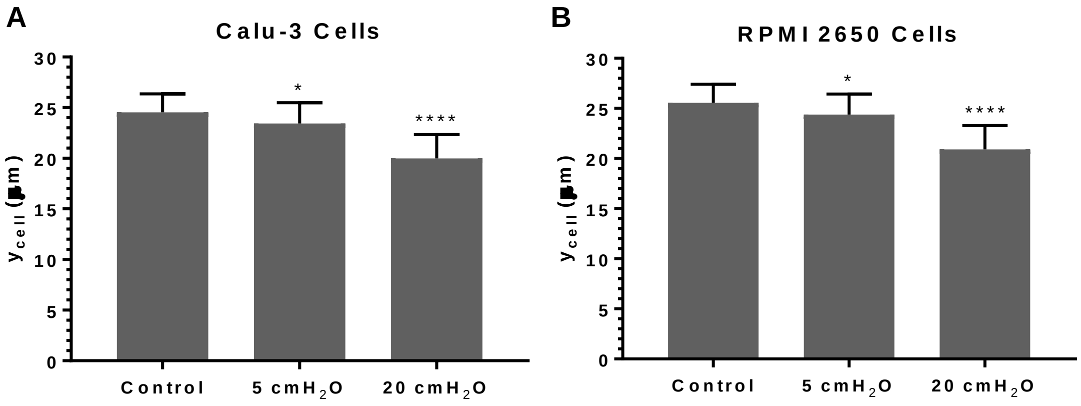

Figure 3.13. Total epithelial cell thickness (y_{cell}, epithelial cell layer plus ASL layer) measured before (control) and after 5 and 20 cmH_2O of CPAP application for 10 minutes. A- y_{cell} values for Calu-3 cells. B- y_{cell} values for RPMI 2650 cells.

$$B = -\frac{\Delta P}{\frac{\Delta V}{V_0}} = -\frac{\Delta P}{\frac{A \cdot y_1 - A \cdot y_0}{A \cdot y_0}} = -\frac{\Delta P}{\frac{y_1 - y_0}{y_0}} \quad (3.4)$$

The resulting bulk modulus obtained at 5 and 20 cmH_2O CPAP for Calu-3 and RPMI 2650 cell lines are displayed in Table 3.1. All the calculated bulk modulus for each pressure and cell line are in the same order of magnitude and in agreement with the tracheal respiratory tissue bulk modulus determined in previous studies [152, 153].

Table 3.1. Bulk modulus for Calu-3 and RPMI 2650 cell lines under 5 and 20 cmH_2O CPAP calculated from the total epithelial cell thickness (y_{cell}) variation measured experimentally.

ΔP (cmH_2O)	***ΔP (kPa)***	**Bulk Modulus *(kPa)* Calu-3 Cells**	**Bulk Modulus *(kPa)* RPMI 2650 Cells**
5	0.491	10.833	10.529
20	1.964	10.548	10.778

3.7.3.5 Measurement of airway surface liquid layer (ASL) thickness variation

To investigate the effect of CPAP on the human upper airway dryness and estimate the ASL water content variation or over-evaporation, the ASL thickness was measured for the first time with the ECIS apparatus. The pure electrical resistance (R), used to determine the TEER values as described in section 3.5.1, also depends on other factors such as temperature, thickness or length, conductor material properties or cross-sectional area. By definition, the electrical resistance (R), and consequently TEER, is described mathematically in equation 3.5, where A corresponds to the cross-sectional area of the electron flow (the effective area of the transwell semipermeable membrane in this case), ρ corresponds to the conductor material electrical resistivity (cell line and ASL layer electrical resistivity) and L corresponds to the length between the electrodes or the thickness of the conductor material (cell layer thickness).

$$TEER\ (\Omega \cdot cm^2) = R\ (\Omega) \cdot A(cm^2) = \ \rho\ (\Omega \cdot cm) \cdot L(cm) \qquad 3.5$$

Hence, the TEER values measured with the ECIS apparatus are proportional to the cell layer thickness (L), since the temperature, the effective area of the transwell semipermeable membrane (A), and the cell layer electrical resistivity (ρ) are constant in all the experiments.

Two humidity scenarios were simulated to measure the thickness variation of the ASL with the ECIS apparatus. The first one was a reference measurement where the CPAP humidifier was set to provide a water saturated compressed airflow at 30°C and 100% RH while the cells where incubated at 37°C (body temperature) in order to generate liquid-vapour equilibrium and annul the water transfer flow between the ASL and the water saturated CPAP airflow. Hence, the cell lines are only exposed to the CPAP compression effect. Second scenario, the CPAP device and humidifier were set to provide pressurized air at 30°C (room temperature) and 70% RH, while the cells where incubated at 37°C to simulate the natural human upper airway conditions [33]. In this case the cell lines are exposed to the CPAP compression effect and the water transfer flow between the ASL and the environment. Therefore, the difference between both scenarios reflects the water transfer thickness variation at each ΔP.

Subsequently, the electrical resistance (TEER) across the monolayer was measured on both cell lines at 4000Hz using the ECIS apparatus after PAP application on holder A at ΔP of 0 (control), 5, 10, 15 and 20 cmH_2O for 10 minutes.

Data on both humidity scenarios and cell lines are shown in Figure 3.14. TEER values increase significantly ($p<0.0001$) with ΔP compared to the control (ΔP of 0) in both cell lines and humidity scenarios, similar to the TEER values measured at 1000 Hz. Looking at both humidity curves, it is seen that the reference curve (100% RH) has significantly higher values compared to the 70% RH curve in both cell lines. Hence, as previously described, the difference between the TEER values at 100%

RH and 70% RH is used to determine the thickness variation of the ASL at each PAP applied in both cell lines.

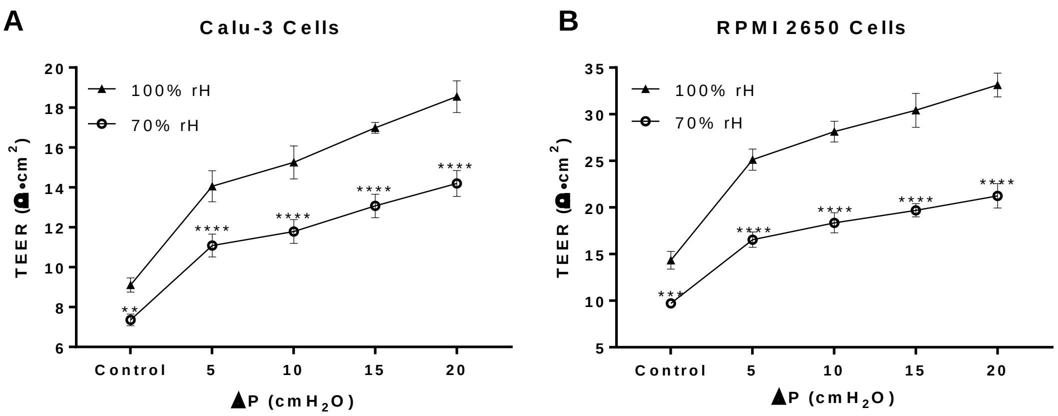

Figure 3.14. TEER measurements at Control (ΔP=0 cmH_2O) and ΔP= 5, 10 15 and 20 cmH_2O using holder A and at two RH: 100% RH (thickness reference) and 70% RH (upper airway conditions). A- TEER measurements for Calu-3 cells. B- TEER measurements for RPMI 2650 cells.

A mathematical explanation of this calculation is outlined in Figure 3.15, where the TEER is divided in two main components, the resistance across the epithelium or cell layer (R_E) and the resistance across the ASL layer (R_{ASL}). Focussing on the control measurements (first column) where no pressure is applied on the cells, it is seen that the resistance component across the epithelium layer remains constant for both humidity scenarios ($R_{E_{0,100}} = R_{E_{0,70}} = R_{E_0}$), and only the resistance across the ASL layer at 70% RH is reduced due to the natural water transfer effect or air conditioning process ($R_{ASL_{0,100}} > R_{ASL_{0,70}}$).

Regarding measurements after PAP application ($\Delta P \neq 0$) (second column), cells under 100% RH and 70% RH environmental conditions are equally compressed showing the same resistance across the epithelium layer, but higher TEER values compared to control, because compressed cells have tighter junctions which hinder the electrical current flow, increasing the resistance ($R_{E_{\Delta P,100}} = R_{E_{\Delta P,70}} = R_{E_{\Delta P}} > R_{E_0}$). The water transfer effect is also only observed at 70% RH where the resistance across the ASL layer is lower than at 100% RH due to the ASL thickness reduction ($R_{ASL_{\Delta P,100}} > R_{ASL_{\Delta P,70}}$).

In summary, comparing the TEER values obtained from each RH analysed, it was observed that the difference between the control and PAP application at 100% RH describes only the cell compression effect ($TEER_{0,100} < TEER_{\Delta P,100}$). The natural water transfer effect is quantified comparing both controls ($\Delta P = 0$) measured under 100% RH and 70% RH, where TEER is reduced due to ASL thickness reduction ($TEER_{0,100} > TEER_{0,70}$). Finally, dryness or over-evaporation effect produced by the increase in air volume due to PAP generation ($\Delta P \neq 0$) is quantified comparing TEER values measured at 100% RH and 70% RH ($TEER_{\Delta P,100} > TEER_{\Delta P,70}$).

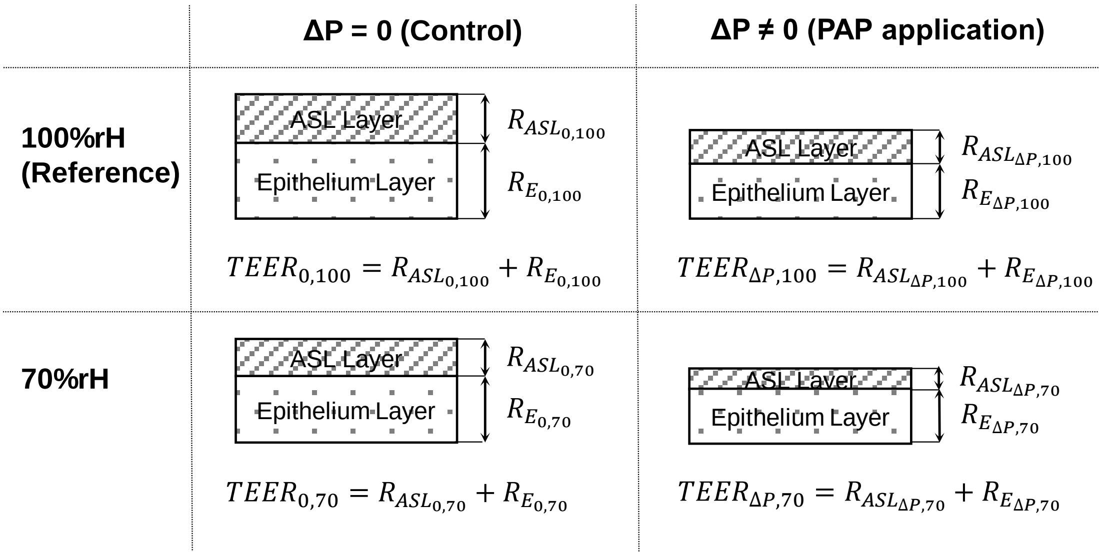

Figure 3.15. A schematic representation of the resistance measured (TEER) and its ASL and epithelium components of the four scenario analysed: ΔP=0 at 100% RH, ΔP=0 at 70% RH, ΔP≠0 at 100% RH, and ΔP≠0 at 70% RH.

The dimensionless ASL thickness reduction is calculated from $TEER_{\Delta P,100}$ (reference) to $TEER_{\Delta P,70}$ for each ΔP analysed in both cell lines according to equation 3.6. The ASL dryness or over-evaporation after PAP application is calculated comparing the previously calculated dimensionless ASL thickness reduction at each ΔP with the control ($\Delta P = 0$) according to equation 3.7. The results obtained are summarized in Table 3.2.

$$ASL\ reduction = \frac{TEER_{\Delta P,100} - TEER_{\Delta P,70}}{TEER_{\Delta P,100}} \qquad 3.6$$

$$ASL\ over-evaporation = \frac{TEER_{0,100} - TEER_{0,70}}{TEER_{0,100}} - \frac{TEER_{\Delta P,100} - TEER_{\Delta P,70}}{TEER_{\Delta P,100}} \qquad 3.7$$

Table 3.2. ASL reduction percentage results for Calu-3 and RPMI 2650 cells due to water transfer effect only (no compression) calculated using experimental TEER data mean for each ΔP. ‡ control measurement, represents the natural water transfer ASL thickness reduction necessary to achieve the air conditioning process.

ΔP cmH_2O	*Calu-3 ASL reduction (%)*	*RPMI 2650 ASL reduction (%)*	*Calu-3 ASL over-evaporation (%)*	*RPMI 2650 ASL over-evaporation (%)*
0 ‡	19.26	32.22	0.00	0.00
5	21.14	34.13	1.88	1.91
10	22.71	34.78	3.45	2.56
15	23.06	35.26	3.80	3.04
20	23.45	35.89	4.19	3.68

3.7.3.6 Measurement of pro-inflammatory marker expressions

The expression of cytokine proteins Interleukin-6 (IL-6), Interleukin 8 (IL-8) and Tumour necrosis factor alpha (TNF-α) have been measured on Calu-3 cells after 5, 10, 15 and 20 cmH_2O CPAP for 10 minutes under 100% RH and 70% RH environmental conditions using holder A and compared with the control at 0 cmH_2O (no pressure applied on the cells).

The concentration of each inflammatory marker from Calu-3 cells as a function of each CPAP pressure applied (ΔP) for both humidity scenarios are shown in Figure 3.16, Figure 3.17 and Figure 3.18. It is seen that the concentration of IL-6 and IL-8 increases significantly after CPAP application and remains stable independently of the ΔP applied. There is not a significant difference on IL-6 ($p \geq 0.800$) or IL-8 ($p \geq 0.1263$) concentrations between both humidity scenarios. TNF-α concentration results do not show any significant increase after CPAP application compared to the controls ($p \geq 0.5169$ and $p \geq 0.6069$ for 70% RH and 100% RH, respectively) and between the humidity scenarios ($p \geq 0.4051$).

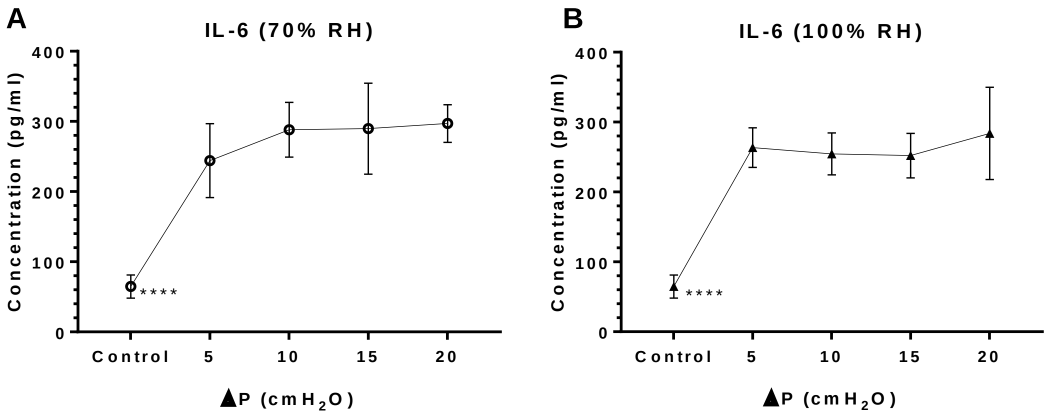

Figure 3.16. IL-6 concentration of Calu-3 cells at Control (ΔP=0 cmH_2O) and ΔP= 5, 10 15 and 20 cmH_2O using holder A for 10 minutes. A- CPAP flow at 70% RH and 30°C (human upper airway conditions). B- CPAP flow at 100% RH and 30°C (thickness reference and water saturated conditions).

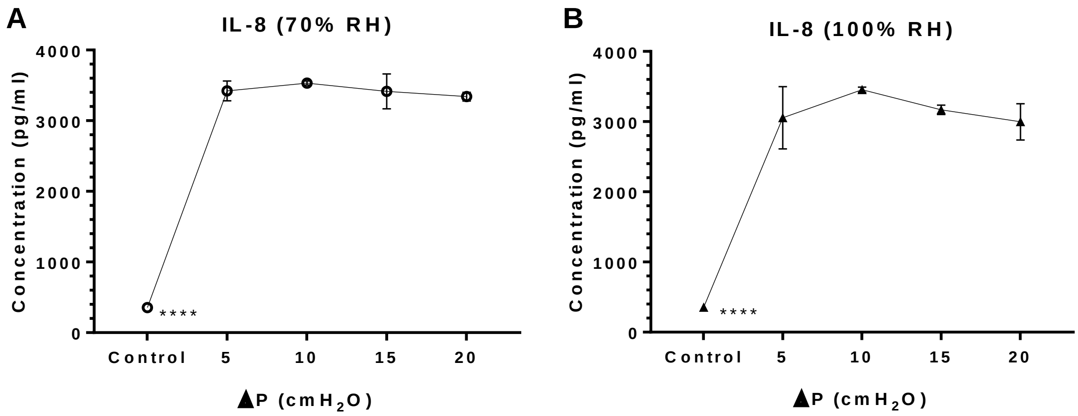

Figure 3.17. IL-8 concentration of Calu-3 cells at Control (ΔP=0 cmH_2O) and ΔP= 5, 10 15 and 20 cmH_2O using holder A for 10 minutes. A- CPAP flow at 70% RH and 30°C (human upper airway conditions). B- CPAP flow at 100% RH and 30°C (thickness reference and water saturated conditions).

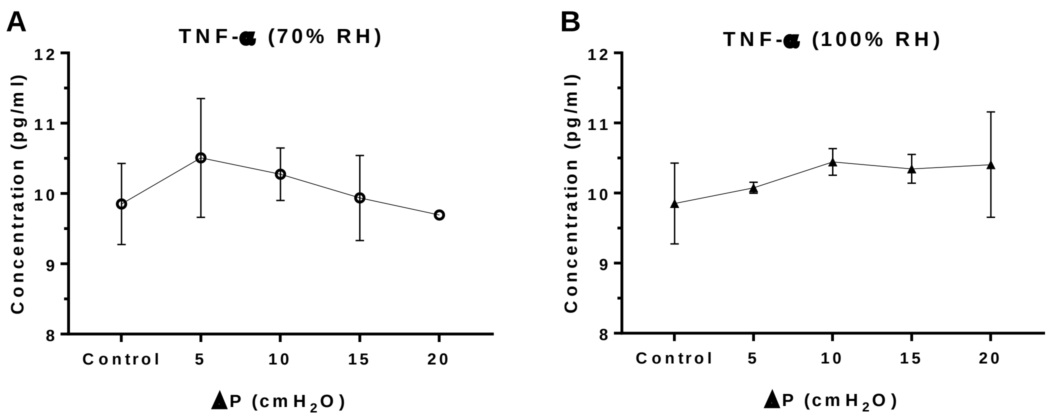

Figure 3.18. TNF-α concentration of Calu-3 cells at Control (ΔP=0 cmH_2O) and ΔP= 5, 10 15 and 20 cmH_2O using holder A for 10 minutes. A- CPAP flow at 70% RH and 30°C (human upper airway conditions). B- CPAP flow at 100% RH and 30°C (thickness reference and water saturated conditions).

These results indicate that Calu-3 cells are inflamed, increasing significantly the IL-6 and IL-8 marker concentrations, after 10 minutes of CPAP application independently of the ΔP applied. Also, it has been proved that the increase in RH can alleviate the ASL dryness or over-evaporation effect, as explained in section 3.7.3.5. However, the increase in RH does not have any effect on the inflammatory marker concentration, Calu-3 cells are equally inflamed at 70% RH than at 100% RH.

3.7.3.7 Optimization of PAP application time to measure mucus secretion rate

The pressure application time has been previously optimized to investigate cell layer integrity, permeability, thickness and inflammation. However, to investigate the effect of the CPAP on the mucus secretion rate, the pressure application time has to be increased and adjusted for this experiment since cell mucus production is a slow physiological process [149].

As previously aimed, the minimum significant pressure application time is desired in order to avoid a bacterial contamination risk. Hence, Calu-3 and RPMI 2650 transwells were washed three times with HEPES to remove the already secreted mucus at time 0 hours. The cell surface was stained to quantify the remaining amount of mucus after washing process, the absolute minimum amount of mucus. Then, cells where incubated at 37°C with 95% RH and 5% CO_2 for 1, 8, 24 and 48 hours with no pressure (0 cmH_2O) and stained. Finally, transwells cultured for 15 days (360 hours) and not washed with HEPES, were stained in order to visualize the absolute maximum amount of mucus. The amount of mucus produced, intensity of blue colour (RGB_B ratio), as a function of time on both cell lines under no CPAP pressure (0 cmH_2O) are shown in Figure 3.19.

The results showed that the RGB_B Ratio values increased linearly as a function of time. The first significant RGB_B Ratio value is found after 8 hours of incubation compared to the control at 0 hours in both cell lines. Hence, to significantly measure how the mucus secretion rate is influenced by the CPAP application, transwells are incubated for 8 hours after washing the already secreted mucus under 5, 10, 15 and 20 cmH_2O CPAP and 0 cmH_2O CPAP as control. This 8 hours of PAP application time is used exclusively to quantify the mucus secretion rate, on the other experiments (cell layer integrity and permeability, cell layer and ASL thickness, and pro-inflammatory markers) transwells are only exposed to 10 minutes of PAP in order to avoid a bacterial contamination risk.

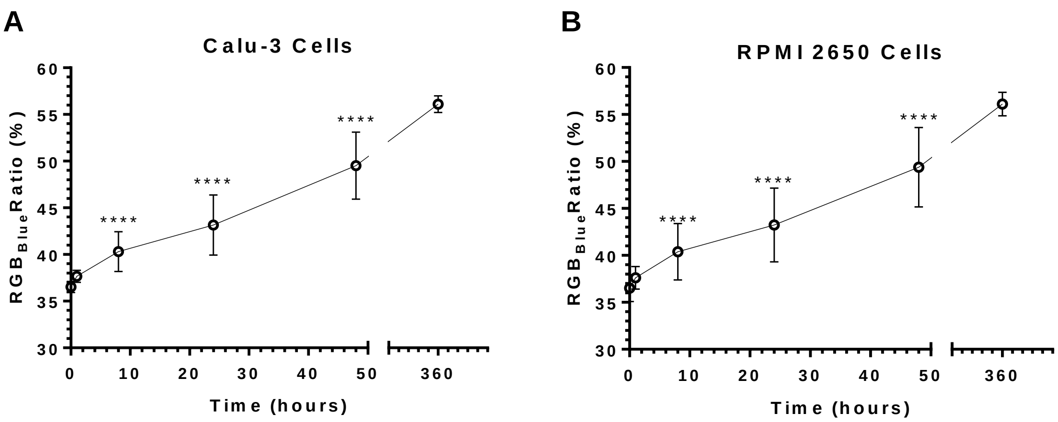

Figure 3.19. Mucus secretion rate measured with the RGB_B Ratio as a function of time cells at ΔP=0 cmH_2O. A- RGB_B Ratio values for Calu-3 cells. B- RGB_B Ratio values for RPMI 2650 cells.

3.7.3.8 Measurement of the mucus secretion rate

To evaluate the effect of pressure on the mucus secretion rate of both epithelial cells, Calu-3 and RPMI 2650 transwells were washed three times with HEPES to remove the already secreted mucus at time 0 hours and incubated at 37°C with 95% RH and 5% CO_2 at 0 (control), 5, 10, 15 and 20 cmH_2O CPAP was applied using holder A for 8 hours. Then, mucus glycoproteins were stained with alcian blue, cell surface images were taken and the RGB_B ratio was calculated to semi-quantitatively measure the amount of mucus produced. Exemplary stained cell surface pictures of Calu-3 and RPMI 2650 after incubation at 0 (control) and 10 cmH_2O CPAP are shown in Figure 3.20.

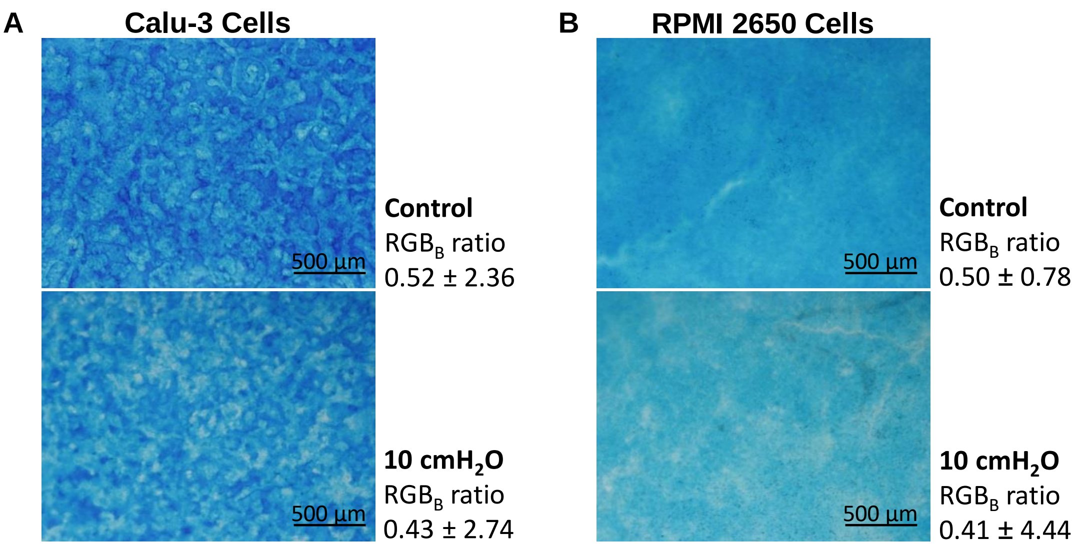

Figure 3.20. Microscopic images and RGB_B ratio of mucus stained with alcian blue on the cell surface of transwells after 8 h of 10 and 0 cmH_2O CPAP application. A- Microscopic images and RGB_B ratio of Calu-3 cells. B- Microscopic images and RGB_B ratio of RPMI 2650.

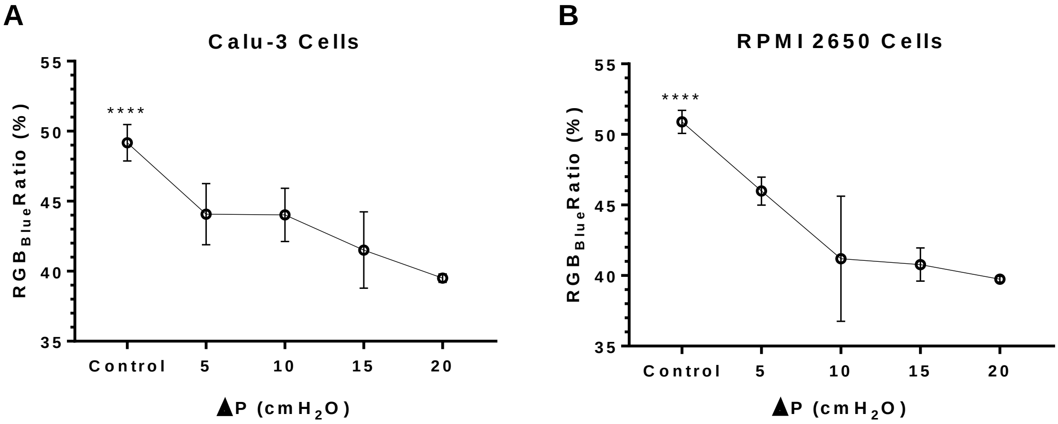

Figure 3.21. RGB_B ratio of mucus stained with alcian blue on the cell surface of transwells at Control (ΔP=0 cmH_2O) and ΔP= 5, 10 15 and 20 cmH_2O CPAP using holder A for 8 hours. A- RGB_B ratio of Calu-3 cells. B- RGB_B ratio of RPMI 2650.

The RGB_B ratio percentage as a function of CPAP pressure applied on both cell lines is displayed in Figure 3.21. It is seen that the amount of mucus secreted under pressure is significantly less than the control, and is lower as the pressure increases from 5 to 20 cmH_2O CPAP in both cell lines.

3.7.4 Effect of superimposed pressure oscillations on human upper airway cell lines

As previously reported, to reduce tissue deformation, some research lines are focused on the possibility that many afferent neural receptors are stimulated by the vibration occurring during snoring [101-104]. Hence, the superimposed positive airway pressure (SPAP), which corresponds to the second pressure scenario, has been generated with a sinusoidal pressure variation signal of ± 1 cmH_2O amplitude and 10, 20 and 30 Hz frequencies superimposed to the 5, 10, 15 and 20 cmH_2O CPAP pressures in order to investigate the effect on the human cultured epithelial cells.

Cell layer integrity and electrical permeability on Calu-3 and RPMI 2650 cell lines after 0 (control), 5 ± 1, 10 ± 1, 15 ± 1 and 20 ± 1 cmH_2O PAP at 10, 20 and 30 Hz for 10 minutes on holder A measured using the ECIS apparatus at 1000 Hz of frequency was evaluated and compared with the previous CPAP results. The TEER values obtained are shown in Figure 3.22.

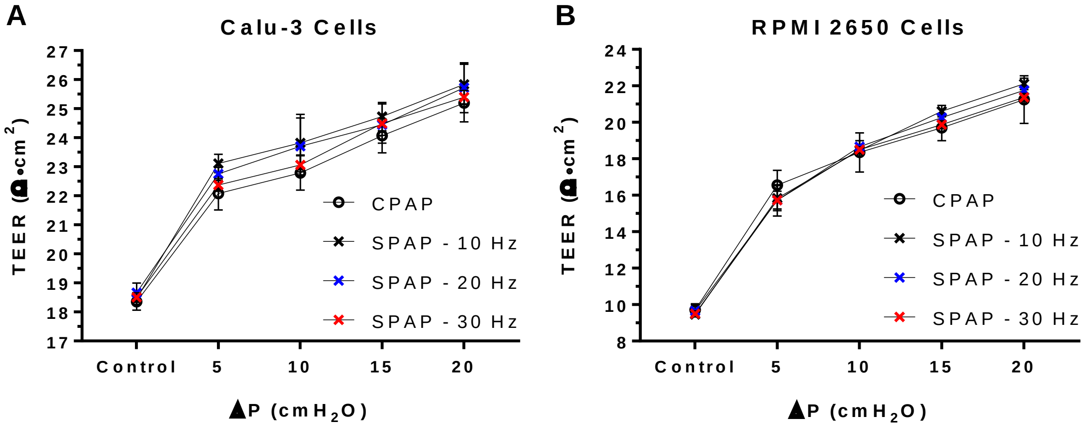

Figure 3.22. TEER values measured at Control (ΔP=0 cmH_2O) and ΔP= 5, 10 15 and 20 cmH_2O of CPAP and ΔP= 5 ± 1, 10 ± 1, 15 ± 1 and 20 ± 1 cmH_2O of SPAP at 10, 20 and 30 Hz with the ECIS apparatus at 1000 Hz using holder A. A- TEER values for Calu-3 cells. B- TEER values for RPMI 2650 cells.

The TEER values measured after the superimposed pressure oscillation follow the same trend as the TEER values obtained after CPAP application, the values increase significantly with ΔP. However, the difference between the superimposed pressure oscillations and the CPAP application is not significant at any frequency. Therefore, the oscillation by itself is going to be studied in more detail and compared with the CPAP at 5 cmH_2O in the next section.

3.7.5 Effect of sinusoidal pressure oscillations (SPO) on human upper airway cell lines

3.7.5.1 Frequency analysis of sinusoidal pressure oscillations (SPO)

The frequency of the sinusoidal pressure oscillation signal is an important parameter to be considered for optimization in order to investigate the effect of PAP on the upper airway cell lines. According to previous literature results, many afferent neural receptors and the human genioglossus muscle are stimulated by the vibration occurring during snoring [85-88]. Hence, the effect of separate 10, 20 and 30 Hz frequencies on a 5 cmH_2O amplitude sinusoidal signal has been investigated to simulate an intermittent pressure on both human epithelial cells.

Calu-3 and RPMI 2650 transwells were placed inside the holder A and each sinusoidal pressure oscillation was applied for 10 minutes (previously optimized time). The effect of the oscillation frequencies on the cell lines was investigated by measuring the TEER at 4000Hz using the ECIS apparatus after each PAP application.

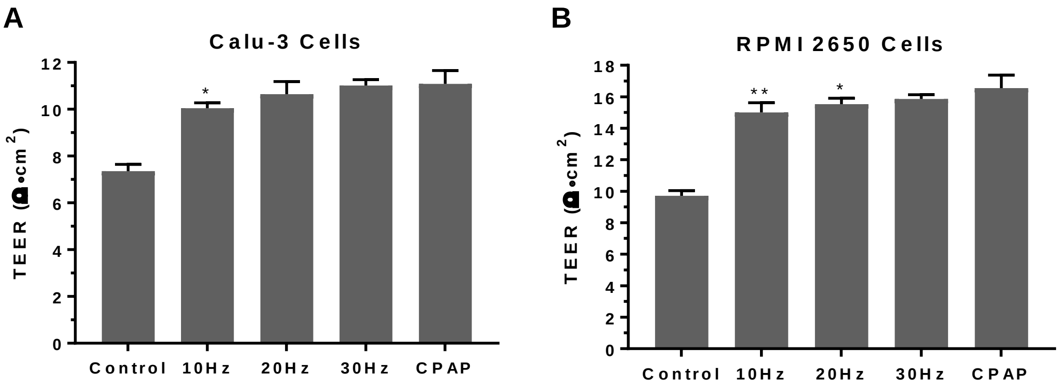

Figure 3.23. TEER values at Control (ΔP=0 cmH_2O), after 5 cmH_2O amplitude sinusoidal pressure oscillations (SPO) at 10, 20 and 30 Hz and after 5 cmH_2O CPAP measured with ECIS at 4000 Hz using holder A. A- TEER measurements for Calu-3 cells. B- TEER measurements for RPMI 2650 cells.

The results obtained for each frequency are compared with the control (no-pressure applied) and the 5 cmH_2O CPAP (continuous pressure) previously measured in section 3.7.3 as shown in Figure 3.23. It is seen that the TEER values increase significantly after 10 minutes of pressure application from the control, which is the lowest value, and gradually 10, 20 and 30 Hz up to the 5 cmH_2O CPAP TEER value, which is the highest measurement, in both cell lines. Hence, the TEER measured after 5 cmH_2O amplitude sinusoidal pressure oscillation at 10 Hz is the most significantly different value compared to CPAP and the closest compared to the control. Therefore, 5 cmH_2O amplitude sinusoidal pressure oscillation (SPO) at 10 Hz applied on Calu-3 and RPMI 2650 cells is analysed in the subsequent experiments and compared with 5 cmH_2O continuous pressure (CPAP) and no pressure controls.

3.7.5.2 Measurement of trans-epithelial electrical resistance (TEER)

Cell layer integrity and electrical permeability on both cell lines after 5 cmH_2O amplitude sinusoidal positive pressure oscillation at 10 Hz for 10 minutes on holder A measured using the ECIS apparatus at 1000 Hz of frequency was evaluated and compared with no pressure controls and 5 cmH_2O CPAP (

Figure 3.24).

In both cell models, ECIS results showed a significant decrease of TEER values after SPO application for 10 minutes in both cell lines. This means that the electrons have a lower resistance to pass through the cell layer, closer to no pressure controls, compared to the 5 cmH_2O CPAP, where the 5 cmH_2O pressure is applied constant and continuous instead of oscillating at 10 Hz. However, the SPO results are still significantly higher than the controls, which indicate that cell integrity remains unaffected, otherwise if the cell layer was damaged, lower TEER values compare to the control were expected.

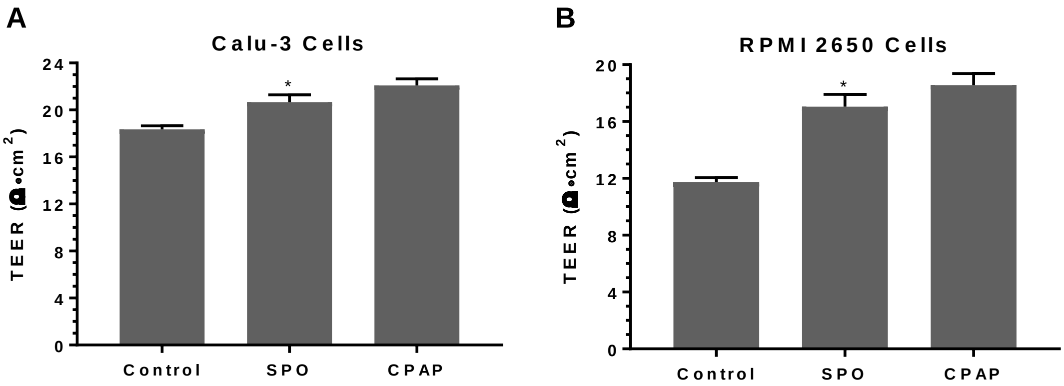

Figure 3.24. TEER values at Control (ΔP=0 cmH_2O), after 5 cmH_2O amplitude SPO at 10 Hz and after 5 cmH_2O CPAP measured with ECIS at 1000 Hz using holder A. A- TEER measurements for Calu-3 cells. B- TEER measurements for RPMI 2650 cells.

3.7.5.3 Measurement of Apparent Permeability (P_{app})

Cell layer integrity and paracellular permeability on both cell lines after 5 cmH_2O amplitude sinusoidal positive pressure oscillation at 10 Hz for 10 minutes on holder A measured by Na-flu transport was evaluated and compared with no pressure controls and 5 cmH_2O CPAP (Figure 3.12).

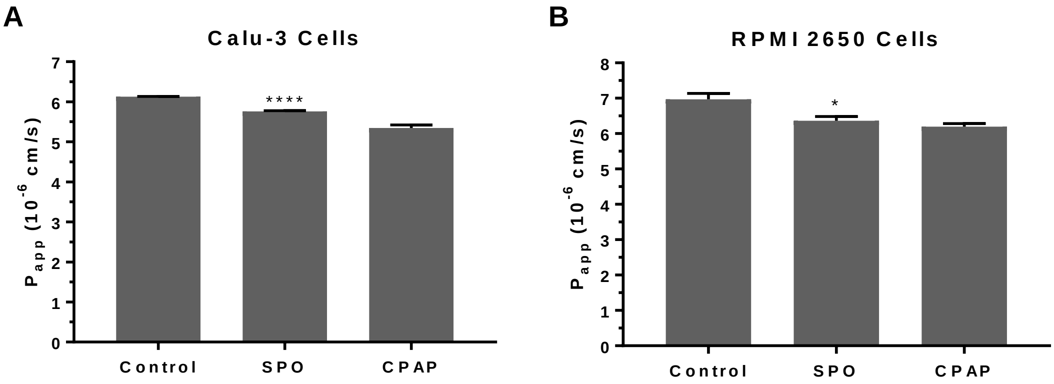

Figure 3.25. Apparent permeability coefficient (P_{app}) at Control (ΔP=0 cmH_2O), after 5 cmH_2O amplitude SPO at 10 Hz and after 5 cmH_2O CPAP using holder A. A- P_{app} values for Calu-3 cells. B- P_{app} values for RPMI 2650 cells.

In both cell models, flu-Na transport across cell layer demonstrated a significant increase of apparent permeability after SPO application, which means that both cell layers are more permeable to the paracellular markers after 10 minutes of pressure application, closer to no pressure controls, compared to the 5 cmH_2O CPAP, where the 5 cmH_2O pressure is applied constant and continuous instead of oscillating at 10 Hz. However, the SPO results are still significantly lower than the controls in both cell layers, which indicate that cell integrity is not affected, otherwise if the cell layer was damaged, higher P_{app} values compared to the control were expected.

3.7.5.4 Measurement of cell layer thickness

Total cell layer thickness (y_{cell}, epithelial cell layer plus ASL layer) before (control) and after 5 cmH_2O amplitude sinusoidal positive pressure oscillation at 10 Hz for 10 minutes using holder A was measured using the Nikon Eclipse Ti Time-Lapse Inverted Microscope (Nikon Instruments, NY, USA) in a humidified atmosphere of 95% air and 5% CO2 at 37°C to avoid cell and ASL dryness, and compared with 5 cmH_2O CPAP measurements. The Calu-3 and RPMI 2650 thickness results are shown in Figure 3.13.

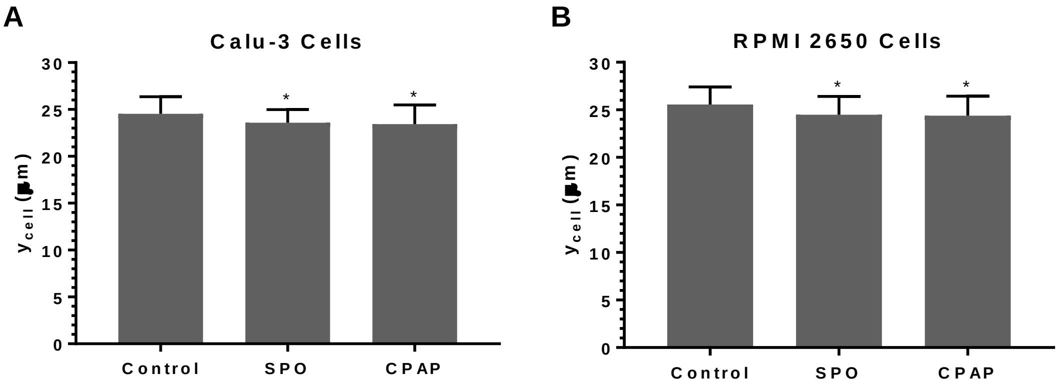

Figure 3.26. Total epithelial cell thickness (y_{cell}, epithelial cell layer plus ASL layer) measured before (control) and after 5 cmH_2O SPO at 10 Hz and 5 cmH_2O CPAP application for 10 minutes. A- y_{cell} values for Calu-3 cells. B- y_{cell} values for RPMI 2650 cells.

Results show a significant thickness reduction after SPO application for 10 minutes, which means that the 5 cmH_2O oscillations at 10 Hz are still able to compress significantly both cell lines. However, no significant difference is found on cell thickness measurements between SPO and CPAP application (p = 0.9191 for Calu-3 cells and p = 0.9670 for RPMI 2650 cells).

3.7.5.5 Measurement of airway surface liquid layer (ASL) thickness variation

As previously described in section 3.7.3.5, two humidity scenarios were simulated to measure the thickness variation of the ASL with the ECIS apparatus at 4000 Hz. The first one was a reference measurement where the CPAP humidifier was set to provide a water saturated compressed airflow at 30°C and 100% RH while the cells where incubated at 37°C (body temperature) in order to generate liquid-vapour equilibrium and annul the water transfer flow between the ASL and the water saturated CPAP airflow. Second scenario, the CPAP device and humidifier were set to provide pressurized air at 30°C (room temperature) and 70% RH, while the cells where incubated at 37°C to simulate the natural human upper airway conditions [18]. Therefore, the difference between both scenarios reflects the water transfer thickness variation at after SPO application at 10 Hz for 10 minutes.

Data on both humidity scenarios and cell lines are shown in Figure 3.27. TEER values measured after SPO application are significantly lower than values measured after CPAP application, but still significantly higher compared to no pressure controls in both cell lines and humidity scenarios, similar to the TEER values measured at 1000 Hz. Looking at the humidity profiles, it is seen that the reference value (100% RH) is significantly higher ($p < 0.0001$ in both *in-vitro* models) than the 70% RH measurement in both cell lines. Hence, as previously described, the difference between the TEER data at 100% RH and 70% RH is used to determine the thickness variation of the ASL after SPO application in both cell lines.

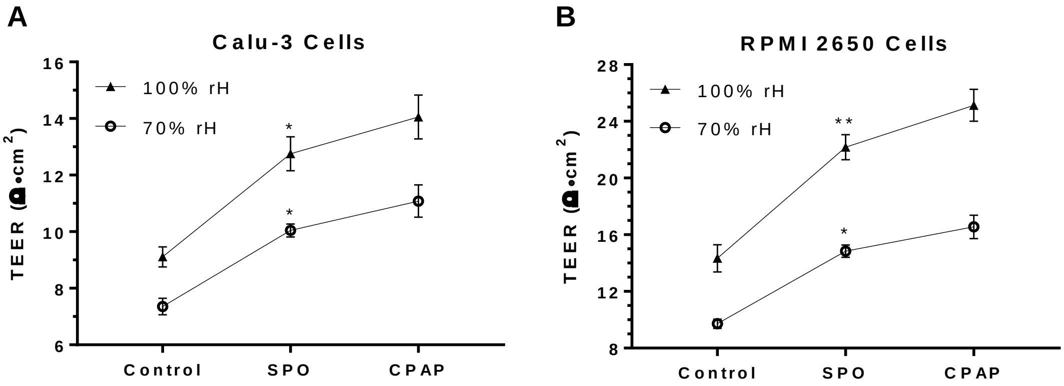

Figure 3.27. TEER measurements at Control (ΔP=0 cmH_2O), after 5 cmH_2O amplitude SPO at 10 Hz and after 5 cmH_2O CPAP measured with ECIS at 4000 Hz using holder A and at two RH: 100% RH (thickness reference) and 70% RH (upper airway conditions). A- TEER measurements for Calu-3 cells. B- TEER measurements for RPMI 2650 cells.

The dimensionless ASL thickness reduction is calculated from $TEER_{\Delta P,100}$ (reference) to $TEER_{\Delta P,70}$ after SPO application in both cell lines according to equation 3.6. The ASL dryness or over-evaporation after pressure is calculated comparing the previously calculated dimensionless ASL thickness reduction with the control ($\Delta P = 0$) according to equation 3.7. The results obtained are summarized in Table 3.3.

Table 3.3. ASL percentage reduction results for Calu-3 and RPMI 2650 cells due to water transfer effect only (no compression) calculated using experimental TEER data mean. ‡ control measurement, represents the natural water transfer ASL thickness reduction necessary to achieve the air conditioning process.

ΔP cmH_2O	*Calu-3 ASL reduction (%)*	*RPMI 2650 ASL reduction (%)*	*Calu-3 ASL over-evaporation (%)*	*RPMI 2650 ASL over-evaporation (%)*
Control ‡	19.27	32.22	0.00	0.00
SPO	21.00	33.09	1.74	0.86
CPAP	21.14	34.13	1.88	1.91

The quantified over-evaporation results or the amount of water dried or reduced on the ASL layer after SPO application is reduced compared to values measured after CPAP application on both cell lines.

3.7.5.6 Measurement of pro-inflammatory marker expressions

The expression of cytokine proteins Interleukin-6 (IL-6), Interleukin 8 (IL-8) and Tumour necrosis factor alpha (TNF-α) have been measured on Calu-3 cells after SPO application at 10 Hz for 10 minutes under 100% RH and 70% RH environmental conditions using holder A and compared with no pressure control and 10 minutes of 5 cmH_2O CPAP application.

The concentration of each inflammatory marker from Calu-3 cells after SPO and CPAP application under both humidity scenarios are shown in Figure 3.28, Figure 3.29 and Figure 3.30. It is seen that the concentration of IL-6 and IL-8 decreases significantly after SPO application compared to CPAP application but still significantly higher than the no pressure controls. There is not a significant difference on IL-6 ($p \geq 0.8085$) or IL-8 ($p \geq 0.1394$) concentrations between both humidity scenarios. TNF-α concentration results do not show any significant increase after CPAP application compared to the controls ($p \geq 0.4409$ and $p \geq 0.8965$ for 70% RH and 100% RH, respectively) and between the humidity scenarios ($p \geq 0.8509$).

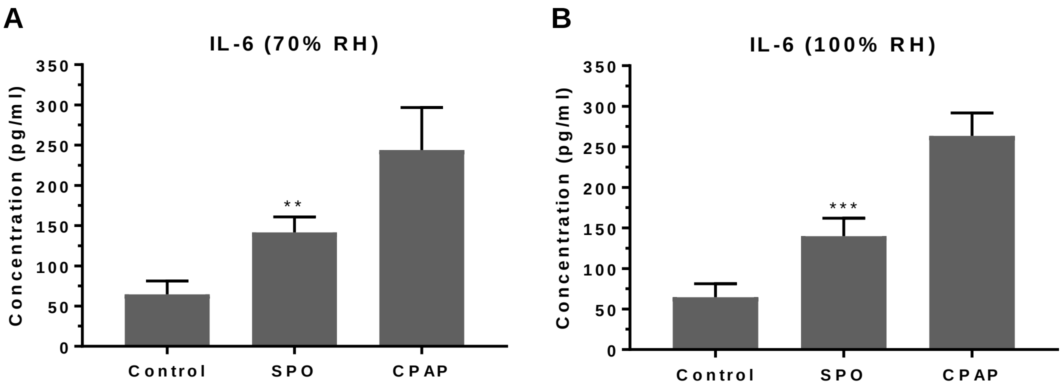

Figure 3.28. IL-6 concentration of Calu-3 cells at Control ($\Delta P=0$ cmH_2O), after 5 cmH_2O amplitude SPO at 10 Hz and after 5 cmH_2O CPAP using holder A for 10 minutes. A- Airflow at 70% RH and 30°C (human upper airway conditions). B- Airflow at 100% RH and 30°C (thickness reference and water saturated conditions).

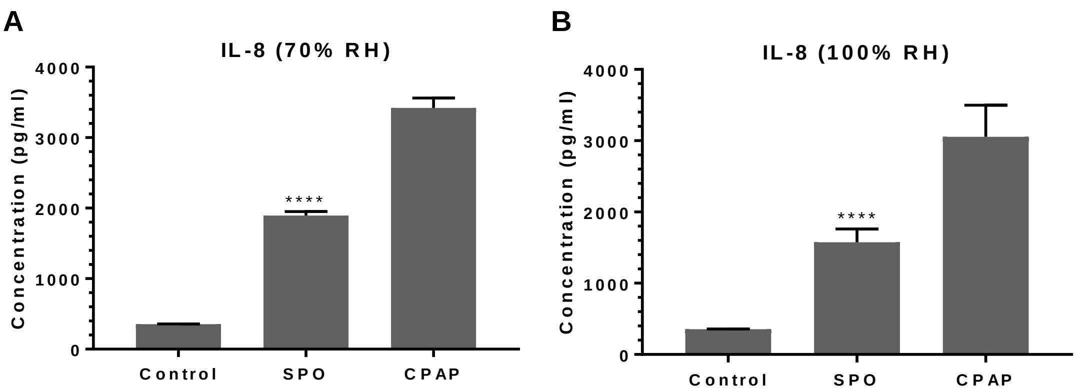

Figure 3.29. IL-8 concentration of Calu-3 cells at Control (ΔP=0 cmH_2O), after 5 cmH_2O amplitude SPO at 10 Hz and after 5 cmH_2O CPAP using holder A for 10 minutes. A- Airflow at 70% RH and 30°C (human upper airway conditions). B- Airflow at 100% RH and 30°C (thickness reference and water saturated conditions).

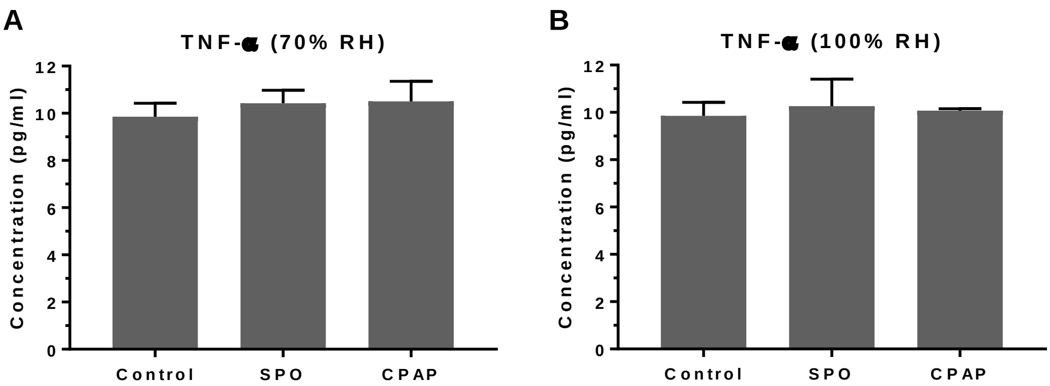

Figure 3.30. TNF-α concentration of Calu-3 cells at Control (ΔP=0 cmH_2O), after 5 cmH_2O amplitude SPO at 10 Hz and after 5 cmH_2O CPAP using holder A for 10 minutes. A- Airflow at 70% RH and 30°C (human upper airway conditions). B- Airflow at 100% RH and 30°C (thickness reference and water saturated conditions).

The IL-6 and IL-8 marker concentration results indicate that Calu-3 cells are still inflamed after 10 minutes of SPO application but significantly less than after CPAP application. Also, it has been proved that the increase in RH does not have any effect on the inflammatory marker concentration, Calu-3 cells are equally inflamed at 70% RH than at 100% RH after 10 minutes of SPO application at 10 Hz.

3.7.5.7 Measurement of the mucus secretion rate

To evaluate the effect of SPO at 10 Hz on the mucus secretion rate of both epithelial cells, Calu-3 and RPMI 2650 transwells were washed three times with HEPES to remove the already secreted mucus at time 0 hours and incubated at 37°C with 95%

RH and 5% CO_2 at 0 (control), 5 cmH_2O SPO at 10 Hz and 5 cmH_2O CPAP was applied using holder A for 8 hours. Then, mucus glycoproteins were stained with alcian blue, cell surface images were taken and the RGB_B ratio was calculated to semi-quantitatively measure the amount of mucus produced.

The RGB_B ratio percentage PAP application on both cell lines is displayed in Figure 3.31. It is seen that the amount of mucus secreted under SPO is significantly higher than under CPAP, but still significantly lower than no pressure controls in both cell lines.

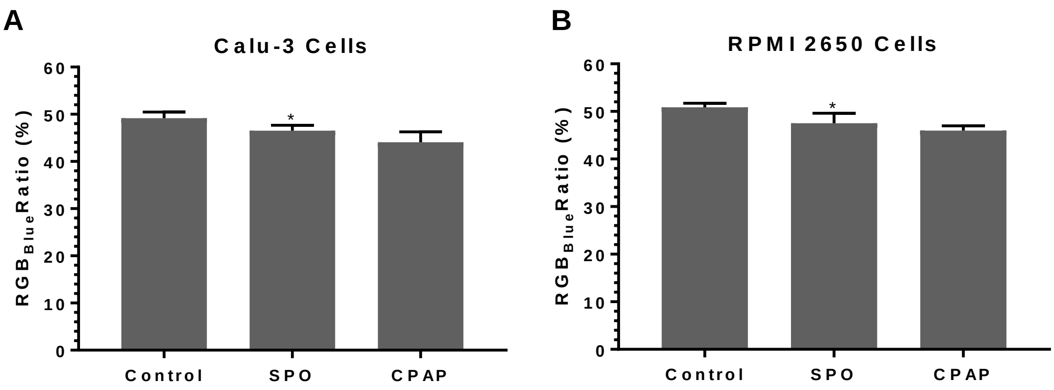

Figure 3.31. RGB_B ratio of mucus stained with alcian blue on the cell surface of transwells at Control ($\Delta P=0$ cmH_2O), after 5 cmH_2O amplitude SPO at 10 Hz and after 5 cmH_2O CPAP using holder A for 8 hours. A- RGB_B ratio of Calu-3 cells. B- RGB_B ratio of RPMI 2650.

3.8 Analysis of the respiratory epithelial cell behaviour under PAP

As stated in the introduction of this chapter, the purpose of this research was to analyse the human respiratory epithelium response under positive airway pressure application. Human airway epithelial Calu-3 cells and nasal RPMI 2650 cells grown in air-liquid interface (ALI) on permeable supports were used as *in-vitro* respiratory models and tested under PAP. Cell viability data indicated that both cell lines could survive the positive pressure application for 8 hours and validated both *in-vitro* models to investigate the effect of PAP on cultured human respiratory epithelial cells.

Two custom-made 3D cell insert holders were designed, optimized and 3D printed to achieve the desired positive pressure on the cell lines at specific airflow conditions to simulate human breathing under PAP. The simplest static airflow trajectory was simulated using the closed-flow holder A directly connected to the CPAP device. The continuous-flow holder B was used to simulate the continuous

PAP dynamic airflow trajectory and the superimposed human breathing cycle to the PAP dynamic airflow trajectory. No significant difference was found in TEER values at ΔP of 20 cmH_2O between the three airflow trajectories in both cell lines, which demonstrates that the airflow trajectories, either static or dynamic flows, do not have any effect on the *in-vitro* models in the experimental time frame considered.

To investigate the effect of the PAP on the cultured human epithelial cells, three experimental setups were designed to generate three gauge or relative PAP scenarios on both cell lines, a continuous positive airway pressure (CPAP), a superimposed sinusoidal positive airway pressure oscillation (SPAP) and a sinusoidal positive airway pressure oscillation (SPO).

The effect of 5, 10, 15 and 20 cmH_2O CPAP on the cell lines was compared with no pressure controls. It was proved that the cell layer was compressed, since the cell thickness layer was significantly reduced after CPAP application. This finding is in agreement with the integrity and permeability results since the cell compression produced after CPAP application squeezes the cell tight junctions and hinders the paracellular transport resulting in an increase in TEER values and consequently a decrease in the P_{app} coefficient. The paracellular transport is directly related to the water transport across the epithelial cell barrier to regulate the ASL water content and keep the optimum mucus and cilia conditions in the human upper airway [14, 53, 58]. It was also proved that there is an over-evaporation effect on the ASL layer after CPAP application. This effect has been quantified and the amount of water dried or reduced on the ASL layer was increasing from 1.880% to 4.191% for Calu-3 cells and from 1.912% to 3.675% for RPMI 2650 cells with ΔP. Pro-inflammatory marker expressions results indicated that Calu-3 cells were inflamed, increasing significantly the IL-6 and IL-8 marker concentrations, after 10 minutes of CPAP application independently of the ΔP applied and the RH used. Finally it has been proved that the CPAP application hinder natural mucus secretion and lubrication with ΔP. Therefore, it has been demonstrated that the CPAP application deforms the epithelial cells and distorts the natural paracellular transport and the mucus secretion rate. Also the increase in air volume to generate the positive pressure disturbs the water transfer between the ASL layer and the compressed air producing an ASL over-evaporation effect. All these findings could directly influence the ASL regulation mechanism and produce dryness, sneezing, rhinorrhea, post-nasal drip, nasal congestion or epistaxis in the upper airways, the side effects reported by LSD patients after therapy. However, as explained in chapter 1 and 2, it has been proven that the increase in RH can alleviate the ASL dryness or over-evaporation effect, but the increase in RH does not have any effect on the inflammatory marker concentration, so epithelial cells are equally inflamed at 70% RH than at 100% RH.

The effect of 5 ± 1, 10 ± 1, 15 ± 1 and 20 ± 1 cmH_2O SPAP at 10, 20 and 30 Hz on both epithelial cells was measured with the ECIS apparatus at 1000 Hz and compared with 5, 10, 15 and 20 cmH_2O CPAP. TEER values showed no significant differences between SPAP and CPAP application at any frequency. This no significant differences could be due to the fact that the superimpose pressure oscillation does not have an effect on the cell physiology, just on the muscle stimulation as described in the literature. Therefore, the oscillation by itself has been studied as a third pressure scenario.

Finally, the effect of 5 cmH_2O amplitude sinusoidal positive airway pressure oscillation at 10 Hz on both cell lines was compared with 5 cmH_2O CPAP. Regarding cell permeability and deformation or compression, even that TEER values are significantly lower after SPO application than CPAP application and P_{app} values are significantly higher after SPO application than CPAP application, no significant difference is found on cell thickness measurements between SPO and CPAP application. It has been quantified that the over-evaporation effect or the amount of water dried or reduced on the ASL layer after SPO application is significantly lower (1.742% and 0.875%, for Calu-3 and RPMI 2650 cells respectively) compared to values measured after CPAP application (1.880% and 1.912%, for Calu-3 and RPMI 2650 cells respectively). Then, regarding pro-inflammatory marker expressions, it has been seen that the concentration of IL-6 and IL-8 decreases significantly after SPO application compared to CPAP application but still significantly higher than the no pressure controls, and also there is not significant difference between high or low relative humidity conditions. At last, it has been proven that the amount of mucus secreted under SPO is significantly higher than under CPAP, but still significantly lower than no pressure controls in both cell lines. In conclusion, these results are in agreement with previous findings, such as an increase in paracellular permeability, compression, ASL over-evaporation and inflammation after SPO compared to CPAP, and proves that the SPO should be further investigated to be incorporated with the actual and commercial PAP device to reduce the side effects produced by the LSD therapies.

3.9 Closure

This chapter described in detail the methodology and experiments performed for cell characterization such as barrier integrity and permeability, cell and ASL thickness measurements, inflammatory response and mucus secretion rate. The design, simulation and optimization of the cell insert holders, compressed airflow trajectories and positive pressure scenarios have also been explained in this chapter. Finally, the results obtained from these experiments have been used to evaluate the effect of different PAP applications and airflow trajectories on Calu-3 and RPMI 2650 epithelial cells.

The next chapter will describe a mathematical model developed to extrapolate the results obtained on the human Calu-3 and RPMI 2650 epithelial and nasal cells to the human respiratory system, specifically to the human upper airways.

Chapter 4

Model formulation and extrapolation of epithelial cell results to the human upper airway

4.1 Introduction

Chapter 3 proved the hypothesis previously formulated, which states that the application of positive pressure may inhibit the natural air conditioning process and deform the respiratory epithelium, leading to disruption of the natural lubrication and explaining the secondary effects reported by LDS patients after the therapy. Calu-3 cells and RPMI 2650 cells grown in air-liquid interface (ALI) on permeable supports were used as *in-vitro* respiratory models to test the effect of different positive pressure scenarios on human airway epithelial cells. It was demonstrated that after PAP application epithelial cells were inflamed regardless of the humidity content in the airflow. Also, paracellular transport, which is directly related to the water flow between the cells, mucus secretion rate and ASL water content were significantly reduced.

The purpose of this chapter is to extrapolate the variation on the ASL layer water content after PAP application quantified on the human *in-vitro* respiratory cell models to the entire human upper airways in order to determine the input temperature and relative humidity of the compressed PAP airflow to overcome the upper airway dryness side effect. Hence, the amount of water required to humidify the PAP airflow and overcome the patient's discomfort after the CPAP therapy will be quantified. Although epithelium inflammation or the lack of mucus secretion from goblet cells produced after PAP therapy is not solved by humidifying the compressed airflow introduced into the respiratory tract to keep the airways open, the use of a proper humidification will increase the comfort of patients using LSD.

Therefore, a simple, efficient, fast computing and realistic 1D human upper airway model is formulated, validated and optimized to predict the heat and water transfer variation between normal breathing and PAP conditions.

The model formulation is explained in sections 4.2 to 4.8, including assumptions, governing equations, boundary conditions and computational strategy. The statistical analysis is described in section 4.9. Then, models results, validation and optimization are detailed in sections 4.10, 4.11 and 4.12 respectively. Finally, the discussion on the results and the closure of the chapter are carried out in sections 4.13 and 4.14.

4.2 Model description and assumptions

One-dimensional (1D), two-dimensional (2D) and three-dimensional (3D) computational models for temperature and water vapour concentration have previously been developed to study air conditioning characteristics in the human respiratory tract. 1D and 2D models are the most popular methods due to their simplicity and efficiency, where air temperature and water vapour concentration are obtained by solving scalar transport equations and energy balance equations based on control volume analysis [33, 74]. 3D models are computationally more demanding because they provide detailed air distributions of velocities, temperature and water vapour concentration, but the computational time and model size is greater compared to 1D models [77-79]. Therefore, the proposed theoretical model is a simple, efficient, fast computing and realistic 1D upper airway representation able to predict the heat and water transfer variation between normal breathing and PAP conditions, which is the significant difference from other models previously described on the literature [33, 74, 77-79].

To facilitate model development, assumptions and simplifications are made to reduce computational complexity whilst maintaining the governing process characteristics. These include:

- The geometry of the human upper airways has been approximated to an idealized symmetric cylinder-based airway model using data previously reported by the literature [33, 74, 154]. Each cylinder corresponds to one of the areas of interest in the upper airways as described in Figure 4.1. The areas of interest are: nasal vestibule, nasal cavity, nasal turbinate proximal nasopharynx, distal nasopharynx, oropharynx, hypopharynx, larynx, proximal trachea and distal trachea.

- The geometry inside each cylinder-based segment is considered uniform, hence the geometric parameters, such as cross-sectional area, diameter and velocity are assumed constant in each cylinder but changes from one segment to another.
- Axial conduction and convection heat along the airway are assumed to be negligible. The radial conduction and convection heat are the main sources of energy to achieve human air conditioning process [33, 74, 154].

- Air and water vapour mixture is considered ideally mixed and homogeneous at the end of each cylinder-based segment.

- Air and water vapour mixture flow is one-dimensional along the axial direction and considered as an ideal gas.

- ASL and epithelial cell layers are considered as a unique homogeneous layer due to the similarities in composition, since both are composed by 95% of water, [46, 53] to determine the radial conduction heat transfer from the blood capillary to ASL outer surface.

- The water content on the ASL outer surface in contact with the airflow is considered in thermodynamic liquid-vapour phase equilibrium, which is determined by Clapeyron equation.

- The flow rate is set as an inlet boundary condition and fixed to generate the desired PAP pressure inside the respiratory system according to the CPAP device specifications.

- The airflow evolution is considered time-independent, according to the previous *in-vitro* model results (Chapter 3). The main interest is in determining how each state variable changes as a function of pressure under normal breathing ($\Delta P=0$) and PAP conditions ($\Delta P>0$) in the inspiration phase of the breathing cycle since it has the highest turbulence airflow impact [78].

- The model is formulated to simulate only a nasal respiration and is solved for the steady-state level.

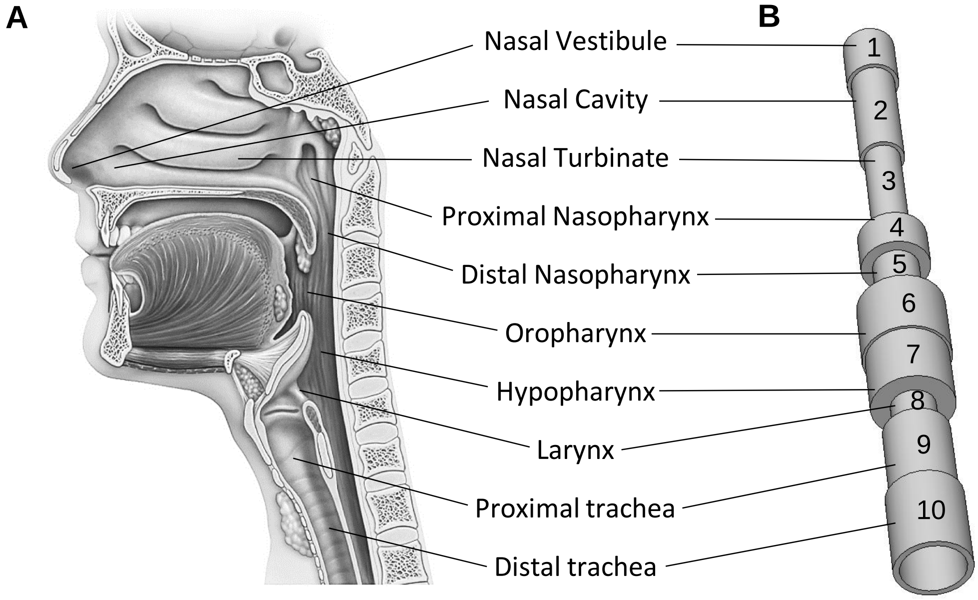

Figure 4.1. Description of the human upper airway regions of interest used to develop the geometrical modelling. A- Human upper airways anatomy [155]. B- The idealized symmetric cylinder-based airway model.

4.3 State variables

Aiming to extrapolate the variation on the ASL layer water content, dryness or over-evaporation effect after PAP application quantified on the human *in-vitro* respiratory cell models to the human upper airways, five state variables are considered to investigate the effect of the LSD devices on the natural air conditioning process. The main objective is to quantify the water transfer flux from the ASL layer to the airflow under each PAP condition, hence the state variables are:

- Airflow temperature (T_A)

- ASL outer surface temperature (T_M)

- Water concentration on the airflow (C_A)

- Water concentration on the ASL layer (C_M)

- Water transfer flux (N)

Hence, the model is formulated and managed by five main equations, which are described in the next section.

4.4 Governing equations

In this part of the chapter scalar transport equations and energy balance equations based on control volume analysis are described to formulate the model. Conservation of mass, momentum and energy are used to calculate water vapour and heat exchange between the ASL and the airflow under 0, 5, 10, 15 and 20 cmH_2O CPAP pressures. 0 cmH_2O CPAP pressure is considered to simulate the normal breathing conditions. The heat and water transfer fluxes in x and y directions along with state variables and parameters considered for physical modelling of the human breathing conditions are outlined in Figure 4.2.

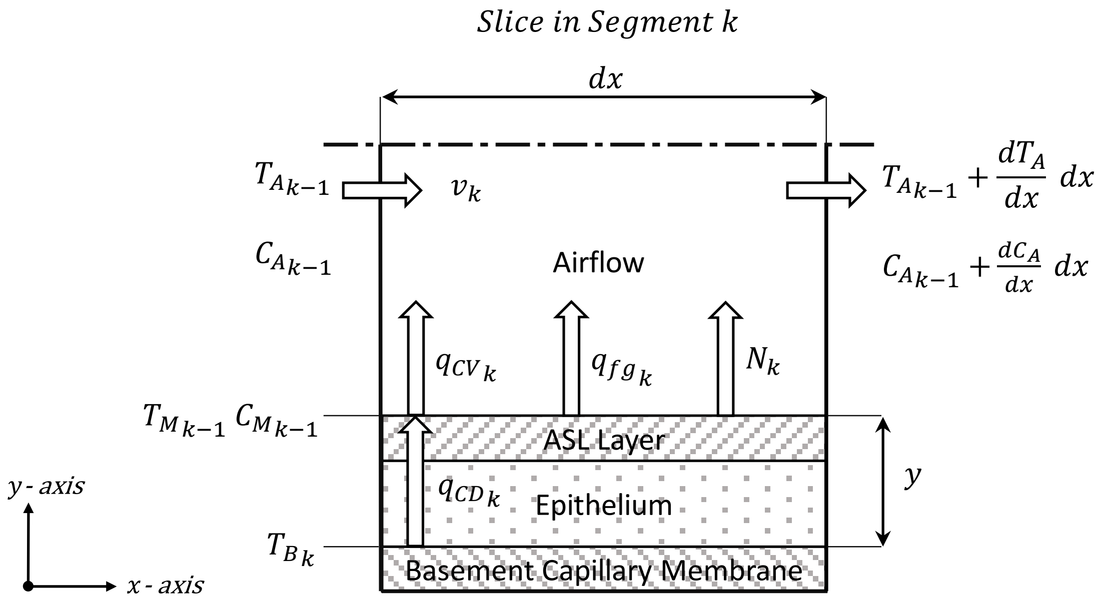

Figure 4.2. Schematic representation of conduction, convection and vaporization heat (q_{CD}, q_{CV}, q_{fg}, respectively) and water transfer (N) fluxes in a dx slice of the segment k, and state variables such as airflow, ASL outer surface and blood temperatures (T_A, T_M, T_B, respectively) and water concentration on the airflow and ASL layer (C_A, C_M, respectively) at the airway distance x.

4.4.1 Mass and energy fluxes along the y-axis

Three heat fluxes per unit area and time are considered in the y-axis: conductive sensible heat from the blood capillary terminals through the epithelium, convective sensible heat from the ASL outer surface to the airflow and latent heat involved in water liquid-gas phase change.

Conductive sensible heat is described in equation 4.1 where heat flux (q_{CD}) is transferred trough the epithelium with specific thickness (y) and thermal conductivity (k_M) as a consequence of the thermal gradient from blood temperature at the basement capillary membrane (T_B) to mucus temperature at the ASL outer surface (T_M).

$$q_{CD}(x) = \frac{k_M}{y}(T_B(x) - T_M(x)) \qquad 4.1$$

Convective sensible heat is described in equation 4.2 where the heat flux (q_{CV}) is transferred as a consequence of thermal gradient, in this case from the ASL outer surface (T_M) to the airflow (T_A) at specific heat transfer coefficient (h_C).

$$q_{CV}(x) = h_C(x)(T_M(x) - T_A(x)) \qquad 4.2$$

The heat transfer coefficient is calculated from equation 4.3, where D is the cross-sectional diameter, k_A is the air thermal conductivity and Nu is the Nusselt number. This dimensionless number is calculated from an empirical correlation of heat and water vapour transfer in human airways validated in the literature [79] and is described in equation 4.4, where D_T is the tracheal diameter and Re is the dimensionless Reynolds number.

$$h_C(x) = \frac{Nu(x)k_A}{D(x)} \qquad 4.3$$

$$Nu(x) = 3.504\left(Re(x)\frac{D(x)}{D_T}\right.^{0.277} \qquad 4.4$$

The latent heat involved in water liquid-gas phase change is described in equation 4.5, where h_{fg} is the water latent heat of vaporization, M_W is the water molecular weight and N is the water molar flux, which is calculated in equation 4.6.

$$q_{fg}(x) = h_{fg}M_W N(x) \qquad 4.5$$

$$N(x) = k_C(x)(C_M(x) - C_A(x)) \qquad 4.6$$

Equation 4.6 is the definition of the convective mass transfer flux generated as a consequence of the water concentration gradient from the ASL outer surface (C_M) to the airflow (C_A) at specific mass transfer coefficient (k_C). This coefficient is calculated from 4.7, where Dif is the diffusivity of water in air and Sh is the dimensionless Sherwood number determined from the bulk heat and mass transfer in the human airways empirical correlation [24] according to equation 4.8.

$$k_C(x) = \frac{Sh(x)\,Dif}{D(x)} \qquad 4.7$$

$$Sh(x) = 3.652\left(Re(x)\frac{D(x)}{D_T}\right)^{0.268} \qquad 4.8$$

Applying conservation of energy across the epithelium and ASL the heat fluxes described in equations 4.1, 4.2 and 4.5 can be combined in one main balance equation 4.9.

$$\frac{k_M}{y}\left(T_B(x) - T_M(x)\right) = h_C(x)\left(T_M(x) - T_A(x)\right) + h_{fg}M_W N(x) \qquad 4.9$$

4.4.2 Mass and energy fluxes along the x-axis

Regarding the x-axis, mass and energy balances are performed on the air phase of each dx slice. The mass balance is described in equation 4.10 where v is the local mean airflow velocity across the airways calculated from the constant inlet flow rate (boundary condition) and the cross-sectional area (CSA) at each section of the model.

$$v(x)\frac{dC_A}{dx} = \frac{4}{D(x)}k_C(x)(C_M(x) - C_A(x)) \qquad 4.10$$

The energy balance is outlined in equation 4.11 where ρ is the air density and C_{pA} and C_{pW} are the air and water heat capacities at constant pressure respectively.

$$v(x)\frac{dT_A}{dx} = \frac{4}{D(x)\rho C_{pA}}\left(h_C(x)\left(T_M(x) - T_A(x)\right) + C_{pW}M_W N(x)(T_M(x) - T_A(x))\right) \qquad 4.11$$

Finally the saturation pressure (P_{sat}) of the thermodynamic water liquid-vapour phase equilibrium on ASL outer surface is determined by the empirical Tetens equation (4.12) which relates the saturation water vapour pressure with the temperature improving the Clapeyron equation. Then, the water concentration at the same saturation conditions on the mucus-air interface (C_M) is determined from the ideal gas equation (4.13) where R is the ideal gas constant.

$$P_{sat}\,(x) = 610.78\,\exp\left(\frac{17.27(T_M(x) - 273.15)}{(T_M(x) - 273.15) + 237.3}\right) \tag{4.12}$$

$$C_M(x) = \frac{P_{sat}\,(x)}{R\,T_M(x)} \cdot 10^{-6} \tag{4.13}$$

Therefore, the theoretical model is managed by five main equations (4.6,4.9, 4.10, 4.11, 4.13) which are used to determine the five state variables (T_A, T_M, C_A, C_M, N) along the upper airways.

4.5 Boundary conditions

Two boundary conditions have been set to characterize the upper airway inlet airflow conditions and the airway wall temperature along the tract. As described in the introduction, the outcome of this theoretical model is to determine the effect of the positive pressure on the upper airways humidification, which is reflected on the resolved state variables evolution along the geometrical cylinder-based segments under the different PAP conditions.

4.5.1 Inlet airflow temperature, water vapour concentration and flowrate

To simulate normal breathing conditions, it has to be considered that LSD devices generate a positive pressure inside the patients' respiratory tract to keep the airways open during sleep. Hence, at rest, breathing is slower and more relaxed and the minute ventilation of a healthy adult, according to the literature, is experimentally determined at 9 L/min [75]. Then, previous researches have stated that the temperature and relative humidity of the microclimate between humans and bed covers (bed environment) are generally maintained around 29°C and 65% respectively during normal sleep [156]. Hence, these values are chosen to characterize the model inlet airflow conditions under normal breathing, when no pressure is applied.

To simulate PAP conditions, the inlet flow rates to achieve the desired pressures inside the respiratory system are given by the CPAP device specifications [157]. Hence, volume flow rates of 48.47, 53.95, 59.42 and 64.91 L/min are used to generate 5, 10, 15 and 20 cmH_2O of constant positive pressure. Then, knowing that the CPAP device operating principle is to introduce pressurized room air into the patient's respiratory system, the temperature and relative humidity inlet airflow conditions under PAP conditions are set according to a room neutral sleeping environment, which corresponds to 22°C and 50% respectively according to the literature [158].

The inlet air water vapour concentration (C_{A_0}) is determined from the relative humidity (rH) using equation 4.14 where $C_{A_{sat}}$ is calculated from equations 4.12 and 4.13 using the inlet air temperature (T_{A_0}), bed environment temperature for normal breathing conditions or room neutral sleeping environmental temperature for PAP conditions.

$$C_{A_0} = \frac{rH \cdot C_{A_{sat}}}{100} \tag{4.14}$$

4.5.2 Airway wall temperature

The wall temperature along the respiratory tract corresponds to the capillary blood temperature (T_B) on the basement membrane as a function of the distance from the nasal vestibule to the distal trachea. Because of the difficulty in obtaining accurate axial blood temperature distribution, T_B has been set as a linear distal increase at a 0.33°C/cm rate from 32°C at the nasal vestibule basement membrane temperature according to previous studies [33, 74-76, 79].

4.6 Parameters affected by PAP application

To determine the parameters directly affected by the PAP application, how the airways are opened and which is the physical phenomena governing this process have to be completely understood. As proved and quantified in the previous chapter 3, there are two main effects that have to be extrapolated to the entire upper airways: the cell or epithelium compression and the ASL dryness or over-evaporation after PAP application. Both effects are outlined in Figure 4.3.

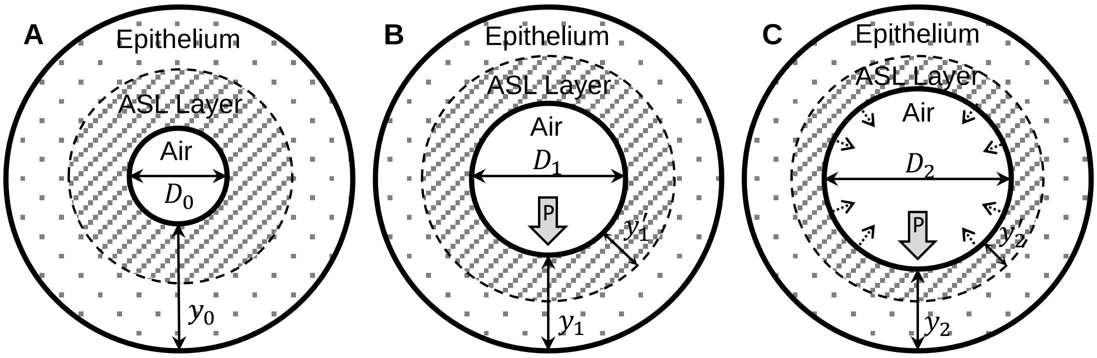

Figure 4.3. Schematic representation of the dimensions evolution cylinder-based airway radial plane dimension evolution when PAP is applied. A- Initial airway dimensions which corresponds to normal breathing conditions ($\Delta P = 0$). B- Airway dimensions evolution when PAP is applied due to tissue compression, calculated from Bulk Modulus, where $D_1 > D_0$, $CCA_1 < CCA_0$ and $y_1 < y_0$. Epithelium and ASL layers are assumed equally compressed. C- Representation of the drying effect when PAP is applied, where the ASL layer thickness is also reduced ($y_2' < y_1'$) due to the water transfer from the ASL layer to the airflow in order to achieve the air conditioning process, hence $D_2 > D_1$ and $y_2 < y_1$.

4.6.1 Epithelium compression after PAP application

LSD introduced pressurized room air into the respiratory system to generate a PAP inside the breathing tract and keep the airways opened during sleep. The positive pressure inside the upper airways generates a radial force normal to the epithelium in order to increase the volume of the airways, and as a consequence of this radial positive force, the epithelium is significantly compressed. The epithelium compression is governed by the Bulk Modulus (B), which was calculated in the previous chapter 3 and proved to be in agreement with the tracheal respiratory tissue bulk modulus according to the literature [152, 153].

Then, the respiratory tract tissue compression, *i.e.* tissue volume reduction, is predicted using the Bulk Modulus equation (4.15), where ΔP and ΔV correspond to the pressure increase and epithelium volume decrease respectively from normal breathing conditions (ΔP=0) to the desired PAP (ΔP≠0), and V_0 is the initial epithelium volume. The equation 4.15 can be written as a function of the circular crown epithelium and ASL area (CCA) since the axial segment length (L) is not affected by the radial positive force generated by the PAP application. Also, it has to be specified that the final airway diameter (D_1) is equal to the sum of the initial airway diameter (D_0), before PAP application, and the epithelium thickness variation ($2 \cdot (y_0 - y_1)$) as described in equation 4.16. This phenomena is described in Figure 4.3A and Figure 4.3B.

$$B = -\frac{\Delta P}{\frac{\Delta V}{V_0}} = -\frac{\Delta P}{\frac{CCA_1 L - CCA_0 L}{CCA_0 L}} = -\frac{\Delta P}{\frac{y_1(y_1 + D_1)}{y_0(y_0 + D_0)} - 1} \quad 4.15$$

$$D_1 = D_0 + 2 \cdot (y_0 - y_1) \quad 4.16$$

4.6.2 ASL dryness or over-evaporation after PAP application

The subsequent effect considered for extrapolation is the ASL dryness or over-evaporation quantified in the two *in-vitro* models after PAP application in previous chapter 3. This is essential to determine the final airway dimensions at the desired PAP (ΔP≠0).

Briefly, it was explained and proved in chapter 3 that the air volume increase produced to generate the PAP hinders the natural air conditioning process and produces ASL dryness or over-evaporation. The water flux from the ASL layer to the airflow needed to achieve the proper relative humidity and reach the equilibrium is higher when PAP is applied because there is more air inside the respiratory system to be humidified than in normal breathing conditions. This increase in water flux from the ASL layer to the airflow produces a decrease in the ASL water content reservoir hence in the ASL thickness.

Mathematically, according to the process outlined in Figure 4.3B and Figure 4.3C, the ASL thickness reduction can be expressed as $(y_1' - y_2')/y_1'$ and is quantified for 5, 10, 15 and 20 cmH_2O CPAP application in previous chapter 3. Also, it is known that the ASL thickness (y') corresponds to 23% of the total epithelial thickness (y) according to the literature [154]. Therefore, the final epithelial thickness (y_2) and airway diameter (D_2) after PAP application are determined from equations 4.17 and 4.18. The final airway cross-sectional area (A) used to determine the model geometry at each PAP simulated is determined from the final airway diameter ($\pi D_2^2/4$).

$$y_2 = 0.77 y_1 + 0.23 y_1 - \left(0.23 y_1 \left(\frac{y_1' - y_2'}{y_1'}\right)\right) \quad 4.17$$

$$D_2 = D_1 + 2 \cdot (y_1 - y_2) \quad 4.18$$

4.7 Computational strategy

The human upper airway PAP model consists of a series of five governing equations solved for each geometrical segment, where the output variables are used as input variables for the next segment following the steps described in Figure 4.4. The same procedure is repeated for each PAP analysed.

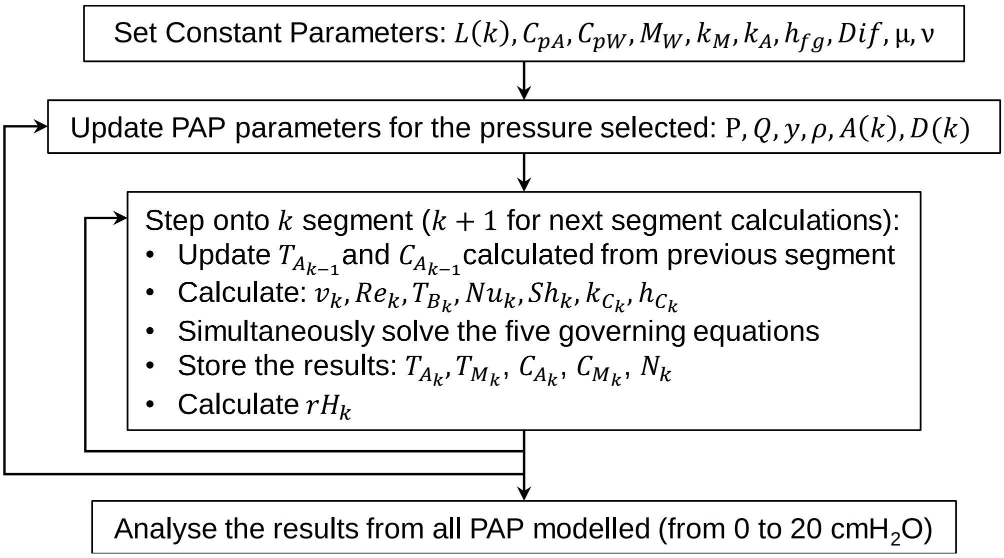

Figure 4.4. Flow diagram of upper airway PAP model outlining the steps to follow to compare the governing state parameters evolution at each PAP selected valid from 0 to 20 cmH_2O.

The model is written, simulated and optimized on MATLAB R2014b (MathWorks®, NSW, Australia), a computer algebra software, where custom scripts and built-in functions, such as $ode45$ and $fsolve$ functions, are used to solve the mathematical system. A lumped parameter approximation is used to simplify the equations and reduce the computational time (see appendix F).

4.8 Summary of Parameters

Although all the parameters and variables are included in the list of abbreviations and symbols, the parameters used to formulate the human upper airway PAP model are also summarized in the foll9owing tables for simplicity. They are divided in three main groups: geometrical parameters, constant variables and variables.

4.8.1 Geometrical Parameters

Table 4.1. Geometrical parameters used to formulate the human upper airway PAP model. It contains the symbol of each parameter, a brief description, mathematical value and unit and the reference number.

Parameters	Description	Value	Units	Ref.
$\boldsymbol{L(k)}$	UA Length Vector	[2.0 4.0 4.0 1.4 1.9 2.3 2.1 1.1 2.7 2.8]	cm	[33]
$\boldsymbol{D_0(k)}$	UA Diameter Vector at ΔP=0	[1.5 1.2 0.6 2.0 1.2 2.5 2.4 1.1 1.8 2.1]	cm	[33]
$\boldsymbol{y}$	Epithelium Thickness at ΔP=0	65	nm	[154]

4.8.2 Constant Variables

Table 4.2. Constant parameters used to formulate the human upper airway PAP model. It contains the symbol of each parameter, a brief description, mathematical value and unit and the reference number.

Variables	Description	Value	Units	Ref.
$\boldsymbol{\Delta P}$	Positive airway Pressure Increase	0, 5, 10, 15, 20	cmH_2O	-
$\boldsymbol{Q}$	Airflow Rate at ΔP=0 cmH_2O	150	cm^3/s	[75]
$\boldsymbol{Q_5}$	Airflow Rate at ΔP=5 cmH_2O	241.25	cm^3/s	[157]
$\boldsymbol{Q}$	Airflow Rate at ΔP=10 cmH_2O	332.5	cm^3/s	[157]
$\boldsymbol{Q_{15}}$	Airflow Rate at ΔP=15 cmH_2O	423.75	cm^3/s	[157]
$\boldsymbol{Q_2}$	Airflow Rate at ΔP=20 cmH_2O	515	cm^3/s	[157]
$\boldsymbol{k_M}$	Epithelial and ASL Thermal Conductivity	0.00144	$cal/cm\ s\ K$	[79]
$\boldsymbol{k}$	Moist Air Thermal Conductivity	6.432e-5	$cal/cm\ s\ K$	[79]
$\boldsymbol{h_{fg}}$	Latent heat of vaporization	578.4	cal/g	[79]
$\boldsymbol{M_W}$	Water Molecular Weight	18.016	g/mol	[79]
$\boldsymbol{Dif}$	Diffusivity of Water Vapour in Air	0.27	cm^2/s	[79]
$\boldsymbol{\rho}$	Density of Moist Air	0.00112	g/cm^3	[79]
$\boldsymbol{\mu}$	Dynamic Viscosity of Moist Air	1.846e-4	$cal/cm\ s\ K$	[79]
$\boldsymbol{_{pA}}$	Moist Air Heat Capacity at Constant Pressure	0.2592	$cal/g\ K$	[79]
$\boldsymbol{_{pW}}$	Water Heat Capacity at Constant Pressure	1	$cal/g\ K$	[79]
$\boldsymbol{R}$	Ideal Gas Constant	8.31	$m^3 Pa/molK$	-
$\boldsymbol{B}$	Bulk Modulus of Respiratory Epithelium	10500	Pa	[152]

4.8.3 Variables

Table 4.3. Variables used to formulate the human upper airway PAP model. It contains the symbol of each parameter, a brief description and the unit of measure.

Variables	Description	Units
T_{A_k}	Local Airflow Temperature	K
T_{M_k}	Local Mucus Temperature at the ASL Outer Surface	K
T_{B_k}	Local Blood Temperature at the Basement Capillary Membrane	K
C_{A_k}	Local Airflow Water Vapour Concentration	mol/cm^3
C_{M_k}	Local Saturation Water Vapour Concentration at the ASL Outer Surface	mol/cm^3
N_k	Local Water Transfer Rate from the ASL Outer Surface to the Airflow	mol/cm^3s
v_k	Local Airflow Velocity	cm/s
A_k	Local Cross-Sectional Area	cm^2
Nu_k	Local Dimensionless Nusselt Number	-
Re_k	Local Dimensionless Reynolds Number	-
Sh_k	Local Dimensionless Sherwood Number	-
k_{C_k}	Local Mass Transfer Coefficient	cm/s
h_{C_k}	Local Heat Transfer Coefficient	$cal/cm^2\ s\ K$
P_{sat_k}	Tetens Saturation Pressure	Pa
rH_k	Relative Humidity	%

4.9 Statistics

Statistical analysis was performed using GraphPad Prism software (GraphPad, San Diego, CA, USA) version 6.07 for windows using one-way analysis of variance (ANOVA), followed by Tukey post hoc analysis for multiple comparisons. Results are presented as mean ± standard deviation (SD). To determine the significance of the results, a probability value (p value) between 0 and 1 is used to test the validity of a claim made about the parameter measured, which is called null hypothesis. Therefore, a small p value ($p < 0.05$) indicates strong evidence against the null hypothesis, which means that the null hypothesis is rejected and there is a significant difference on the parameter measured hence on the results (* $p < 0.05$, ** $p < 0.01$, *** $p < 0.001$ and **** $p < 0.0001$) [150, 151].

4.10 Heat and Water Transport PAP Model Results

The purpose of this chapter was to extrapolate the variation on the ASL layer water content, dryness or over-evaporation effect after PAP application, quantified on the human *in-vitro* respiratory cell models to the human upper airways and formulate a model to quantify the water transfer flux from the ASL layer to the airflow in the human upper airways. To achieve the objective, five state variables were defined: airflow temperature (T_A), ASL outer surface temperature (T_M), water concentration on the airflow (C_A), water concentration on the ASL layer (C_M) and water transfer flux (N). To determine the evolution of each state variable along the respiratory tract, five governing scalar transport equations and energy balance equations based on the idealized symmetric cylinder-based airway control volume have been solved for each pressure condition: 0 (normal breathing conditions), 5, 10, 15 and 20 cmH_2O.

The evolution of the five state variables (T_A, T_M, C_A, C_M, N) and the airflow relative humidity (rH) along the upper airways have been analysed and compared for each pressure scenario simulated. The relative humidity has been included in the results because it is an indicative parameter of how much more water vapour is needed in the PAP compressed air to overcome the dryness side effect reported by LSD patients.

The temperature and water vapour concentration evolution along the upper airways distance, according to the airway cylinder number, on the ASL outer surface (T_M and C_M respectively) are represented in Figure 4.5A and Figure 4.5B respectively. Results show a significant reduction of temperature and water vapour concentration on the ASL outer airflow interface for each PAP applied compared to normal breathing conditions (control at $\Delta P=0$). The same trend is observed in both figures because the water vapour concentration at the ASL outer surface is based on the thermodynamic water saturated liquid-vapour equilibrium and depends on the ASL outer temperature exclusively.

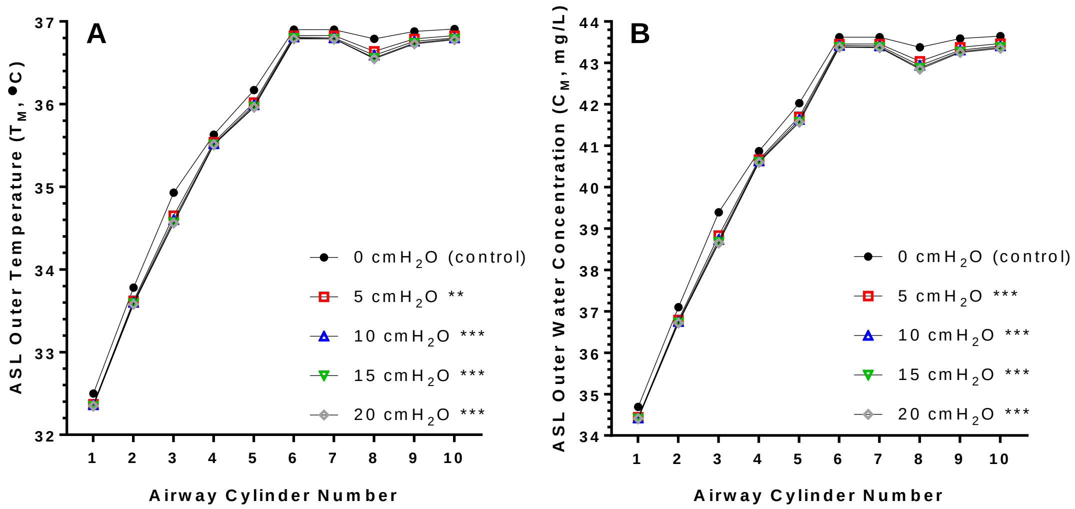

Figure 4.5. Evolution of ASL outer surface temperature (A) and water vapour concentration (B) along the upper airway cylinder at ΔP=0, 5, 10, 15 and 20 cmH2O. 1- Nasal Vestibule, 2- Nasal Cavity, 3- Nasal Turbinate, 4- Proximal Nasopharynx, 5- Distal Nasopharynx, 6- Oropharynx, 7- Hypopharynx, 8- Larynx, 9- Proximal trachea, 10- Distal trachea.

Regarding the airflow conditions, the mean temperature, water vapour concentration, water flux from the ASL layer to the airflow and relative humidity evolution (T_M, C_M, N and rH respectively) as a function of the upper airways distance or airway cylinder number are represented in Figure 4.6A, Figure 4.6B, Figure 4.6C and Figure 4.6D respectively.

Results show a significant reduction of airflow temperature (average of 5°C) and water vapour concentration (average of 5 mg/L) for each PAP applied compared to normal breathing conditions (control at ΔP=0), higher than the difference observed on the ASL outer airflow interface in Figure 4.5. Also, the airflow temperature and water vapour concentration evolution at ΔP≠0 has a more noticeable effect compared to the ASL outer airflow interface, which is more disparate at higher pressures.

The water flux is the transport of water molecules from the ASL to the airflow as a function of area and time, and it is the parameter used to quantify the mass transfer effect, water transfer in our case. It is significantly greater when the pressure is applied, which means that the liquid water reservoir on the ASL layer has to be greater than in normal conditions (ΔP=0) in order to have enough water to achieve the thermodynamic liquid-vapour phase equilibrium on the ASL outer surface and prevent ASL dryness. The amount of water supplied to the airflow to achieve air conditioning and hence equilibrium is determined by the water flux (N) from the ASL layer to the airflow.

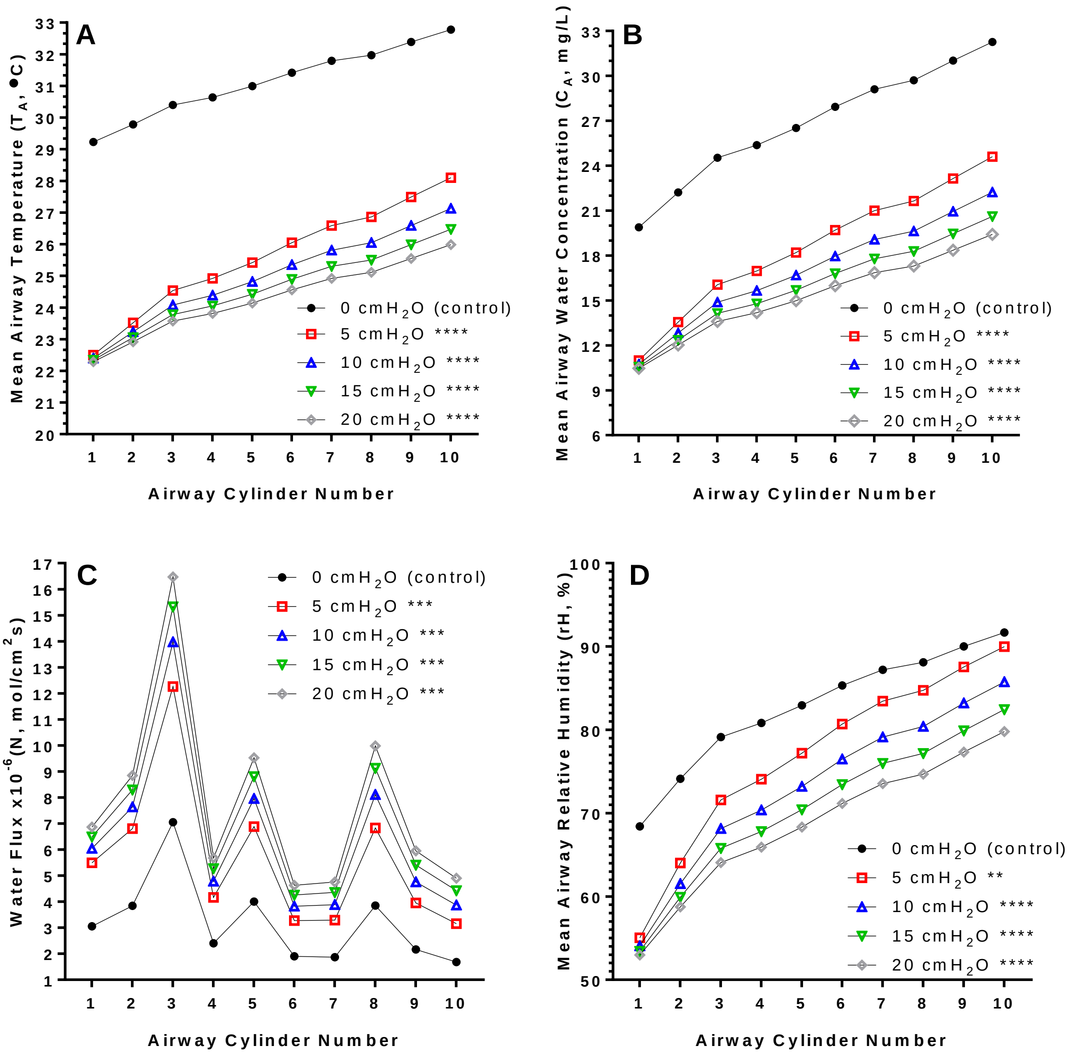

Figure 4.6. Evolution of mean airflow temperature (A), water vapour concentration (B), water flux (C) and relative humidity (D) along the upper airway cylinder at ΔP=0, 5, 10, 15 and 20 cmH2O. 1- Nasal Vestibule, 2- Nasal Cavity, 3- Nasal Turbinate, 4- Proximal Nasopharynx, 5- Distal Nasopharynx, 6- Oropharynx, 7- Hypopharynx, 8- Larynx, 9- Proximal trachea, 10- Distal trachea.

The mean airway relative humidity is a parameter calculated from the mean airway water concentration and temperature, and represents the amount of water vapour present in the airflow at each upper airway section (cylinder). It is also significantly reduced after PAP application and noticeable at higher pressures.

4.11 Heat and Water Transport PAP Model Validation

To validate the human upper airway PAP model, the results obtained for the normal breathing conditions scenario (ΔP=0) have been compared with previous literature research on human air conditioning process. The results obtained for each pressure condition (5, 10, 15 and 20 cmH_2O) have been compared with the experimental results obtained in the two epithelial cell *in-vitro* models.

The temperature and water concentration, in ASL outer surface and mean airflow, water flux and relative humidity evolution as a function of the upper airway distance obtained from the mathematical model under normal breathing conditions (control at ΔP=0) are in agreement with the inspiration airflow evolution obtained in air-conditioning models previously developed on the literature [33, 36, 74-79, 100, 159]

It is important to note that in chapter 3, to measure cell layer characteristics, a minimum significant pressure application time was optimized in order to avoid a bacterial contamination risk and avoid mucus secretion which would interfere in the parameter reading. Hence, during the experiments, the PAP was applied for only 10 minutes in order to quantify exclusively the ASL thickness reduction due to water transfer from the ASL to the airflow, otherwise higher exposure times will allow the cell line to recompose the ASL with mucus secretion.

Based on the law of conservation of mass, it is possible to state that the ASL layer thickness reduction quantified experimentally corresponds to the amount of water molecules transferred from the ASL layer to the airflow, which is the water flux. Hence, model validation is achieved comparing the flux increase of water molecules transferred from the ASL layer to the airflow (N) due to ΔP increase determined theoretically with the mathematical human upper airway PAP model, with the ASL thickness (y) reduction quantified experimentally after each PAP application.

To determine the flux increase as a function of the pressure variation, the water flux average is calculated from all model sections (cylinders) at each pressure (N_{AV}). Then, the dimensionless increase is calculated from the water flux average at ΔP=0 cmH_2O (control) (N_{AV_0}) to the water flux average at ΔP≠0 (PAP application) ($N_{AV_{\Delta P}}$), as described in the first part of equation 4.19.

$$N_{Increase} \approx \left(\frac{N_{AV_{\Delta P}} - N_{AV_0}}{N_{AV_0}}\right)_{Theoretical} \approx \left(\frac{\Delta TEER_{\Delta P} - \Delta TEER_0}{\Delta TEER_0}\right)_{Experimental} \qquad 4.19$$

The experimental water flux increase due to ASL thickness decrease as a function of the pressure variation was quantified in chapter 3. Briefly, the measured TEER values are compared between the 70% RH and 100% RH scenarios at specific pressure with the control measurement (no PAP application, ΔP=0) as described in the second part of equation 4.19. The resulting theoretical and experimental water flux increase as a function of the pressure variation (ΔP) on both epithelial cell in-vitro models, Calu-3 and RPMI 2650 cells, are shown in Figure 4.7.

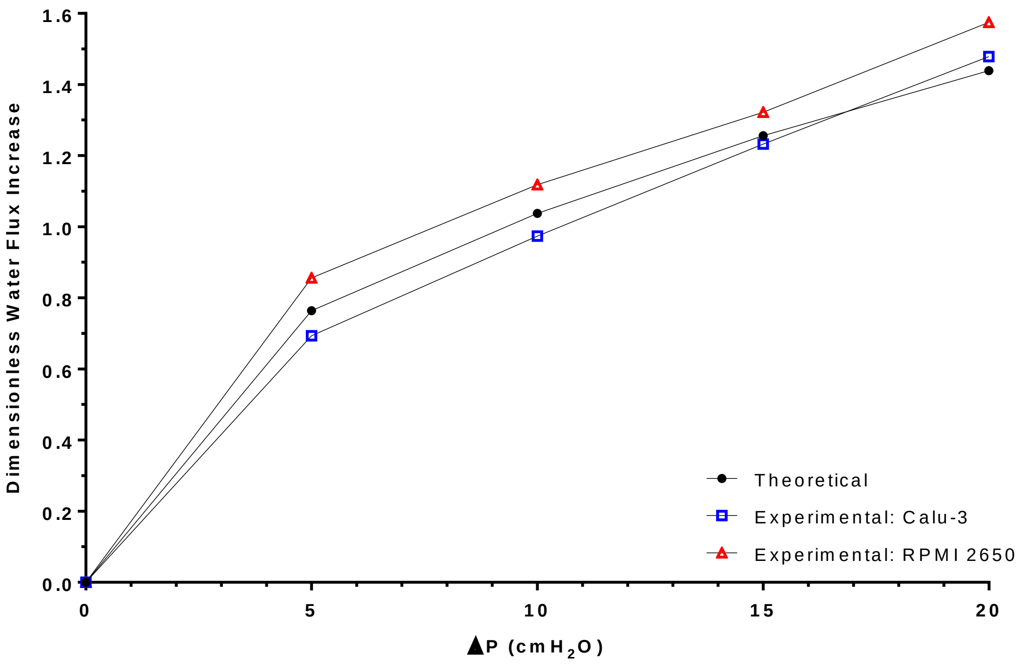

Figure 4.7. Theoretical and experimental, from Calu-3 and RPMI 2650 cells lines, dimensionless water flux increase as a function of pressure variation (ΔP). No significant difference is found on the results which validates the theoretical model.

The results show a similar water flux rise trend proportional to the increase in pressure application. A two-way analysis of variance (ANOVA) followed by Tukey post hoc analysis for multiple comparisons was performed to determine the variation between the results at each ΔP. No significant difference is found between the theoretical or experimental results at each pressure ($p>0.05$), which corroborates the similarity of the results and validates the model.

4.12 Heat and Water Transport PAP Model Input Optimization

In previous literature, intense research has been done to solve the dryness side effect incorporating convective heat transfer humidifiers into the LSD in order to provide an extra humidification on the room compressed air introduced into the respiratory system to generate the PAP [100, 157]. Although it has been proved in chapter 3 that epithelium inflammation or the lack of mucus secretion from goblet cells produced after PAP therapy is not solved by humidifying the respiratory tract, the use of a proper humidification will increase the comfort of patients using LSD.

Hence, a failure in air-conditioning under PAP therapy and dryness side effect are currently corrected increasing the inlet temperature and humidity in inspired air to help the airflow to reach 37°C and 44 mgH_2O/L at the main bronchi with the LSD convective heat transfer humidifier. The determination of the rise in temperature and humidity on inspired air is qualitatively determined by the LSD patient when the dryness side effect is relieved. However, an excess of moisture can be provided because the humidity requirements are not quantitatively determined. Hence, the final goal of this chapter is to optimize the model input variables (air temperature and water vapour concentration) to approximate the previous results obtained under the different pressures analysed (Figure 4.6, $\Delta P \neq 0$) to the normal breathing conditions where no pressure is applied (Control, $\Delta P=0$).

The main airway temperature, water concentration, relative humidity and water flux evolution along the upper airway simulated for normal breathing conditions (Control, $\Delta P=0$), using the inlet parameters set at 29°C and 65%rH for bed environment conditions, have been considered as a reference. Then the inlet parameters for each pressure scenario have been increased, starting from the neutral sleeping environmental conditions 22°C and 50%rH, until no significant difference is found between the new main airway temperature, water concentration, relative humidity and water flux evolution along the upper airway and the reference results (Control, $\Delta P=0$).

The optimum inlet conditions for each pressure analysed are presented in Table 4.4 and the resulting main airway temperature, water concentration, relative humidity and water flux evolution along the upper airway obtained using the optimum inlet air temperature and water concentration for each pressure are shown in Figure 4.8. A two-way analysis of variance (ANOVA) followed by Dunnett's analysis for multiple comparisons is performed to determine the variation between the reference parameters evolution ($\Delta P=0$) and the results at each ΔP. No significant difference (p>0.05) is found between the resulting data and the reference after the third section which corresponds to the nasal turbinate.

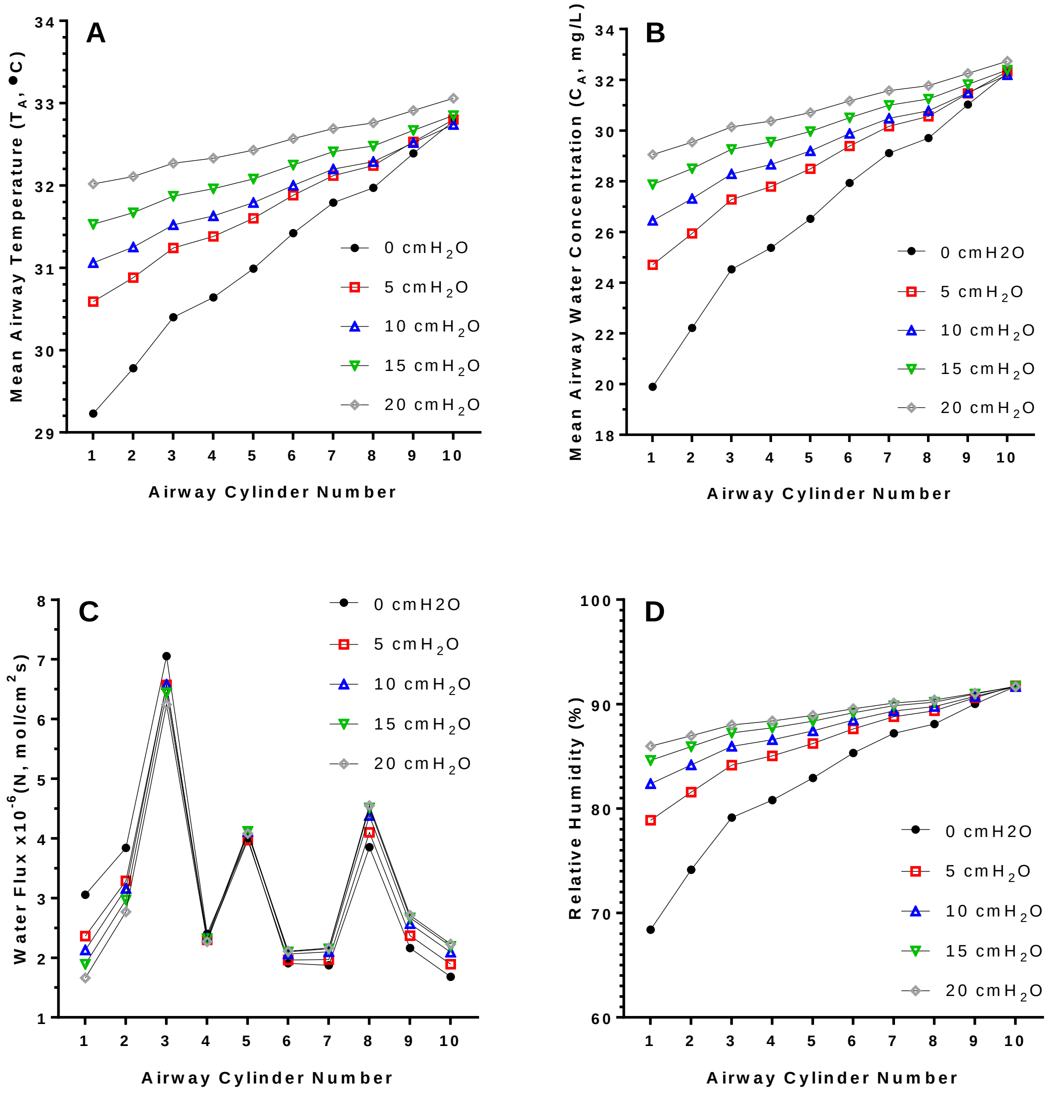

Figure 4.8. Evolution of mean airflow temperature (A), water vapour concentration (B), water flux (C) and relative humidity (D) along the upper airway cylinder at ΔP=0, 5, 10, 15 and 20 cmH₂O using optimum inlet conditions. 1- Nasal Vestibule, 2- Nasal Cavity, 3- Nasal Turbinate, 4- Proximal Nasopharynx, 5- Distal Nasopharynx, 6- Oropharynx, 7- Hypopharynx, 8- Larynx, 9- Proximal trachea, 10- Distal trachea. No significant difference is found on the results after the third cylinder (Nasal Turbinate).

Table 4.4. Optimum inlet airflow temperature (T_{A_0}), relative humidity (rH_0) and water vapour concentration (C_{A_0}) for each PAP application analysed.

ΔP (cmH_2O)	T_{A_0} (℃)	rH_0 (%)	(mg/L)
5	30.5	77.5	24.15
10	31	81.5	26.08
15	31.5	84	27.62
20	32	85.5	28.87

4.13 Analysis of the quantified optimum input T and RH of PAP airflow

The purpose of this chapter was to extrapolate the variation on the ASL layer water content after PAP application quantified on the human *in-vitro* respiratory cell models to the entire human upper airways. Although epithelium inflammation or the lack of mucus secretion from goblet cells produced after PAP therapy is not solved by humidifying the compressed airflow introduced into the respiratory tract to keep the airways open, the use of a proper humidification will increase the comfort of patients using LSD. Hence, a human upper airway theoretical model based on mass and heat transfer equations has been proposed and validated to extrapolate the results to the entire upper airways, predict the failure of the natural air conditioning and quantify the extra water vapour needed in the room compressed air introduced into the respiratory system to generate the PAP and overcome the ASL layer side effect when PAP is applied.

The initial heat and water transport PAP model results show a significant reduction of temperature and water vapour concentration on the ASL outer airflow interface for each PAP applied compared to normal breathing conditions (control at $\Delta P=0$). A similar trend is observed in both state variables because the water vapour concentration at the ASL outer surface is based on the thermodynamic water saturated liquid-vapour equilibrium and depends on the ASL outer temperature exclusively. In addition, a higher reduction is observed in the airflow temperature and water vapour concentration for each PAP applied compared to normal breathing conditions (control at $\Delta P=0$), which is more disparate at higher pressures. Regarding water transfer from the ASL layer to the compressed airflow, the water flux as a function of area and time is significantly greater when the pressure is applied. The mean airway relative humidity is also significantly reduced after PAP application and noticeable at higher pressures.

Then, to validate the human upper airway PAP model, the results obtained for the normal breathing conditions scenario ($\Delta P=0$) have been compared with previous literature research on human air conditioning process. The results obtained for each pressure condition (5, 10, 15 and 20 cmH_2O) have been compared with the experimental results obtained in the two epithelial cell *in-vitro* models, because based on the law of conservation of mass, the ASL layer thickness reduction quantified experimentally corresponds to the amount of water molecules transferred from the ASL layer to the airflow, which is the water flux. Results show no significant differences between the theoretical or experimental water transfer data at each pressure, which corroborates the similarity of the results and validates the model.

Finally the model input variables (inlet airflow temperature and water concentration) have been optimized to approximate the previous state variables obtained under the different pressures analysed (ΔP≠0) to the normal breathing conditions where no pressure is applied (ΔP=0). These quantified input variables can be used to initially set the LSD convective heat transfer humidifier conditions according to the pressure targeted for each patient.

4.14 Closure

This chapter described in detail a human upper airway PAP model based on mass and heat transfer equations to extrapolate the epithelial cell *in-vitro* results obtained in chapter 3 to the entire human upper airways and predict the failure of the natural air conditioning and overcome the ASL layer side effect when PAP is applied to LSD patients. The model has been satisfactorily validated and the model input variables (inlet airflow temperature and water concentration) have been optimized to approximate the resulting state variables obtained under the different PAP scenarios to normal breathing conditions (ΔP=0). Finally, the quantified input variables can be used to initially set the LSD convective heat transfer humidifier conditions according to the pressure targeted for each patient.

In the next chapter, a miniaturized, affordable and eco-friendly device able to uptake water from expiration and release it into the inspiration flow according to the previously quantified input values will be designed and analysed to reduce LSD dimensions and make it comfortable and attractive for patients.

Chapter 5

A proposal for humidifying the inspired gas by using recovered moisture from the expired gas

5.1 Introduction

In Chapter 4, the variation of water content in the ASL layer under different positive pressure scenarios was quantified. From this, the amount of water needed to be introduced into the respiratory system in order to overcome the dryness side effect was also determined.

The goal of this chapter is to develop a proposal for humidifying the inspired gas by using recovered moisture from the expired airflow, and to achieve the humidity quantified in the previous chapter. Simple hydrophilic materials can absorb water to a certain extent, but only releases moisture upon mechanical action, such as wringing or centrifugation. However, certain polymers known as “smart materials” can change their properties under the influence of temperature, pH or light. From the literature, it has been found that cotton treated with poly(N-isopropylacrylamide) (PNIPAM), which is a temperature-responsive polymer, can allow the cotton to switch between hydrophilic and hydrophobic states. In other words, it can collect water at one temperature and release water at another temperature. The PNIPAM is also an eco-friendly and biocompatible material, which is an essential requirement for its application in medical devices [160-162]

In the course of this investigation, the properties of this smart material have been optimized in order to achieve the maximum amount of water vapour uptake and release in the shortest time. Two substrate materials, polyvinyl alcohol (PVA) and organic cotton fabric, have been investigated as substrates for PNIPAM grafting. Since the structure of the thermo-responsive polymer has been seen to affect its properties, different methods were used to perform the PNIPAM grafting. Hence, both linear and branched PNIPAM, along with different chain length or molecular weights of polymer were synthesized and the water release rate analysed in order to optimize the smart material for this specific application.

An introduction describing the PNIPAM polymer and the polymerization method used is presented in sections 5.2 and 5.3. The materials, chemicals and the methodology followed to synthesize the polymer are described in section 5.4. Then, the techniques used to characterize the polymer and analyse its performance along with the statistical analysis are explained in sections 5.5 and 5.6. The analysis of the substrate material, polymer structure and chain length or molecular weight constitute the results of this chapter and is described in section 5.7. Finally, sections 5.8 and 5.9 correspond to the discussion of the results and the closure of the chapter, respectively.

5.2 Poly(N-isopropylacrylamide) (PNIPAM): Description and properties

In this section, a brief summary of the literature on PNIPAM behaviour is provided before the structural design of the smart material and the results obtained are presented. A brief description of the thermo-responsive systems available and why PNIPAM was chosen was reported in chapter 2. Here, a more detailed description of PNIPAM behaviour is reported focusing the attention on the fundamental aspects related to the thesis objectives.

The smart behaviour of PNIPAM is directly related to the molecular structure of this polymer (Figure 5.1). Its structure is composed of an n-alkane backbone from which amide functionalities depart, terminating with an isopropyl group. The amide groups are able to form hydrogen bonds with water molecules when a specific molecular orientation occurs [120].

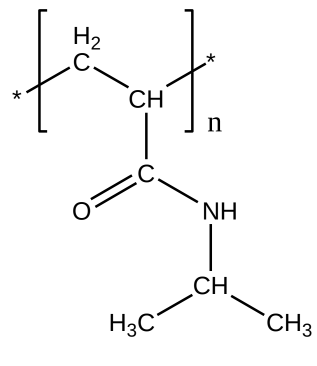

Figure 5.1. Molecular structure of linear PNIPAM repeating unit composed of an n-alkane backbone from which amide functionalities depart, terminating with an isopropyl group.

The strong interaction of polar solvents such as water (which contain atoms with different electronegativities), with the amide groups within PNIPAM causes polymer solvation. The solvated polymer forms an organized structure with the amide and isopropyl groups. With a temperature increase, this eco-friendly temperature-sensitive polymer undergoes a hydrophilic-to-hydrophobic transition, when the polymer precipitates and turns into a coiled conformation. This transition, triggered by changes in free-energy, takes place at a specific temperature range between 30°C and 35°C which is called lower critical solution temperature (LCST). Hence, below the LCST and in the presence of water, the PNIPAM structure is predominantly hydrophilic and the amide groups tend to form inter-molecular hydrogen bonds with the surrounding water molecules. Above the LCST, intramolecular hydrogen bonds between neighbouring amide groups within the PNIPAM polymer are formed, which are energetically more favourable at higher temperatures, and the water molecules associated with the side groups are expelled into the bulk water [120, 135]. This process is outlined in Figure 5.2.

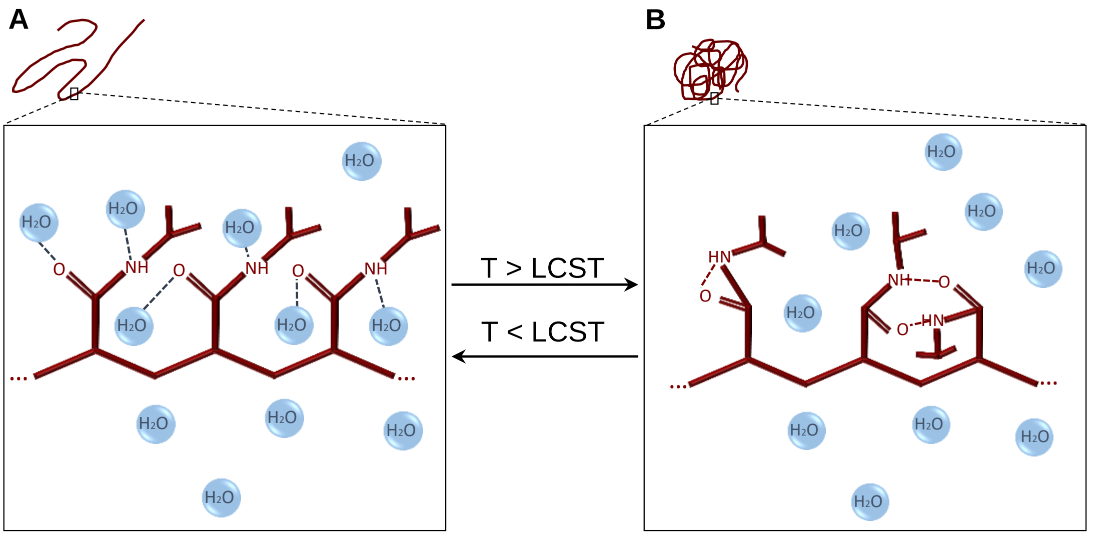

Figure 5.2. Illustration of temperature induced linear PNIPAM phase transition in water solvent. A- Solution temperature below LCST, linear and hydrophilic PNIPAM conformation. B- Solution temperature above LCST, coiled and hydrophobic PNIPAM conformation.

Depending on the microstructure of the macromolecule the LCST can be modified and adjusted to the specific application. For example, the addition of a hydrophilic group induces a shift of the LCST toward higher temperature while hydrophobic groups have the opposite effect and the addition of hydrophilic acrylic acid into the network structure leads to rapid deswelling. Hence, it is possible to synthesize a very specific PNIPAM polymer able to accomplish the desired specifications.

However, a balance has to be made in order to achieve a polymer relatively easy to manufacture in order to be viable for application in industry [163].

In this section, the polymer behaviour of single chains dispersed in a bulk solution has been explained. However PNIPAM has wide applications as a copolymer or being part of other materials such as in stimuli-responsive membranes, which change their physicochemical properties in response to changes in the environmental temperature, or in tissue engineering applications. In these applications, the polymer is synthesized on a substrate and the behaviour of the smart polymer can change. While the driving forces that lead to solvation and precipitation are the same as the polymer in bulk solution (hydrophobic and hydrophilic effects), once PNIPAM chains are incorporated onto a surface, the dense packing of the brushes and the interactions with the substrate can lead to an alteration of the transition process [138, 139, 163, 164].

The structural changes of a smart temperature-responsive polymer combined with the highly rough surface of a fibrous material, leads to reversible and repeatable switching between two extreme wettability states, superhydrophobic and superhydrophilic, which were found by Yang, H. *et al.* [140]. They covered the hydrophilic surface of cotton fabric with a layer of PNIPAM polymer whose chains were grown from the fibre surface with a concentric orientation creating a highly rough surface at the micrometre level. Their results demonstrated that this new material was able to absorb water from a humid environment, below the LCST and release it upon a temperature change at constant humid air flow. The absorption and desorption process is outlined in Figure 5.3. They determined the transition temperature to be at 32°C. Hence, below LCST the polymer had a coiled structure (hydrophilic state) and formed intermolecular hydrogen bonds between the polymer amide and the surrounding water molecules. Above the LCST the polymer had a globule structure (hydrophobic state) and stablish intramolecular bonds between amide groups and release the water molecules previously absorbed.

It was proven that the polymer undergoes a gradual collapse instead of a sharp phase separation. When the temperature increases, the brushes tend to gradually shrink, starting from the outer region of the chains, and finally the brushes collapse onto the substrate expelling the remaining water. The transition of PNIPAM synthesized chains is slower compared to the polymer in bulk solution and can be extended over a broader temperature range depending on the polymer structure. It has been established in previous literature that the effect of the molecular weight related to polymer thickness and chain density affect the final properties, but the effect on the structural transition rate has not been studied in detail [138, 139]. Therefore, aiming to develop a smart material able to absorb and desorb the maximum amount of water vapour in the lowest time possible, different substrate materials and PINPAM structures are evaluated in this chapter.

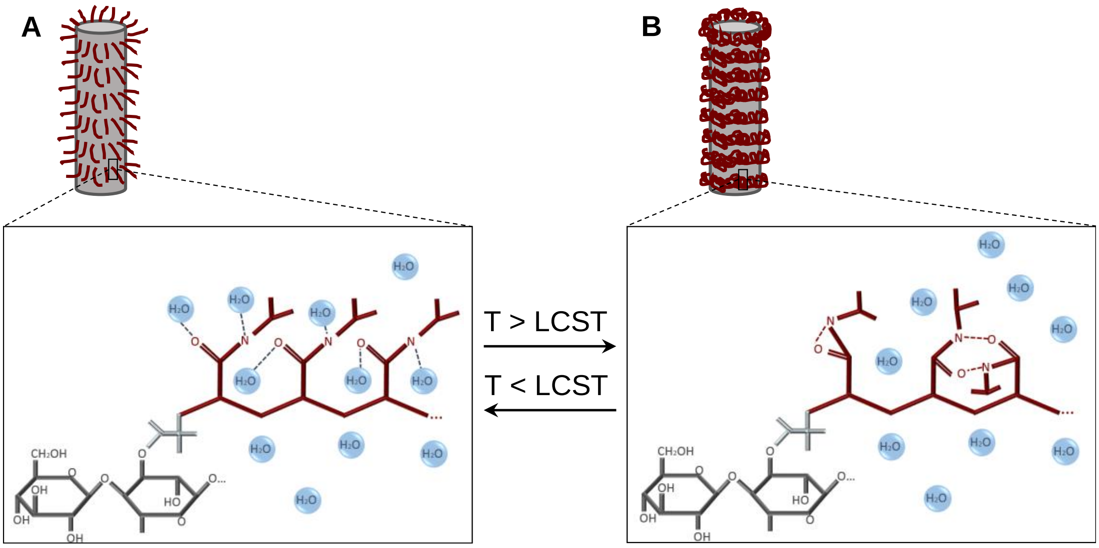

Figure 5.3. Illustration of temperature induced phase transition of PNIPAM synthetized on a cotton fibre and a humidified environment (with water vapour molecules). A- Environmental temperature below LCST, hydrophilic PNIPAM conformation stretched and normal to the cotton fibre. B- Environmental temperature above LCST, hydrophobic PNIPAM conformation collapsed around the cotton fibre.

5.3 Atom Transfer Radical Polymerization

Atom transfer radical polymerization (ATRP) is a controlled polymerization reaction without chain-breaking, based on the use of radical polymerization to convert monomers to a polymer. This technique is used to synthesize well-defined polymers with a precise molecular architecture [165-168]. The ATRP mechanism is outlined in Figure 5.4. The propagation process starts when homolytic cleavage of the alkyl-halogen bond (R-X) by a transition metal complex in a lower oxidation state (Mt^n-Y) generates an alkyl radical (R·) and a transition metal complex in a higher oxidation state (X-Mt^{n+1}-Y). The formed radicals can initiate the polymerization by adding across the double bond of a vinyl monomer (M), propagate, and terminate by either coupling (R-R), disproportionation, or be reversibly deactivated by the transition metal complex in the higher oxidation state.

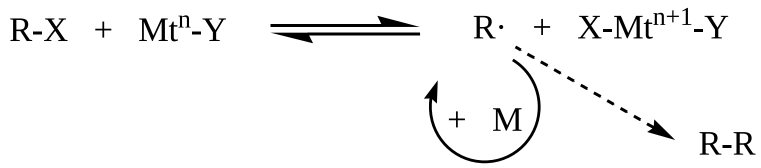

Figure 5.4. Atom transfer radical polymerization (ATRP) mechanism, where R-X represents the alkyl halide, Mt^{n}-Y is the transition metal complex in the lower oxidation state, R· represents the alkyl radical, X-Mt^{n+1}-Y is the transition metal complex in the higher oxidation state bonded to the alkane, M is the vinyl monomer and R-R represents the termination step of the polymerization by coupling.

Using this polymerization method, it is possible to produce complex structured polymers with high molecular weight and low polydispersity index due to the control achieved on the process, since all chains start growing at the same time. Hence, to maintain control of the reaction, and to achieve a narrow polydispersity index and molar mass distribution, it is necessary to have a homogeneous system, a fast initiation rate and fast exchange between active and inactive species in order to allow all chains to start to grow simultaneously. The main difficulty it to completely eliminate the transition metal once the synthesis is accomplished. This is solved by increasing the activity of the catalyst in order to reduce the quantity of metal used. Hence, the catalyst sensitivity toward oxygen and oxidant molecules has to be reduced by performing the polymerization process in an inert atmosphere [165-168].

ATRP was therefore the method chosen to synthetize the PNIPAM, to obtain diverse structures on different substrate materials without the need for expensive laboratory equipment. The technique is a method applicable to industrial processes to produce the desired smart engineered material.

5.4 Smart material preparation

In this section, the substrate materials, chemicals and the methodology followed to synthesize the PNIPAM polymer using the ATRP method, along with the purification procedures are explained in detail.

5.4.1 Substrate materials

In section 2, it was stated that the thermal transition and structural behaviour of the PNIPAM synthesized chains depends directly on the polymer structure, including the molecular weight and dispersity of polymer chains grown. The selection of the substrate material is crucial in order to have the maximum number of active sites available to grow the PNIPAM, which directly affects the dispersity of synthetized polymer chains. Also, the structure of the substrate material has to contain a significant amount of alcohol side groups to allow the polymer growth at high grafting yield and ensure maximum water uptake. Finally, the final product must be eco-friendly and biodegradable in order to satisfy the final smart material specifications. Hence, according to these requirements, two substrate materials have been selected to be analysed: poly(vinyl alcohol) (PVA) and organic cotton.

PVA is a hydrophilic, water-soluble, colourless and odourless polymer used in a wide range of applications such as papermaking, textiles, adhesive or coatings. It is an atactic material that exhibits crystallinity and in terms of microstructure, it is composed of 1,3-diol linkages. It melts at 200°C and above this temperature the polymer starts degrading. PVA is purchased in a sponge-like macrostructure with heterogeneous porosity in order to allow water vapour molecules to pass through the material without physical restrictions as shown in Figure 5.5 [127-133].

A **B**

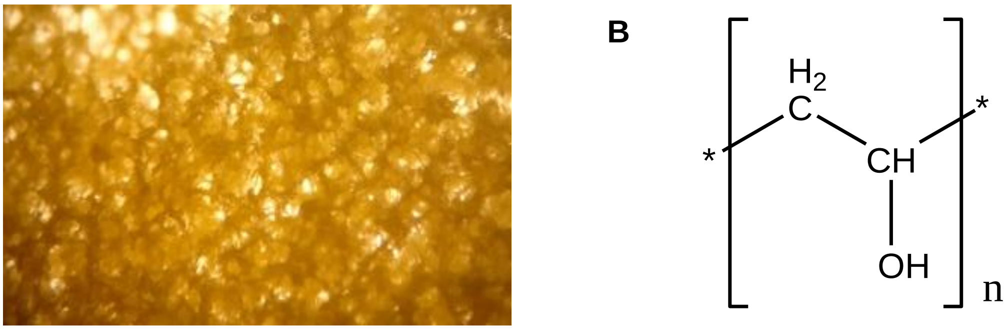

Figure 5.5. Poly (vinyl alcohol) (PVA) substrate. A- Picture of the purchased PVA sponge-like macrostructure showing the heterogeneous porosity. B- Chemical microstructure of the PVA.

Organic cotton is grown using methods and materials that have a low impact on the environment. It is a natural soft white fibrous substance which surrounds the seeds of the cotton plant (*Gossypium*) and is made into textile fibre or thread for sewing. Cotton fabrics are hard weaving, comfortable and capable of being coloured. Cellulose is the main component of the cotton structure (99%). It is a macromolecule made up of a long chain of glucose molecules linked by C-1 to C-4 oxygen bridges called glycoside bonds. The glucose units are linked together in a beta-cellobiose conformation which from the repeating unit of the polymer chain as shown in Figure 5.6. The three hydroxyl groups, one primary and two secondary, in each repeating cellobiose unit of cellulose are chemically reactive and keep the fibre molecules closely packed in parallel. This is why cotton cellulose has a high degree of polymerization and crystallinity. Cellulose fibres are also a strong material, which can be heated up to 250°C before decomposition [169, 170]. The cotton fabric used in the experiments was purchased as a medical bandaging to ensure purity and sterility.

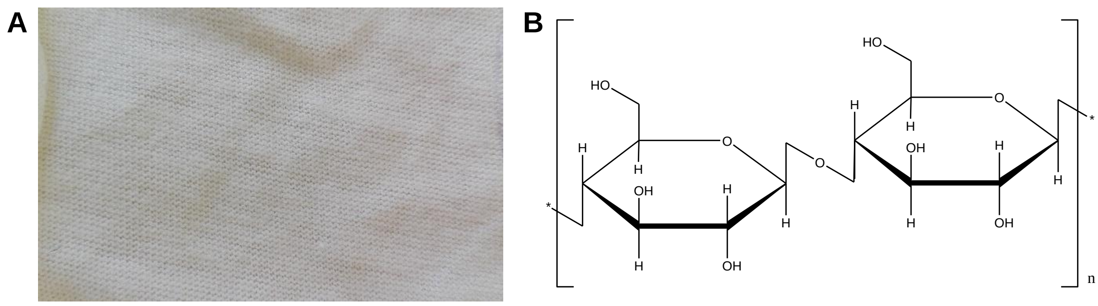

Figure 5.6. Organic cotton fabric substrate. A- Picture of the purchased medical cotton bandage showing the macrostructure. B- Chemical microstructure of cellulose.

5.4.2 Chemicals

The chemical products used to polymerize the PNIPAM were: ethanol (99.5%), methanol (99.9%), acetone (99.8%) dry tetrahydrofuran (THF) (99.8%), 4-(dimethylamino) pyridine (DMAP) (99%), triethylamine (TEA) (99%), bromoisobutyrate (BiB) (99%), copper(I)bromide (CuBr) (98%), N-Isopropylacrylamide (NIPAM) (99.5%), pentamethyldiethylenetriamine (PMDETA) (99%), ethyl 2-(bromomethyl) acrylate (EBMA) (98%), dimethylformamide (DMF) (99.8%), deuterated 4-methanol (Methanol-d_4) (99.96%) and sodium hydroxide (NaOH) (97%). All products were obtained from Sigma Aldrich (Merck) New Zealand.

5.4.3 Linear PNIPAM synthesis

The ATRP method has been used to grow linearly PNIPAM chains from the hydrophilic surface of the substrate material. The polymerization process has two important steps: the substrate surface modification and the grafted PNIPAM polymerization.

5.4.3.1 Immobilization of the ATRP-initiator: substrate surface modification

The first step is the substrate surface modification or the immobilization of the ATRP-initiator onto the substrate material, where one bromine atom of the initiator (bromoisobutyrate, BiB) reacts with one alcohol group forming an oxygen-bromine covalent bond between the substrate and the initiator [163, 171]. The reaction mechanism is outlined in Figure 5.7 and the methodology followed has been optimized to ensure the best temperature and reaction times as described below:

- The substrate material was washed in an aqueous solution containing a commercial soap-detergent with magnetic stirring for 1 hour at 100°C, to remove dust and impurities. Then, it is rinsed with water, acetone and ethanol.
  This procedure is repeated three times.

- The substrate material was dried at 80°C under vacuum for 24 hours. This is a crucial step because the substrate material has to be completely dry to achieve a high reaction yield.

- Each side of the substrate material was exposed to 234 nm UV light wavelength for 30 minutes in order to activate the alcohol functional groups.

- Then the substrate was added into a round-bottom flask containing THF and a magnetic stirrer.

- The flask was sealed, connected to an active nitrogen gas line and left in an ultrasonic bath for 30 minutes in order to remove the oxygen from the flask and generate an inert atmosphere.

- Then, the flask was sealed with a nitrogen balloon to generate a positive pressure and a catalytic amount of DMAP, TEA and an excess of BiB were added into the solution.

- The reaction was kept at 40°C under magnetic stirring for 24 hours.

- The ATRP-initiator or BiB-substrate product was rinsed thoroughly and consecutively for 3 times with THF, ethanol, acetone and water.

- The BiB-substrate was dried at 80°C under vacuum for 24 hours. As stated before, this is a crucial step since the substrate material has to be completely dry to achieve a high reaction yield.

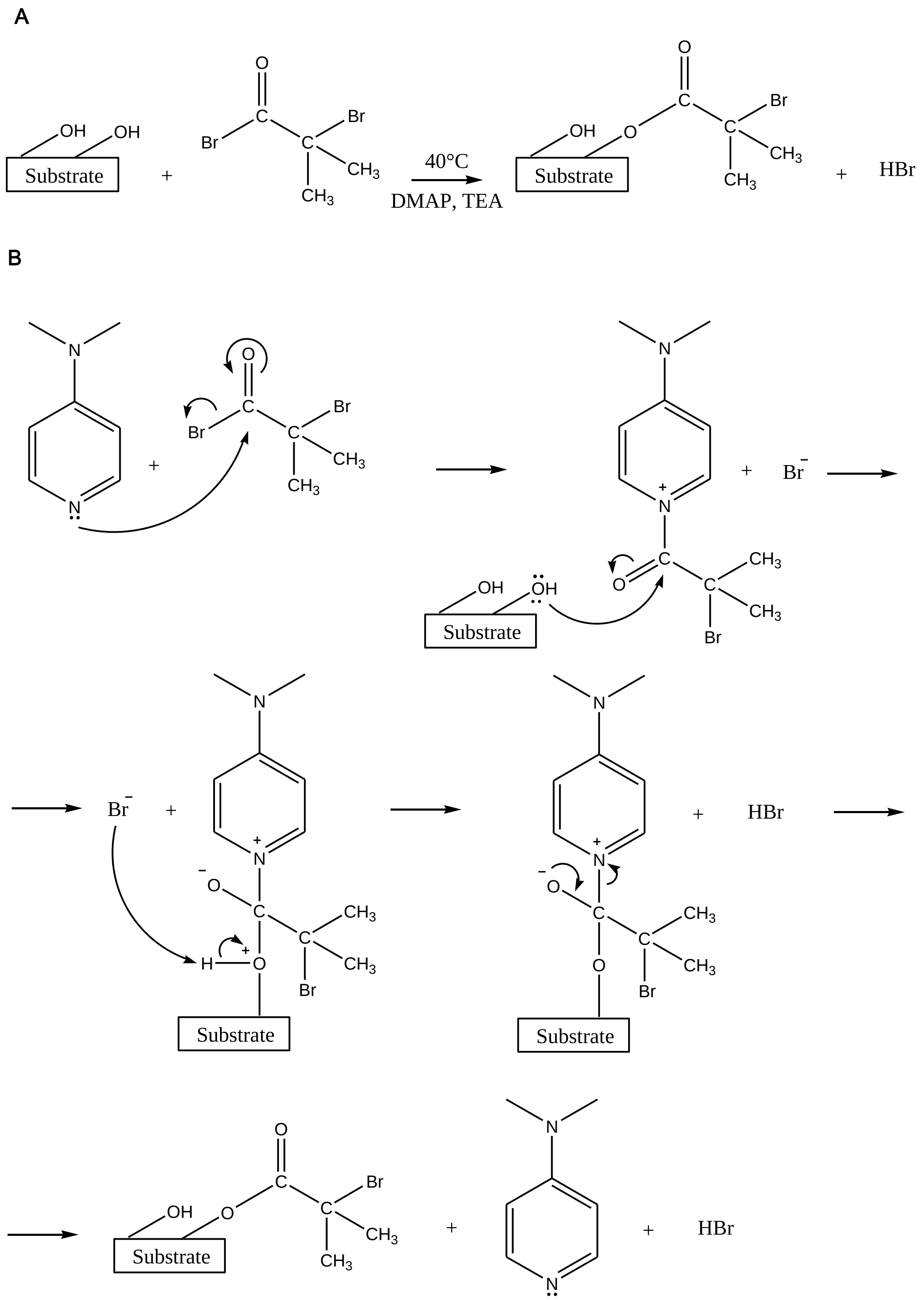

Figure 5.7. Immobilization of the ATRP-initiator on the substrate. A- Main reaction. B- Reaction mechanism.

5.4.3.2 Grafting of NIPAM from the BiB-Substrate: Linear PNIPAM polymerization

In the second stage, the polymerization process starts from the monomer (NIPAM) reacting with the second bromine of the ATRP-initiator already bonded to the substrate. There are two essential components in this reaction: PNIPAM and Copper bromide. The PNIPAM is the polymer going to be grafted for its properties. The Copper bromide is the ATRP catalyst. It switches its valence electrons from Cu I to Cu II and back. With this, it can repeatedly attract and repel the second bromide of the BiB-substrate. The Br atom is replaced by a radical, which subsequently results in the reaction between the BiB-substrate and PNIPAM [163, 171]. The reaction mechanism is outlined in Figure 5.8 and the methodology followed has been optimized to ensure the best temperature and reaction times as described below:

- A methanol/Milli-Q-water solution (30:10) was added into a round-bottom flask containing a magnetic stirrer.

- The flask was sealed, connected to an active nitrogen gas line and left in an ultrasonic bath for 30 minutes in order to remove the oxygen from the flask and generate an inert atmosphere.

- A catalytic amount of CuBr, NIPAM and the BiB-substrate were added into a Schlenk flask. The flask was sealed and connected to an active nitrogen gas line to remove the oxygen and generate an inert atmosphere.

- Then, the methanol/Milli-Q-water solution and PMDETA were added into the Schlenk flask. The solution was frozen by liquid nitrogen and sequentially degassed by three freeze-vacuum-nitrogen-thaw cycles to remove the remaining oxygen. This is the most effective method of degassing a solvent.

- The flask was connected to a vacuum line and immerse in liquid nitrogen until the solvent was completely frozen.

- Then, vacuum was generated for 2-3 minutes and the flask was removed from the liquid nitrogen to allow the solvent to thaw and any gas bubbles trapped in the solvent to escape into the headspace of the flask. This process was repeated three times.

- The flask was filled with nitrogen and sealed with a balloon to generate a positive pressure.

- The reaction was kept at 40°C under magnetic stirring for 48 hours.

- The PNIPAM-substrate product was rinsed thoroughly and consecutively for 3 times with ethanol, acetone and water and dried at 50°C under vacuum for 24

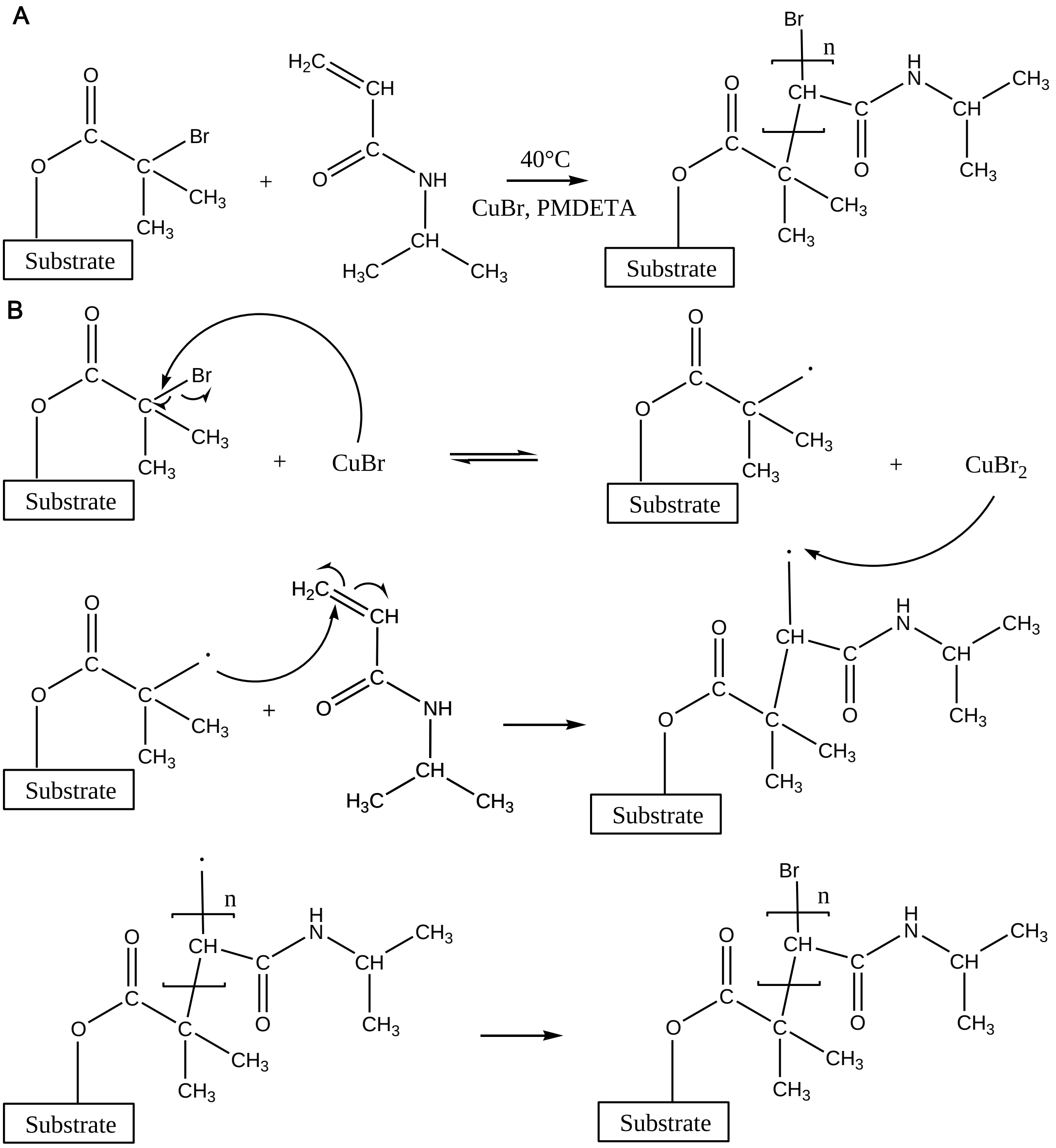

Figure 5.8. Linear grafting of NIPAM from the BiB-Substrate. A- Main reaction. B- Reaction mechanism.

5.4.4 Branched PNIPAM synthesis

Polymer architecture plays an important role in the final properties of the smart material synthetized. Compared to their linear analogues, branched polymers may exhibit significantly different behaviours due to a pronounced effect of reduced chain entanglement and hydrodynamic volume [136, 172-175]. Thus, a branched PNIPAM was grafted from the substrate material for further investigation. The water vapour desorption performance was compared with the linear PNIPAM previously described.

The substrate surface modification or the immobilization of the ATRP-initiator on the substrate material step, where one bromine atom of the initiator (bromoisobutyrate, BiB) reacts with one alcohol group forming an oxygen-bromine covalent bond between the substrate and the initiator agent, follows the same methodology as the linear PNIPAM grafting. Next, the ATRP method was used to grow the PNIPAM from the hydrophilic surface of the substrate material. To synthesize branched PNIPAM, the polymerization process has three important steps: the initial grafted PNIPAM polymerization, the addition of ethyl 2-(bromomethyl)acrylate (EBMA) to initiate the branched points, and the PNIPAM polymerization from the EBMA. The reaction mechanism is outlined in Figure 5.9 and the methodology followed has been optimized to ensure the best temperature and reaction times as described below:

- A methanol/Milli-Q-water solution (30:10) was added into a round-bottom flask containing a magnetic stirrer. The flask was sealed, connected to an active nitrogen gas line and left in an ultrasonic bath for 30 minutes in order to remove the oxygen from the flask and generate an inert atmosphere.

- A catalytic amount of CuBr, NIPAM and the BiB-substrate were added into a Schlenk flask. The flask was sealed and connected to an active nitrogen gas line to remove the oxygen and generate an inert atmosphere. Then, the methanol/Milli-Q-water solution and PMDETA were added into the Schlenk flask. The solution was frozen by liquid nitrogen and sequentially degassed by three freeze-vacuum-nitrogen-thaw cycles to remove the remaining oxygen.

- The flask was connected to a vacuum line and immersed in liquid nitrogen until the solvent was completely frozen. Then, vacuum was generated for 2-3 minutes and the flask was removed from the liquid nitrogen to allow the solvent to thaw and any gas bubbles trapped in the solvent to escape into the headspace of the flask. This process was repeated three times. The flask was filled with nitrogen and sealed with a balloon to generate a positive pressure.

- The reaction was kept at 40°C under magnetic stirring for 1 hour. Then, EBMA was added into the solution and the reaction was kept at 40°C under magnetic stirring for 48 hours. The PNIPAM-substrate product was rinsed thoroughly and consecutively for 3 times with ethanol, acetone and water and dried at 50°C under vacuum for 24 hours.

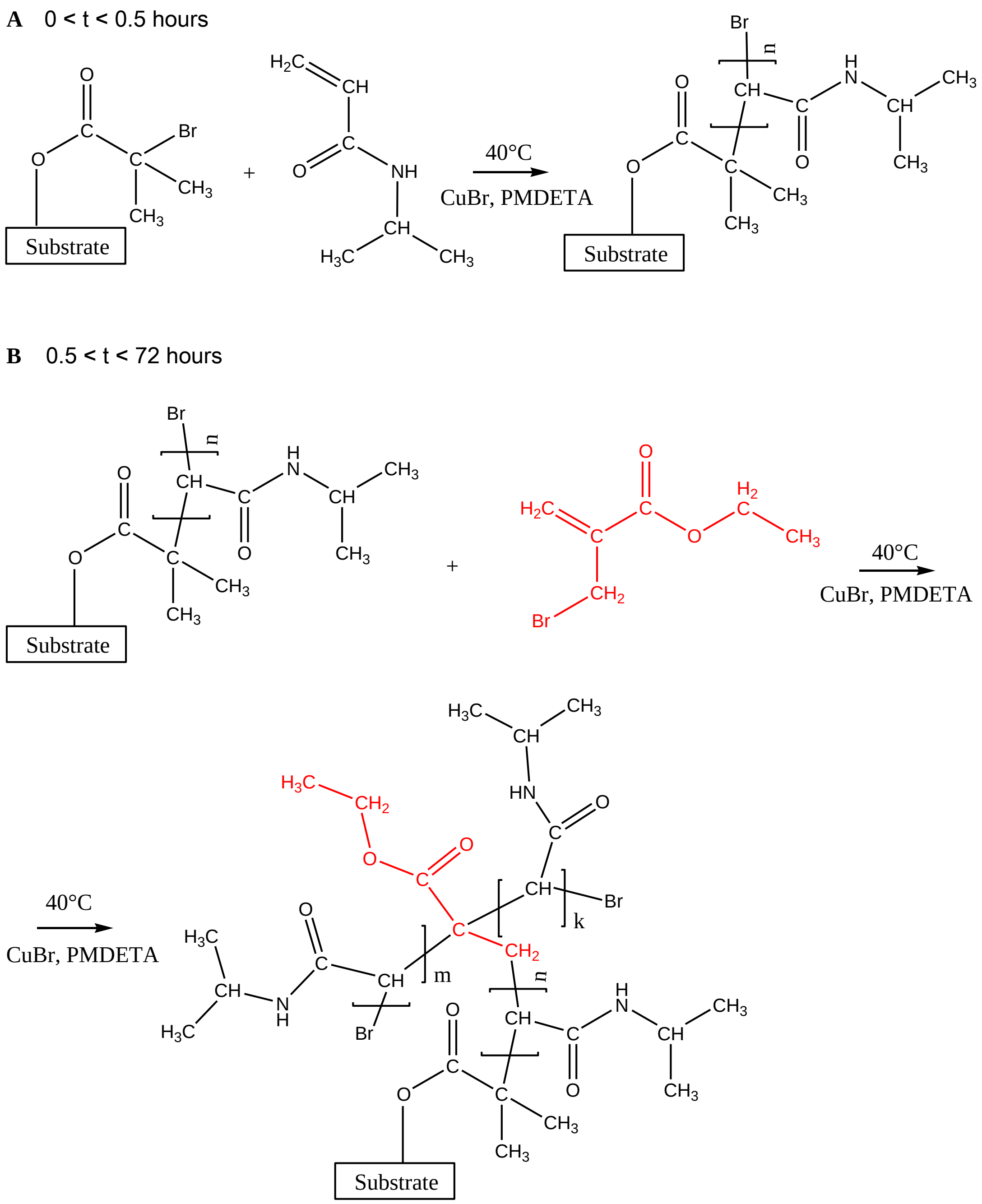

Figure 5.9. Reaction scheme of branched grafting of NIPAM from the BiB-Substrate. A- From the reaction start to 30 minutes, the PNIPAM is growing linearly. B- After 30 minutes, the EBMA

(highlighted in red) is added into the solution to generate the branched points from where PNIPAM starts growing and generates the branches.

5.4.5 Extended purification procedure

The PNIPAM-substrate smart material is synthesized to be in contact with the human breathing cycle and to humidify the inspired gas by using recovered moisture from the expired gas. Hence, it is very important to purify the material and eliminate any traces of monomer, catalyst and solvent before starting the humidification experiments.

The methodology followed to perform the extended purification step has been optimized to ensure the best temperature and reaction times as described below:

- The PNIPAM-substrate was Soxhlet extracted with methanol in reflux for 1 hour to remove the non-reacted monomer residue, any polymer absorbed at the surface but not covalently bonded and any remaining catalyst complexes.

- After the extraction procedure the PNIPAM-substrate was dried at 50°C under vacuum for 24 hours and stored in an incubator at 50°C to ensure the material was dry before starting the next set of experiments.

5.5 Smart material characterization

Different techniques have been used in this research to monitor the polymerization process, to ensure qualitatively and quantitatively the successful synthesis of PNIPAM, to analyse the thermal transition performance and to determine the final PNIPAM molecular weight. The techniques and methodology used are explained in detail in this section.

5.5.1 Proton nuclear magnetic resonance (^1H NMR)

Nuclear Magnetic Resonance (NMR) spectroscopy is a non-invasive analytical technique used to determine and quantify the content, purity and molecular structure of a sample. There is a wide variety of one and two dimensional NMR techniques available including carbon (^{13}C-NMR) and correlated spectroscopy (COSY) between others, but the proton nuclear magnetic resonance (^{1}H NMR), which is used to identify the carbon-hydrogen framework of an organic compound, was chosen to monitor the polymerization process and measure the amount of monomer reacted as a function of time [176].

To understand the measurements carried out during the experiments, a brief explanation of the operating principle of ^{1}H NMR is presented. The atomic nucleus hydrogen (or a proton) is a spinning charged particle which generates a magnetic field. Without an external applied magnetic field, the nuclear spins are randomly orientated. However, when an external magnetic field is present, the atomic nucleus align themselves either with the field of the external magnet or against it. The energy absorbed to align the nuclei has a specific wavelength and frequency and when the external magnetic field stops, the spin returns to its randomly orientated base level and energy is emitted at a specific frequency called the resonant frequency. As the precise resonant frequency of each nucleus depends on the magnetic field applied, a proton reference frequency is needed. Tetramethylsilane (TMS) is generally used as the reference in most experiments because it emits a low frequency signal and it can easily be removed from the sample by evaporation due to its volatile properties [176].

However, the frequency measured is not easy to assess due to its magnitude and large number of decimals, so a new parameter is defined to analyse the signals obtained. The chemical shift (δ) is measured in parts per million (ppm) and quantifies how far the signal emitted from the proton (f_{Proton}) is compared to the TMS reference compound signal (f_{TMS}) and the magnetic field applied from the spectrometer ($f_{spectrometer}$). It is calculated according to equation 5.1. The NMR spectrum or proton chemical shifts range from 0 ppm (TMS reference signal) to 15 ppm and is identical for a specific proton regardless of the spectrometer used [176].

$$Chemical\ Shift\ (\delta) = \frac{f_{Proton}\ (Hz) - f_{TMS}\ (Hz)}{f_{spectrometer}\ (MHz)} \tag{5.1}$$

The signal produced from the nucleus of interest is also affected by the orientation of the neighbouring nuclei and this effect is known as spin-spin coupling. As a consequence, the signal is divided into two or more lines depending on the number of chemically bonded protons in the vicinity of the observed nuclei. The size of the splitting is called coupling constant (J) and is independent of the magnetic field and measured as absolute frequency (Hz). Some common and simple coupling patterns are: the singlet (one peak) which is the signal emitted from a nuclei that does not have any neighbour proton, the doublet (two peaks) which is the signal emitted from a nuclei that has one neighbour proton or the triplet (three peaks) which is the signal emitted from a nuclei that has two neighbour protons. These patterns can have extra signals or be distorted depending on the complexity of the chemical structure of the molecule analysed [176].

Finally, the integration of a signal or area under the signal, corresponds to the relative number of protons that give rise to each peak or group of peaks. According to Beer's Law, the amount of energy absorbed or transmitted is proportional to a certain number of mols present, so the area under each signal is proportional to the amount of energy absorbed or transmitted and the number of equivalent protons that emitted the energy and generated signal integrated [176]. This measurement was used to the monitor the polymerization process and quantify the amount of monomer reacted or diminished in the solution as a function of time in the experiments compared to the DMF reference which is not involved in the reaction.

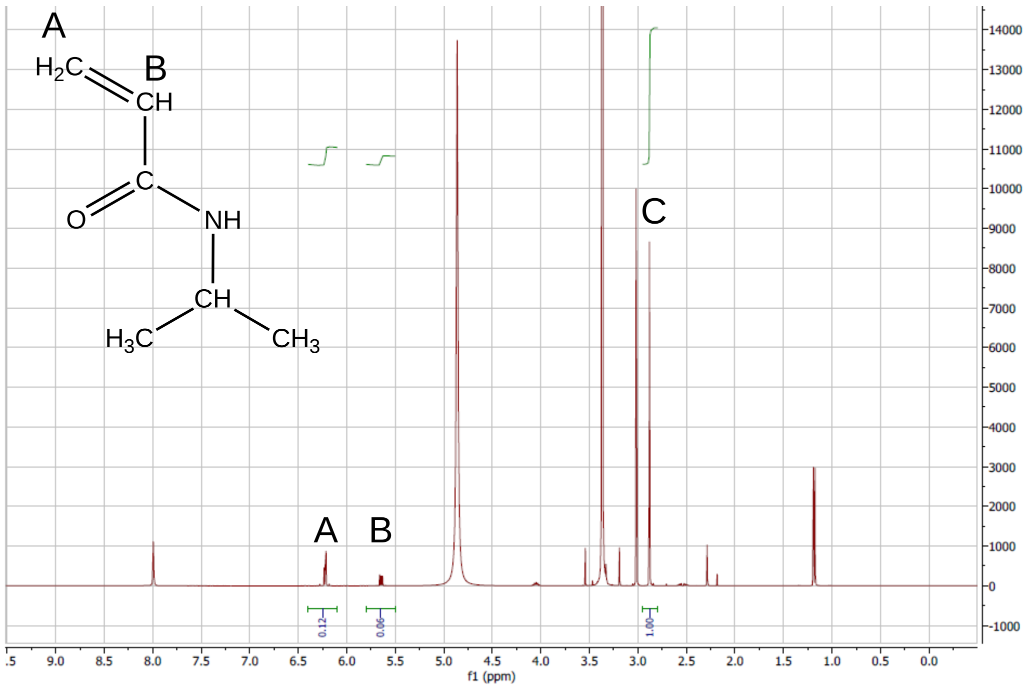

Figure 5.10. Exemplary NMR spectra of a time 0 second reaction mixture sample. Peaks A and B correspond to the NIPAM signal. Peak C corresponds to the DMF stretch vibration band which is used as a reference to perform the integration tool.

^{1}H NMR measurements were performed on a Bruker Ascend^{TM} 400 MHz spectrometer. The proton chemical shifts were recorded in ppm downfield using TMS as a reference and each measurement was averaged from a total of 16 scans. To determine the monomer conversion in time, Methanol-d_4 was used as solvent and DMF was used as an internal reference. Samples of the reacting mixture were taken at 0, 1, 8, 24, 48 hours from the reaction start to monitor the NIPAM grafting (second step), and immediately injected into a sealed NMR tube for the ^{1}H NMR experiments. The NMR spectra was obtained through the Bruker software (TopSpin v3.5) and exported to be analysed with the MestReNova v12.0.2 software. An exemplary spectrum is shown in Figure 5.10.

5.5.2 Fourier transform infrared spectroscopy (FTIR)

FTIR infrared spectroscopy is a technique used to obtain an infrared spectrum of absorption or emission of a solid, liquid or gas sample. It is used in many analytical applications, especially for polymers and organic compound identification. The IR radiation emitted from the spectrometer is passed through the material being analysed where some radiation is absorbed by the sample and some passes through (or transmitted). The absorbed IR radiation excites the molecules into a higher vibrational state and the wavelength of light absorbed is a function of the energy difference between the at-rest and excited vibrational states. The wavelengths absorbed by the sample are characteristic of its molecular structure. Then, when the resulting signal reaches the detector, a mid-infrared (4000 to 200 cm^{-1} wavelength) spectrum is generated representing a unique molecular 'fingerprint' of the sample. The FTIR uses interferometry, where different waves are superimposed to generate an interference and information about the material placed in the IR beam is extracted. The Fourier Transform results in a patterned spectrum which is used to identify or quantify the sample analysed, since molecules exhibit specific IR fingerprints [177]. In this research, FTIR spectroscopy was used to establish the success of the reaction by comparing the bare substrate spectra with the BiB-substrate and PNIPAM-substrate results.

FTIR spectra were collected with the Nicolet iS10 spectrometer (ThermoFisher Scientific) using the iS10 smart iTR basic analysis in absorbance mode. The background and sample collection were recorded with 32 scans at a spectral resolution of 4 cm^{-1}. The OMNIC^{TM} v9.2.86 software was used to set the analysis specifications and analyse the spectra.

5.5.3 Energy Dispersive X-Ray Spectroscopy (EDS)

Energy Dispersive X-Ray Spectroscopy (EDS) is a chemical analytical technique used in conjunction with scanning electron microscopy (SEM). The SEM generates a beam of incident electrons, between 100 eV and 30,000 eV of energy, in an electron column above the sample chamber. The electrons are focused by a series of lenses and directed onto the sample surface. Then, the sample surface is scanned by the electrons for imaging. The incident electrons cause electrons to be emitted from the sample due to elastic and inelastic scattering events on the surface of the sample. To create an SEM image, the SEM column and sample chamber are under vacuum to allow the electrons to travel freely from the electron beam source to the sample and then to the detectors. Thus, the emitted electrons are detected at each position of the scanned area and the intensity of the emitted electron signal is displayed as brightness on a display monitor and image file. SEM imaging can be performed on conductive or nonconductive samples, but nonconductive materials have to be coated with a thin film of a conductive material to generate conductivity [178].

When the sample is bombarded by the SEM electron beam, electrons are expelled from the surface. The resulting electron vacancies on the sample surface are filled by electrons from a higher state, and an x-ray is emitted to balance the energy difference between the two electron states. EDS detects x-rays emitted from the sample to characterize the elemental composition of the sample, since the signal emitted is unique for each element. The energy detected from each incident x-ray is displayed on the computer monitor for further data evaluation [178]. In this research, the EDS data is used to determine chemical composition of the bare substrate, BiB-substrate and PNIPAM-substrate synthesized.

Image Resolution: 512 by 384　　Acc. Voltage: 15.0 kV
Image Pixel Size: 0.83 µm　　Magnification: 300

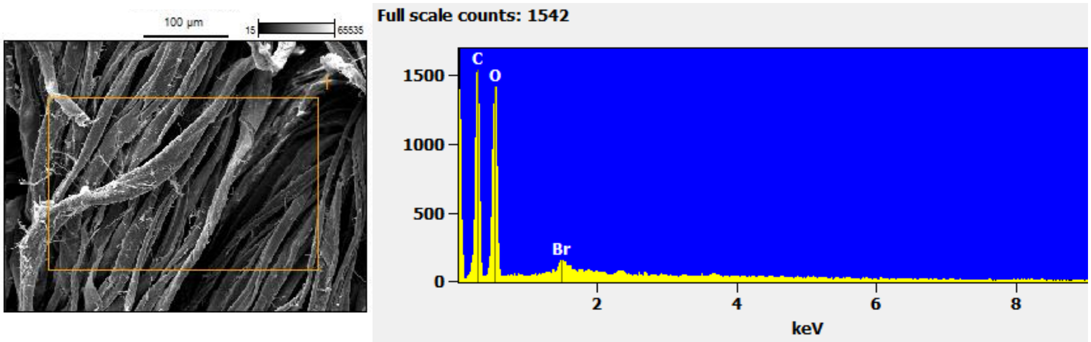

Figure 5.11. EDS result showing the sample image, resolution, pixel size, magnification and counts associated to C, O and Br.

The EDS spectra were obtained with the SU-70 Analytical Field Emission Scanning Electron Microscope (Hitachi) using the NSS software for X-Ray microanalysis v3.0 (ThermoFisher Scientific). The acceleration voltage was set at 15 kV with 2000X magnification. Finally, the spectrum of x-ray energy versus counts was evaluated to determine the elemental composition of the sample scanned. An exemplary EDS result is shown in Figure 5.11.

5.5.4 Simultaneous Thermal Analysis (STA)

Simultaneous Thermal Analysis (STA) corresponds to the simultaneous application of Thermal Gravimetric Analysis (TGA) and Differential Scanning Calorimetry (DSC) to one sample in a single instrument, where the test conditions are identical for the TGA and DSC signals.

TGA is a method of thermal analysis where the mass of a sample is measured continuously while the temperature is changed over time. This measurement provides information about the physiochemical behaviour of the sample, including phase transitions, absorption and desorption, or chemical oxidation and reduction. A typical thermogravimetric analyser consists of a programmable control temperature and a sample pan located onto a precision balance, all inside a furnace. The temperature is generally increased at constant rate to incur a thermal reaction. The thermal reaction occurs when generally the temperature is increased at constant rate under a variety of atmospheres including ambient air, vacuum, inert gas or oxidizing/reducing gases. The thermogravimetric data collected from a thermal reaction or TGA curve is represented as a plot of mass or percentage of initial mass on the y axis versus temperature or time on the x-axis. The TGA curve can be used for materials characterization through analysis of characteristic decomposition patterns specially used in polymers [179, 180]. In this research, the TGA curve is used to quantify the amount of water vapour released from the smart material synthesized.

DSC is a thermo-analytical technique used to measure the amount of heat required to increase the temperature of a sample compared to a reference as a function of time. It is mainly used for analysing polymeric thermal transitions. Basically, when the sample undergoes a physical transformation, more or less heat, depending on whether the process is exothermic (heat is released from the sample) or endothermic (heat is absorbed by the sample), will need to flow into the sample compared to the reference in order to keep the same temperature. The result obtained from a DSC experiment is the heat flux versus temperature or time [179, 180]. This technique is used to determine the LCST and the degradation temperature of the synthesized PNIPAM-substrates.

PNIPAM-substrate samples were placed in a 100% RH environment at room temperature for four hours before the STA analysis in order to ensure the samples were saturated having the maximum water vapour absorbed. STA experiments were made with a Jupiter STA 449 F5 (Netzsh, Germany). A baseline was created with a temperature profile ranging from 20°C to 200°C with a heating rate of 15°C/min and under argon gas flow at 20 ml/min. Then, the sample was weighted and placed inside an aluminium (Al) pan. The Al lid was punctured to allow water vapour leave the Al pan when the temperature rises. The experiment setup and result analysis were performed with the Netzsch Proteus Software v6.1.

5.5.5 Cleavage of the grafted PNIPAM for characterization purposes

To measure the molecular weight of the PNIPAM synthesized on the substrate material, the polymer chains were cleavage from the substrate and dialyzed against water to isolate different possible polymer sizes. Dialysis is a classic laboratory technique based on the diffusion of molecules across a semi-permeable membrane to separate molecules based on size. A sample and a buffer solution are placed on opposite sides of a dialysis porous membrane, and the sample molecules that are larger than the pores are retained on the sample side of the membrane, but the small molecules pass through the membrane reducing its concentration. The cleavage of the grafted PNIPAM mechanism is based on the hydrolysis of the BiB ester and is outlined in Figure 5.12. The optimized methodology followed is described below:

- The PNIPAM-substrate was immersed in a 2% NaOH aqueous solution under magnetic stirring for 48 hours at room temperature. The solution was filtered through a glass filter to remove the substrate material. Extra water was added to rinse the substrate and ensure all the polymer was removed.

- The filtered solution was dialyzed against water, used as a buffer solution, with a 3.5 kDa SnakeSkin™ dialysis tubing (ThermoFisher) to remove the

NaOH unreacted for 24 hours. The buffer solution was replaced three times to ensure a high separation yield.

- Then, the sample solution was dialyzed against water with a 7 kDa SnakeSkin™ dialysis tubing (ThermoFisher) to remove the PNIPAM chains with a molecular weight lower than 7,000 g/mol. The process was kept for 24 hours, the buffer solution was replaced three times and kept for further characterization.

- The remaining sample solution was then dialyzed against water with a 20 kDa SnakeSkin™ dialysis tubing (ThermoFisher) to remove the PNIPAM chains with a molecular weight lower than 20,000 g/mol. The process was kept for 24 hours, the buffer solution was replaced three times and kept for further characterization. The remaining sample and water buffer solutions were collected and evaporated in a Rotavapor® to collect the solid fractions.

- All solid fractions, with a molecular weight below 10,000 g/mol, between 10,000 g/mol and 20,000 g/mol, and above 20,000 g/mol, were weighted for further characterization.

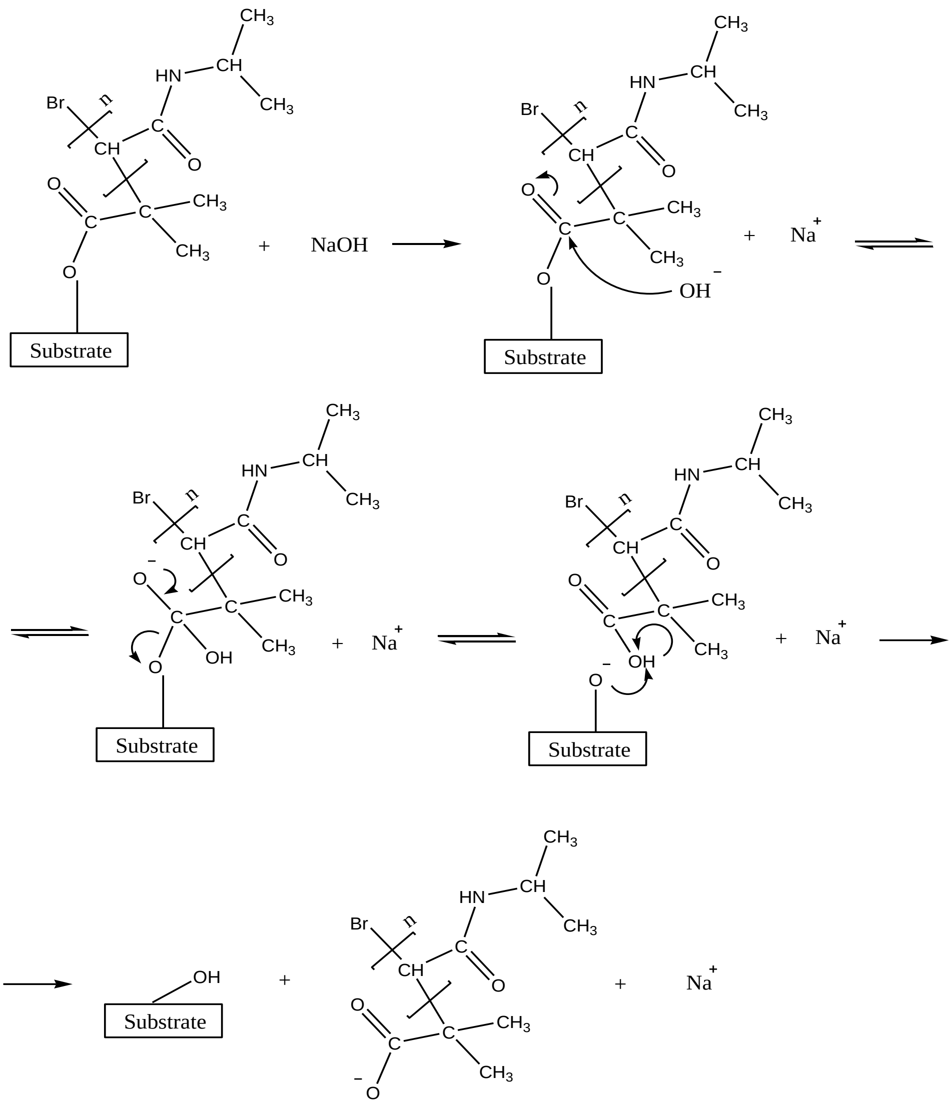

Figure 5.12. Cleavage mechanism of the grafted PNIPAM from the substrate material with 2% NaOH.

5.6 Statistical analysis

Statistical analysis was performed using GraphPad Prism software (GraphPad, San Diego, CA, USA) version 6.07 for Windows using one-way and two-way analysis of variance (ANOVA), followed by Tukey post hoc analysis for multiple comparisons. Results are presented as mean ± standard deviation (SD). To determine the significance of the results, a probability value (p value) between 0 and 1 is used to test the validity of a claim made about the parameter measured, which is called null hypothesis. Therefore, a small p value ($p < 0.05$) indicates strong evidence against the null hypothesis, which means that the null hypothesis is rejected and there is a significant difference on the parameter measured hence on the results (* $p < 0.05$, ** $p < 0.01$, *** $p < 0.001$ and **** $p < 0.0001$) [150, 151].

5.7 Results

Aiming to synthetize a smart material able to uptake the maximum amount of water vapour and release it in the shortest possible time, linear and branched PNIPAM brushes were grafted from the PVA and cotton substrates by an ATRP procedure. After the purification process, the resulting smart material was characterized looking at the reaction success, morphology, chain length or molecular weight and water vapour desorption performance. First of all, the difference between PNIPAM grafted on PVA and cotton substrates was analysed. Then, the performance of linear and branched PNIPAM was compared. Finally, different PNIPAM molecular weights, 5, 15 and 50 kDa, were compared and analysed to optimize the performance of the smart material according to the specific application, namely, humidifying the inspired gas by using recovered moisture from the expired flow.

5.7.1 Analysis of substrate material: PVA vs. Cotton

In this section, the linear PNIPAM grafted on PVA and cotton substrates were compared and analysed. First, three same-sized PVA and three same-sized cotton samples were washed, dried and weighed in order to quantify the number of OH groups available and determine the excess amount of BiB reagent needed to succeed in the substrate surface modification reaction. The BiB excess amount used was three times more than the stoichiometric amount required.

The molar mass of the BiB ($C_4H_6Br_2O$) is 229.9 g/mol, the PVA repeating unit $(C_2H_4O)_n$ is 44 g/mol and the weight of the three prepared PVA samples was 0.225 ± 0.003 g. Hence, to determine the excess BiB required to modify the PVA surface it is important to consider that one PVA molecule has only one OH group (Figure 5.5B), so one mol of PVA corresponds to one mol of OH and one mol of BiB, since one BiB molecule reacts with one OH group (Figure 5.7). However, as a three times excess is used in the reaction, three mols of BiB are used to determine the excess amount required as outlined in equation 5.2.

$$0.225 \pm 0.003\ g\ PVA \cdot \frac{1\ mol\ PVA}{44\ g\ PVA} \cdot \frac{1\ mol\ OH}{1\ mol\ PVA} \cdot \frac{3\ mols\ BiB}{1\ mol\ OH} \cdot \frac{229.9\ g\ BiB}{1\ mol\ BiB} \qquad 5.2$$

The molar mass of the cellulose repeating unit (CL) $(C_6H_{10}O_5)_n$ is 162.14 g/mol and the weight of the three prepared cotton samples was 0.886 ± 0.004 g. According to previous literature results of PNIPAM grafted from CL, the BiB reacts only with the primary OH group and one molecule of CL has only on primary OH group (Figure 5.6B). Hence, one mol of CL corresponds to one mol of OH and one mol of BiB, since one BiB molecule reacts with one OH group (Figure 5.7). But, as stated before, three mols of BiB are used to determine the excess amount required as outlined in equation 5.3.

$$0.886 \pm 0.004\ g\ CL \cdot \frac{1\ mol\ CL}{162.14\ g\ CL} \cdot \frac{1\ mol\ OH}{1\ mol\ CL} \cdot \frac{3\ mols\ BiB}{1\ mol\ OH} \cdot \frac{229.9\ g\ BiB}{1\ mol\ BiB} \quad 5.3$$

In order to investigate the success of the immobilization of the BiB (ATRP-initiator) on the substrate material, the presence of BiB on the PVA and cotton fabric was analysed by EDS since the only molecular difference between the substrates and the BiB-cotton is the presence of bromine (Br). Hence, the weight percentage of carbon (C), oxygen (O) and bromine (Br) were determined for the three PVA and three cotton samples at different surface points. The resulting weight percentage of each component for each substrate material is shown in Table 5.1.

Table 5.1. EDS data showing the weight percentage (%) of C, O and Br averaged for the three BiB-PVA and three BiB-cotton samples (n=3).

Substrates	**Weight (%) of C**	**Weight (%) of O**	**Weight (%) of Br**
PVA	48.517 ± 1.231	44.700 ± 0.550	3.817 ± 0.685
Cotton	49.533 ± 1.978	43.613 ± 1.636	5.920 ± 0.387

The presence of BiB on the substrate was also quantified comparing the sample weight before and after the immobilization of the BiB reaction, where the weight difference corresponds to the amount of BiB reacted. Table 5.2 summarizes the results of the PVA and cotton samples. The third column shows the amount of BiB reacted according to the weight (%) of Br determined from the EDS since one mol of Br (molecular weight of 79.9 g/mol) corresponds to one mol of BiB. The amount of BiB calculated from the weight difference method and the EDS data is in agreement since it is not significantly different.

Table 5.2. Amount of BiB present in the cotton fabric according to the weight difference (first column) and according to the EDS data (second column) (n=3).

Substrates	**Weight difference: BiB reacted (g)**	**EDS data: BiB reacted (g)**
PVA	0.034 ± 0.015	0.028 ± 0.008
Cotton	0.158 ± 0.054	0.173 ± 0.026

The amount of BiB reacted on the PVA substrate is significantly lower ($p < 0.0001$) compared to the quantity reacted on the cotton fabric. This could be explained by the differences in physical structure of these two substrates. The cotton substrate is a fabric which has more space between the fibres, so the BiB has an easier access to react with the OH groups. The PVA has a sponge-like structure, which might have obstructed entry of BiB and hinder its reaction with the OH groups at the interior of the structure.

To determine the amount of NIPAM required to synthesize the PNIPAM from the BiB-substrate with 15 kDa or 15000 g/mol of molecular weight, it is important to consider that one PNIPAM chain (1 mol) grows from one BiB molecule attached to the substrate (1 mol) as previously explained in Figure 5.8. Hence, the amount of NIPAM needed to be grafted in both substrates is calculated from equation 5.4.

.

$$g\ BiB\ reacted \cdot \frac{1\ mol\ BiB}{229.9\ g\ BiB} \cdot \frac{1\ mol\ PNIPAM}{1\ mol\ BiB} \cdot \frac{15000\ g\ PNIPAM}{1\ mol\ PNIPAM} \approx g\ NIPAM \qquad 5.4$$

Then, samples of the reacting mixture were taken at 0, 1, 8, 24 and 48 hours from the reaction start, to monitor the grafting of NIPAM from the BiB-Substrate (second step), and immediately injected into a sealed NMR tube containing the methanol-d_4 solvent and DMF internal reference. Then, the NMR spectra was obtained and the NIPAM signals were integrated with respect to the DMF signals (full spectra and signals identified in Figure 5.10). The sample analysed at time 0 was used to set the 0% monomer conversion. The NIPAM conversion (%) as a function of time for PNIPAM synthesis on PVA and cotton substrates is shown in Figure 5.13. The amount of monomer reacted increases logarithmically and stabilizes after 24 hours achieving a 65 % conversion from the PVA substrate and 67 % conversion from cotton substrate. No significant difference is found between both curves.

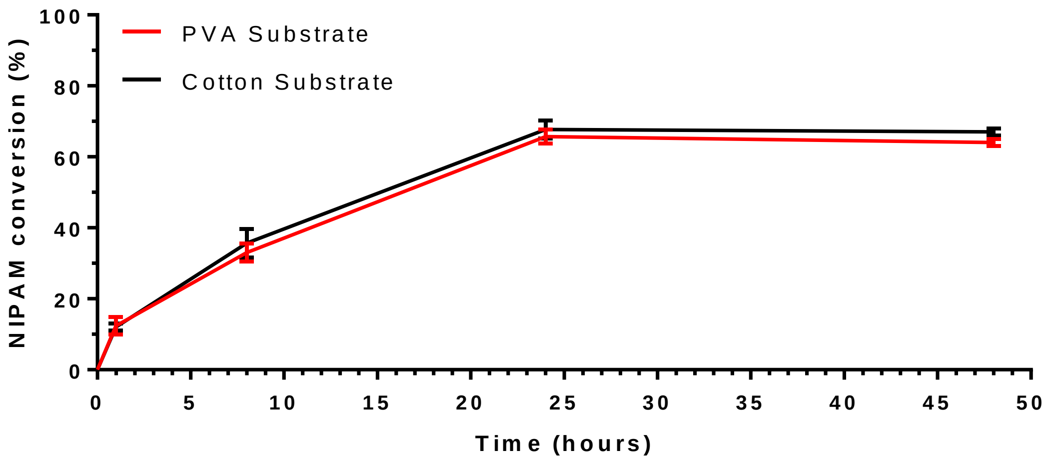

Figure 5.13. NIPAM conversion (%) as a function of time for PNIPAM synthesis on PVA (red line) and cotton (black line) substrates.

In order to investigate the success of the PNIPAM synthesis, the presence of the polymer on the PVA and cotton fabric was analysed by EDS since the only molecular difference between the BiB-substrates and the PNIPAM is the nitrogen (N). Hence, the weight percentage of carbon (C), oxygen (O) and nitrogen (N) were determined for the three PVA and three cotton samples at different surface points. The resulting weight percentage of each component for each substrate material is summarized in Table 5.3.

Table 5.3. EDS data showing the weight percentage (%) of C, O, N averaged for the three PNIPAM-PVA and three PNIPAM-cotton samples (n=3).

Substrates	Weight (%) of C	Weight (%) of O	Weight (%) of N
PVA	48.677 ± 0.956	37.803 ± 1.488	10.873 ± 0.646
Cotton	48.860 ± 1.010	37.231 ± 1.328	11.630 ± 1.324

The presence of PNIPAM on the substrate was also quantified comparing the sample weight before and after the NIPAM grafting reaction, where the weight difference corresponds to the amount of PNIPAM synthesized. Table 5.4 summarizes the results of the three PVA samples and the three cotton samples. The third column shows the amount of PNIPAM reacted according to the weight (%) of N determined from the EDS since one mol of N (molecular weight of 16 g/mol) corresponds to one mol of PNIPAM. The fourth column corresponds to the amount of polymer reacted according the conversion of NIPAM (%) determined by the NMR spectra evolution as a function of time. The amount of PNIPAM calculated from the weight difference method, the EDS data and the NMR results is in agreement since it is not significantly different.

Table 5.4. Amount of BiB present in the cotton fabric according to the weight difference (first column) and according to the EDS data (second column) (n=3).

Substrates	**Weight difference: PNIPAM reacted (g)**	**EDS data: PNIPAM reacted (g)**	**NMR data: PNIPAM reacted (g)**
PVA	1.015 ± 0.125	1.114 ± 0.183	1.183 ± 0.182
Cotton	6.529 ± 0.107	7.110 ± 0.421	6.941 ± 0.851

The amount of PNIPAM reacted on the PVA substrate is significantly lower ($p < 0.0001$) compared to the quantity reacted on the cotton fabric in all three methods. This is explained by the fact that lower amounts of BiB reacted on the PVA substrate and there were less grafting points available to graft the NIPAM. Hence, in order to compare the performance of both substrates it is important to determine theoretically the chain length or molecular weight of the grafted PNIPAM. It is known that one PNIPAM chain grows from one BiB molecule attached to the substrate and the amount of PNIPAM and BiB reacted on each substrate is already determined. Assuming that all chains has the same length, the theoretical molecular weight of the PNIPAM grafted from the PVA substrate is 9713.27 Da or g/mol, and the theoretical molecular weight of the PNIPAM grafted from the cotton substrate is 10099.59 Da or g/mol. Therefore, is possible to proceed with the water vapour desorption rate performance of both samples since their chain lengths are in the same order of magnitude.

To investigate the performance of the smart material, PNIPAM-PVA and PNIPAM-cotton samples were analysed with the STA technique. The TGA and DSC curves were obtained simultaneously for each sample and analysed as a function of temperature. During the thermal phase transition, PNIPAM exhibit an endothermic peak due to the breaking of hydrogen bonds with the surrounding water vapour molecules detectable with the DSC. The signal was designated by the peak onset and the temperature value, which corresponds to the LCST, was determined from the intersection between two tangent lines from the baseline and slope of the endothermic peak.

To determine the mass reduction rate, the first derivative of the TGA curve was calculated. Then, the sample mass reduction was measured from 20°C to 55°C, when a plateau was reached. This mass decrease corresponds to the amount of water released from the PNIPAM-substrate sample. The LCST and the water vapour release (%/min) results are outlined in Figure 5.14.

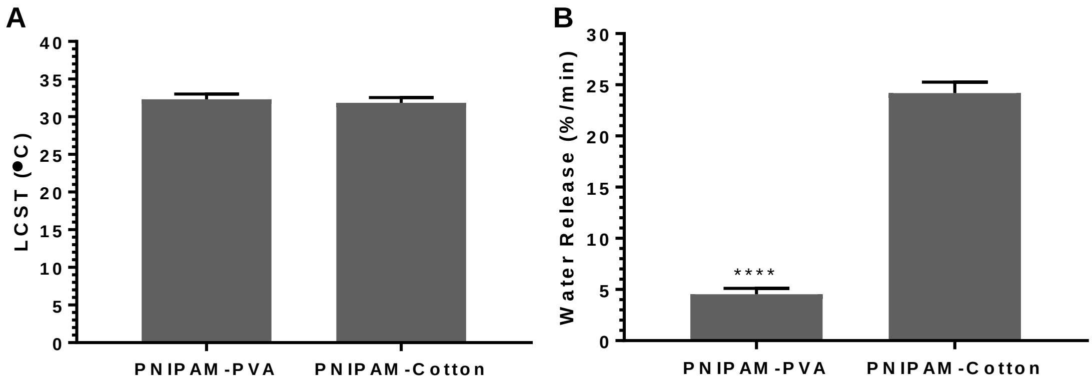

Figure 5.14. STA results. A- LSCT of PNIPAM-PVA and PNIPAM-Cotton substrates determined from the DSC curve. B- Water vapour release (%/min) of PNIPAM-PVA and PNIPAM-Cotton substrates determined from the TGA curve.

The results show no significant difference between the LCST determined in both PNIPAM-substrates, which is around 32°C as theoretically expected. However, the water vapour release rate from the PNIPAM-PVA samples is significantly lower than the PNIPAM-Cotton samples. This could be explained by the fact that, even if the grafted PNIPAM chains have similar molecular weight (around 10 kDa) in both substrates, the number of polymer chains grown from the PVA substrate is significantly lower, seven times less, than that grown from the cotton substrate. Therefore, the cotton fabric substrate was selected to be used in the next experiments because of its high number of BiB sites formed.

5.7.2 Analysis of polymer structure: Linear vs. Branched

It has been shown in the previous analysis that the best water vapour desorption performance is achieved by grafting the PNIPAM onto a cotton fabric substrate due to its high number of BiB sites formed. Hence, the aim of this section is to investigate the effect of the linear and branched PNIPAM grafted on the cotton fabric substrate.

First, 6 cotton samples were prepared at the same size than previous samples analysed to ensure the repeatability of the results. Then, the samples were washed, dried and weighted in order to quantify how much BiB reacted after the substrate surface modification reaction. The same excess amount of BiB calculated in previous sections was used as a reagent (equation 5.3).

In order to investigate the success of the first reaction, the immobilization of the BiB (ATRP-initiator) on the substrate material, the presence of BiB on the fabric was investigated by EDS since the only molecular difference between the bare cotton fabric and the BiB-cotton is the bromine (Br). Hence, the weight percentage of carbon (C), oxygen (O) and bromine (Br) were determined for the 6 samples at different surface points. The resulting weight percentage of each component is summarized in Table 5.5.

Table 5.5. EDS data showing the weight percentage (%) of C, O and Br averaged for the 9 BiB-cotton samples (n=6).

Weight (%) of C	Weight (%) of O	Weight (%) of Br
49.390 ± 1.491	43.958 ± 1.259	5.432 ± 0.721

The presence of BiB on the fabric was also quantified comparing the sample weight before and after the immobilization of the BiB, where the weight difference corresponds to the amount of BiB reacted. Table 5.6 summarizes the results that were averaged since no significant difference was found between the 6 samples. The second column shows the amount of BiB reacted according to the weight (%) of Br determined from the EDS since one mol of Br (molecular weight of 79.9 g/mol) corresponds to one mol of BiB. Both results are in agreement.

Table 5.6. Amount of BiB present in the cotton fabric according to the weight difference (first column) and according to the EDS data (second column) (n=6).

Weight difference: BiB reacted (g)	EDS data: BiB reacted (g)
0.126 ± 0.014	0.138 ± 0.008

To determine the amount of NIPAM required to synthesize the PNIPAM from the BiB-substrate with 15 kDa or 15000 g/mol of molecular weight for both structures linear and branched, it is important to consider that one PNIPAM chain (1 mol) grows from one BiB molecule attached to the substrate (1 mol) as previously explained in Figure 5.8. Hence, the amount of NIPAM needed to be grafted on the substrates is calculated from equation 5.4. The amount of EBMA required to generate one branched point per chain is calculated in the same way, since one mol of BiB corresponds to one mol of EBMA. Due to the addition of EBMA to generate the branched points, the PNIPAM synthesis was not monitored by NMR due to the spectral overlap of EBMA and NIPAM which can lead to erroneous measurements.

In order to investigate the success of the linear and branched PNIPAM synthesis, the presence of the polymer on cotton fabric was analysed by EDS since the only molecular difference between the BiB-substrates and the PNIPAM is the nitrogen (N). Hence, the weight percentage of carbon (C), oxygen (O) and nitrogen (N) were determined for the three branched and three linear samples at different surface points. The resulting weight percentage of each component for each polymer structure is shown in Table 5.7.

Table 5.7. EDS data showing the weight percentage (%) of C, O, N averaged for the three branched and three linear PNIPAM-Cotton samples (n=3).

PNIPAM	Weight (%) of C	Weight (%) of O	Weight (%) of N
Branched	48.657 ± 0.956	41.060 ± 1.488	10.283 ± 0.646
Linear	48.860 ± 1.010	37.231 ± 1.328	11.630 ± 1.324

The presence of PNIPAM on the substrate was also quantified comparing the sample weight before and after the NIPAM grafting reaction, where the weight difference corresponds to the amount of PNIPAM synthetized. Table 5.8 summarizes the results that were averaged since no significant difference was found between the three linear and the three branched PNIPAM samples. The third column shows the amount of PNIPAM reacted according to the weight (%) of N determined from the EDS since one mol of N (molecular weight of 16 g/mol) corresponds to one mol of PNIPAM. The amount of PNIPAM calculated from the weight difference method and the EDS data is in agreement since it is not significantly different.

Table 5.8. Amount of PNIPAM present in the cotton fabric according to the weight difference (first column) and according to the EDS data (second column) (n=3).

PNIPAM	Weight difference: PNIPAM reacted (g)	EDS data: PNIPAM reacted (g)

Branched	3.815 ± 0.125	4.014 ± 0.583
Linear	6.529 ± 0.107	7.110 ± 0.421

The amount of PNIPAM reacted following the branched method is significantly lower ($p < 0.001$) compared to the quantity reacted on the linear synthesis method. This is explained by the fact that side reactions can be generated with high probability. In this case a side PNIPAM product could be synthetized with the EBMA by itself instead of growing branches from the substrate. The possible side reactions can be analysed in detail, but this is a path that moves away from the objective set out in this research. Hence, both theoretical branched and linear structures are analysed with the STA to compare their water desorption performance and determine the optimal structure.

The TGA and DSC curves were obtained simultaneously for each sample and analysed as a function of temperature. During the thermal phase transition, PNIPAM exhibit an endothermic peak due to the breaking of hydrogen bonds with the surrounding water vapour molecules detectable with the DSC. The signal was designated by the peak onset and the temperature value, which corresponds to the LCST, was determined from the intersection between two tangent lines from the baseline and slope of the endothermic peak. To determine the mass reduction rate, the first derivative of the TGA curve was calculated. Then, the sample mass reduction was measured from 20°C to 55°C, when a plateau was reached. This mass decrease corresponds to the amount of water released from the PNIPAM-substrate sample. The LCST and the water vapour release (%/min) results are outlined in Figure 5.15.

The results show no significant difference between the LCST determined in both PNIPAM structures, which is around 32°C as theoretically expected. However, the water vapour release rate from the branched PNIPAM samples is significantly lower than the linear PNIPAM samples. This could be explained by the fact that, there is less polymer grafted on the substrate and the material absorbs less amount of water vapour. Also, the possible synthetized PNIPAM branches could slow down the conformational change from the linear to the coiled structure, resulting in a lower water release rate [172, 174]. Therefore, the linear PNIPAM synthetized in a cotton fabric substrate is selected to be further optimized comparing different molecular weights in the next section.

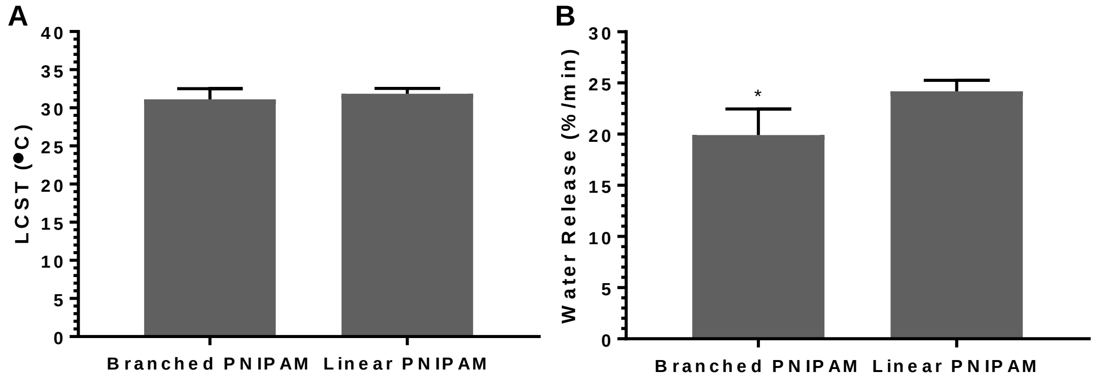

Figure 5.15. STA results. A- LSCT of branched and linear PNIPAM-Cotton substrates determined from the DSC curve. B- Water vapour release (%/min) of branched and linear PNIPAM-Cotton substrates determined from the TGA curve.

5.7.3 Analysis of polymer molecular weight: 5, 15, 50 kDa

It has been shown in the above analyses than the best water vapour desorption performance is achieved grafting linearly the PNIPAM onto a cotton fabric substrate. Hence, the aim of this section is to investigate the effect of different molecular weights of grafted linear PNIPAM on a cotton fabric substrate.

First, 9 cotton samples were prepared at the same size than previous samples to ensure the repeatability of the results. Then, the samples were washed, dried and weighted in order to quantify how much BiB reacted after the substrate surface modification reaction. The same excess amount of BiB as calculated in previous sections was used as a reagent (equation 5.3).

In order to investigate the success of the first reaction, the immobilization of the BiB (ATRP-initiator) on the substrate material modifying its surface, FTIR in absorbance mode was used. Figure 5.16 shows the comparison of the FTIR spectra of the bare cotton fabric and the BiB modified samples. The spectra of the BiB-cotton samples showed one band at 1740 cm^{-1} which corresponds to the stretch vibration of ester carbonyl group formed to link the BiB to the cotton fabric [180]. This band is absent in the bare cotton fabric spectra.

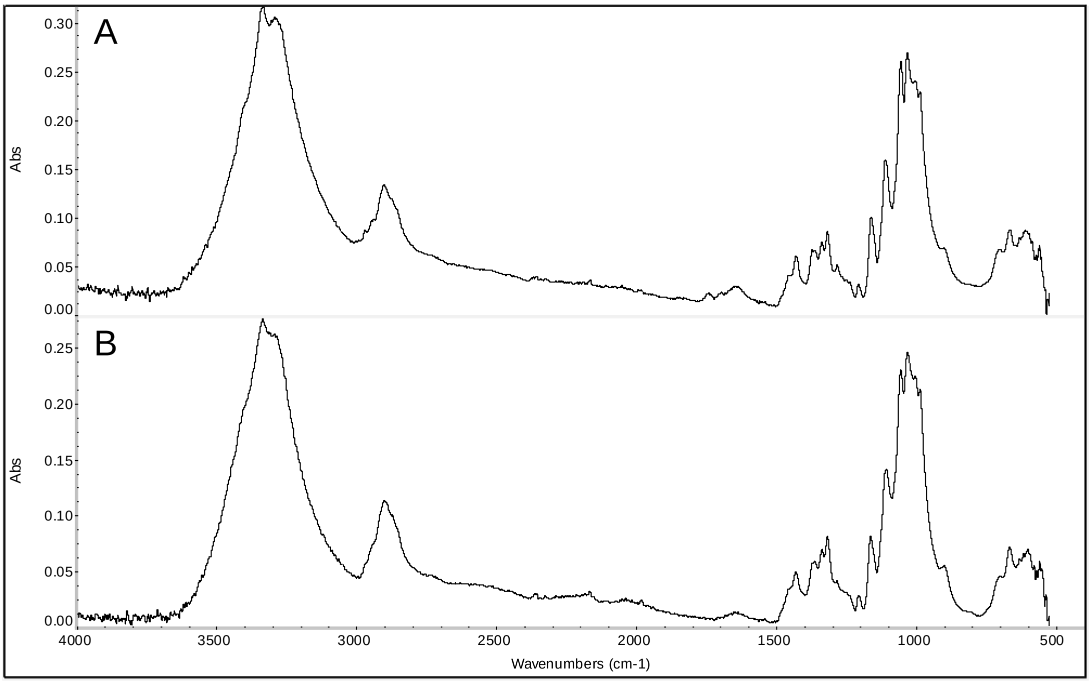

Figure 5.16. FTIR spectrums. A- BiB-Cotton sample spectra. B- Bare cotton spectra.

In addition to FTIR spectra, the presence of BiB on the fabric was investigated by EDS since the only molecular difference between the bare cotton fabric and the BiB-cotton is the bromine (Br). Hence, the weight percentage of carbon (C), oxygen (O) and bromine (Br) were determined for the 9 samples at different surface points. The resulting weight percentage of each component is summarized in Table 5.9.

Table 5.9. EDS data showing the weight percentage (%) of C, O and Br averaged for the 9 BiB-cotton samples (n=9).

Weight (%) of C	**Weight (%) of O**	**Weigh t(%) of Br**
49.632 ± 1.431	44.066 ± 1.135	5.567 ± 0.647

The presence of BiB on the fabric was also quantified comparing the sample weight before and after the immobilization of the BiB reaction, where the weight difference corresponds to the amount of BiB reacted. Table 5.10 summarizes the results obtained for the 9 samples. The second column shows the amount of BiB reacted according to the weight (%) of Br determined from the EDS since one mol of Br (molecular weight of 79.9 g/mol) corresponds to one mol of BiB. Both results are in agreement.

Table 5.10. Amount of BiB present in the cotton fabric according to the weight difference (first column) and according to the EDS data (second column) (n=9).

Weight difference: BiB reacted (g)	EDS data: BiB reacted (g)
0.128 ± 0.044	0.157 ± 0.008

To determine the amount of NIPAM required to synthetize the PNIPAM from the BiB-substrate with 5 kDa or 5000 g/mol, 15 kDa or 15,000 g/mol and 50 kDa or 50,000 g/mol of molecular weight, it is important to consider that one PNIPAM chain (1 mol) grows from one BiB molecule attached to the substrate (1 mol) as previously explained in Figure 5.8. Hence, the amount of NIPAM needed to be grafted in both substrates is calculated from equation 5.4 but using 5000, 15000 or 50000 g/mol of PNIPAM according to the desired final PNIPAM molecular weight.

Then, samples of the reacting mixture were taken at 0, 1, 8, 24 and 48 hours from the reaction start, to monitor the grafting of NIPAM from the BiB-Substrate (second step), and immediately injected into a sealed NMR tube containing the methanol-d_4 solvent and DMF internal reference. Then, the NMR spectra was obtained and the NIPAM signals were integrated with respect to the DMF signals (full spectra and signals identified in Figure 5.10). The sample analysed at time 0 was used to set the 0% monomer conversion. The NIPAM conversion (%) as a function of time for 5 kDa, 15 kDa and 50 kDa PNIPAM synthetized on cotton substrates is shown in Figure 5.17.

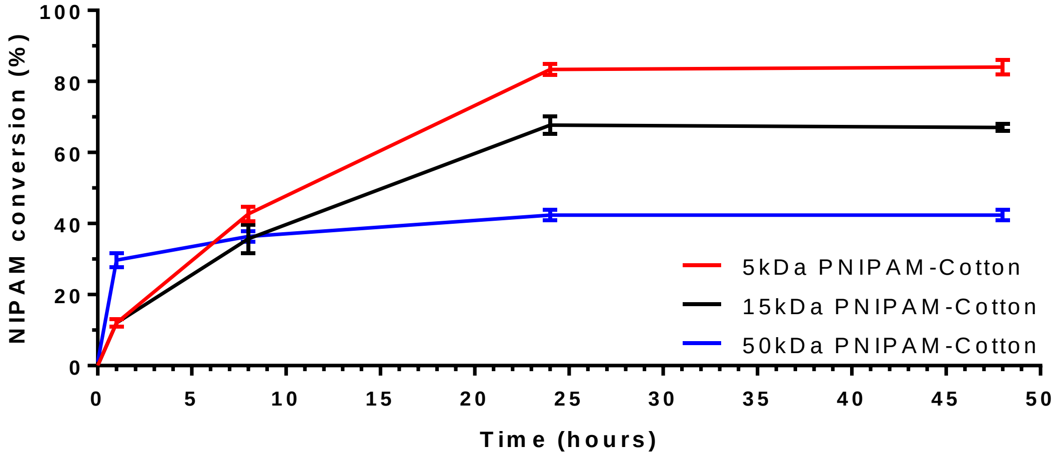

Figure 5.17. NIPAM conversion (%) as a function of time for 5kDa (red line), 15kDa (black line) and 50kDa (blue line) PNIPAM synthetized on cotton substrates.

The amount of monomer reacted increases logarithmically and stabilizes after 24 hours. The 5 and 15 kDa curves follow a similar trend being the last one stabilized with less monomer conversion, 84% and 67% conversion for 5 and 15 kDa PNIPAM-Cotton samples respectively. However, the 50 kDa curve shows a fast monomer conversion in the first hour and the stabilized slowly until a 42% conversion is achieved. This could be explain by the fact that the monomer concentration in the solution to achieve a high molecular weight polymer is significantly higher and the other samples and can affect the free movement of the monomer or saturation.

In order to investigate the success of the PNIPAM synthesis, FTIR in absorbance mode was used. Figure 5.18 shows the comparison of the FTIR spectra of the bare cotton fabric and the PNIPAM-Cotton samples. The spectrums of the PNIPAM-Cotton samples show two bands at 1650 cm^{-1} and 1540 cm^{-1} which correspond to the typical amide and carbonyl stretch vibrations of PNIPAM, the band II is absent in the bare cotton fabric spectra and the vibration band at 1635 cm^{-1} is attributed to absorbed water [180].

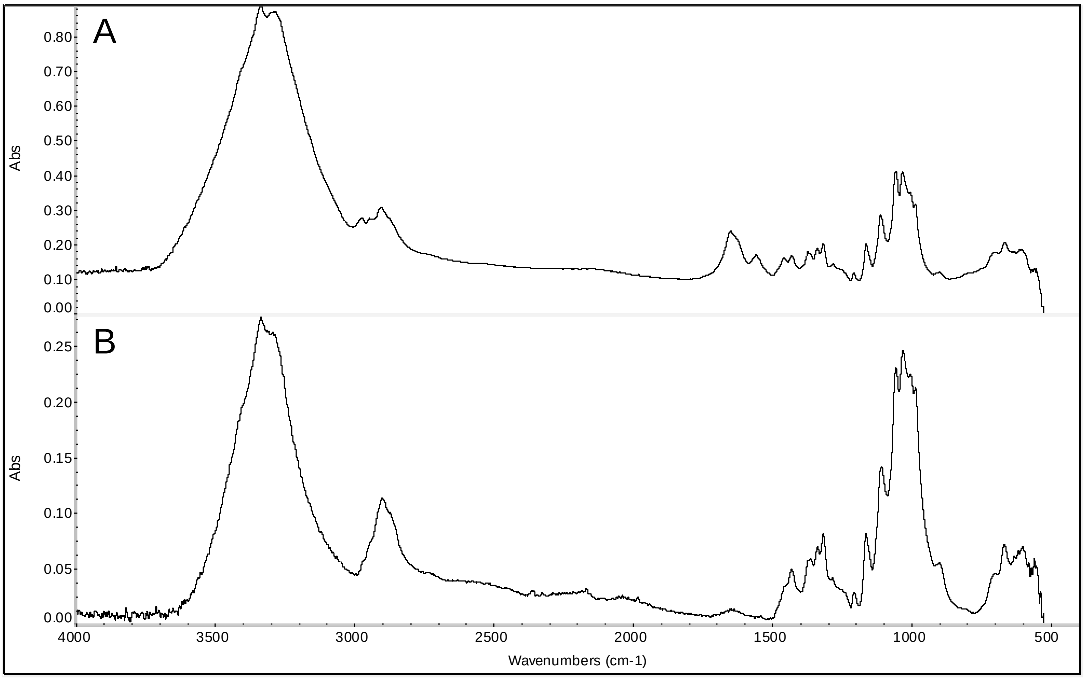

Figure 5.18. FTIR spectrums. A- PNIPAM-Cotton sample spectra. B- Bare cotton spectra.

In addition to FTIR spectra, the presence of the polymer on the cotton fabric was analysed by EDS since the only molecular difference between the BiB-substrates and the PNIPAM is the nitrogen (N). Hence, the weight percentage of carbon (C), oxygen (O) and nitrogen (N) were determined for the three 5 kDa PNIPAM-Cotton, the three 15 kDa PNIPAM-Cotton and three 50 kDa PNIPAM-Cotton samples at different surface points. The resulting weight percentage of each component (Table 5.11) for each molecular weight PNIPAM synthetized were averaged since not significant difference was found between each three sample sets.

Table 5.11. EDS data showing the weight percentage (%) of C, O, N averaged for the three 5 kDa, 15 kDa and 50 kDa PNIPAM-cotton samples (n=3).

PNIPAM-Cotton	Weigh (%) of C	Weigh (%) of O	Weigh (%) of N
5 kDa	47.783 ± 2.252	37.230 ± 1.328	10.553 ± 1.072
15 kDa	48.860 ± 1.010	37.231 ± 1.328	11.630 ± 1.324
50 kDa	48.353 ± 0.518	37.8031 ± 1.488	10.550 ± 1.483

The presence of PNIPAM on the substrate was also quantified comparing the sample weight before and after the NIPAM grafting reaction, where the weight difference corresponds to the amount of PNIPAM synthesized. Table 5.12 summarizes the results that were averaged since no significant difference was found between the three samples sets. The third column shows the amount of PNIPAM reacted according to the weight (%) of N determined from the EDS since one mol of N (molecular weight of 16 g/mole) corresponds to one mol of PNIPAM. The fourth column corresponds to the amount of polymer reacted according the conversion of NIPAM (%) determined by the NMR spectra evolution as a function of time. The amount of PNIPAM calculated from the weight difference method, the EDS data and the NMR results is in agreement since it is not significantly different.

Table 5.12. Amount of BiB present in the cotton fabric according to the weight difference (first column) and according to the EDS data (second column) (n=3).

PNIPAM-Cotton	Weight difference: PNIPAM reacted (g)	EDS data: PNIPAM reacted (g)	NMR data: PNIPAM reacted (g)
5 kDa	1.931 ± 0.125	2.512 ± 1.583	2.329 ± 1.982
15 kDa	6.529 ± 0.107	7.110 ± 1.421	6.941 ± 1.851
50 kDa	10.627 ± 0.118	9.927 ± 1.219	11.784 ± 1.957

In order to compare the performance of both substrates it is important to determine theoretically the chain length or molecular weight of the grafted PNIPAM. It is known that one PNIPAM chain grows from one BiB molecule attached to the substrate and the amount of PNIPAM and BiB reacted on each substrate is already determined. Assuming that all chains has the same length, the theoretical molecular weight of the 5 kDa PNIPAM is 4183.102 Da or g/mole, the 15 kDa PNIPAM is 10099.59 Da or g/mol and the 50 kDa PNIPAM is 21165.17 Da or g/mole. To prove that these values are accurate, the PNIPAM of each sample is cleavage and dialysed obtaining different solid fraction according to the molecular weight: between 3.5 and 7 kDa (3.5 < Mw < 7), between 7 and 20 kDa (7 < Mw < 20) and more than 20 kDa (20 < Mw). The results are shown in Figure 5.19. The 90% of the 5 kDa PNIPAM solid fraction is in between 3.5 and 7 kDa, which is in agreement with the theoretical estimation, and only the 10% is between 7 and 20 kDa. The 80% of the of the 15 kDa PNIPAM solid fraction is in between 7 and 20 kDa, which is in agreement with the theoretical estimation, and the 20% is between 3.5 and 7 kDa. The 60% of the of the 50 kDa PNIPAM solid fraction is above 20 kDa, which is in agreement with the theoretical estimation, and the 40% is between 7 and 20 kDa. Although, this is not a technique to measure the exact polymer molecular weight, it is a method to prove the synthesis of a low, medium and high PNIPAM molecular weight, to compare the water vapour desorption rate performance of the samples.

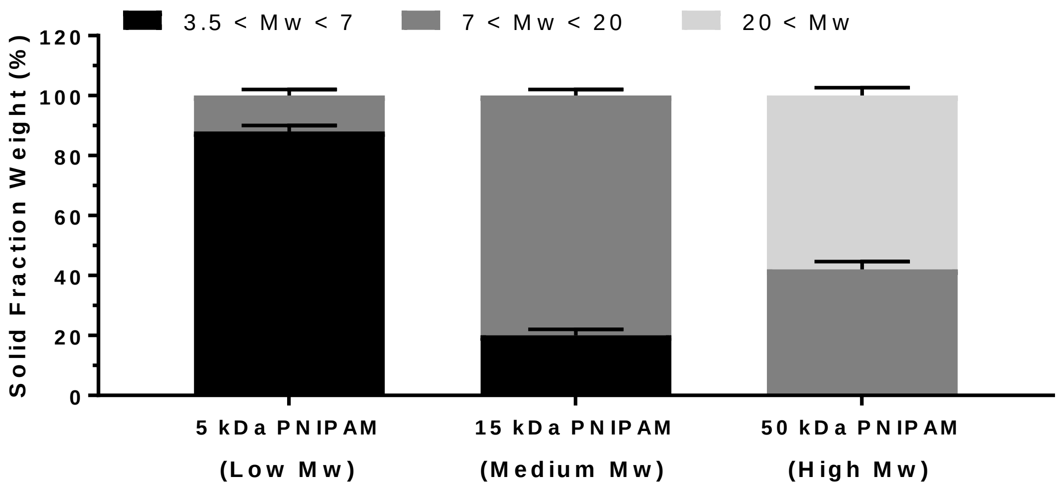

Figure 5.19. Dialysis results of solid fraction weight (%) of the 5 kDa (low Mw), 15 kDa (medium Mw) and 50 kDa (High) PNIPAM samples. The solid fraction are divided in Mw between 3.5 and 7 kDa, between 7 and 20 kDa and above 20 kDa.

To investigate the performance of the smart material, low, medium and high Mw PNIPAM-cotton samples were analysed with the STA technique. The TGA and DSC curves were obtained simultaneously for each sample and analysed as a function of temperature. During the thermal phase transition, PNIPAM exhibit an endothermic peak due to the breaking of hydrogen bonds with the surrounding water vapour molecules detectable with the DSC. The signal was designated by the peak onset and the temperature value, which corresponds to the LCST, was determined from the intersection between two tangent lines from the baseline and slope of the endothermic peak. To determine the mass reduction rate, the first derivative of the TGA curve was calculated. Then, the sample mass reduction was measured from 20°C to 55°C, when a plateau was reached. This mass decrease corresponds to the amount of water released from the PNIPAM-substrate sample. The LCST and the water vapour release (%/min) results are outlined in Figure 5.20.

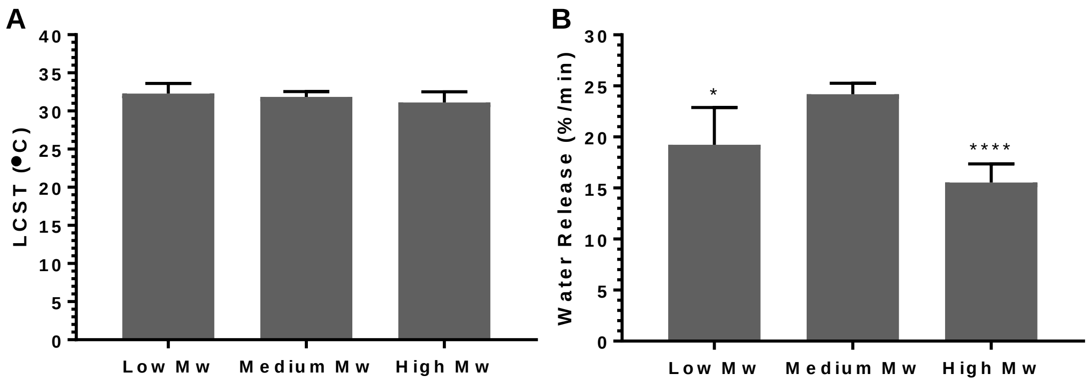

Figure 5.20. STA results. A- LSCT of low, medium and high Mw PNIPAM-Cotton samples determined from the DSC curve. B- Water vapour release (%/min) of low, medium and high PNIPAM-Cotton samples determined from the TGA curve.

The results show no significant difference between the LCST determined in the three molecular weight PNIPAM samples, which is around 32°C as theoretically expected. However, the water vapour release rate from the low Mw and high Mw PNIPAM samples are significantly lower than the Medium Mw PNIPAM samples. This could be explained by the fact that the low Mw samples does not have enough PNIPAM grafted so absorbs less water vapour molecules than the medium Mw samples, and the high Mw PMIPAM samples absorb more water vapour molecules but are not able to release them as fast as the medium Mw samples [181, 182]. Therefore, a medium Mw (between 7 and 20 kDa) PNIPAM-Cotton fabric substrate is selected to be tested in human breath in the next experiments because of its optimal thermal performance.

5.8 Assessment of the optimized PNIPAM smart material

As stated in the introduction of this chapter, the purpose of this research was to develop a proposal for humidifying the inspired gas by using recovered moisture from the expired airflow, and to achieve the humidity previously quantified. To achieve it, the thermo-responsive PNIPAM smart polymer has been optimized in order to uptake the maximum amount of water vapour and release it in the shortest time.

Two substrate materials, polyvinyl alcohol (PVA) and organic cotton fabric, have been investigated to achieve the maximum PNIPAM grafting yield. It was shown that the amount of BiB reacted on the PVA substrate was significantly lower compared to the quantity reacted on the cotton fabric. This could be explained by the differences in physical structure of these two substrates. The cotton substrate is a fabric which has more space between the fibres, so the BiB reagent has easier access to react with the OH groups. The PVA has a sponge-like structure, which might have obstructed BiB and hinder its reaction with the OH groups available. Also, the amount of PNIPAM reacted on the PVA substrate was significantly lower compared to the quantity reacted on the cotton fabric in all three methods, as expected due to the fact that lower amount of BiB was reacted on the PVA substrate and there were fewer grafting points available to graft the NIPAM. Finally, the results showed no significant difference between the LCST determined in both PNIPAM-substrates, which was around 32°C as theoretically expected. However, the water vapour release rate from the PNIPAM-PVA samples was significantly lower than the PNIPAM-Cotton samples. This is explained by the fact that, even if the grafted PNIPAM chains have similar molecular weight (around 10 kDa) in both substrates, the number of polymer chains grown from the PVA substrate is significantly lower, seven times less, than that grown from the cotton substrate. Therefore, the cotton fabric substrate was selected to be used in the next experiments because of its high number of BiB sites formed and available for further reaction.

Next, linear and branched PNIPAM were synthesized in the cotton substrate to compare the final water desorption rate. The results showed that the amount of PNIPAM reacted following the branched method was significantly lower compared to the quantity reacted on the linear synthesis method. This is explained by the fact that side reactions can be generated with high probability, and in this case, a side PNIPAM product could be synthesized with the EBMA by itself instead of growing branches from the substrate. The possible side reactions were not further investigated in this study because this is a path that moves away from the objective set out in this research. The STA results showed no significant difference between the LCST determined in both PNIPAM structures, which is around 32°C as theoretically expected. However, the water vapour release rate from the branched PNIPAM samples was significantly lower than the linear PNIPAM samples, because there is less polymer grafted on the substrate and the material absorbs less amount of water vapour. Also, the possible synthesized PNIPAM branches could slow down the conformational change from the linear to the coiled structure, resulting in a lower water release rate [172, 174, 181, 182].

Finally, linear PNIPAM was synthetized on the cotton substrate at low, medium and high molecular weights: below 7 kDa, between 7 and 20 kDa and above 20 kDa respectively. The STA results showed no significant difference between the LCST determined in the three molecular weight PNIPAM samples, which was around 32°C as theoretically expected. However, the water vapour release rate from the low MW and high MW PNIPAM samples were significantly lower than the Medium MW PNIPAM samples. This could be explained by the fact that the low MW samples do not have enough PNIPAM grafted so absorbs less water vapour molecules than the medium MW samples, and the high MW PMIPAM samples absorb more water vapour molecules but are not able to release them as fast as the medium MW samples [172, 174, 181, 182]. Therefore, a medium Mw (between 7 and 20 kDa) PNIPAM-Cotton fabric substrate is selected to be tested on human participants in the next experiments because of its optimal thermal performance. This optimized smart material is able to achieve a water vapour release rate of 24.2 ± 1.054 %/min, which corresponds to the weight percentage of water vapour released per minute, at a LCST of 32°C. This means that, below 32°C the smart material absorbs the surrounding water vapour molecules and release them when the temperature is higher than 32°C achieving a water vapour release rate up to 24.2 ± 1.054 %/min. These results showed no significant differences between the three samples analysed, which proves repeatability of the results.

5.9 Closure

This chapter proposed a smart material for humidifying the inspired gas by using recovered moisture from the expired airflow, to achieve the humidity quantified in the previous chapter. The methodology used to synthesize the PNIPAM and the techniques used for characterization and optimization are described in detail. The optimized smart material was able to achieve a water vapour release rate of 24.2 ± 1.054 %/min, which corresponds to the weight percentage of water vapour released per minute, at a LCST of 32°C. This means that, below 32°C the smart material absorbs the surrounding water vapour molecules and release them when the temperature is higher than 32°C achieving a water vapour release rate up to 24.2 ± 1.054 %/min. These results showed no significant differences between the three samples analysed, which proved repeatability of the results.

In the next chapter, this smart material is synthesized on a large scale and clinical trials are performed with 21 volunteers to test the humidifying proposal developed in this chapter.

Chapter 6

Design, Performance and Validation of a Self-Humidifying Device

6.1 Introduction

In Chapter 5, a proposal for humidifying the inspired gas by using recovered moisture from the expired airflow, and achieve the humidity requirements previously quantified was developed. A smart material was synthetized using PNIPAM grafted from a commercial organic cotton fabric and optimized to ensure the maximum amount of water vapour uptake and release in the shortest time. The water release rate achieved by the smart material was 24.2 ± 1.054 %/min, which corresponds to the weight percentage of water vapour released per minute, and the LCST was quantified at 32°C. This means that, below 32°C the smart material absorbs the surrounding water vapour molecules and releases them when the temperature is higher than 32°C achieving a water vapour release rate up to 24.2 ± 1.054 %/min. These results showed no significant differences between the three samples analysed, which proved repeatability of the results.

As previously stated, LSD devices, such as asthma nebulizers, positive airway pressure devices, respirators or even tracheotomy, are used to restore or provide a proper respiration cycle in some patients. These therapies disturb the natural lubrication and normal air conditioning process because there is an increase in pressure and turbulent effect, or the nasal cavity, which is the most important air conditioning part, is bypassed. Breathing devices, can cause drying and trauma of the mucosa where ciliated cells are inactivated and reduced [31]. Hence, inspired air has to be warmed and humidified in order to reach the lungs at 37°C with 100% relative humidity, and maintain an optimum mucociliary transport. This effect was analysed and the amount of water needed to be added into the respiratory system and overcome the dryness side effect was quantified in chapters 3 and 4.

The purpose of this chapter is to develop a miniaturized, affordable and eco-friendly self-humidifying device using the smart material and validate its performance with 21 volunteers. The objectives of the self-humidifying device are to humidify the inspired airflow up to the humidity levels required by using recovered moisture from expiration, warm the air and adjust the water delivered into the respiratory system.

In the course of this investigation, the design of the self-humidifying device is described in section 6.2 including the location of the smart material, the humidity adjustment, temperature control and humidification performance. The clinical protocol followed to test the smart fabric with 21 volunteers is explained in section 6.3 describing the participant election criteria, experimental setup, data validation and experimental protocol, and the statistical analysis is described in section 6.4. Then, the performance of the smart fabric is analysed in section 6.5 for 0, 5, 10, 15 and 20 cmH_2O CPAP pressures. Finally, sections 6.6 and 6.7 correspond to the discussion and closure of the chapter respectively.

6.2 Self-humidifying device design

As stated before, in this part of the chapter the working principle and design of the self-humidifying device using the smart material to humidify the inspired airflow up to the humidity levels required by using recovered moisture from expiration, warm the air and adjust the water delivered into the respiratory system are explained in detail.

6.2.1 Location of the smart material in LSD

The smart material (PNIPAM-Cotton fabric) is the main component of the self-humidifying device, since the synthetized fabric is able to absorb surrounding water vapour molecules at temperatures higher than the LCST, set at 32°C, and releases them at temperatures below the LCST. Hence, to achieve a good performance, the fabric has to be in contact with the human breath *i.e.* in both inspiration and expiration airflows. Also, it is important to note that the main application of the device is to provide the humidity required to overcome the dryness side effect caused by the LSD devices, so the self-humidifying device is used as an additional component of LSD replacing current convective heated humidifiers. The CPAP device is used as representative of LSD in this investigation. Therefore, the best location to place the smart material is inside the CPAP mask, where the pressurized inflow is in contact with the inspiration and expiration airflows. The smart fabric is lining all the inner surface of a commercial CPAP mask in order to achieve the maximum airflow contact as outlined in Figure 6.1.

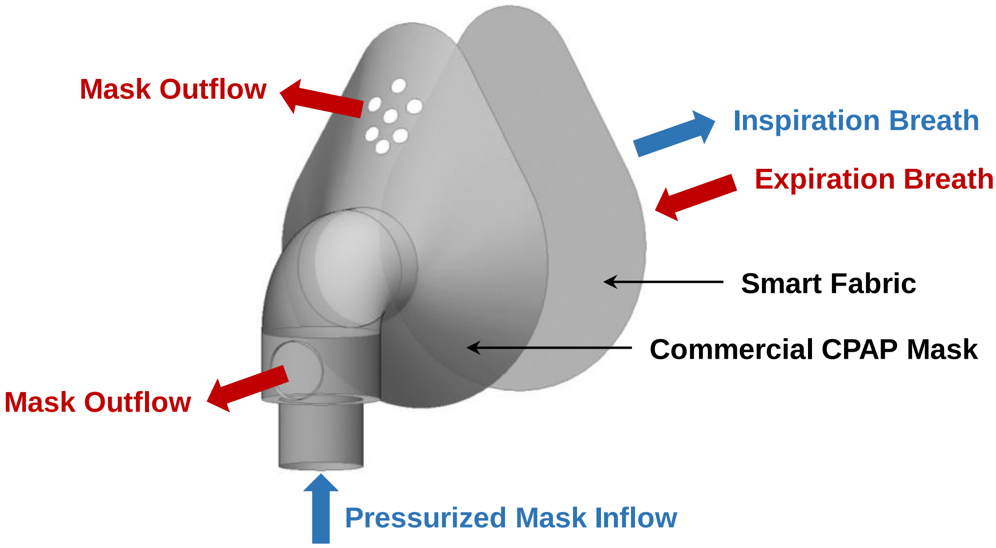

Figure 6.1. Diagram showing the commercial CPAP facial mask, the smart fabric location lining the inner surface of the mask and the airflow directions including the inspiration and expiration of the breathing cycle.

6.2.2 Humidity adjustment of the smart material

One of the requirements of the self-humidifying device is to humidify the inspired airflow by using recovered moisture from expiration and adjust the water delivered into the respiratory system.

Based on the results obtained in the previous chapter, the TGA curves obtained from the optimized PNIPAM-Cotton samples were used to calculate the water release rate, but more information can be extracted from the curves, such as the amount of water vapour released as a function of temperature. These data are used in this section to develop a curve representing the amount of water vapour released from the smart fabric as a function of the temperature applied. The resulting mean relation between the fabric temperature and the percentage of water released is shown in Figure 6.2.

The percentage of water vapour provided depends on the weight of the synthetized smart fabric *i.e.* 4 g of synthetized smart fabric heated above 40°C is able to provide 1.02 g of water vapour or 4 g of synthetized smart fabric at 33°C is able to provide

0.6 g of water vapour. Hence, the water vapour release can be adjusted depending on the temperature of the smart fabric.

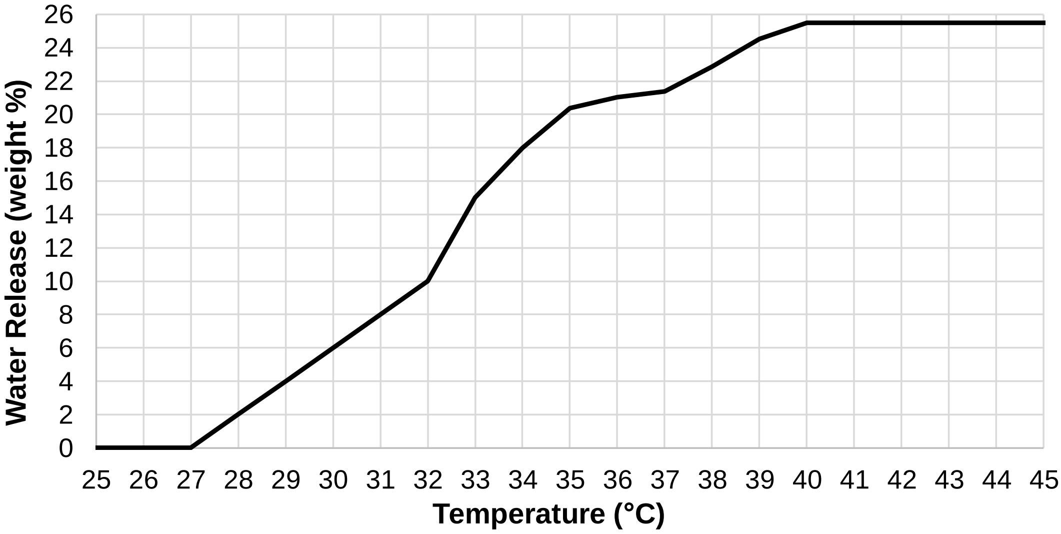

Figure 6.2. Relation curve between the water vapour release percentage and the temperature of the smart fabric.

6.2.3 Temperature control of the smart material

It has been seen that the temperature of the smart fabric is the most important parameter to control the performance of the self-humidifying device. Hence, once the smart material is synthetized, the fabric is sewn with an insulated resistor filament to increase the surface temperature and change the polymer properties.

Copper is an eco-friendly metal, because it can be recycled and reused multiple times, soft, malleable and ductile, with very high thermal and electrical conductivity [183]. Due to its reasonable price and properties, an insulated copper filament is chosen as a resistor filament to control the temperature of the fabric. The filament is sewn covering the entire fibrous surface to maximize the heat transfer properties, and provide a fast heating response and a uniform temperature distribution on the smart fabric. Both filament ends are welded with 1 mm 60% tin / 40% lead resin core solder to two male copper snaps, which are sewn to the fabric with cotton thread. The female snaps are fixed to the mask and connected to a power supply to provide current through the filament and heat the fabric. Hence, this setup allows the smart fabric to be connected and disconnected to the CPAP mask and hence the power supply, the times needed to be washed or replaced.

The electrical resistance of the entire setup is measured with a UNI-T UT61E multimeter (True RMS Multimeters) at room temperature in order to determine the theoretical relationship between the temperature provided and the resistance of the system. Equation 6.1 relates the electrical resistance with the temperature of the system, where R_0 corresponds to the resistance at room temperature T_0, and α is the temperature coefficient of the conductor material, which is assumed to be 100% copper.

$$R = R_0 \cdot \left(1 + \alpha \cdot (T - T_0)\right) \tag{6.1}$$

The resulting temperature distribution on the smart fabric will vary according to the voltage delivered from the power supply. For health and safety reasons the voltage applied should not be higher than 12V and the temperature reached should be below 60°C [183, 184].

6.2.4 Humidification performance of the smart material

The working principle of the self-humidifying device is explained in this section. In use during expiration, the power supply is off and no current is provided to the resistor filament in order to keep the smart material at room temperature, typically below LCST. Under these conditions PNIPAM-molecules are predominantly hydrophilic and the amide-groups form inter-molecular hydrogen bonds with the surrounding water vapour molecules. Expiration flow is generally at 100% relative humidity and the PNIPAM-Cotton material is moisture saturated and absorbs the maximum number of water molecules from the expiration breath, expelling dry air out of the CPAP mask.

When the expiration flow has ended, (after three seconds approximately) and inspiration flow starts, the power supply is switched on passing current though the resistor filament. Depending on the voltage and current provided, the PNIPAM-cotton material is heated up to a temperature above LCST. Under these conditions the hydrophobic isopropyl-methyl groups tend to establish polymer-polymer interactions and the water molecules previously absorbed are released into the inspiration airflow. Fresh air passes through the fabric, the temperature is increased and moisture is added to the incoming air such that warm humid air is provided to the patient.

During the next expiration, the power supply is off in order to allow the fabric temperature to reduce below the LCST due to the heat transfer produced from the pressurized room air generated on the CPAP device and introduced into the CPAP mask. This process is outlined in Figure 6.3.

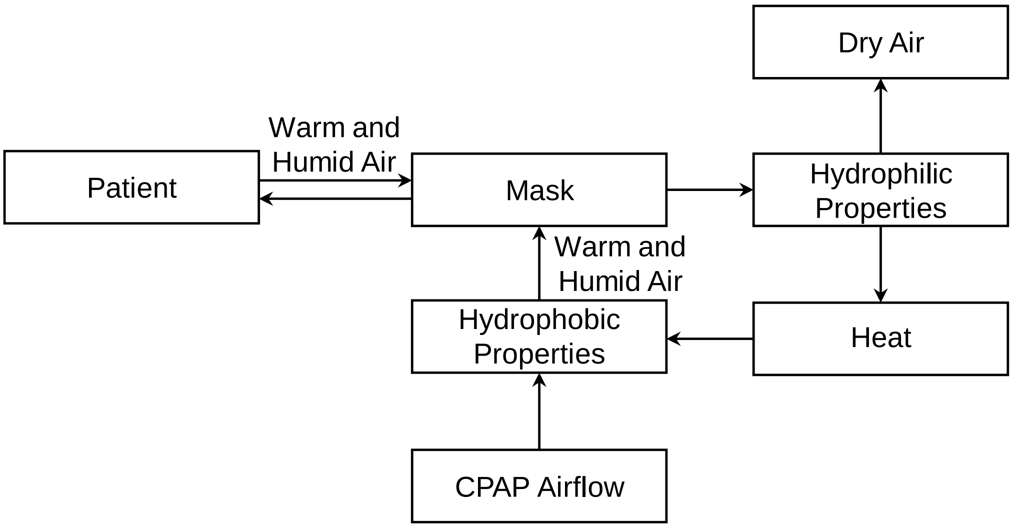

Figure 6.3. Diagram showing the working principle or humidification performance of the smart material.

6.3 Clinical protocol

Aiming to test the humidifying performance of the self-humidifying device on 21 volunteers, an ethical application EA1 was prepared, submitted and approved by the AUT ethics committee. The application was approved on the 3rd of May 2018 and granted for three years until the 3rd of May 2021. Participant information sheets, questionnaires and consent forms were discussed and signed prior to the initiation of the study (see appendixes A, B, C, D and E).

6.3.1 Participants

21 volunteers were recruited between the ages of 21 and 55, where 38.1% were females and 61.9% males. Only healthy volunteers were invited to participate in the study, people with cardiovascular or respiratory problems and unable to wear a mask were excluded from the study. An otolaryngologist expert in CPAP therapy was consulted to verify that the study is completely harmless. Therefore, healthy volunteers do not experience discomfort or embarrassment using the test. However, since not all people find breathing masks comfortable due to the flow rate applied, if

the volunteer finds the test uncomfortable, the mask can be removed easily at any time and the test is stopped immediately.

After eligibility, the height and weight were recorded before starting the trials in order to find a correlation with the results if there were any. The data obtained from each participant is shown in Table 6.1.

Table 6.1. Data obtained from the 21 volunteers recruited. It includes the gender (M or F), age (years), height (cm) and weight (Kg).

Volunteers	**Gender (F or M)**	**Age (years)**	**Height (cm)**	**Weight (Kg)**
1	F	28	170	50
2	M	26	183	93
3	M	27	180	75
4	F	21	163	56
5	M	22	181	75
6	M	38	164	62
7	M	28	178	75
8	F	46	165	62
9	M	29	170	70
10	F	22	168	63
11	M	31	173	57
12	M	34	178	70
13	F	25	170	58
14	M	34	160	65
15	M	29	172	62
16	M	31	178	89
17	M	25	174	64
18	F	32	165	72
19	M	25	173	70
20	F	28	157	48
21	F	55	165	75

6.3.2 Experimental setup

To perform the clinical trials and test the humidity performance of the self-humidifying device, three linear and medium Mw PNIPAM-cotton samples were synthetized following the polymerization protocol described in the previous chapter 5. Then, the samples were sewed with the insulated copper filament, the ends were welded to the male copper snaps and sewed to the fabric with a cotton thread to ensure its fixation. The dimensions of the resulting smart material are shown in Figure 6.4.

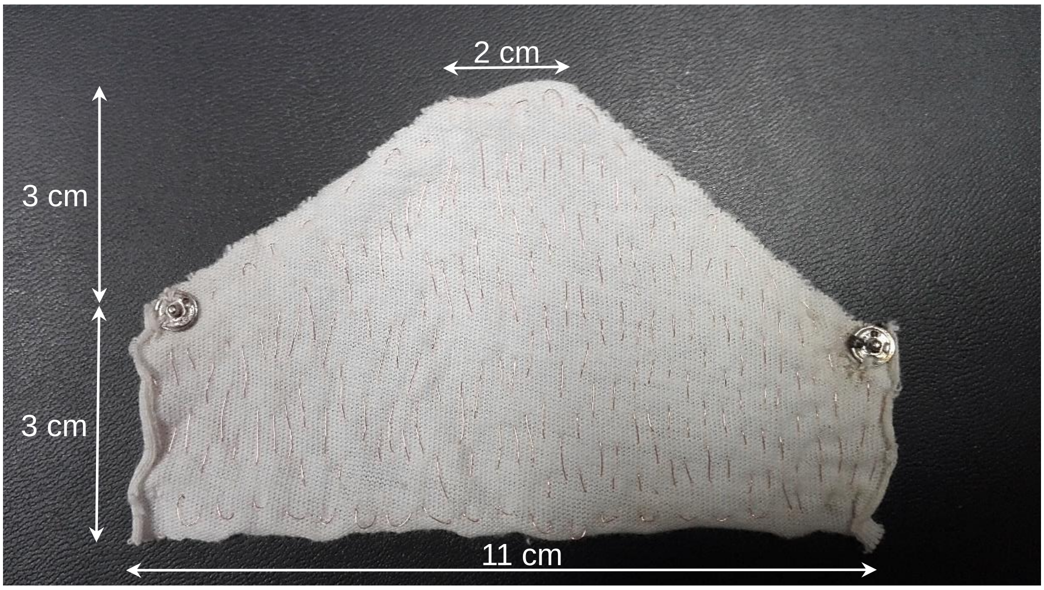

Figure 6.4. Dimensions of the smart material. The sample shown is sewed with the insulated copper filament and the ends are welded to the male copper snaps which are sewed to the fabric with cotton thread.

The female copper snaps were glued to the F&P Simplus CPAP mask (FP Healthcare, NZ) and welded to copper wires. Both wires were connected to the EL155R power supply (TTi) to provide the desired current and voltage to the filament. A SRD-05VDC-SL-C relay (Songle®) was connected between the power supply and one of the female copper snaps attached to the mask in order to switch the power on and off. The relay was connected to the UNO Arduino board and the computer. The SHT15 temperature and humidity sensor (Sensirion AG, Switzerland) was placed inside the CPAP mask and connected to the same UNO Arduino board. A C++ code was written using the Arduino v1.6.11 software to set the relay switch on and off times and collect the environmental temperature (T) and relative humidity (RH) data provided by the SHT15 sensor (see appendix G). Then, a commercial CPAP device (FP Healthcare, NZ) was used to provide the positive airway pressure in the respiratory tract, 0 (CPAP device off), 5, 10, 15 and 20 cmH_2O pressures were used in the trials, and a 2080P digital manometer (Digitron, UK) was connected to the mask to ensure that the smart material is not increasing the flowrate resistance and the pressure reading corresponds to the set on the CPAP device. Finally, the volunteer wears the CPAP mask to provide the breathing cycle which is tested during the trials. This experimental setup is outlined in Figure 6.5.

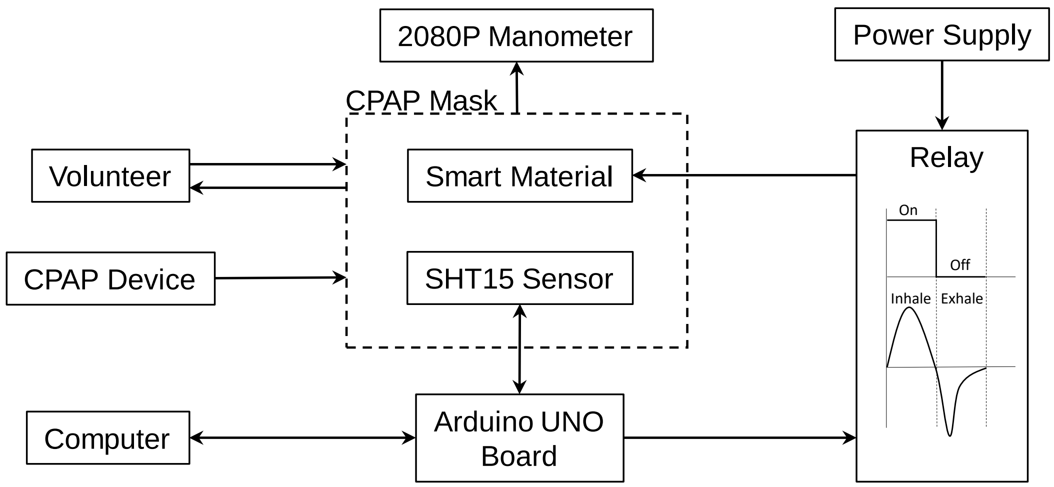

Figure 6.5. Diagram describing the experimental setup used in the clinical trials to test the self-humidifying device with 21 volunteers.

6.3.3 Data validation

Aiming to test the humidifying performance of the self-humidifying device on 21 volunteers, the RH and T evolution inside the mask containing the smart material were measured with the SHT15 sensor. Then, the data obtained from each volunteer at each pressure applied from the CPAP (0, 5, 10, 15 and 20 cmH_2O) was compared.

A control measurement was achieved with the CPAP device with no humidification at each pressure *i.e*. the volunteer was breathing with the CPAP mask connected to the CPAP device, but without the smart fabric. Hence, it is possible to measure how much absolute humidity provides the smart fabric compared to a non-humidified CPAP performance and check if it satisfies the humidity levels quantified in chapter 4 and required to overcome the dryness side effect on the upper airways.

A third scenario was considered to validate the humidity provided by the smart fabric at each pressure. The volunteer was breathing with the CPAP mask, without the smart fabric, connected to the CPAP device with the CPAP humidifier working at level 7 in order to provide the maximum humidity to the respiratory system. Hence, it is possible to compare the humidity provided by the smart fabric with the one provided by the commercial CPAP humidifier and check if they are in the same order of magnitude. The setup used in these three scenarios is described schematically in Figure 6.6.

A Control (No humidification)	Volunteer	+	CPAP Mask: - Sensor	+	CPAP Device: - Pressure: 0 (off), 5, 10, 15, 20 cmH_2O - Humidity: level 0 (off)
B Smart Fabric Humidification	Volunteer	+	CPAP Mask: - Sensor - Smart Fabric	+	CPAP Device: - Pressure: 0 (off), 5, 10, 15, 20 cmH_2O - Humidity: level 0 (off)
C CPAP Humidifier Performance	Volunteer	+	CPAP Mask: - Sensor	+	CPAP Device: - Pressure: 5, 10, 15, 20 cmH_2O - Humidity: level 7 (max.)

Figure 6.6. Schematic description of the setup used in the three scenarios. A- Control measurement where no humidification is applied. Hence neither the smart fabric nor the CPAP humidifier are used during the measurement. B- Measure of the humidification provided by the smart fabric where the CPAP humidifier is off at level 0. C- Measure of the maximum humidification provided by the CPAP humidifier (level 7), where the smart fabric is not connected, for data validation.

6.3.4 Experimental protocol

The experimental protocol followed for each volunteer to measure the humidity performance achieved through the three humidity scenarios previously explained, is presented in this section. To prove repeatability of the results, sample A was tested with 7 volunteers, sample B with 7 volunteers and the same with sample C, and all the materials were washed and sterilized with 70% ethanol (Sigma Aldrich, NZ) before each test. The methodology followed with each volunteer is described below:

- The volunteer was invited to wear the CPAP mask without the smart fabric and disconnected from the CPAP device and breathe for 5 minutes. The RH and T data was used to analyse the shape of the breathing cycle and to determine the time of the inspiration and expiration phases. Then, the relay was adjusted to switch on the power during inspiration and switch it off during expiration. The data was also used to quantify the natural humidity evolution without any extra humidification at 0 cmH_2O pressure.

- The smart fabric was connected to the CPAP mask and the electrical resistance of the system was measured to calculate the current and voltage needed to achieve a maximum temperature of 42°C. Ohm's law and 6.1 were used to calculate the values.
- The volunteer was invited to wear the CPAP mask containing the smart material and disconnected from the CPAP device and breathe for 5 minutes. The E5 IR camera (FLIR) was used to measure the temperature evolution on the fabric surface and ensure the minimum and maximum temperatures were around 26°C and 42°C respectively. The T and RH readings were used to determine the humidity provided by the smart fabric at 0 cmH_2O pressure.

- Then, the CPAP device was set to provide 5 cmH_2O positive pressure and was connected to the mask. The volunteer was invited to wear the CPAP mask without the smart fabric and breathe for 5 minutes. Then, the volunteer was invited to wear the CPAP mask with the smart fabric and breathe for 5 minutes. Finally, the volunteer was invited to wear the CPAP mask without the smart fabric but with the CPAP humidifier working at level 7 (providing the maximum humidification), and breathe for 5 minutes. The temperature on the fabric surface was measured multiple times with the E5 IR camera to adjust the current and voltage provided and ensure the minimum and maximum temperatures were around 26°C and 42°C respectively. The maximum current and voltage provided to the copper resistor filament were 1.5 A and 5.28 V respectively.

- The last step was repeated with 10, 15 and 20 cmH_2O positive airway pressures and the T and RH data were collected and stored for a posterior analysis.

6.4 Statistical analysis

Statistical analysis was performed using GraphPad Prism software (GraphPad, San Diego, CA, USA) version 6.07 for windows using one-way analysis of variance (ANOVA), followed by Tukey post hoc analysis for multiple comparisons. Results are presented as mean ± standard deviation (SD) of 21 independent experiments (n = 21). To determine the significance of the results, a probability value (p value) between 0 and 1 is used to test the validity of a claim made about the parameter measured, which is called null hypothesis. Therefore, a small p value ($p < 0.05$) indicates strong evidence against the null hypothesis, which means that the null hypothesis is rejected and there is a significant difference on the parameter measured hence on the results (* $p < 0.05$, ** $p < 0.01$, *** $p < 0.001$ and **** $p < 0.0001$) [150, 151].

6.5 Results

The temperature and humidity data obtained from each experiment is analysed in this section. The performance of the smart fabric is analysed in each volunteer under the five CPAP pressures (including the 0 cmH_2O no pressure) and the three scenarios: no humidification, humidification provided by the smart fabric and humidification provided by the CPAP humidifier at level 7 (maximum humidification).

6.5.1 Performance of the smart fabric under 0 cmH_2O pressure

In this section, the temperature and humidity results of the smart fabric under 0 cmH_2O pressure are analysed, *i.e.* the experiments are performed with the CPAP device disconnected from the CPAP mask. The breathing cycle of the volunteers was identified with the RH and T data measured with the SHT-15 sensor and obtained every 0.1 seconds for 5 minutes. The curves described a wave close to a sinusoidal signal, where the maximum peak corresponded to the end of the expiration with high relative humidity and temperature values inside the CPAP mask, and the minimum peak corresponded to the end of the inspiration with low relative humidity and temperature values inside the mask. Each inspiration and expiration times of each breathing cycle measured for 5 minutes were averaged to obtain a mean inspiration and expiration time value for each volunteer. The results are summarized in Table 6.2. The data obtained for each volunteer was used on the C++ Arduino code to set the relay switch on and off times. During the inspiration time, the relay is switched on and current is provided to the fabric to allow water release from the fabric and warm the airflow. During the expiration time, the relay is switched off and no current is provided to the smart fabric to allow the temperature drop and PNIPAM water absorption from expiration moisture.

Table 6.2. Mean inspiration and expiration times (seconds) measured from the 21 volunteers recruited using the T and RH data obtained for 5 minutes.

Volunteers	Inspiration Time (seconds)	Expiration Time (seconds)
1	3.2	3.5
2	2.8	3.3
3	2.4	3.5
4	2.1	2.8
5	3.2	3.1
6	1.8	2.7
7	3.1	3.3
8	1.7	2.7
9	2.2	3.2
10	3.3	3.4
11	3.0	3.2
12	2.8	3.1
13	1.6	3.0
14	2.5	2.8
15	2.9	3.1
16	3.2	3.4
17	2.7	2.9
18	2.9	3.4
19	2.5	3.2
20	1.9	2.8
21	3.1	3.3

The current and voltage provided from the power supply to achieve a minimum temperature on the fabric of 26ºC and a maximum temperature of 42ºC, above and below the LCST measured at 32ºC and provided the maximum water delivery from the smart fabric according to the Figure 6.2 were 0.7 A and 2.27 V. These values were adjusted to overcome the effect of the flowrate on the temperature increase and heat dissipation. The temperature on the smart fabric was measured with the IR camera multiple times during the 5 minute experiment, and the values obtained were not significantly different from the theoretical targets.

The AH is calculated from the T and RH curves as a function of time using the empirical Tetens equation (6.2) which relates the saturation water vapour density

(SVD, mg/L) with the temperature (T, °C) improving the Clapeyron equation, and equation 6.3.

$$SVD = 5.018 + (0.32321 \cdot T) + (8.1847 \cdot 10^{-3} \cdot T^2) + (3.1241 \cdot 10^{-4} \cdot T^3) \qquad 6.2$$

$$RH = \frac{AH}{SVD} \cdot 100 \qquad 6.3$$

In order to set a unique value for each volunteer and parameter measured, a window is considered for each breathing cycle to determine the median value during this time. The median is chosen because this statistical parameter considers the amount of data close to the maximum or minimum peaks. Then, the mean of all median values determined for each breathing cycle window during the 5 minute experiments are calculated to obtain a unique value per curve, experiment and volunteer.

Figure 6.7 shows the AH (mg/L) (A) and T (ºC) (B) values measured for the 21 volunteers under the control scenario, where no humidity was provided, and under the heat and humidity provided from the smart fabric, where three equally-synthetized samples were tested (A, B and C). The results show that the AH and T provided from the three smart fabric samples are significantly higher than the control. Also, no significant differences are found between the AH or T obtained from each of the three samples, which proves repeatability of the smart fabric synthesis or manufacturing.

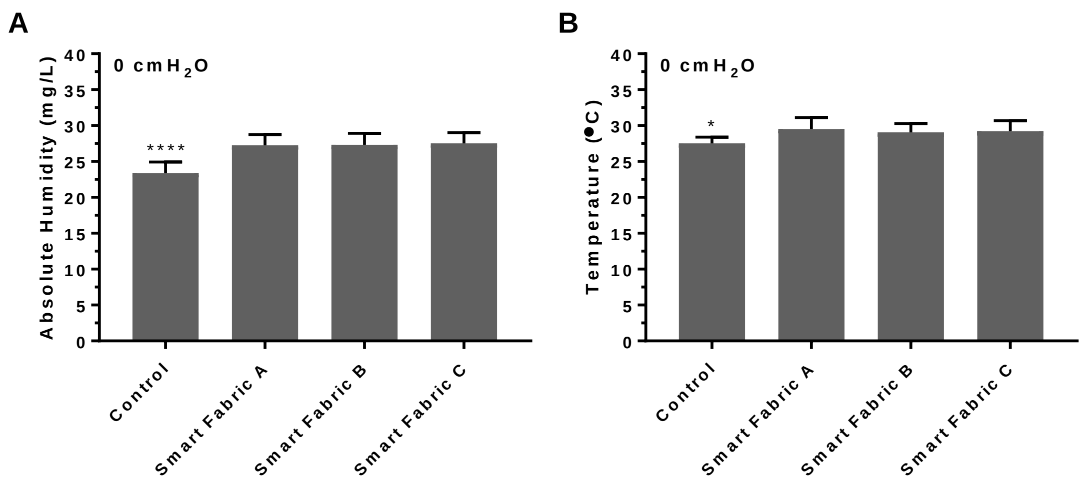

Figure 6.7. Clinical data obtained from 21 volunteers at 0 cmH_2O (no CPAP used). A- Absolute humidity inside the CPAP mask obtained from the control and the three equally-synthetized smart

fabrics A, B and C. B- Environmental temperature inside the CPAP mask obtained from the control and the three equally-synthetized smart fabrics A, B and C.

6.5.2 Performance of the smart fabric under 5 cmH_2O pressure

In this section, the temperature and humidity results of the smart fabric under 5 cmH_2O pressure are analysed, *i.e.* the CPAP device is connected to the CPAP mask and set at 5 cmH_2O. The current and voltage provided from the power supply to achieve a minimum temperature on the fabric of 26ºC and a maximum temperature of 42ºC, above and below the LCST measured at 32ºC and provide the maximum water delivering from the smart fabric according to the Figure 6.2 were 1.35 A and 4.67 V. These values were adjusted to overcome the effect of the flowrate provided by the CPAP on the temperature increase and heat dissipation. The temperature on the smart fabric was measured with the IR camera multiple times during the 5 minute experiment, and the values obtained were not significantly different from the theoretical targets. The pressure was also measured multiple times inside the CPAP mask using the digital manometer to ensure that the smart material is not increasing the flowrate resistance and the pressure reading corresponds to the set on the CPAP device. The measured pressure values were not significantly different from the 5 cmH_2O set at the CPAP device.

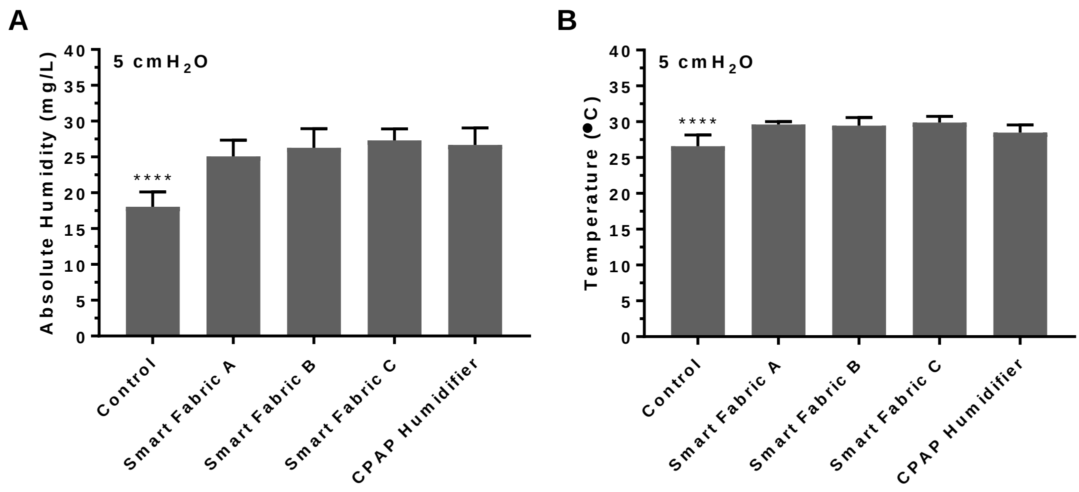

Figure 6.8. Clinical data obtained from 21 volunteers at 5 cmH_2O. A- Absolute humidity inside the CPAP mask obtained from the control, the three equally-synthetized smart fabrics A, B and C, and the commercial CPAP humidifier. B- Environmental temperature inside the CPAP mask obtained from the control, the three equally-synthetized smart fabrics A, B and C, and the commercial CPAP humidifier.

The AH is calculated from the temperature and relative humidity curves with 6.2 and 6.3 as previously explained, and the mean AH (mg/L) and T (ºC) values are shown in Figure 6.8A and Figure 6.8B, respectively, under the three scenarios: control where no humidity is provided, the heat and humidity provided by the three smart fabric samples (A, B and C), and the heat and humidity provided by the commercial convective heated CPAP humidifier at the maximum level 7. The results show that the AH and T provided from the three smart fabric samples are significantly higher than the control. No significant differences are found between the AH or T obtained from each of the three samples, which proves repeatability of the smart fabric synthesis or manufacturing. Also, no significant differences are found between the humidity and heat provided from any of the three samples and the commercial CPAP humidifier, which proves that the smart fabric is able to provide the same maximum values than the current humidifier.

6.5.3 Performance of the smart fabric under 10 cmH_2O pressure

In this section, the temperature and humidity results of the smart fabric under 10 cmH_2O are analysed, *i.e.* the CPAP device is connected to the CPAP mask and set at 10 cmH_2O. The current and voltage provided from the power supply to achieve a minimum temperature on the fabric of 26ºC and a maximum temperature of 42ºC, above and below the LCST measured at 32ºC and provide the maximum water delivering from the smart fabric according to the Figure 6.2 were 1.4 A and 4.81 V. These values were adjusted to overcome the effect of the flowrate provided by the CPAP on the temperature increase and heat dissipation. The temperature on the smart fabric was measured with the IR camera multiple times during the 5 minute experiment, and the values obtained were not significantly different from the theoretical targets. The pressure was also measured multiple times inside the CPAP mask using the digital manometer to ensure that the smart material is not increasing the flowrate resistance and the pressure reading corresponds to the set on the CPAP device. The measured pressure values were not significantly different from the 10 cmH_2O set at the CPAP device.

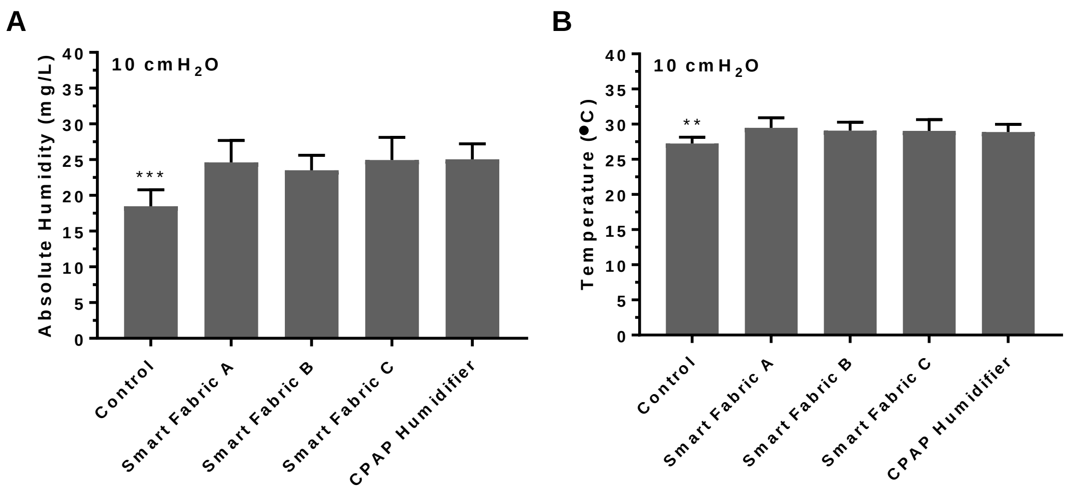

Figure 6.9. Clinical data obtained from 21 volunteers at 10 cmH_2O. A- Absolute humidity inside the CPAP mask obtained from the control, the three equally-synthetized smart fabrics A, B and C, and the commercial CPAP humidifier. B- Environmental temperature inside the CPAP mask obtained from the control, the three equally-synthetized smart fabrics A, B and C, and the commercial CPAP humidifier.

The AH is calculated from the temperature and relative humidity curves with equations 6.2 and 6.3 as previously explained, and the mean AH (mg/L) and T (ºC) values are shown in Figure 6.9A and Figure 6.9B, respectively, under the three scenarios: control where no humidity is provided, the heat and humidity provided by the three smart fabric samples (A, B and C), and the heat and humidity provided by the commercial convective heated CPAP humidifier at the maximum level 7. The results show that the AH and T provided from the three smart fabric samples are significantly higher than the control. No significant differences are found between the AH or T obtained from each of the three samples, which proves repeatability of the smart fabric synthesis or manufacturing. Also, no significant differences are found between the humidity and heat provided from any of the three samples and the commercial CPAP humidifier, which proves that the smart fabric is able to provide the same maximum values than the current humidifier.

6.5.4 Performance of the smart fabric under 15 cmH_2O pressure

In this section, the temperature and humidity results of the smart fabric under 15 cmH_2O are analysed, *i.e.* the CPAP device is connected to the CPAP mask and set at 15 cmH_2O. The current and voltage provided from the power supply to achieve a minimum temperature on the fabric of 26ºC and a maximum temperature of 42ºC, above and below the LCST measured at 32ºC and provide the maximum water delivering from the smart fabric according to the Figure 6.2 were 1.45 A and 4.99 V. These values were adjusted to overcome the effect of the flowrate provided by the CPAP on the temperature increase and heat dissipation. The temperature on the smart fabric was measured with the IR camera multiple times during the 5 minute experiment, and the values obtained were not significantly different from the theoretical targets. The pressure was also measured multiple times inside the CPAP mask using the digital manometer to ensure that the smart material is not increasing the flowrate resistance and the pressure reading corresponds to the set on the CPAP device. The measured pressure values were not significantly different from the 15 cmH_2O set at the CPAP device.

The AH is calculated from the temperature and relative humidity curves with 6.2 and 6.3 as previously explained, and the mean AH (mg/L) and T (ºC) values are shown in Figure 6.10A and Figure 6.10B, respectively, under the three scenarios: control where no humidity is provided, the heat and humidity provided by the three smart fabric samples (A, B and C), and the heat and humidity provided by the commercial convective heated CPAP humidifier at the maximum level 7. The results show that the AH and T provided from the three smart fabric samples are significantly higher than the control. No significant differences are found between the AH or T obtained from each of the three samples, which proves repeatability of the smart fabric synthesis or manufacturing. Also, no significant differences are found between the humidity and heat provided from any of the three samples and the commercial CPAP humidifier, which proves that the smart fabric is able to provide the same maximum values than the current humidifier.

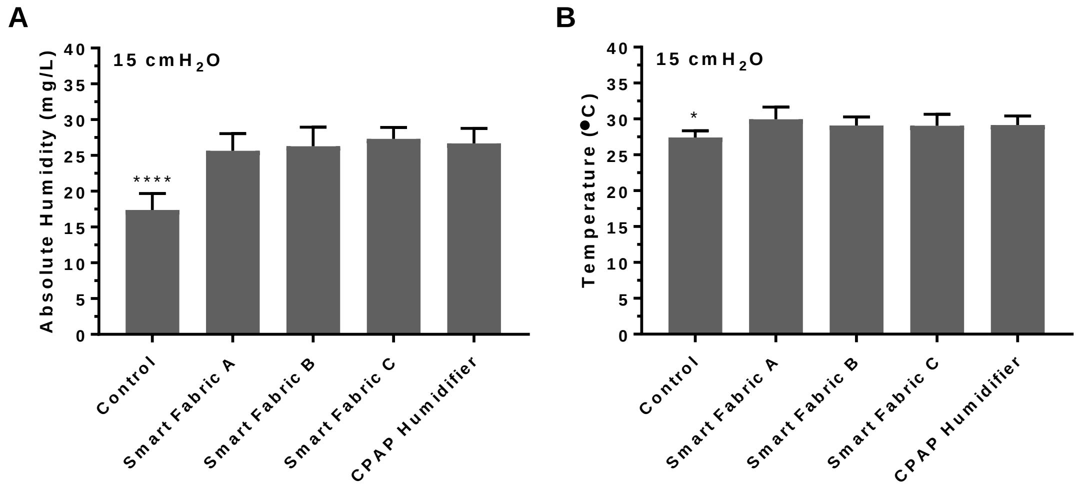

Figure 6.10. Clinical data obtained from 21 volunteers at 15 cmH_2O. A- Absolute humidity inside the CPAP mask obtained from the control, the three equally-synthetized smart fabrics A, B and C, and the

commercial CPAP humidifier. B- Environmental temperature inside the CPAP mask obtained from the control, the three equally-synthetized smart fabrics A, B and C, and the commercial CPAP humidifier.

6.5.5 Performance of the smart fabric under 20 cmH_2O pressure

In this section, the temperature and humidity results of the smart fabric under 20 cmH_2O are analysed, *i.e.* the CPAP device is connected to the CPAP mask and set at 20 cmH_2O. The current and voltage provided from the power supply to achieve a minimum temperature on the fabric of 26ºC and a maximum temperature of 42ºC, above and below the LCST measured at 32ºC and provide the maximum water delivering from the smart fabric according to the Figure 6.2 were 1.5 A and 5.26 V. These values were adjusted to overcome the effect of the flowrate provided by the CPAP on the temperature increase and heat dissipation. The temperature on the smart fabric was measured with the IR camera multiple times during the 5 minute experiment, and the values obtained were not significantly different from the theoretical targets. The pressure was also measured multiple times inside the CPAP mask using the digital manometer to ensure that the smart material is not increasing the flowrate resistance and the pressure reading corresponds to the set on the CPAP device. The measured pressure values were not significantly different from the 20 cmH_2O set at the CPAP device.

The AH is calculated from the temperature and relative humidity curves with 6.2 and 6.3 as previously explained, and the mean AH (mg/L) and T (ºC) values are shown in Figure 6.11A and Figure 6.11B, respectively, under the three scenarios: control where no humidity is provided, the heat and humidity provided by the three smart fabric samples (A, B and C), and the heat and humidity provided by the commercial convective heated CPAP humidifier at the maximum level 7. The results show that the AH and T provided from the three smart fabric samples are significantly higher than the control. No significant differences are found between the AH or T obtained from each of the three samples, which proves repeatability of the smart fabric synthesis or manufacturing. Also, no significant differences are found between the humidity and heat provided from any of the three samples and the commercial CPAP humidifier, which proves that the smart fabric is able to provide the same maximum values than the current humidifier.

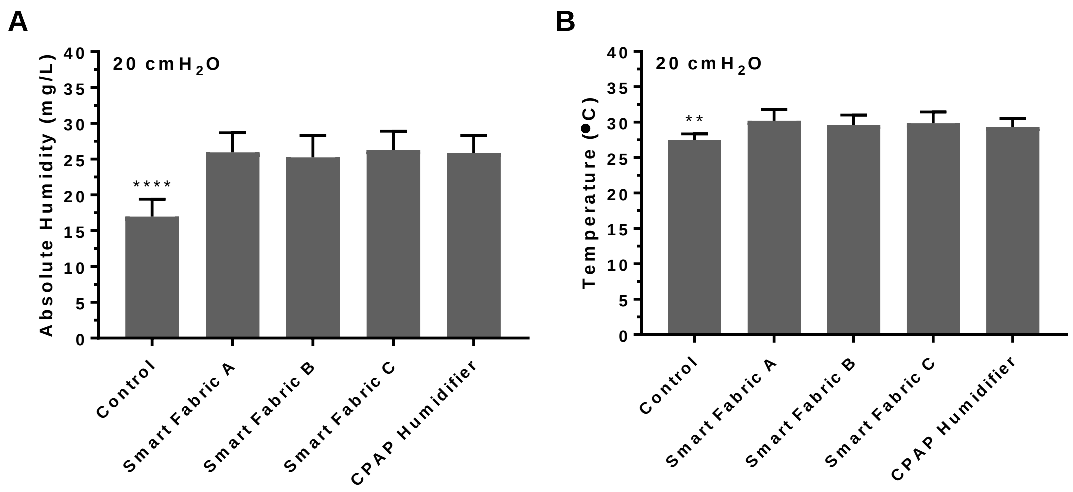

Figure 6.11. Clinical data obtained from 21 volunteers at 20 cmH_2O. A- Absolute humidity inside the CPAP mask obtained from the control, the three equally-synthetized smart fabrics A, B and C, and the commercial CPAP humidifier. B- Environmental temperature inside the CPAP mask obtained from the control, the three equally-synthetized smart fabrics A, B and C, and the commercial CPAP humidifier.

6.6 Analysis of the self-humidifying device performance

The purpose of this chapter was to develop a miniaturized, affordable and eco-friendly self-humidifying device using the smart material and validate its performance with 21 volunteers. The requirements of the self-humidifying device performance were: 1) humidify the inspired airflow up to the humidity levels required and determined in chapter 4 by using recovered moisture from expiration, 2) warm the air and 3) adjust the water delivered into the respiratory system. The main application of the self-humidifying device is to provide the humidity required to overcome dryness, a side effect caused by the LSD devices, so the device is used as an additional component of the LSD replacing current convective heated humidifiers and reducing the LSD dimensions. In particular the CPAP device is used as LSD in this investigation.

The main component of the self-humidifying device is the smart material (PNIPAM-Cotton fabric) optimized in chapter 5. The smart fabric was placed lining all the inner surface of a commercial CPAP mask in order to be in contact with the human breath *i.e.* with both inspiration and expiration airflows. Hence, the synthetized fabric was able to absorb surrounding water vapour molecules at temperatures higher than the LCST, set at 32°C, and release them at temperatures below the LCST.

Based on the PNIPAM-Cotton TGA curves obtained in the previous chapter, a curve representing the amount of water vapour released from the smart fabric as a function of the temperature applied was developed. Hence, it is possible to adjust the water delivered from the self-humidifying device into the respiratory system with the operation temperature range. According to the curve developed in section 2.2, the maximum water delivery is achieved with an operation temperature range of 26°C and 42°C.

The smart fabric is sewn with an insulated resistor filament to increase the surface temperature and change the polymer properties, since the temperature of the smart fabric is the most important parameter to control the performance of the self-humidifying device. The resistor filament is connected to a relay and power supply using metallic snaps in order to provide the desired current to the system. In use during expiration, the power supply is off and no current is provided to the resistor filament in order to keep the smart material at room temperature, below LCST. Under these conditions PNIPAM-molecules are predominantly hydrophilic and the amide-groups form inter-molecular hydrogen bonds with the surrounding water vapour molecules. Expiration flow is generally at 100% relative humidity and the PNIPAM-Cotton material is moisture saturated and absorbs the maximum number of water molecules from the expiration breath, expelling dry air out of the CPAP mask. Then, when the expiration flow has ended, (after three seconds approximately) and inspiration flow starts, the power supply is switched on passing current though the resistor filament. Depending on the voltage and current provided, the PNIPAM-cotton material is heated up to a temperature above LCST. Under these conditions the hydrophobic isopropyl-methyl groups tend to establish polymer-polymer interactions and the water molecules previously absorbed are released into the inspiration airflow. Fresh air passes through the fabric, the temperature is increased and moisture is added to the incoming air such that warm humid air is provided to the volunteer.

Three scenarios were considered on the clinical experiments. A control measurement was achieved with the CPAP device no humidified at each pressure *i.e*. the volunteer was breathing with the CPAP mask connected to the CPAP device, but without the smart fabric. Then, the performance of the self-humidifying device was measured with the volunteer breathing into the CPAP mask containing the smart fabric and connected to the CPAP device. Finally, a third scenario was considered to validate the humidity provided by the smart fabric at each pressure. Hence, the volunteer was breathing with the CPAP mask, without the smart fabric, connected to the CPAP device with the CPAP humidifier working at level 7 in order to provide the maximum humidity to the respiratory system.

The performance of the smart fabric is analysed in each volunteer under the five CPAP pressures (including the 0 cmH_2O no pressure) and the three scenarios: no humidification, humidification provided by the smart fabric and humidification provided by the CPAP humidifier at level 7 (maximum humidification).

The results obtained in all the positive pressures analysed, 0, 5, 10, 15 and 20 cmH_2O show that the AH and T provided from the three smart fabric samples were significantly higher than the control and even higher that the theoretical values obtained in chapter 4. This means that the self-humidifying device is able to warm the air and humidify the inspired airflow up to the humidity levels required by using recovered moisture from expiration and hence overcome the dryness side effect. No significant differences are found between the AH or T obtained from each of the three samples, which proves repeatability of the smart fabric synthesis or manufacturing. Also, no significant differences are found between the humidity and heat provided from any of the three samples and the commercial CPAP humidifier, which proves that the smart fabric is able to provide the same maximum values and is able to replace the current convective heated humidifier and reduce the current LSD dimensions.

The data obtained showed no correlation between the environmental room conditions, age, height, weight or gender of the 21 volunteers, which means that the performance of the self-humidifying device does not depend on the subject and can be used in any situation and patient with a proper configuration. Also, due to the structure of the smart material, the airflow passes freely through the fabric providing a proper ventilation with no increase in flowrate resistance. Hence, the LSD titration positive pressure is not affected by the addition of the self-humidifying device.

6.7 Closure

This chapter described how to develop a miniaturized, affordable and eco-friendly self-humidifying device using the smart PNIPAM-Cotton fabric. The performance of the resulting self-humidifying device was validated with 21 volunteers. It was proved that the device was able to humidify the inspired airflow up to the humidity levels required, that were determined theoretically in chapter 4, by using recovered moisture from expiration, warming the air and adjusting the water delivered into the respiratory system.

With this chapter the final objective of the PhD research is achieved, and the next chapter summarizes and discusses all the results obtained during the research, states the conclusions and proposes the future work.

Chapter 7

Discussion and Future Work

7.1 Introduction

This chapter discusses the main outcomes of this research and explains the proposed future work. The results obtained from the human epithelium *in-vitro* cell models are discussed in section 7.2. The optimum humidity values obtained from the 1D human upper airway model are discussed in section 7.3. Then, optimized properties and structure of the smart fabric are discussed in section 7.4. The clinical results obtained from the designed and prototyped self-humidifying device are described in section 7.5. Finally, the proposed future work is described in section 7.6.

7.2 Respiratory epithelial cell behaviour under positive airway pressure

In chapter 3, the human respiratory epithelium response under positive airway pressure application was analysed. Human airway epithelial Calu-3 cells and nasal RPMI 2650 cells grown in air-liquid interface (ALI) on permeable supports were used as *in-vitro* respiratory models and tested under PAP. Cell viability data indicated that both cell lines could survive the positive pressure application for 8 hours. This means that both *in-vitro* models can be used to investigate the effect of PAP on cultured human respiratory epithelial cells and obtain valid and representative results of the human epithelium.

Two custom-made 3D cell insert holders were designed, optimized using flow simulations and 3D printed to achieve the desired positive pressure on the cell lines at specific airflow conditions to simulate human breathing under PAP. The simplest static airflow trajectory was simulated using the closed-flow holder A directly connected to the CPAP device. The continuous-flow holder B was used to simulate the continuous PAP dynamic airflow trajectory and the superimposed human breathing cycle to the PAP dynamic airflow trajectory. The effect of the airflow trajectories on the cells was analysed with the ECIS device, and no significant difference was found in TEER values at ΔP of 20 cmH_2O between the three airflow trajectories in both cell lines. This demonstrates that the airflow trajectories, either static or dynamic flows, do not have any effect on the *in-vitro* models in the experimental time frame considered (8 hours). This could be explained by how the cell holder is designed since, due to the transwell shape, cells are not in direct contact with the main airflow, they are placed inside the well 2 cm depth as described in Figure 7.1. Hence, the three airflow trajectories could have the same effect on the cells, independently of being static or dynamic.

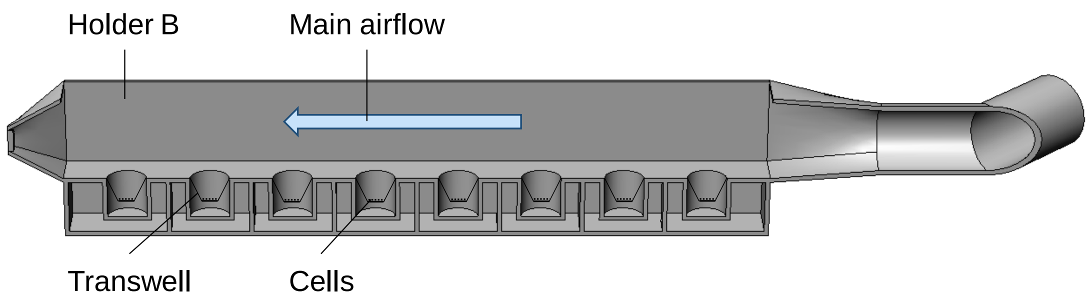

Figure 7.1. Front plane section of well holder B. Schematic representation of transwell shape, cell position and main airflow direction.

To investigate the effect of the PAP on the cultured human epithelial cells, three experimental setups were designed to generate three gauge or relative PAP scenarios on both cell lines: a continuous positive airway pressure (CPAP) which represents to the current CPAP therapy, a superimposed sinusoidal positive airway pressure oscillation (SPAP) which represents the possible improvements according to the literature analysed in chapter 2, and a sinusoidal positive airway pressure oscillation (SPO) to analyse the effect of the oscillation by itself.

The effect of 5, 10, 15 and 20 cmH_2O CPAP on the cell lines was compared with no pressure controls. It was proved that the cell layer was compressed, since the cell thickness layer was significantly reduced after CPAP application. This finding is in agreement with the integrity and permeability results since the cell compression produced after CPAP application squeezes the cell tight junctions and hinders the paracellular transport resulting in an increase in TEER values and consequently a decrease in the Papp coefficient. The paracellular transport is directly related to the water transport across the epithelial cell barrier to regulate the ASL water content and keep the optimum mucus and cilia conditions in the human upper airway [14, 53, 58]. It was also proved that there is an over-evaporation effect on the ASL layer after CPAP application. This effect has been quantified and the amount of water dried or reduced on the ASL layer was increasing from 1.88% to 4.19% for Calu-3 cells and from 1.91% to 3.67% for RPMI 2650 cells with ΔP. Pro-inflammatory marker expression results indicated that Calu-3 cells were inflamed, increasing significantly the IL-6 and IL-8 marker concentrations, after 10 minutes of CPAP application independently of the ΔP applied and the RH used. Finally it has been proved that the CPAP application hinder natural mucus secretion and lubrication with ΔP. Therefore, it has been demonstrated that the CPAP application deforms the epithelial cells, and hinders the natural paracellular transport and mucus secretion rate. Also the addition in air volume to generate the positive pressure, increases the water transfer between the ASL layer and the airflow producing an ASL over-evaporation effect. All these findings could directly influence the ASL regulation mechanism and produce dryness, sneezing, rhinorrhea, post-nasal drip, nasal congestion or epistaxis in the upper airways, the side effects reported by LSD patients after therapy. However, as explained in chapter 1 and 2, it has been proven that the increase in RH can alleviate the ASL dryness or over-evaporation effect, but the increase in RH on the airflow does not improve the mucus secretion rate or produce a reduction of the inflammatory marker concentration, since epithelial cells are equally inflamed at 70% RH than at 100% RH.

The effect of 5 ± 1, 10 ± 1, 15 ± 1 and 20 ± 1 cmH_2O SPAP at 10, 20 and 30 Hz on both epithelial cells was measured with the ECIS apparatus at 1000 Hz and compared with 5, 10, 15 and 20 cmH_2O CPAP. TEER values showed no significant differences between SPAP and CPAP application at any frequency. This no significant differences could be due to the fact that the *in-vitro* cell models could not be sensitive enough to a ± 1 cmH_2O oscillation and hence the superimpose pressure oscillation does not have an effect on the cell physiology, just on the muscle stimulation as described in the literature. Therefore, to investigate this effect in more detail, the oscillation by itself has been studied as a third pressure scenario with a higher signal amplitude.

Finally, the effect of 5 cmH_2O amplitude sinusoidal positive airway pressure oscillation at 10 Hz on both cell lines was compared with 5 cmH_2O CPAP. Regarding cell permeability and deformation or compression, even that TEER values are significantly lower after SPO application than CPAP application and Papp values are significantly higher after SPO application than CPAP application, no significant difference is found on cell thickness measurements between SPO and CPAP application. This could mean that the cell relaxation or decompression time is higher than 0.1 seconds (10 Hz). So, the cell layer could not have enough time to recover the initial shape and thickness. It has been quantified that the over-evaporation effect or the amount of water dried or reduced on the ASL layer after SPO application is significantly lower (1.74% and 0.87%, for Calu-3 and RPMI 2650 cells respectively) compared to values measured after CPAP application (1.88% and 1.91%, for Calu-3 and RPMI 2650 cells respectively). Then, regarding pro-inflammatory marker expressions, it has been seen that the concentration of IL-6 and IL-8 decreases significantly after SPO application compared to CPAP application but still significantly higher than the no pressure controls, and also there is not significant difference between high or low relative humidity conditions. At last, it has been proven that the amount of mucus secreted under SPO is significantly higher than under CPAP, but still significantly lower than no pressure controls in both cell lines. In conclusion, these results were in agreement with previous findings, since an increase in paracellular permeability, compression, ASL over-evaporation and inflammation after SPO is observed compared to CPAP. This means that the side effects studied after PAP application on the human epithelium, such as dryness, inflammation or less mucus secretion, are reduced with SPO application. This could be explained by the fact that, while CPAP applies 5 cmH_2O constant pressure, SPO oscillates the pressure between 0 and 5 cmH_2O at 10 Hz providing a time release to the epithelium at pressures close to 0 cmH_2O. These findings proved that the SPO should be further investigated to be incorporated with the current commercial PAP devices since the pressure oscillation can improve the mucus secretion rate and reduce epithelial cell inflammation, and hence reduce the side effects produced by the LSD therapies.

7.3 Model formulation and extrapolation of epithelial cell results to the human upper airway

In chapter 4, a 1D human upper airway PAP model based on mass and heat transfer equations was formulated to extrapolate the variation on the ASL layer water content after PAP application quantified on the human *in-vitro* respiratory cell models to the entire human upper airways, and determine the input temperature and relative humidity of the compressed PAP airflow needed to overcome the upper airway dryness side effect. Although epithelium inflammation or the lack of mucus secretion from goblet cells produced after PAP therapy is not solved by humidifying the compressed airflow introduced into the respiratory tract to keep the airways open, the use of a proper humidification will increase the comfort of patients using LSD. Hence, a simple, efficient, fast computing and realistic 1D upper airway representation able to predict the heat and water transfer variation between normal breathing and PAP conditions has been proposed and validated to extrapolate the results to the entire upper airways, predict the failure of the natural air conditioning and quantify the extra water vapour and temperature needed in the room compressed air introduced into the respiratory system to generate the PAP and overcome the ASL layer side effect after the therapy.

The initial heat and water transport PAP model results show a significant reduction of temperature and water vapour concentration on the ASL outer airflow interface for each PAP applied compared to normal breathing conditions (control at $\Delta P=0$). The same trend is observed in both state variables since the water vapour concentration at the ASL outer surface is based on the thermodynamic water saturated liquid-vapour equilibrium and depends on the ASL outer temperature exclusively. In addition, a higher reduction is observed in the airflow temperature and water vapour concentration for each PAP applied compared to normal breathing conditions (control at $\Delta P=0$), which is more disparate at higher pressures. Regarding water transfer from the ASL layer to the compressed airflow, the water flux as a function of area and time is significantly greater when the pressure is applied. The mean airway relative humidity is also significantly reduced after PAP application and noticeable at higher pressures. These results can be explained by the fact that under PAP conditions, there is a higher volume inside the respiratory system and the ASL layer, which is the humidifying water source for air conditioning, is reduced as proven in the experimental results. In other words, there is more air to humidify and less water to do it. Hence, it is possible to expect a reduction in humidity and temperature along the respiratory tract under PAP conditions, which proves the inefficiency of the natural air conditioning process under LSD therapy.

Then, to validate the human upper airway PAP model, the results obtained for the normal breathing conditions scenario ($\Delta P=0$) have been compared with previous literature research on human air conditioning process. The results obtained for each pressure condition (5, 10, 15 and 20 cmH2O) have been compared with the experimental results obtained in the two epithelial cell *in-vitro* models, since based on the law of conservation of mass, the ASL layer thickness reduction quantified experimentally corresponds to the amount of water molecules transferred from the ASL layer to the airflow, which is the water flux. Results show no significant differences between the theoretical or experimental water transfer data at each pressure, which corroborates the similarity of the results and validates the model formulated.

Finally the model input variables (inlet airflow temperature and water concentration) have been optimized to approximate the RH and T distribution inside the respiratory tract obtained under the different pressures analysed ($\Delta P \neq 0$) to the normal breathing conditions where no pressure is applied ($\Delta P=0$). Therefore, the quantified and optimized input variables (RH and T) can be used to initially set the LSD convective heat transfer humidifier conditions according to the pressure targeted for each patient. It is important to note that the optimized input variables are between 30 and 32°C and 24 and 29 mg/L (AH) depending on the pressure applied, and the maximum humidity provided by the current commercial convective heated humidifier is 33 mg/L at 32°C, which means that the optimum range is covered by the current commercial devices.

7.4 A proposal for humidifying the inspired gas by using recovered moisture from the expired gas

In chapter 5, a proposal for humidifying the inspired gas by using recovered moisture from the expired airflow, and to achieve the humidity quantified in chapter 4 was developed. To achieve it, the thermo-responsive PNIPAM smart polymer was optimized in order to achieve the maximum amount of water vapour uptake and release it in the shortest time.

Two substrate materials, polyvinyl alcohol (PVA) and organic cotton fabric, have been investigated to achieve the maximum PNIPAM grafting yield. It was shown that the amount of BiB reacted on the PVA substrate was significantly lower compared to the quantity reacted on the cotton fabric. This could be explained by the differences in physical structure of these two substrates. The cotton substrate is a fabric which has more space between the fibres, so the BiB reagent has easier access to react with the OH groups. The PVA has a sponge-like structure, which might have obstructed BiB and hinder its reaction with the OH groups available. Also, the amount of PNIPAM reacted on the PVA substrate was significantly lower compared to the quantity reacted on the cotton fabric in all three methods, as expected due to the fact that lower amount of BiB was reacted on the PVA substrate and there were fewer grafting points available to graft the NIPAM. Finally, the results showed no significant difference between the LCST determined in both PNIPAM-substrates, which was around 32°C as theoretically expected. However, the water vapour release rate from the PNIPAM-PVA samples was significantly lower than the PNIPAM-Cotton samples. This is explained by the fact that, even if the grafted PNIPAM chains have similar molecular weight (around 10 kDa) in both substrates, the number of polymer chains grown from the PVA substrate is significantly lower, seven times less, than that grown from the cotton substrate, so less PNIPAM reacted means less water absorbed and released. Therefore, the cotton fabric substrate was selected to be used in the next experiments because of its high number of BiB sites formed and available for further polymerization.

Next, linear and branched PNIPAM were synthesized in the cotton substrate to compare the final water desorption rate. The results showed that the amount of PNIPAM reacted following the branched method was significantly lower compared to the quantity reacted on the linear synthesis method. This is explained by the fact that side reactions can be generated with high probability, and in this case, a side PNIPAM product could be synthesized with the EBMA by itself instead of growing branches from the substrate. The possible side reactions were not further investigated in this study because this is a path that moves away from the objective set out in this research. The STA results showed no significant difference between the LCST determined in both PNIPAM structures, which is around 32°C as theoretically expected. However, the water vapour release rate from the branched PNIPAM samples was significantly lower than the linear PNIPAM samples, because as discussed before for the PVA substrate, there is less polymer grafted on the substrate and the material absorbs less amount of water vapour. Also, the possible synthesized bulky PNIPAM branches could slow down the conformational change from the linear to the coiled structure, resulting in a lower water release rate [172, 174, 181, 182].

Finally, linear PNIPAM was synthetized on the cotton substrate at low, medium and high molecular weights: below 7 kDa, between 7 and 20 kDa and above 20 kDa respectively. The STA results showed no significant difference between the LCST determined in the three molecular weight PNIPAM samples, which was around 32°C as theoretically expected. However, the water vapour release rate from the low MW and high MW PNIPAM samples were significantly lower than the medium MW PNIPAM samples. This could be explained by the fact that the low MW samples do not have enough PNIPAM grafted so absorbs less water vapour molecules than the medium MW samples, and the high MW PMIPAM samples absorb more water vapour molecules but are not able to release them as fast as the medium MW samples [172, 174, 181, 182]. Therefore, a medium Mw (between 7 and 20 kDa) PNIPAM-Cotton fabric was selected to be tested on human participants because of its optimal thermal performance. Clinical trials are needed in order to validate the performance of the PNIPAM-Cotton fabric and measure the amount of water absorbed from the expiration breath and released to the inspiration flow. This optimized smart material is able to achieve a water vapour release rate of 24.2 %/min, which corresponds to the weight percentage of water vapour released per minute, at a LCST of 32°C. This means that, below 32°C the smart material absorbs the surrounding water vapour molecules and release them when the temperature is higher than 32°C achieving a water vapour release rate up to 24.2 %/min. These results showed no significant differences between the three samples analysed, which proves repeatability of the results.

The molecular weight accuracy and high precision polymerization process are not parameters considered in this chapter. The aim of the research is to develop a miniaturized self-humidifying device able to be manufactured and used in industrial applications. Therefore, the use of specific equipment and accuracy during the polymerization process is avoided in this investigation since it is directly reflected in the manufacturing cost if the product is commercialized.

7.5 Design, Performance and Validation of a Self-Humidifying Device

In chapter 6, a miniaturized, affordable and eco-friendly self-humidifying device using the smart material was designed and developed, and its performance was validated with 21 volunteers in order to prove and measure the efficiency of the device. The requirements of the self-humidifying device performance were: 1) humidify the inspired airflow up to the humidity levels required and determined in chapter 4 by using recovered moisture from expiration, 2) warm the air and 3) adjust the water delivered into the respiratory system. The main application of the self-humidifying device was to provide the humidity required to overcome dryness, a side effect caused by the LSD devices, so the device is used as an additional component of the LSD replacing current convective heated humidifiers and reducing the LSD dimensions. In particular the CPAP device is used as LSD in this investigation.

The main component of the self-humidifying device is the smart material (PNIPAM-Cotton fabric) optimized in chapter 5. The smart fabric was placed lining all the inner surface of a commercial CPAP mask in order to be in contact with the human breath *i.e.* with both inspiration and expiration airflows. Hence, the synthetized fabric was able to absorb surrounding water vapour molecules at temperatures higher than the LCST, set at 32°C, and release them at temperatures below the LCST.

Based on the PNIPAM-Cotton TGA curves obtained in the previous chapter 5, a curve representing the amount of water vapour released from the smart fabric as a function of the temperature applied was developed. Hence, it is possible to adjust the water delivered from the self-humidifying device into the respiratory system with the operation temperature range. The maximum water delivery is achieved with expiration temperatures below 26°C and inspiration flow temperatures above 42°C.

The smart fabric is sewn with an insulated resistor filament to increase the surface temperature and change the polymer properties, since the temperature of the smart fabric is the most important parameter to control the performance of the self-humidifying device. The resistor filament is connected to a relay and power supply using metallic snaps in order to provide the desired current to the system. In use during expiration, the power supply is off and no current is provided to the resistor filament in order to keep the smart material at room temperature, below LCST. Under these conditions PNIPAM-molecules are predominantly hydrophilic and the amide-groups form inter-molecular hydrogen bonds with the surrounding water vapour molecules. Expiration flow is generally at 100% relative humidity and the PNIPAM-Cotton material is moisture saturated and absorbs the maximum number of water molecules from the expiration breath, expelling dry air out of the CPAP mask. Then, when the expiration flow has ended, (after three seconds approximately) and inspiration flow starts, the power supply is switched on passing current though the resistor filament. Depending on the voltage and current provided, the PNIPAM-cotton material is heated up to a temperature above LCST. Under these conditions the hydrophobic isopropyl-methyl groups tend to establish polymer-polymer interactions and the water molecules previously absorbed are released into the inspiration airflow. Fresh air passes through the fabric, the temperature is increased and moisture is added to the incoming air such that warm humid air is provided to the volunteer.

Three scenarios were considered on the clinical experiments. A control measurement was achieved with the CPAP device no humidified at each pressure *i.e*. the volunteer was breathing with the CPAP mask connected to the CPAP device, but without the smart fabric. Then, the performance of the self-humidifying device was measured with the volunteer breathing into the CPAP mask containing the smart fabric and connected to the CPAP device. Finally, a third scenario was considered to validate the humidity provided by the smart fabric at each pressure. Hence, the volunteer was breathing with the CPAP mask, without the smart fabric, connected to the CPAP device with the CPAP humidifier working at level 7 in order to provide the maximum humidity to the respiratory system.

The performance of the smart fabric was analysed in each volunteer under the five CPAP pressures (including the 0 cmH_2O, no pressure) and the three scenarios: no humidification, humidification provided by the smart fabric and humidification provided by the CPAP humidifier at level 7 (maximum humidification).

The results obtained in all the positive pressures analysed, 0, 5, 10, 15 and 20 cmH_2O show that the AH and T provided from the three smart fabric samples were significantly higher than the control and even higher that the theoretical values obtained in chapter 4 (between 30 and 32°C and 24 and 29 mg/L AH depending on the pressure applied). This means that the self-humidifying device is able to warm the air and humidify the inspired airflow up to the humidity levels required by using recovered moisture from expiration and hence overcome the dryness side effect. No significant differences are found between the AH or T obtained from each of the three samples, which proves repeatability of the smart fabric synthesis or manufacturing. Also, no significant differences are found between the humidity and heat provided from any of the three samples and the commercial CPAP humidifier, which proves that the smart fabric is able to provide the same maximum values and is able to replace the current convective heated humidifier and reduce the current LSD dimensions.

The data obtained showed no correlation between the age, height, weight or gender of the 21 volunteers, which means that the performance of the self-humidifying device does not depend on the subject and can be used in any situation and patient with a proper configuration. Also, due to the structure of the smart material, the airflow passes freely through the fabric providing proper ventilation with no increase in flowrate resistance. Hence, the LSD titration positive pressure is not affected by the addition of the self-humidifying device.

The advantages of the self-humidifying device developed in this research work over other water-less humidifiers such us heat and moisture exchangers (HMEs) are that the proposed device is able to warm the air up to 35°C, adjust de amount of water delivered from 0 to 32 mgH_2O/L, achieve the same humidity levels than the provided by the heated convective humidifier and it can be washed and reused.

7.6 Proposed future work

It is believed that the outcomes of this project can be further used in the following:

- In this investigation has been proven that there is an ASL over-evaporation effect which produces dryness on the upper airways. The over-evaporation of the ASL water content is compensated, and hence dryness effect alleviated, with the external humidification provided by the commercial convective heated humidifier or the self-humidifying device. However, it has also been proved that the 10 minutes PAP application produces inflammation on the epithelial cells and reduces the mucus secretion rate. Hence, further investigation is needed to analysed the PAP effect in longer exposure times and in how to alleviate these side effects and palliate the discomfort and unacceptance from the CPAP patients after the therapy.
- It has been proven that the pressure oscillations (PO) can alleviate the decrease in cell permeability, mucus secretion rate, inflammation, cell compression and ASL over-evaporation effect produced by the continuous pressure application (CPAP). Therefore, if funding is available, the effect of PO should be further investigated to develop a prototype able to provide the CPAP coupled with PO and be clinically tested with CPAP patients.
- The viability of the self-humidifying device developed in this research has been successfully proven. This device can be used in a wide range of industrial applications. Hence, a new phase of the project should be started looking at the commercialization of this device, possible applications, new prototyping and clinical testing, manufacturing and cost analysis.

References

[1] Saladin, K.S. (2008). Human Anatomy (Second). New York: McGraw-Hill.

[2] Atsuta, S. and Majima, Y. (1998). Nasal mucociliary clearance of chronic sinusitis in relation to rheological properties of nasal mucus. Rhinology & Laryngology, 107(1), 47-51.

[3] Hayashi, T., Kawakami, M., Sasaki, S., Katsumata, T., Mori, H., Yoshida, H., and Nakahari, T. (2005). ATP regulation of ciliary beat frequency in rat tracheal and distal airway epithelium. Exp Physiol, 90(4), 535-44.

[4] Quraishi, M.S., Jones, N.S., and Mason, J. (1998). The rheology of nasal mucus: a review. Clin Otoloryngol, 23, 403-413.

[5] Silberberg, A. (1982). Rheology of mucus, mucociliary interaction, and ciliary activity. Cell Motility Supplement, 1, 25-28.

[6] Widdicombe, J.H. (2002). Regulation of the depth and composition of airway surface liquid. J Anat, 201, 313-318.

[7] Rogers, D.F. (2007). Physiology of airway mucus secretion and pathophysiology of hypersecretion. Respiratory care, 52(9), 1134-1149.

[8] Gelman, R.A. and Meyer, F.A. (1979). Mucociliary transference rate and mucus viscoelasticity dependence on dynamic storage and loss modulus. Am Rev Respir Dis, 120, 553-557.

[9] Theatre, E., Bours, V., and Oury, C. (2009). A P2X ion channel-triggered NF-kappaB pathway enhances TNF-alpha-induced IL-8 expression in airway epithelial cells. Am J Respir Cell Mol Biol, 41(6), 705-13.

[10] Majima, Y., Harada, T., Shimizu, T., Takeuchi, K., Sakakura, Y., Yasuoka, S., and Yoshinaga, S. (1999). Effect of biochemical components on rheologic properties of nasal mucus in chronic sinusitis. Am J Respir Crit Med, 160, 421-426.

[11] Yeager, H. (1971). Tracheobronchial secretions. Chest, 50, 493-509.

[12] Girod, S., Zahm, J.M., Plotkowski, C., Beck, G., and Puchelle, E. (1992). Role of the physicochemical properties of mucus in the protection of the respiratory epithelium. Eur Respir J, 5, 477-487.

[13] Dulfano, M.J. and Adler, K.B. (1975). Physical properties of sputum VII: Rheologic properties and mucociliary transport. American Review of Respiratory Disease, 112, 341-347.

[14] Horvath, G. and Sorscher, E.J. (2008). Luminal fluid tonicity regulates airway ciliary beating by altering membrane stretch and intracellular calcium. Cell Motil Cytoskeleton, 65(6), 469-75.

[15] Kirkness, J.P., Eastwood, P.R., Szollosi, I., Platt, P.R., Wheatley, J.R., Amis, T.C., and Hillman, D.R. (2003). Effect of surface tension of mucosal lining liquid on upper airway mechanics in anesthetized humans. J Appl Physiol (1985), 95(1), 357-63.

[16] Majima, Y., Hirata, K., Takeuchi, K., Hattori, M., and Sakakura, Y. (1990). Effects of orally administered drugs on dynamic viscoelasticity of human nasal mucus. Am Rev Respir, 141, 79-83.

[17] Verma, M., Seto-Poon, M., Wheatley, J.R., Amis, T.C., and Kirkness, J.P. (2006). Influence of breathing route on upper airway lining liquid surface tension in humans. J Physiol, 574(3), 859-66.

[18] West, J.B. (2013). Pulmonary Pathophysiology: The Essentials (Eighth). USA: Lippincott Williams & Wilkins.

[19] Tsai, W.H. (2003). Obstructive sleep apnea. Canadian Sleep Society, 1.

[20] Tobin, M.J., Birch, S.J., and Sackner, M.A. (1983). Bıathlng Patterns. I: Normal Subjects. Chest, 84(2), 202-205.

[21] Morgenthaler, T.I., Kagramanov, V., Hanak, V., and Decker, P.A. (2006). Complex sleep apnea syndrome: is it a unique clinical syndrome? Sleep, 29(9), 1203–1209.

[22] Ahmed, M.H. and Byrne, C.D. (2010). Obstructive sleep apnea syndrome and fatty liver: Association or causal link? World Journal of Gastroenterology, 16(34), 4243.

[23] Aurora, R.N., Chowdhuri, S., Ramar, K., Bista, S.R., Casey, K.R., Lamm, C.I., Kristo, D.A., Mallea, J.M., Rowley, J.A., Zak, R.S., and Tracy, S.L. (2012). The treatment of central sleep apnea syndromes in adults: practice parameters with an evidence-based literature review and meta-analyses. Sleep, 35(1), 17-40.

[24] Guimaraes, K.C., Drager, L.F., Genta, P.R., Marcondes, B.F., and Lorenzi-Filho, G. (2009). Effects of oropharyngeal exercises on patients with moderate obstructive sleep apnea syndrome. Am J Respir Crit Care Med, 179(10), 962-6.

[25] Martinez-Garcia, M.A., Campos-Rodriguez, F., Soler-Cataluna, J.J., Catalan-Serra, P., Roman-Sanchez, P., and Montserrat, J.M. (2012). Increased incidence of nonfatal cardiovascular events in stroke patients with sleep apnoea: effect of CPAP treatment. Eur Respir J, 39(4), 906-12.

[26] Al-Jumaily, A.M., Mithraratne, P., Gradon, L., and White, D. (2003). Modelling and simulation of a breathing system. ASME, 1-6.

[27] Chan, H., Al-Jumaily, A.M., D'Arcy, A.E., and Makinson, D. (2004). Pressure control for constant pressure masks. Proc Insti Mech Engrs, 218, 1191-1194.

[28] Teschler, H., Berthon-Jones, M., Thompson, A.B., Henkel, A., Henry, J., and Konietzko, N. (1996). Automated continuous positive airway pressure titration for obstructive sleep apnea syndrome. Am J Respir Crit Care Med, 154, 734-740.

[29] Behbehani, K. and Kang, T.H. (1989). A microprocessor-based sleep apnea ventilator. Sleep & Respiration, 2, 332-333.

[30] Vennelle, M., White, S., Riha, R.L., Mackay, T.W., Engleman, H.M., and Douglas, N.J. (2010). Randomized controlled trial of variable-pressure versus fixed-pressure continuous positive airway pressure (CPAP) treatment for patients with obstructive sleep apnea/hypopnea syndrome (OSAHS). Sleep, 33(2), 267-271.

[31] Malik, N.W. and Kenyon, G.S. (2004). Changes in the nasal airway mucosa and in nasal symptoms following continuous positive airway pressure (N-CPAP) for obstructive sleep apnea. Aust J Otolaryng, 7(1), 17-20.

[32] Wolf, M., Naftali, S., Schroter, R.C., and Elad, D. (2004). Air-conditioning characteristics of the human nose. The Journal of Laryngology & Otology, 118, 87–92.

[33] Hanna, L.M. and Scherer, P.W. (1986). A theoretical model of localized heat and water vapor transport in the human respiratory tract. Journal of biomechanical engineering, 108(1), 19-27.

[34] Chouly, F., Van Hirtum, A., Lagrée, P.Y., Pelorson, X., and Payan, Y. (2006). Simulation of the retroglossal fluid-structure interaction during Obstructive Sleep Apnea. Springer-Verlag, 4072, 48–57.

[35] Chouly, F., Van Hirtum, A., Lagrée, P.Y., Pelorson, X., and Payan, Y. (2008). Numerical and experimental study of expiratory flow in the case of major upper airway obstructions with fluid–structure interaction. Journal of Fluids and Structures, 24(2), 250-269.

[36] Elad, D., Wolf, M., and Keck, T. (2008). Air-conditioning in the human nasal cavity. Respiratory physiology & neurobiology, 163(1-3), 121-7.

[37] Mylavarapu, G., Mihaescu, M., Gutmark, E., Murugappan, S., and Kalra, M. (2010). Fluid structure interaction analysis in human upper airways to understand sleep apnea. 48th AIAA Aerospace Sciences Meeting Including the New Horizons Forum and Aerospace Exposition, 1-9.

[38] Mylavarapu, G., Murugappan, S., Mihaescu, M., Kalra, M., Khosla, S., and Gutmark, E. (2009). Validation of computational fluid dynamics methodology used for human upper airway flow simulations. J Biomech, 42(10), 1553-9.

[39] Toremalm, N.G. (1961). Air flow patterns and ciliary activity in the trachea after tracheostomy. Oto-laryng Stockh, 53, 442-454.

[40] Roessler, F., Grossenbacher, R., and Walt, H. (1998). Effects of tracheotomy on human tracheobronchial mucosa: a scanning electron microscopic study. Laryngoscope, 98, 1261-1267.

[41] Brumback, A.C., Lieber, J.L., Angleson, J.K., and Betz, W.J. (2004). Using FM1-43 to study neuropeptide granule dynamics and exocytosis. Methods, 33(4), 287-94.

[42] Bukowy, Z., Zietkiewicz, E., and Witt, M. (2011). In vitro culturing of ciliary respiratory cells - a model for studies of genetic diseases. J Appl Genet, 52(1), 39-51.

[43] Cone, R.A. (2009). Barrier properties of mucus. Adv Drug Deliv Rev, 61(2), 75-85.

[44] Davidovich, N.E., Kloog, Y., Wolf, M., and Elad, D. (2011). Mechanophysical stimulations of mucin secretion in cultures of nasal epithelial cells. Biophys J, 100(12), 2855-64.

[45] Davies, D.J., Ward, R.J., and Heylings, J.R. (2004). Multi-species assessment of electrical resistance as a skin integrity marker for in vitro percutaneous absorption studies. Toxicol In Vitro, 18(3), 351-8.

[46] Even-Tzur, N., Kloog, Y., Wolf, M., and Elad, D. (2008). Mucus secretion and cytoskeletal modifications in cultured nasal epithelial cells exposed to wall shear stresses. Biophys J, 95(6), 2998-3008.

[47] Fulcher, M.L., Gabriel, S., Burns, K.A., Yankaskas, J.R., and Randell, S.H. (2005). Well-Differentiated Human Airway Epithelial Cell Cultures Trans.). Methods in Molecular Medicine: Human Cell Culture Protocols (ed., Vol. 107, pp. 183-206). Totowa, NJ: Humana Press Inc.

[48] Ghadiri, M., Mamlouk, M., Spicer, P., Jarolimek, W., Grau, G.E., Young, P.M., and Traini, D. (2016). Effect of polyunsaturated fatty acids (PUFAs) on airway epithelial cells' tight junction. Pulm Pharmacol Ther, 40, 30-8.

[49] Grainger, C.I., Greenwell, L.L., Lockley, D.J., Martin, G.P., and Forbes, B. (2006). Culture of Calu-3 cells at the air interface provides a representative model of the airway epithelial barrier. Pharm Res, 23(7), 1482-90.

[50] Haghi, M., Young, P.M., Traini, D., Jaiswal, R., Gong, J., and Bebawy, M. (2010). Time- and passage-dependent characteristics of a Calu-3 respiratory epithelial cell model. Drug Dev Ind Pharm, 36(10), 1207-14.

[51] Joo, N.S., Saenz, Y., Krouse, M.E., and Wine, J.J. (2002). Mucus secretion from single submucosal glands of pig. Stimulation by carbachol and vasoactive intestinal peptide. J Biol Chem, 277(31), 28167-75.

[52] Koeppen, M., McNamee, E.N., Brodsky, K.S., Aherne, C.M., Faigle, M., Downey, G.P., Colgan, S.P., Evans, C.M., Schwartz, D.A., and Eltzschig, H.K. (2013). Detrimental role of the airway mucin Muc5ac during ventilator-induced lung injury. Mucosal Immunol, 6(4), 762-75.

[53] Kreda, S.M., Okada, S.F., van Heusden, C.A., O'Neal, W., Gabriel, S., Abdullah, L., Davis, C.W., Boucher, R.C., and Lazarowski, E.R. (2007). Coordinated release of nucleotides and mucin from human airway epithelial Calu-3 cells. J Physiol, 584(Pt 1), 245-59.

[54] Lai, S.K., Wang, Y.Y., Wirtz, D., and Hanes, J. (2009). Micro- and macrorheology of mucus. Adv Drug Deliv Rev, 61(2), 86-100.

[55] Lechanteur, A., das Neves, J., and Sarmento, B. (2018). The role of mucus in cell-based models used to screen mucosal drug delivery. Adv Drug Deliv Rev, 124, 50-63.

[56] Marin, L., Traini, D., Bebawy, M., Colombo, P., Buttini, F., Haghi, M., Ong, H.X., and Young, P. (2013). Multiple dosing of simvastatin inhibits airway mucus production of epithelial cells: implications in the treatment of chronic obstructive airway pathologies. Eur J Pharm Biopharm, 84(3), 566-72.

[57] Pozzoli, M., Ong, H.X., Morgan, L., Sukkar, M., Traini, D., Young, P.M., and Sonvico, F. (2016). Application of RPMI 2650 nasal cell model to a 3D printed apparatus for the testing of drug deposition and permeation of nasal products. Eur J Pharm Biopharm, 107, 223-33.

[58] Shan, J., Huang, J., Liao, J., Robert, R., and Hanrahan, J.W. (2011). Anion secretion by a model epithelium: more lessons from Calu-3. Acta Physiol (Oxf), 202(3), 523-31.

[59] Shumilov, D., Popov, A., Fudala, R., Akopova, I., Gryczynski, I., Borejdo, J., Gryczynski, Z., and Grygorczyk, R. (2014). Real-time imaging of exocytotic mucin release and swelling in Calu-3 cells using acridine orange. Methods, 66(2), 312-24.

[60] Szulcek, R., Bogaard, H.J., and van Nieuw Amerongen, G.P. (2014). Electric cell-substrate impedance sensing for the quantification of endothelial proliferation, barrier function, and motility. J Vis Exp, (85).

[61] Verdugo, P. (2012). Supramolecular dynamics of mucus. Cold Spring Harb Perspect Med, 2(11).

[62] Wine, J.J. and Joo, N.S. (2004). Submucosal glands and airway defense. Proc Am Thorac Soc, 1(1), 47-53.

[63] Xu, Z., Zuo, Y., Wang, J., Yu, Z., Peng, F., Chen, Y., Dong, Y., Hu, X., Zhou, Q., Ma, H., Bao, Y., and Chen, M. (2015). Overexpression of the regulator of G-protein signaling 5 reduces the survival rate and enhances the radiation response of human lung cancer cells. Oncol Rep, 33(6), 2899-907.

[64] Zhu, S., Kato, S., Murakami, S., and Hayashi, T. (2005). Study on inhalation region by means of CFD analysis and experiment. Building and Environment, 40(10), 1329-1336.

[65] Paloc, C., Bello, F., Kitney, R.I., and Darzi, A. (2002). Online Multiresolution Volumetric Mass Spring Model for Real Time Soft Tissue Deformation. Springer Berlin Heidelberg, 2489, 219-226.

[66] Nedel, L.P. and Thalmann, D. (1998). Real Time Muscle Deformations Using Mass-Spring Systems Trans.). In (Ed.),^(Eds.), (ed., Vol. pp. 156-165). Computer Graphics International Proceedings.

[67] Mollemans, W., Schutyser, F., Cleynenbreugel, J.V., and Suetens, P. (2004). Fast Soft Tissue Deformation with Tetrahedral Mass Spring Model for Maxillofacial Surgery Planning Systems. Springer Berlin Heidelberg, 3217, 371-379.

[68] Duysak, A., Zhang, J.J., and Ilankovan, V. (2003). Efficient modelling and simulation of soft tissue deformation using mass-spring systems. International Congress Series, 1256, 337-342.

[69] (2004). Higher versus Lower Positive End-Expiratory Pressures in Patients with the Acute Respiratory Distress Syndrome. New England Journal of Medicine, 351(4), 327-336.

[70] Dreyfuss, D., Basset, G., Soler, P., and Saumon, G. (1985). Intermittent Positive-Pressure Hyperventilation with High Inflation Pressures Produces Pulmonary Microvascular Injury in Rats. American Review of Respiratory Disease, 132(4), 880-884.

[71] Meduri, G.U., Cook, T.R., Turner, R.E., Cohen, M., and Leeper, K.V. (1996). Noninvasive Positive Pressure Ventilation in Status Asthmaticus. Chest, 110(3), 767-774.

[72] Oka, S., Kubota, Y., Yamashiro, T., Ogata, S., Ninomiya, T., Ito, S., and Shirasuna, K. (2005). Effects of Positive Pressure in Odontogenic Keratocysts. Journal of Dental Research, 84(10), 913-918.

[73] Zhu, Y., Chidekel, A., and Shaffer, T.H. (2010). Cultured Human Airway Epithelial Cells (Calu-3): A Model of Human Respiratory Function, Structure, and Inflammatory Responses. Critical Care Research and Practice, 2010, 8.

[74] Daviskas, E., Gonda, I., and Anderson, S.D. (1990). Mathematical modeling of heat and water transport in human respiratory tract. Journal of Applied Physiology, 69(1), 362-372.

[75] Daigle, C.C., Chalupa, D.C., Gibb, F.R., Morrow, P.E., Oberdörster, G., Utell, M.J., and Frampton, M.W. (2003). Ultrafine Particle Deposition in Humans During Rest and Exercise. Inhalation Toxicology, 15(6), 539-552.

[76] Tawhai, M.H. and Hunter, P.J. (2004). Modeling Water Vapor and Heat Transfer in the Normal and the Intubated Airways [journal article]. Annals of Biomedical Engineering, 32(4), 609-622.

[77] Feng, Y., Kleinstreuer, C., Castro, N., and Rostami, A. (2016). Computational transport, phase change and deposition analysis of inhaled multicomponent droplet–vapor mixtures in an idealized human upper lung model. Journal of Aerosol Science, 96, 96-123.

[78] Xi, J., Kim, J., and Si, X.A. (2016). Effects of nostril orientation on airflow dynamics, heat exchange, and particle depositions in human noses. European Journal of Mechanics - B/Fluids, 55, 215-228.

[79] Wu, D., Tawhai, M.H., Hoffman, E.A., and Lin, C.-L. (2014). A Numerical Study of Heat and Water Vapor Transfer in MDCT-Based Human Airway Models. Annals of Biomedical Engineering, 42(10), 2117-2131.

[80] Plowman, L., Lauff, D.C., Berthon-Jones, M., and Sullivan, C.E. (1990). Waking and genioglossus muscle responses to upper airway pressure oscillation in sleeping dogs. J Appl Physiol, 68(6), 2564-2573.

[81] Zhang, S. and Mathew, O.P. (1992). Response of laryngeal mechanoreceptors to high-frequency pressure oscillation. J Appl Physiol, 73(1), 219-223.

[82] Brancatisano, A., Van der Touw, T., O'Neill, N., and Amis, T.C. (1996). Influence of upper airway pressure oscillations on soft palate muscle electromyographic activity. J Appl Physiol, 81(3), 1190-1196.

[83] Eastwood, P.R., Satoh, M., Curran, A.K., Zayas, M.T., Smith, C.A., and Dempsey, J.A. (1999). Inhibition of inspiratory motor output by high-frequency low-pressure oscillations in the upper airway of sleeping dogs. Journal of Physiology, 517(1), 259-271.

[84] Henke, K.G. and Sullivan, C.E. (1993). Effects of high-frequency oscillating pressures on upper airway muscles in humans. J Appl Physiol, 75(2), 856-862.

[85] Badia, R., Farre, R., Rigau, J., Uribe, M.E., Navajas, D., and Monserrat, J.M. (2001). Forced oscillation measurements do not affect upper airway muscle tone or sleep in clinical studies. Eur Respir J, 18, 335-339.

[86] Fogel, R.B., Trinder, J., White, D.P., Malhotra, A., Raneri, J., Schory, K., Kleverlaan, D., and Pierce, R.J. (2005). The effect of sleep onset on upper airway muscle activity in patients with sleep apnoea versus controls. J Physiol, 564(Pt 2), 549-62.

[87] Lo, Y.L., Jordan, A.S., Malhotra, A., Wellman, A., Heinzer, R.A., Eikermann, M., Schory, K., Dover, L., and White, D.P. (2007). Influence of wakefulness on pharyngeal airway muscle activity. Thorax, 62(9), 799-805.

[88] Morrell, M.J., Arabi, Y., Zahn, B.R., Meyer, K.C., Skatrud, J.B., and Safwan Badr, M. (2002). Effect of surfactant on pharyngeal mechanics in sleeping humans: implications for sleep apnoea. European Respiratory Journal, 20(2), 451-457.

[89] Fodil, R., Ribreau, C., Louis, B., Lofaso, F., and Isabey, D. (1997). Interaction between steady flow and individualised compliant segments: Application to upper airways. Medical and Biological Engineering and Computing 35(6), 638-648.

[90] Elliott, N.S.J., Lucey, A.D., Heil, M., Eastwood, P.R., and Hillman, D.R. (2011). Modelling and simulation of fluid-structure interactions in human snoring. 19th International congress on Modeling and Simulation, 530-536.

[91] Chouly, F., Hirtum, A.V., Lagree, P.Y., Paoli, J.R., Pelorson, X., and Payan, Y. (2006). Simulation of the Retroglossal Fluid-Structure Interaction During Obstructive Sleep Apnea. Springer-Verlag Berlin Heidelberg, 4072, 48-57.

[92] Farre, R., Rotger, M., Monserrat, J.M., and Navajas, D. (1997). A system to generate simultaneous forced oscillation and continuous positive airway pressure. Eur Respir J, 10, 1349-1353.

[93] Navajas, D., farre, R., Rotger, M., Badia, R., Puig-de-Morales, M., and Monserrat, J.M. (1998). Assessment of Airflow Obstruction during CPAP by Means of Forced Oscillation in Patients with Sleep Apnea. American Journal of Respiratory and Critical Care Medicine, 157(5), 1526-1530.

[94] Oostveen, E., MacLeod, D., Lorino, H., Farre, R., Hantos, Z., Desager, K., and Marchal, F. (2003). The forced oscillation technique in clinical practice: methodology, recommendations and future developments. European Respiratory Journal, 22(6), 1026-1041.

[95] Pham, Q.T., Bourgkard, E., Chau, N., Willim, G., Megherbi, S.E., Teculescu, D., Bohadana, A., and Bertrand, J.P. (1995). Forced oscillation technique (FOT): a new tool for epidemiology of occupational lung diseases? European Respiratory Journal, 8(8), 1307-1313.

[96] Vanderveken, O.M., Oostveen, E., Boudewyns, A.N., Verbraecken, J.A., Van de Heyning, P.H., and De Backer, W.A. (2005). Quantification of pharyngeal patency in patients with sleep-disordered breathing. ORL J Otorhinolaryngol Relat Spec, 67(3), 168-79.

[97] Randerath, W.J., Schraeder, O., Galetke, W., Feldmeyer, F., and Ruhle, K.H. (2001). Autoadjusting CPAP therapy based on impedance efficacy, compliance and acceptance. Am J Respir Crit Care Med, 163, 652-657.

[98] Ficker, J.H., Clarenbach, C.F., Neukirchner, C., Fuchs, F.S., Wiest, G.H., Schahin, S., Harsch, I.A., and Hahn, E.G. (2003). Auto-CPAP therapy based on the forced oscillation technique. Biomed Technik, 48, 68-72.

[99] Konermann, M., Sanner, B.M., Vyleta, M., Laschewski, F., Groetz, J., Sturm, A., and Zidek, W. (1998). Use of conventional and self-adjusting nasal continuous positive airway pressure for treatment of severe obstructive sleep apnea syndrome. Chest, 113(3), 714-718.

[100] Reinikainen, L.M. and Jaakkola, J.J.K. (2003). Significance of humidity and temperature on skin and upper airway symptoms. Indoor Air, 13, 334-352.

[101] Keck, T., Leiacker, R., Riechelmann, H., and Rettinger, G. (2000). Temperature Profile in the Nasal Cavity. Laryngoscope, 110, 651–654.

[102] Çengel, Y.A. (2007). Transferencia de calor y masa: un enfoque práctico (Third). México, D.F.: McGraw-Hill.

[103] Wiest, G.H., Fuchs, F.S., Brueckl, W.M., Nusko, G., Harsch, I.A., Hahn, E.G., and Ficker, J.H. (2000). In vivo efficacy of heated and non-heated humidifiers during nasal continuous positive airway pressure (nCPAP)-therapy for obstructive sleep apnoea. Respiratory Medicine, 94, 364-368.

[104] Randerath, W.J., Meier, J., Genger, H., Domanski, U., and Ruhle, K.H. (2002). Efficiency of cold passover and heated humidification under continuous positive airway pressure. European Respiratory Journal, 20(1), 183-186.

[105] Wiest, G.H., Foerst, J., Fuchs, F.S., Schmelzer, A.H., Hahn, E.G., and Ficker, J.H. (2001). In vivo efficacy of two heated humidifiers used during CPAP-therapy for obstructive sleep apnea under various environmental conditions. Sleep, 24(4), 435-440.

[106] Martins de Araújo, M.T., Vieira, S.B., Vasquez, E.C., and Fleury, B. (2000). Heated humidification or face mask to prevent upper airway dryness during continuous positive airway pressure therapy. Chest, 117(1), 142-147.

[107] Carter, B.G., Whittington, N., Hochmann, M., and Osborne, A. (2002). The effect of inlet gas temperatures on heated humidifier performance. Journal of Aerosol Medicine, 15(1), 7-13.

[108] Todd, D.A., Boyd, J., Lloyd, J., and John, E. (2001). Inspired gas humidity during mechanical ventilation: Effects of humidification chamber, Airway temperature prove and Environmental conditions. J Peadiatr: Child Health, 37, 489-494.

[109] British Standards Institution. (1970). Specifications for humidifiers for use with breathing machines (BS 4494). London: The institution.

[110] American National Standards Institute. (1979). American national standards for humidifiers and nebulizers for medical use. (ANSI Z79.9-179). New York: The institute.

[111] Wiest, G.H., Harsch, I.A., Fuchs, F.S., Kitzbichler, S., Bogner, K., Brueckl, W.M., Hahn, E.G., and Ficker, J.H. (2002). Initiation of CPAP Therapy for OSA: Does Prophylactic Humidification during CPAP Pressure Titration Improve Initial Patient Acceptance and Comfort? Respiration, 69, 406–412.

[112] Alluri, H.K., Ronda, S.R., Settalluri, V.S., Bondili, J.S., Suryanarayana, V., and Venkateshwar, P. (2007). Biosorption: An eco-friendly alternative for heavy metal removal. African Journal of Biotechnology, 6(25), 2924-2931.

[113] Bedane, A.H., Huang, Q., Xiao, H., and Eić, M. (2012). Mass transfer of water vapor, carbon dioxide and oxygen on modified cellulose fiber-based materials. Nordic Pulp and Paper Research Journal, 27(2), 409-417.

[114] Fraga-Dubreuil, J., Famelart, M., and Bazureau, J.P. (2002). Ecofriendly fast synthesis of hydrophilic Poly(ethyleneglycol)-Ionic liquid matrices for liquid-phase organic synthesis. Organic Process Research & Development, 6, 374-378.

[115] G. Ingale, A. (2013). Biogenic Synthesis of Nanoparticles and Potential Applications: An Eco- Friendly Approach. Journal of Nanomedicine & Nanotechnology, 04(02).

[116] Gontard, N., Thibault, R., Cuq, B., and Guilbert, S. (1996). Influence of relative humidity and film composition on oxygen and carbon dioxide permeabilities of edible films. J. Agric. Food Chem., 44(4), 1064-1069.

[117] Mujica-Paz, H. and Gontard, N. (1997). Oxygen and carbon dioxide permeability of wheat gluten film: Effect of relative humidity and temperature. J. Agric. Food Chem., 45, 4101-4105.

[118] Liu, S., Zhou, L., Wang, P., Zhang, L., Shao, Z., and Yi, B. (2012). Poly(ether sulfone)–sulfonated poly(ether ether ketone) blend ultrafiltration/nanofiltration-based proton-conductive membranes with improved performance for H2/Cl2 fuel cell application. Journal of Materials Chemistry, 22(38), 20512.

[119] Wang, H., Wang, E., Liu, Z., Gao, D., Yuan, R., Sun, L., and Zhu, Y. (2015). A novel carbon nanotubes reinforced superhydrophobic and superoleophilic polyurethane sponge for selective oil–water separation through a chemical fabrication. Journal of Materials Chemistry A, 3, 266–273.

[120] Lynden-Bell, R.M. and Rasaiah, J.C. (1997). From hydrophobic to hydrophilic behaviour: A simulation study of solvation entropy and free energy of simple solutes. J. Chem. Phys, 107(6), 1981-1991.

[121] Nguyen, D.D., Tai, N.-H., Lee, S.-B., and Kuo, W.-S. (2012). Superhydrophobic and superoleophilic properties of graphene-based sponges fabricated using a facile dip coating method. Energy & Environmental Science, 5(7), 7908.

[122] Oh, K.T., Bronich, T.K., and Kabanov, A.V. (2004). Micellar formulations for drug delivery based on mixtures of hydrophobic and hydrophilic Pluronic® block copolymers. Journal of Controlled Release, 94(2-3), 411-422.

[123] Srinivasa, P.C. and Tharanathan, R.N. (2007). Chitin/Chitosan — Safe, Ecofriendly Packaging Materials with Multiple Potential Uses. Food Reviews International, 23(1), 53-72.

[124] Islam, M.R., Xue, X., Mao, S., Zhao, X., Eneji, A.E., and Hu, Y. (2011). Superabsorbent polymers (SAP) enhance efficient and eco-friendly production of corn (Zea mays L.) in drought affected areas of northern China. African Journal of Biotechnology, 10(24), 4887-4894.

[125] Lin, N., Bruzzese, C., and Dufresne, A. (2012). TEMPO-oxidized nanocellulose participating as crosslinking aid for alginate-based sponges. ACS Appl Mater Interfaces, 4(9), 4948-59.

[126] Yadav, M., Rhee, K.Y., Jung, I.H., and Park, S.J. (2013). Eco-friendly synthesis, characterization and properties of a sodium carboxymethyl cellulose/graphene oxide nanocomposite film. Cellulose, 20(2), 687-698.

[127] DeMerlis, C.C. and Schoneker, D.R. (2003). Review of the oral toxicity of polyvinyl alcohol (PVA). Elsevier Science, 41, 319–326.

[128] Karimi, A., Navidbakhsh, M., and Faghihi, S. (2014). Fabrication and mechanical characterization of a polyvinyl alcohol sponge for tissue engineering applications. Perfusion, 29(3), 231-7.

[129] Paradossi, G., Cavalieri, F., Chiessi, E., Spagnoli, C., and Cowman, M.K. (2003). Ply(vinyl alcohol) as versatile biomaterial for potential biomedical applications. Journal of Materials Science: Materials in Medicine, 14, 687-691.

[130] Ramaraj, B. and Poomalai, P. (2006). Ecofriendly poly(vinyl alcohol) and coconut shell powder composite films: Physico-mechanical, thermal

properties, and swelling studies. Journal of Applied Polymer Science, 102(4), 3862-3867.

[131] Karimi, A., Navidbakhsh, M., and Haghi, A.M. (2014). An Experimental Study on the Structural and Mechanical Properties of Polyvinyl Alcohol Sponge Using Different Stress-Strain Definitions. Advances in Polymer Technology, 33(S1), n/a-n/a.

[132] Wang, Y., Chang, C., and Zhang, L. (2009). Effects of Freezing/Thawing Cycles and Cellulose Nanowhiskers on Structure and Properties of Biocompatible Starch/PVA Sponges. Macromolecular Materials and Engineering, NA-NA.

[133] Choi, S.M., Singh, D., Kumar, A., Oh, T.H., Cho, Y.W., and Han, S.S. (2013). Porous Three-Dimensional PVA/Gelatin Sponge for Skin Tissue Engineering. International Journal of Polymeric Materials, 62(7), 384-389.

[134] Matanović, M.R., Kristl, J., and Grabnar, P.A. (2014). Thermoresponsive polymers: Insights into decisive hydrogel characteristics, mechanisms of gelation, and promising biomedical applications. International Journal of Pharmaceutics, 472(1), 262-275.

[135] Guilherme, M.R., Silva, R., Girotto, E.M., Rubira, A.F., and Muniz, E.C. (2003). Hydrogels based on PAAm network with PNIPAAm included: hydrophilic–hydrophobic transition measured by the partition of Orange II and Methylene Blue in water. Polymer, 44(15), 4213-4219.

[136] Kuckling, D., Harmon, M.E., and Frank, C.W. (2002). Photo-Cross-Linkable PNIPAAm Copolymers. 1: Synthesis and characterization of constrained temperature-responsive hydrogel layers. Macromolecules, 35, 6377-6383.

[137] Tomer, N., Mondal, S., Wandera, D., Wickramasinghe, S.R., and Husson, S.M. (2009). Modification of Nanofiltration Membranes by Surface-Initiated Atom Transfer Radical Polymerization for Produced Water Filtration. Separation Science and Technology, 44(14), 3346-3368.

[138] Wandera, D., Himstedt, H.H., Marroquin, M., Wickramasinghe, S.R., and Husson, S.M. (2012). Modification of ultrafiltration membranes with block copolymer nanolayers for produced water treatment: The roles of polymer chain density and polymerization time on performance. Journal of Membrane Science, 403-404, 250-260.

[139] Wandera, D., Wickramasinghe, S.R., and Husson, S.M. (2011). Modification and characterization of ultrafiltration membranes for treatment of produced water. Journal of Membrane Science, 373(1-2), 178-188.

[140] Yang, H., Zhu, H., Hendrix, M.M., Lousberg, N.J., de With, G., Esteves, A.C., and Xin, J.H. (2013). Temperature-triggered collection and release of water from fogs by a sponge-like cotton fabric. Adv Mater, 25(8), 1150-4, 1149.

[141] Lock, J.Y., Carlson, T.L., and Carrier, R.L. (2018). Mucus models to evaluate the diffusion of drugs and particles. Advanced Drug Delivery Reviews, 124, 34-49.

[142] Srinivasan, B., Kolli, A.R., Esch, M.B., Abaci, H.E., Shuler, M.L., and Hickman, J.J. (2015). TEER Measurement Techniques for In Vitro Barrier Model Systems. Journal of Laboratory Automation, 20(2), 107-126.

[143] Wegener, J., Hakvoort, A., and Galla, H.-J. (2000). Barrier function of porcine choroid plexus epithelial cells is modulated by cAMP-dependent pathways in vitro. Brain Research, 853(1), 115-124.

[144] Lo, C.-M., Keese, C.R., and Giaever, I. (1999). Cell–Substrate Contact: Another Factor May Influence Transepithelial Electrical Resistance of Cell Layers Cultured on Permeable Filters. Experimental Cell Research, 250(2), 576-580.

[145] Berger, J.T., Voynow, J.A., Peters, K.W., and Rose, M.C. (1999). Respiratory Carcinoma Cell Lines. American Journal of Respiratory Cell and Molecular Biology, 20(3), 500-510.

[146] Tanaka, T., Narazaki, M., and Kishimoto, T. (2014). IL-6 in Inflammation, Immunity, and Disease. Cold Spring Harb Perspect Biol, 6(10).

[147] Donnelly, S.C., Haslett, C., Strieter, R.M., Kunkel, S.L., Walz, A., Robertson, C.R., Carter, D.C., Pollok, A.J., and Grant, I.S. (1993). Interleukin-8 and development of adult respiratory distress syndrome in at-risk patient groups. The Lancet, 341(8846), 643-647.

[148] Keatings, V.M., Collins, P.D., Scott, D.M., and Barnes, P.J. (1996). Differences in interleukin-8 and tumor necrosis factor-alpha in induced sputum from patients with chronic obstructive pulmonary disease or asthma. American Journal of Respiratory and Critical Care Medicine, 153(2), 530-534.

[149] Dong, W., Matsuno, Y.-k., and Kameyama, A. (2012). A Procedure for Alcian Blue Staining of Mucins on Polyvinylidene Difluoride Membranes. Analytical Chemistry, 84(20), 8461-8466.

[150] Multivariate Analysis Trans.). The Blackwell Encyclopedia of Sociology (ed., Vol. pp.).

[151] Hanna, A.R.G., Rao, C., and Athanasiou, T. (2010). Graphs in Statistical Analysis Trans.) [Hanna2010]. Key Topics in Surgical Research and Methodology (ed., Vol. pp. 441-475). Berlin, Heidelberg: Springer Berlin Heidelberg.

[152] Miller, T.L., Altman, A.R., Tsuda, T., and Shaffer, T.H. (2007). An ultrasound imaging method for in vivo tracheal bulk and Young's moduli of elasticity. Journal of Biomechanics, 40(7), 1615-1621.

[153] Wang, J.-Y., Mesquida, P., Pallai, P., Corrigan, C.J., and Lee, T.H. (2011). Dynamic Properties of Human Bronchial Airway Tissues. ArXiv e-prints. Advance online publication. Retrieved from https://ui.adsabs.harvard.edu/#abs/2011arXiv1111.5645W

[154] Yu, K.N., Lau, B.M.F., and Nikezic, D. (2006). Assessment of environmental radon hazard using human respiratory tract models. Journal of Hazardous Materials, 132(1), 98-110.

[155] The, anatomy, and body. (2018). The upper respiratory tract Trans.). In (Ed.),^(Eds.), (ed., Vol. pp.).

[156] Okamoto-Mizuno, K. and Mizuno, K. (2012). Effects of thermal environment on sleep and circadian rhythm [journal article]. Journal of Physiological Anthropology, 31(1), 14.

[157] Fisher, and, Paykel, and Healthcare. (2012). Icon ™ + Novo: Use and Care Manual. Auckland, NZ.

[158] Lin, Z. and Deng, S. (2008). A study on the thermal comfort in sleeping environments in the subtropics—Developing a thermal comfort model for sleeping environments. Building and Environment, 43(1), 70-81.

[159] McFadden, E.R., Pichurko, B.M., Bowman, H.F., Ingenito, E., Burns, S., Dowling, N., and Solway, J. (1985). Thermal mapping of the airways in humans. Journal of Applied Physiology, 58(2), 564-570.

[160] Lima, L.H., Morales, Y., and Cabral, T. (2016). Ocular Biocompatibility of Poly-N-Isopropylacrylamide (pNIPAM). Journal of Ophthalmology, 2016, 6.

[161] Cooperstein, M.A. and Canavan, H.E. (2013). Assessment of cytotoxicity of (N-isopropyl acrylamide) and Poly(N-isopropyl acrylamide)-coated surfaces. Biointerphases, 8(1), 19.

[162] Patenaude, M. and Hoare, T. (2012). Injectable, Degradable Thermoresponsive Poly(N-isopropylacrylamide) Hydrogels. ACS Macro Letters, 1(3), 409-413.

[163] Sun, S. and Wu, P. (2011). Tailoring the morphology of branched poly(N-isopropylacrylamide) via self-condensing atom-transfer radical copolymerization and its unique self-assembly behavior in alcohol. Soft Matter, 7(16), 7526.

[164] Wandera, D., Wickramasinghe, S.R., and Husson, S.M. (2010). Stimuli-responsive membranes. Journal of Membrane Science, 357(1-2), 6-35.

[165] Qiu, J., Charleux, B., and Matyjaszewski, K. (2001). Controlled/living radical polymerization in aqueous media: homogeneous and heterogeneous systems. Progress in Polymer Science, 26(10), 2083-2134.

[166] Matyjaszewski, K. and Müller, A.H.E. (2006). 50 years of living polymerization. Progress in Polymer Science, 31(12), 1039-1040.

[167] Pintauer, T. and Matyjaszewski, K. (2005). Structural aspects of copper catalyzed atom transfer radical polymerization. Coordination Chemistry Reviews, 249(11), 1155-1184.

[168] Ran, J., Wu, L., Zhang, Z., and Xu, T. (2014). Atom transfer radical polymerization (ATRP): A versatile and forceful tool for functional membranes. Progress in Polymer Science, 39(1), 124-144.

[169] Trivedi, M.K., Nayak, G., Patil, S., Tallapragada, R.M., and Mishra, R. (2015). Impact of Biofield Treatment on Chemical and Thermal Properties of Cellulose and Cellulose Acetate. Journal of Bioengineering & Biomedical Science, 5(3).

[170] Szcześniak, L., Rachocki, A., and Tritt-Goc, J. (2008). Glass transition temperature and thermal decomposition of cellulose powder [journal article]. Cellulose, 15(3), 445-451.

[171] Lai, E.-P., Wang, Y.-X., Wei, Y., and Li, G. (2016). Preparation of Uniform-Sized and Dual Stimuli-Responsive Microspheres of Poly(N-Isopropylacrylamide)/Poly(Acrylic acid) with Semi-IPN Structure by One-Step Method. Polymers, 8(3), 90.

[172] Carter S., Hunt B., and S., R. (2005). Highly Branched Poly(N-isopropylacrylamide)s with Imidazole End Groups Prepared by Radical Polymerization in the Presence of a Styryl Monomer Containing a Dithioester Group. Macromolecules, 38, 4595-4603.

[173] Tao, W. and Yan, L. (2010). Thermogelling of highly branched poly(N-isopropylacrylamide). Journal of Applied Polymer Science, 118(6), 3391-3399.

[174] Xu, J., Ye, J., and Liu, S. (2007). Synthesis of Well-Defined Cyclic Poly(N-isopropylacrylamide) via Click Chemistry and Its Unique Thermal Phase Transition Behavior. Macromolecules, 40(25), 9103-9110.

[175] Matyjaszewski, K., Gaynor, S.G., Kulfan, A., and Podwika, M. (1997). Preparation of Hyperbranched Polyacrylates by Atom Transfer Radical Polymerization. 1. Acrylic AB* Monomers in “Living” Radical Polymerizations. Macromolecules, 30(17), 5192-5194.

[176] Hore, P.J. (2015). Nuclear Magnetic Resonance. UK: Oxford University Press.

[177] Beattie, D.A., Addai-Mensah, J., Beaussart, A., Franksb, G.V., and Yeap, K.-Y. (2014). In situ particle film ATR FTIR spectroscopy of poly (N-isopropyl acrylamide) (PNIPAM) adsorption onto talc. Phys. Chem. Chem. Phys., 16, 25143--25151.

[178] Goldstein, J.I., Newbury, D.E., Michael, J.R., Ritchie, N.W.M., Scott, J.H.J., and Joy, D.C. (2017). Scanning Electron Microscapy and X-Ray Microanalysis. USA: Springer.

[179] Van Humbeeck, J. (1998). Chapter 11 - Simultaneous Thermal Analysis. In M. E. Brown Trans.). Handbook of Thermal Analysis and Calorimetry (ed., Vol. 1, pp. 497-508). Elsevier Science.

[180] Yang, H., Esteves, A.C.C., Zhu, H., Wang, D., and Xin, J.H. (2012). In-situ study of the structure and dynamics of thermo-responsive PNIPAAm grafted on a cotton fabric. Polymer, 53(16), 3577-3586.

[181] Plunkett, K.N., Zhu, X., Moore, J.S., and Leckband, D.E. (2006). PNIPAM Chain Collapse Depends on the Molecular Weight and Grafting Density. Langmuir, 22(9), 4259-4266.

[182] Zhu, X., Yan, C., Winnik, F.M., and Leckband, D. (2007). End-Grafted Low-Molecular-Weight PNIPAM Does Not Collapse above the LCST. Langmuir, 23(1), 162-169.

[183] Gómez, F., Guzmán, J.I., and Tilton, J.E. (2007). Copper recycling and scrap availability. Resources Policy, 32(4), 183-190.

[184] Olson, W.H. (2008). Electrical Safety Trans.). Medical Instrumentation Application and Design (Fourth ed., Vol. pp.). USA: John Wiley & Sons.

Appendix A

Ethical Approval

3 May 2018

Ahmed Al Jumaily

Faculty of Design and Creative Technologies

Dear Ahmed

Re Ethics Application: **18/139 An investigation into the upper airway humidification**

Thank you for providing evidence as requested, which satisfies the points raised by the Auckland University of Technology Ethics Committee (AUTEC).

Your ethics application has been approved for three years until 3 May 2021.

Standard Conditions of Approval

1. A progress report is due annually on the anniversary of the approval date, using form EA2, which is available online through http://www.aut.ac.nz/researchethics.
2. A final report is due at the expiration of the approval period, or, upon completion of project, using form EA3, which is available online through http://www.aut.ac.nz/researchethics.
3. Any amendments to the project must be approved by AUTEC prior to being implemented. Amendments can be requested using the EA2 form: http://www.aut.ac.nz/researchethics.
4. Any serious or unexpected adverse events must be reported to AUTEC Secretariat as a matter of priority.
5. Any unforeseen events that might affect continued ethical acceptability of the project should also be reported to the AUTEC Secretariat as a matter of priority.

Please quote the application number and title on all future correspondence related to this project.

AUTEC grants ethical approval only. If you require management approval for access for your research from another institution or organisation then you are responsible for obtaining it. You are reminded that it is your responsibility to ensure that the spelling and grammar of documents being provided to participants or external organisations is of a high standard.

For any enquiries, please contact ethics@aut.ac.nz

Yours sincerely,

Kate O'Connor
Executive Manager
Auckland University of Technology Ethics Committee

Cc: sgraubar@aut.ac.nz

Appendix B

Participant Information Sheet

Date Information Sheet Produced:

2 May 2018

Project Title

An investigation into the upper airway humidification

An Invitation

My name is Sandra Grau Bartual. I hold a Master of Science degree in Chemical Engineering and a Master of Science degree in Materials and Process Technology. I am doing this research as part of the Doctor of Philosophy degree in Biomedical Engineering at Auckland University of Technology (AUT).

The analysis of the airflow temperature and relative humidity inside a commercial CPAP mask is needed to test a modified cotton fabric able to maximize the hydrophilic/hydrophobic properties of the natural fibres.

This Participant information Sheet is sent to you to provide further detailed information and to invite you to participate in this research. If you are a healthy volunteer without cardiovascular or respiratory problems, and interested in participating in this research, please contact the primary researcher, Sandra Grau Bartual, *sandra.graubartual@aut.ac.nz* or 921999 ext. 8617.

This participation is voluntary, and any participant may withdraw at any time prior to the completion of data collection without being disadvantaged in any way.

What is the purpose of this research?

CPAP (Continuous Positive Airway Pressure) system helps provide breathing support to patients with Obstructive Sleep Apnoea (OSA). This is a sleeping disorder, which affects millions of people worldwide. CPAP system provides and transfers a continuous positive air pressure to the nose and/or mouth to prevent the airways from obstruction or collapse. However, the existing CPAP system has some deficiencies, for example, there has been a lot of rejection by patients of CPAP devices due to the humidifier size and the discomfort of the therapy.

This research focuses on analysing the airflow temperature and relative humidity inside a commercial CPAP mask (Fig. 1) in order to reduce the discomfort reported by CPAP patients. A harmless and eco-friendly modified cotton fabric (Fig. 2) able to maximize the water absorption/desorption properties of the natural fibres covers the inner part of a commercial CPAP mask, not in contact with the skin, to regulate the airflow water vapour content generated by the commercial CPAP device and the breathing cycle. The temperature inside the mask will range from 22°C to 37°C (same harmless range of temperature than the provided by a commercial CPAP device) to control the fabric properties. The airflow temperature and relative humidity will be measured with a commercial sensor (Fig. 3) placed inside the commercial CPAP mask (not in contact with the skin or fabric).

The research will result in the publication of a thesis, as well as research papers that will be published in international journals and refereed conference proceedings.

Fig. 1 Commercial CPAP mask from Fisher and Paykel healthcare.

Fig. 2 Modified cotton fabric.

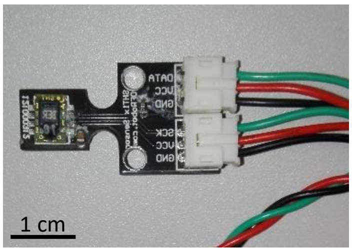

Fig. 3 Commercial temperature and humidity sensor from Sensirion.

How was I identified and why am I being invited to participate in this research?

You are being invited to participate in this study because you have shown interest in participating in this research upon answer the advertisement.

Only healthy volunteers are invited to participate in this study, people with cardiovascular or respiratory problems and unable to wear a mask will be excluded from the study.

How do I agree to participate in this research?

After reading this Participant Information Sheet, if you agree to participate in the study, please contact the primary researcher (PhD student Sandra Grau Bartual) by email or phone call. Then we will discuss a convenience meeting time in order to proceed with the consent form first and then the questionnaire and data collection.

Your participation in this research is voluntary (it is your choice) and whether or not you choose to participate will neither advantage nor disadvantage you. You are able to withdraw from the study at any time. If you choose to withdraw from the study, then you will be offered the choice between having any data that is identifiable as belonging to you removed or allowing it to continue to be used. However, once the findings have been produced, removal of your data may not be possible.

What will happen in this research?

At the meeting time, we will discuss any doubts or questions regarding the study and if everything is clear you will sign the consent form, complete the basic questionnaire and proceed with the data collection.

You will be invited to seat and wear a CPAP mask containing the fabric and the relative humidity and temperature sensor and breathe normally for 10 minutes. The mask will be connected to a CPAP device, which will provide room pressurized air at 0, 5, 10, 15 and 20 cmH2O (2 minutes at each pressure). Humidity and temperature will be collected continuously every second during the 10 minutes that the experiment takes.

I will instruct you on how to carry out the test, but briefly, you have to breathe normally and relax while the data is collected without any effort, contact or interaction. Finally, the data obtained will be analysed using suitable computer software at the Institute of Biomedical Technologies (IBTec).

What are the discomforts and risks?

An otolaryngologist expert in CPAP therapy has been consulted to verify that the study is completely harmless. Therefore, you will not experience discomfort or embarrassment using the test. However, not all people find breathing masks comfortable due to the flow rate applied. In this case, if you find it uncomfortable, you will be able to remove the mask easily at any time and the test will be stopped immediately.

What are the benefits?

This research aims to analyse the validity of the modified cotton fabric to reduce the discomfort of CPAP patients. If the results are successful, a new CPAP device will be proposed and developed using the modified cotton, which will result in a more comfortable CPAP therapy. Therefore, there are no direct benefits for you.

In addition, I may obtain a degree as a results of the research, which will result in the publication of a thesis, as well as research papers that will be published in international journals and refereed conference proceedings.

How will my privacy be protected?

The meeting to proceed with the consent form, questionnaire and data collection will be private and confidential. Also, you will not be identified in the final report, only aggregate data will be reported in such a form that no individuals or groups can be identified from it.

What are the costs of participating in this research?

At the meeting time, you will have 5 to 10 minutes to read, sign and discuss the consent form and the questionnaire, and another 10 minutes are required to collect the data. Therefore, you will give 15 to 20 minutes to the project.

What opportunity do I have to consider this invitation?

After receiving this Participant Information Sheet, you will have one week to decide your participation in the study. Then, if you agree to proceed, a mutually agreeable time will be arranged for the study to be undertaken.

Will I receive feedback on the results of this research?

Yes, you will be informed verbally about the results obtained once your data collection is finished.

What do I do if I have concerns about this research?

Any concerns regarding the nature of this project should be notified in the first instance to the Project Supervisor, Prof Ahmed Al-Jumaily, *ahmed.al-jumaily@aut.ac.nz,* 921 9999 ext 9777.

Concerns regarding the conduct of the research should be notified to the Executive Secretary of AUTEC, Kate O'Connor, *ethics@aut.ac.nz* , 921 9999 ext 6038.

Whom do I contact for further information about this research?

Please keep this Information Sheet and a copy of the Consent Form for your future reference. You are also able to contact the research team as follows:

Researcher Contact Details:

Name: Sandra Grau Bartual

Email: sandra.graubartual@aut.ac.nz

Phone: 9219999 ext. 8617

Project Supervisor Contact Details:

Name: Prof Ahmed Al-Jumaily

Email: ahmed.al-jumaily@aut.ac.nz

Phone: 9219999 ext. 9777

Appendix C

Consent Form

Project title:	An investigation into the upper airway humidification
Project Supervisor:	Prof Ahmed Al-Jumaily
Researcher:	Sandra Grau Bartual

- ○ I have read and understood the information provided about this research project in the Information Sheet dated 11 April 2018.
- ○ I have had an opportunity to ask questions and to have them answered.
- ○ I understand that taking part in this study is voluntary (my choice) and that I may withdraw from the study at any time without being disadvantaged in any way.
- ○ I understand that if I withdraw from the study then I will be offered the choice between having any data that is identifiable as belonging to me removed or allowing it to continue to be used. However, once the findings have been produced, removal of my data may not be possible.
- ○ I do not have cardiovascular or respiratory problems such as sleep apnoea.
- ○ I agree to take part in this research.
- ○ I am aware that the data collected for this project will be maintained for a period of 10 years.
- ○ I am aware that the data collected from this project may be used in journal and conference publications of this research. A summary of this activity and global findings may be given on the Institute of Biomedical Technologies website, *<u>www.aut .ac.nz/ibtec/</u>* in an anonymous form to overview the research work being undertaken within the institute.

Participant's number:...

Paticipant's signature:...

Participant's name:..

Date:

Appendix D

Questionnaire

Project title: An investigation into the upper airway humidification

Project Supervisor: Prof Ahmed Al-Jumaily

Researcher: Sandra Grau Bartual

- Age: ……………………………..
- Gender: ……………………………..
- Height (Approx): ……………………………..
- Weight (Approx): ……………………………..

Participant's number:...……………………………………

Paticipant's signature:..……………………………………

Participant's name:......................……………………………………………………………

Date:

Appendix E

External consultation Letter

Jim Bartley
Ear Nose & Throat Surgeon

ENT Auckland Ltd.
10 Owens Rd, Epsom, Auckland.
Tel: 0-9-631 0475 Fax: 0-9-631 0478

27th March 2018

AUT Ethics Committee
Auckland University of Technology
Auckland New Zealand.

To whom it may concern

The pressure required by most patients with obstructive sleep apnoea using CPAP machines ranges between 5 and 15 cm H_2O. A typical CPAP machine can deliver pressures up to 20 cm H_2O. More specialised CPAP units can deliver up to 30 cm H_2O. Pressures this high are used in some patients with obstructive sleep apnoea. There will be no harm in using a CPAP device pressure up to 20 cm H_2O for less than 5 minutes in healthy people who do not have obstructive sleep apnoea.

Kind regards
Yours sincerely

J Bartley

Jim Bartley *FPMANZCA, FRACS*
Otolaryngologist
Honorary Associate Professor University of Auckland
[HealthLink EDI: entauckl]

Appendix F

Matlab Model Code

```
%Initial Conditions

CA0 = [5.549E-07 5.549E-07 5.549E-07 5.549E-07 5.549E-07 5.549E-07
5.549E-07 5.549E-07 5.549E-07 5.549E-07]; % mol/cm3 - room absolute
humidity 10mg/L (50% rH) - 10mg/L * 1g/1000mg * 1L/1000cm3 *
1mol/18.02g
TM0 = [303.15 303.15 303.15 303.15 303.15 303.15 303.15 303.15
303.15 303.15]; % K
TA0 = [295.15 295.15 295.15 295.15 295.15 295.15 295.15 295.15
295.15 295.15]; % K - room temperature

Y0 = [CA0; TM0; TA0];

%Call fsolve
fhandle = @P5_Equations;
Y = fsolve(fhandle,Y0);

%Display answers
disp(Y)


function F = P5_Equations(Y)
%Geometry data
L = [2.0 4.0 4.0 1.4 1.9 2.3 2.1 1.1 2.7 2.8]; %cm
De = [1.5 1.2 0.6525 2.0 1.2 2.55 2.4 1.1 1.8 2.1]; %cm
D = De+0.000663961; %cm
xL = [L(1) sum(L(1:2)) sum(L(1:3)) sum(L(1:4)) sum(L(1:5))
sum(L(1:6)) sum(L(1:7)) sum(L(1:8)) sum(L(1:9)) sum(L(1:10))];

Q = 241.25; %cm3/s (6L/min)
y = 0.006168019; %cm (500um ASL layer height)
P = 101325+490.3325; %Pa
rho = 0.00112; %g/cm3 (dry air at 300K)

Cpa = 0.2592; %cal/gK (dry air at 300K)
Cpw = 1; %cal/gK (liquid water at 300K)
Mw = 18.016; %g/mol
kw = 0.00144; %cal/cmsK (liquid water conductivity at 300K)
hfg = 578.4; %cal/g (evaporation heat of water)

mu = 1.846e-4; %g/cms (dry air dynamic viscosity at 300K)
vv = mu/rho; %cm2/s (dry air kinematic viscosity at 300K)
a = 0.2207; %cm2/s (dry air diffusivity at 300K)
ka = 6.432e-5; %cal/scmK (dry air thermal conductivity)
```

```
Pr = vv/a; %Prantld Number

for i=1
% OUTPUT: Name our 3 unknowns vector Y

CA(i) = Y(1,i);
TM(i) = Y(2,i);
TA(i) = Y(3,i);

A(i) = pi*(D(i)/2)^2; %cm2
v(i) = Q/A(i); %cm/s

Di = 0.27; % cm2/s (diffusivity of water in air at 300K)
%Di1 = exp(log(0.177)+0.41*log(v1)); % cm2/s (diffusivity
Daviskas1990 Appendix C)
Re(i)= rho*v(i)*D(i)/mu; %Reynolds Number
Sc = vv/Di; %Schmith Number
%Nu(i) = 0.0886*(Re(i)^0.681)*(Pr^0.33); %Nusselt Number
%Sh(i) = 0.0886*(Re(i)^0.681)*(Sc^0.33); %Sherwood Number
Nu(i) = 3.504*(Re(i)*(D(i)/D(9)))^0.277; %Nusselt Number
Sh(i) = 3.652*(Re(i)*(D(i)/D(9)))^0.268; %Sherwood Number

kc(i) = Sh(i)*Di/D(i); %mass transfer coefficient
hc(i) = Nu(i)*ka/D(i); %heat transfer coefficient
%hc1 = 0.0024

TB(i) = (32+273.15)+0.33*(xL(i)); %K
CAi = 1.34004E-06; %mol/cm3 - room absolute humidity 10mg/L (50% rH)
- 10mg/L * 1g/1000mg * 1L/1000cm3 * 1mol/18.02g
TAi = 303.65; %K room temperature


%%INPUT: 3 equations
f1(i) = (CA(i)-CAi)-((4*kc(i)*L(i)*(((0.61078e-3*exp((17.27*(TM(i)-
273.15))/((TM(i)-273.15)+237.3)))/(8.314*TM(i)))-
CA(i)))/(D(i)*v(i)*3));
f2(i) = (TA(i)-TAi)-(((4*L(i))/(D(i)*v(i)*rho*Cpa*3))*(hc(i)*(TM(i)-
TA(i))+(Cpw*Mw*kc(i)*(((0.61078e-3*exp((17.27*(TM(i)-
273.15))/((TM(i)-273.15)+237.3)))/(8.314*TM(i)))-CA(i))*(TM(i)-
TA(i)))));
f3(i) = (kw*(TB(i)-TM(i))/y)-hc(i)*(TM(i)-TA(i))-
Mw*hfg*(kc(i)*(((0.61078e-3*exp((17.27*(TM(i)-273.15))/((TM(i)-
273.15)+237.3)))/(8.314*TM(i)))-CA(i)));


F(1,i)=f1(i);
F(2,i)=f2(i);
F(3,i)=f3(i);

end


for i=2:1:10 %Nasal Vestibule
% OUTPUT: Name our 3 unknowns vector Y

CA(i) = Y(1,i);
TM(i) = Y(2,i);
TA(i) = Y(3,i);
```

```
A(i) = pi*(D(i)/2)^2; %cm2
v(i) = Q/A(i); %cm/s

Di = 0.27; % cm2/s (diffusivity of water in air at 300K)
%Di1 = exp(log(0.177)+0.41*log(v1)); % cm2/s (diffusivity
Daviskas1990 Appendix C)
Re(i)= rho*v(i)*D(i)/mu; %Reynolds Number
Sc = vv/Di; %Schmith Number
%Nu(i) = 0.0886*(Re(i)^0.681)*(Pr^0.33); %Nusselt Number
%Sh(i) = 0.0886*(Re(i)^0.681)*(Sc^0.33); %Sherwood Number
Nu(i) = 3.504*(Re(i)*(D(i)/D(9)))^0.277; %Nusselt Number
Sh(i) = 3.652*(Re(i)*(D(i)/D(9)))^0.268; %Sherwood Number


kc(i) = Sh(i)*Di/D(i); %mass transfer coefficient
hc(i) = Nu(i)*ka/D(i); %heat transfer coefficient
%hc1 = 0.0024

TB(i) = (32+273.15)+0.33*(xL(i)); %K
if TB(i)<=310.15
    TB(i) = (32+273.15)+0.33*(xL(i));

else
    TB(i) = 310.15;
end


%%INPUT: 3 equations
f1(i) = (CA(i)-CA(i-1))-((4*kc(i)*L(i)*(((0.61078e-
3*exp((17.27*(TM(i)-273.15))/((TM(i)-
273.15)+237.3)))/(8.314*TM(i)))-CA(i)))/(D(i)*v(i)*3));
f2(i) = (TA(i)-TA(i-1))-
(((4*L(i))/(D(i)*v(i)*rho*Cpa*3))*(hc(i)*(TM(i)-
TA(i))+(Cpw*Mw*kc(i)*(((0.61078e-3*exp((17.27*(TM(i)-
273.15))/((TM(i)-273.15)+237.3)))/(8.314*TM(i)))-CA(i))*(TM(i)-
TA(i)))));
f3(i) = (kw*(TB(i)-TM(i))/y)-hc(i)*(TM(i)-TA(i))-
Mw*hfg*(kc(i)*(((0.61078e-3*exp((17.27*(TM(i)-273.15))/((TM(i)-
273.15)+237.3)))/(8.314*TM(i)))-CA(i)));


F(1,i)=f1(i);
F(2,i)=f2(i);
F(3,i)=f3(i);

end


end

function F = P10_Equations(Y)
%Geometry data

L = [2.0 4.0 4.0 1.4 1.9 2.3 2.1 1.1 2.7 2.8]; %cm
De = [1.5 1.2 0.6525 2.0 1.2 2.55 2.4 1.1 1.8 2.1]; %cm
D = De+0.001300997; %cm
```

```
xL = [L(1) sum(L(1:2)) sum(L(1:3)) sum(L(1:4)) sum(L(1:5))
sum(L(1:6)) sum(L(1:7)) sum(L(1:8)) sum(L(1:9)) sum(L(1:10))];

Q = 332.5; %cm3/s (6L/min)
y = 0.005849502; %cm (500um ASL layer height)
P = 101325+980.665; %Pa
rho = 0.00112; %g/cm3 (dry air at 300K)

Cpa = 0.2592; %cal/gK (dry air at 300K)
Cpw = 1; %cal/gK (liquid water at 300K)
Mw = 18.016; %g/mol
kw = 0.00144; %cal/cmsK (liquid water conductivity at 300K)
hfg = 578.4; %cal/g (evaporation heat of water)

mu = 1.846e-4; %g/cms (dry air dynamic viscosity at 300K)
vv = mu/rho; %cm2/s (dry air kinematic viscosity at 300K)
a = 0.2207; %cm2/s (dry air diffusivity at 300K)
ka = 6.432e-5; %cal/scmK (dry air thermal conductivity)
Pr = vv/a; %Prantld Number

for i=1
% OUTPUT: Name our 3 unknowns vector Y

CA(i) = Y(1,i);
TM(i) = Y(2,i);
TA(i) = Y(3,i);

A(i) = pi*(D(i)/2)^2; %cm2
v(i) = Q/A(i); %cm/s

Di = 0.27; % cm2/s (diffusivity of water in air at 300K)
%Di1 = exp(log(0.177)+0.41*log(v1)); % cm2/s (diffusivity
Daviskas1990 Appendix C)
Re(i)= rho*v(i)*D(i)/mu; %Reynolds Number
Sc = vv/Di; %Schmith Number
%Nu(i) = 0.0886*(Re(i)^0.681)*(Pr^0.33); %Nusselt Number
%Sh(i) = 0.0886*(Re(i)^0.681)*(Sc^0.33); %Sherwood Number
Nu(i) = 3.504*(Re(i)*(D(i)/D(9)))^0.277; %Nusselt Number
Sh(i) = 3.652*(Re(i)*(D(i)/D(9)))^0.268; %Sherwood Number

kc(i) = Sh(i)*Di/D(i); %mass transfer coefficient
hc(i) = Nu(i)*ka/D(i); %heat transfer coefficient
%hc1 = 0.0024

TB(i) = (32+273.15)+0.33*(xL(i)); %K
CAi = 1.44759E-06; %mol/cm3 - room absolute humidity 10mg/L (50% rH)
- 10mg/L * 1g/1000mg * 1L/1000cm3 * 1mol/18.02g
TAi = 304.15; %K room temperature


%%INPUT: 3 equations
f1(i) = (CA(i)-CAi)-((4*kc(i)*L(i)*(((0.61078e-3*exp((17.27*(TM(i)-
273.15))/((TM(i)-273.15)+237.3)))/(8.314*TM(i)))-
CA(i)))/(D(i)*v(i)*3));
f2(i) = (TA(i)-TAi)-(((4*L(i))/(D(i)*v(i)*rho*Cpa*3))*(hc(i)*(TM(i)-
TA(i))+(Cpw*Mw*kc(i)*(((0.61078e-3*exp((17.27*(TM(i)-
273.15))/((TM(i)-273.15)+237.3)))/(8.314*TM(i)))-CA(i))*(TM(i)-
TA(i)))));
```

```
f3(i) = (kw*(TB(i)-TM(i))/y)-hc(i)*(TM(i)-TA(i))-
Mw*hfg*(kc(i)*(((0.61078e-3*exp((17.27*(TM(i)-273.15))/((TM(i)-
273.15)+237.3)))/(8.314*TM(i)))-CA(i)));


F(1,i)=f1(i);
F(2,i)=f2(i);
F(3,i)=f3(i);

end

 for i=2:1:10 %Nasal Vestibule
% OUTPUT: Name our 3 unknowns vector Y

CA(i) = Y(1,i);
TM(i) = Y(2,i);
TA(i) = Y(3,i);

A(i) = pi*(D(i)/2)^2; %cm2
v(i) = Q/A(i); %cm/s

Di = 0.27; % cm2/s (diffusivity of water in air at 300K)
%Di1 = exp(log(0.177)+0.41*log(v1)); % cm2/s (diffusitivity
Daviskas1990 Appendix C)
Re(i)= rho*v(i)*D(i)/mu; %Reynolds Number
Sc = vv/Di; %Schmith Number
%Nu(i) = 0.0886*(Re(i)^0.681)*(Pr^0.33); %Nusselt Number
%Sh(i) = 0.0886*(Re(i)^0.681)*(Sc^0.33); %Sherwood Number
Nu(i) = 3.504*(Re(i)*(D(i)/D(9)))^0.277; %Nusselt Number
Sh(i) = 3.652*(Re(i)*(D(i)/D(9)))^0.268; %Sherwood Number


kc(i) = Sh(i)*Di/D(i); %mass transfer coefficient
hc(i) = Nu(i)*ka/D(i); %heat transfer coefficient
%hc1 = 0.0024

TB(i) = (32+273.15)+0.33*(xL(i)); %K
if TB(i)<=310.15
    TB(i) = (32+273.15)+0.33*(xL(i));

else
    TB(i) = 310.15;
end


%%INPUT: 3 equations
f1(i) = (CA(i)-CA(i-1))-((4*kc(i)*L(i)*(((0.61078e-
3*exp((17.27*(TM(i)-273.15))/((TM(i)-
273.15)+237.3)))/(8.314*TM(i)))-CA(i)))/(D(i)*v(i)*3));
f2(i) = (TA(i)-TA(i-1))-
(((4*L(i))/(D(i)*v(i)*rho*Cpa*3))*(hc(i)*(TM(i)-
TA(i))+(Cpw*Mw*kc(i)*(((0.61078e-3*exp((17.27*(TM(i)-
273.15))/((TM(i)-273.15)+237.3)))/(8.314*TM(i)))-CA(i))*(TM(i)-
TA(i)))));
f3(i) = (kw*(TB(i)-TM(i))/y)-hc(i)*(TM(i)-TA(i))-
Mw*hfg*(kc(i)*(((0.61078e-3*exp((17.27*(TM(i)-273.15))/((TM(i)-
273.15)+237.3)))/(8.314*TM(i)))-CA(i)));
```

```
F(1,i)=f1(i);
F(2,i)=f2(i);
F(3,i)=f3(i);

end


end

function F = P15_Equations(Y)
%Geometry data
L = [2.0 4.0 4.0 1.4 1.9 2.3 2.1 1.1 2.7 2.8]; %cm
De = [1.5 1.2 0.6525 2.0 1.2 2.55 2.4 1.1 1.8 2.1]; %cm
D = De+0.001916672; %cm
xL = [L(1) sum(L(1:2)) sum(L(1:3)) sum(L(1:4)) sum(L(1:5))
sum(L(1:6)) sum(L(1:7)) sum(L(1:8)) sum(L(1:9)) sum(L(1:10))];

Q = 423.75; %cm3/s (6L/min)
y = 0.005541664; %cm (500um ASL layer height)
P = 101325+1470.9975; %Pa
rho = 0.00112; %g/cm3 (dry air at 300K)

Cpa = 0.2592; %cal/gK (dry air at 300K)
Cpw = 1; %cal/gK (liquid water at 300K)
Mw = 18.016; %g/mol
kw = 0.00144; %cal/cmsK (liquid water conductivity at 300K)
hfg = 578.4; %cal/g (evaporation heat of water)

mu = 1.846e-4; %g/cms (dry air dynamic viscosity at 300K)
vv = mu/rho; %cm2/s (dry air kinematic viscosity at 300K)
a = 0.2207; %cm2/s (dry air diffusivity at 300K)
ka = 6.432e-5; %cal/scmK (dry air thermal conductivity)
Pr = vv/a; %Prantld Number

for i=1
% OUTPUT: Name our 3 unknowns vector Y

CA(i) = Y(1,i);
TM(i) = Y(2,i);
TA(i) = Y(3,i);

A(i) = pi*(D(i)/2)^2; %cm2
v(i) = Q/A(i); %cm/s

Di = 0.27; % cm2/s (diffusivity of water in air at 300K)
%Di1 = exp(log(0.177)+0.41*log(v1)); % cm2/s (diffusitivity
Daviskas1990 Appendix C)
Re(i)= rho*v(i)*D(i)/mu; %Reynolds Number
Sc = vv/Di; %Schmith Number
%Nu(i) = 0.0886*(Re(i)^0.681)*(Pr^0.33); %Nusselt Number
%Sh(i) = 0.0886*(Re(i)^0.681)*(Sc^0.33); %Sherwood Number
Nu(i) = 3.504*(Re(i)*(D(i)/D(9)))^0.277; %Nusselt Number
Sh(i) = 3.652*(Re(i)*(D(i)/D(9)))^0.268; %Sherwood Number

kc(i) = Sh(i)*Di/D(i); %mass transfer coefficient
hc(i) = Nu(i)*ka/D(i); %heat transfer coefficient
%hc1 = 0.0024
```

```
TB(i) = (32+273.15)+0.33*(xL(i)); %K
CAi = 1.53248E-06; %mol/cm3 - room absolute humidity 10mg/L (50% rH)
- 10mg/L * 1g/1000mg * 1L/1000cm3 * 1mol/18.02g
TAi = 304.65; %K room temperature


%%INPUT: 3 equations
f1(i) = (CA(i)-CAi)-((4*kc(i)*L(i)*(((0.61078e-3*exp((17.27*(TM(i)-
273.15))/((TM(i)-273.15)+237.3)))/(8.314*TM(i)))-
CA(i)))/(D(i)*v(i)*3));
f2(i) = (TA(i)-TAi)-(((4*L(i))/(D(i)*v(i)*rho*Cpa*3))*(hc(i)*(TM(i)-
TA(i))+(Cpw*Mw*kc(i)*(((0.61078e-3*exp((17.27*(TM(i)-
273.15))/((TM(i)-273.15)+237.3)))/(8.314*TM(i)))-CA(i))*(TM(i)-
TA(i)))));
f3(i) = (kw*(TB(i)-TM(i))/y)-hc(i)*(TM(i)-TA(i))-
Mw*hfg*(kc(i)*(((0.61078e-3*exp((17.27*(TM(i)-273.15))/((TM(i)-
273.15)+237.3)))/(8.314*TM(i)))-CA(i)));


F(1,i)=f1(i);
F(2,i)=f2(i);
F(3,i)=f3(i);

end


for i=2:1:10 %Nasal Vestibule
% OUTPUT: Name our 3 unknowns vector Y

CA(i) = Y(1,i);
TM(i) = Y(2,i);
TA(i) = Y(3,i);

A(i) = pi*(D(i)/2)^2; %cm2
v(i) = Q/A(i); %cm/s

Di = 0.27; % cm2/s (diffusivity of water in air at 300K)
%Di1 = exp(log(0.177)+0.41*log(v1)); % cm2/s (diffusitivity
Daviskas1990 Appendix C)
Re(i)= rho*v(i)*D(i)/mu; %Reynolds Number
Sc = vv/Di; %Schmith Number
%Nu(i) = 0.0886*(Re(i)^0.681)*(Pr^0.33); %Nusselt Number
%Sh(i) = 0.0886*(Re(i)^0.681)*(Sc^0.33); %Sherwood Number
Nu(i) = 3.504*(Re(i)*(D(i)/D(9)))^0.277; %Nusselt Number
Sh(i) = 3.652*(Re(i)*(D(i)/D(9)))^0.268; %Sherwood Number


kc(i) = Sh(i)*Di/D(i); %mass transfer coefficient
hc(i) = Nu(i)*ka/D(i); %heat transfer coefficient
%hc1 = 0.0024

TB(i) = (32+273.15)+0.33*(xL(i)); %K
if TB(i)<=310.15
    TB(i) = (32+273.15)+0.33*(xL(i));

else
    TB(i) = 310.15;
end
```

```
%%INPUT: 3 equations
f1(i) = (CA(i)-CA(i-1))-((4*kc(i)*L(i)*(((0.61078e-
3*exp((17.27*(TM(i)-273.15))/((TM(i)-
273.15)+237.3)))/(8.314*TM(i)))-CA(i)))/(D(i)*v(i)*3));
f2(i) = (TA(i)-TA(i-1))-
(((4*L(i))/(D(i)*v(i)*rho*Cpa*3))*(hc(i)*(TM(i)-
TA(i))+(Cpw*Mw*kc(i)*(((0.61078e-3*exp((17.27*(TM(i)-
273.15))/((TM(i)-273.15)+237.3)))/(8.314*TM(i)))-CA(i))*(TM(i)-
TA(i)))));
f3(i) = (kw*(TB(i)-TM(i))/y)-hc(i)*(TM(i)-TA(i))-
Mw*hfg*(kc(i)*(((0.61078e-3*exp((17.27*(TM(i)-273.15))/((TM(i)-
273.15)+237.3)))/(8.314*TM(i)))-CA(i)));


F(1,i)=f1(i);
F(2,i)=f2(i);
F(3,i)=f3(i);

end



end

function F = P20_Equations(Y)
%Geometry data
L = [2.0 4.0 4.0 1.4 1.9 2.3 2.1 1.1 2.7 2.8]; %cm
De = [1.5 1.2 0.6525 2.0 1.2 2.55 2.4 1.1 1.8 2.1]; %cm
D = De+0.002533294; %cm
xL = [L(1) sum(L(1:2)) sum(L(1:3)) sum(L(1:4)) sum(L(1:5))
sum(L(1:6)) sum(L(1:7)) sum(L(1:8)) sum(L(1:9)) sum(L(1:10))];

Q = 515; %cm3/s (6L/min)
y = 0.005233353; %cm (500um ASL layer height)
P = 101325+1961.33; %Pa
rho = 0.00112; %g/cm3 (dry air at 300K)

Cpa = 0.2592; %cal/gK (dry air at 300K)
Cpw = 1; %cal/gK (liquid water at 300K)
Mw = 18.016; %g/mol
kw = 0.00144; %cal/cmsK (liquid water conductivity at 300K)
hfg = 578.4; %cal/g (evaporation heat of water)

mu = 1.846e-4; %g/cms (dry air dynamic viscosity at 300K)
vv = mu/rho; %cm2/s (dry air kinematic viscosity at 300K)
a = 0.2207; %cm2/s (dry air diffusivity at 300K)
ka = 6.432e-5; %cal/scmK (dry air thermal conductivity)
Pr = vv/a; %Prantld Number

for i=1
% OUTPUT: Name our 3 unknowns vector Y

CA(i) = Y(1,i);
TM(i) = Y(2,i);
TA(i) = Y(3,i);
```

```
A(i) = pi*(D(i)/2)^2; %cm2
v(i) = Q/A(i); %cm/s

Di = 0.27; % cm2/s (diffusivity of water in air at 300K)
%Di1 = exp(log(0.177)+0.41*log(v1)); % cm2/s (diffusitivity
Daviskas1990 Appendix C)
Re(i)= rho*v(i)*D(i)/mu; %Reynolds Number
Sc = vv/Di; %Schmith Number
%Nu(i) = 0.0886*(Re(i)^0.681)*(Pr^0.33); %Nusselt Number
%Sh(i) = 0.0886*(Re(i)^0.681)*(Sc^0.33); %Sherwood Number
Nu(i) = 3.504*(Re(i)*(D(i)/D(9)))^0.277; %Nusselt Number
Sh(i) = 3.652*(Re(i)*(D(i)/D(9)))^0.268; %Sherwood Number

kc(i) = Sh(i)*Di/D(i); %mass transfer coefficient
hc(i) = Nu(i)*ka/D(i); %heat transfer coefficient
%hc1 = 0.0024

TB(i) = (32+273.15)+0.33*(xL(i)); %K
CAi = 1.60200E-06; %mol/cm3 - room absolute humidity 10mg/L (50% rH)
- 10mg/L * 1g/1000mg * 1L/1000cm3 * 1mol/18.02g
TAi = 305.15; %K room temperature


%%INPUT: 3 equations
f1(i) = (CA(i)-CAi)-((4*kc(i)*L(i)*(((0.61078e-3*exp((17.27*(TM(i)-
273.15))/((TM(i)-273.15)+237.3)))/(8.314*TM(i)))-
CA(i)))/(D(i)*v(i)*3));
f2(i) = (TA(i)-TAi)-(((4*L(i))/(D(i)*v(i)*rho*Cpa*3))*(hc(i)*(TM(i)-
TA(i))+(Cpw*Mw*kc(i)*(((0.61078e-3*exp((17.27*(TM(i)-
273.15))/((TM(i)-273.15)+237.3)))/(8.314*TM(i)))-CA(i))*(TM(i)-
TA(i)))));
f3(i) = (kw*(TB(i)-TM(i))/y)-hc(i)*(TM(i)-TA(i))-
Mw*hfg*(kc(i)*(((0.61078e-3*exp((17.27*(TM(i)-273.15))/((TM(i)-
273.15)+237.3)))/(8.314*TM(i)))-CA(i)));



F(1,i)=f1(i);
F(2,i)=f2(i);
F(3,i)=f3(i);

end


for i=2:1:10 %Nasal Vestibule
% OUTPUT: Name our 3 unknowns vector Y

CA(i) = Y(1,i);
TM(i) = Y(2,i);
TA(i) = Y(3,i);

A(i) = pi*(D(i)/2)^2; %cm2
v(i) = Q/A(i); %cm/s

Di = 0.27; % cm2/s (diffusivity of water in air at 300K)
%Di1 = exp(log(0.177)+0.41*log(v1)); % cm2/s (diffusitivity
Daviskas1990 Appendix C)
Re(i)= rho*v(i)*D(i)/mu; %Reynolds Number
Sc = vv/Di; %Schmith Number
%Nu(i) = 0.0886*(Re(i)^0.681)*(Pr^0.33); %Nusselt Number
```

```
%Sh(i) = 0.0886*(Re(i)^0.681)*(Sc^0.33); %Sherwood Number
Nu(i) = 3.504*(Re(i)*(D(i)/D(9)))^0.277; %Nusselt Number
Sh(i) = 3.652*(Re(i)*(D(i)/D(9)))^0.268; %Sherwood Number


kc(i) = Sh(i)*Di/D(i); %mass transfer coefficient
hc(i) = Nu(i)*ka/D(i); %heat transfer coefficient
%hc1 = 0.0024

TB(i) = (32+273.15)+0.33*(xL(i)); %K
if TB(i)<=310.15
    TB(i) = (32+273.15)+0.33*(xL(i));

else
    TB(i) = 310.15;
end


%%INPUT: 3 equations
f1(i) = (CA(i)-CA(i-1))-((4*kc(i)*L(i)*(((0.61078e-
3*exp((17.27*(TM(i)-273.15))/((TM(i)-
273.15)+237.3)))/(8.314*TM(i)))-CA(i)))/(D(i)*v(i)*3));
f2(i) = (TA(i)-TA(i-1))-
(((4*L(i))/(D(i)*v(i)*rho*Cpa*3))*(hc(i)*(TM(i)-
TA(i))+(Cpw*Mw*kc(i)*(((0.61078e-3*exp((17.27*(TM(i)-
273.15))/((TM(i)-273.15)+237.3)))/(8.314*TM(i)))-CA(i))*(TM(i)-
TA(i)))));
f3(i) = (kw*(TB(i)-TM(i))/y)-hc(i)*(TM(i)-TA(i))-
Mw*hfg*(kc(i)*(((0.61078e-3*exp((17.27*(TM(i)-273.15))/((TM(i)-
273.15)+237.3)))/(8.314*TM(i)))-CA(i)));


F(1,i)=f1(i);
F(2,i)=f2(i);
F(3,i)=f3(i);

end



end
```

Appendix G

Arduino Relay and SHT35D Code

```
unsigned long time;
#include <Wire.h>
#include "ClosedCube_SHT31D.h"

ClosedCube_SHT31D sht3xd;

int in1 = 7;

void setup()
{
  Wire.begin();

  Serial.begin(9600);
  Serial.println("Clinical Trials - June 2018");

  sht3xd.begin(0x45); // I2C address: 0x44 or 0x45

  pinMode(in1, OUTPUT);
  digitalWrite(in1, HIGH);
}

void loop()
{
  printResult("ClockStrech Mode",
sht3xd.readTempAndHumidity(SHT3XD_REPEATABILITY_HIGH,
SHT3XD_MODE_CLOCK_STRETCH, 50));

  digitalWrite(in1, LOW);
  delay(500);

  printResult("ClockStrech Mode",
sht3xd.readTempAndHumidity(SHT3XD_REPEATABILITY_HIGH,
SHT3XD_MODE_CLOCK_STRETCH, 50));

  digitalWrite(in1, LOW);
  delay(500);

  printResult("ClockStrech Mode",
sht3xd.readTempAndHumidity(SHT3XD_REPEATABILITY_HIGH,
SHT3XD_MODE_CLOCK_STRETCH, 50));

  digitalWrite(in1, LOW);
  delay(500);
```

```
  printResult("ClockStrech Mode",
sht3xd.readTempAndHumidity(SHT3XD_REPEATABILITY_HIGH,
SHT3XD_MODE_CLOCK_STRETCH, 50));

  digitalWrite(in1, LOW);
  delay(500);

  printResult("ClockStrech Mode",
sht3xd.readTempAndHumidity(SHT3XD_REPEATABILITY_HIGH,
SHT3XD_MODE_CLOCK_STRETCH, 50));

  digitalWrite(in1, LOW);
  delay(500);

  printResult("ClockStrech Mode",
sht3xd.readTempAndHumidity(SHT3XD_REPEATABILITY_HIGH,
SHT3XD_MODE_CLOCK_STRETCH, 50));

  digitalWrite(in1, LOW);
  delay(500);

  printResult("ClockStrech Mode",
sht3xd.readTempAndHumidity(SHT3XD_REPEATABILITY_HIGH,
SHT3XD_MODE_CLOCK_STRETCH, 50));

  digitalWrite(in1, HIGH);
  delay(500);

  printResult("ClockStrech Mode",
sht3xd.readTempAndHumidity(SHT3XD_REPEATABILITY_HIGH,
SHT3XD_MODE_CLOCK_STRETCH, 50));

  digitalWrite(in1, HIGH);
  delay(500);

  printResult("ClockStrech Mode",
sht3xd.readTempAndHumidity(SHT3XD_REPEATABILITY_HIGH,
SHT3XD_MODE_CLOCK_STRETCH, 50));

  digitalWrite(in1, HIGH);
  delay(500);

  printResult("ClockStrech Mode",
sht3xd.readTempAndHumidity(SHT3XD_REPEATABILITY_HIGH,
SHT3XD_MODE_CLOCK_STRETCH, 50));

  digitalWrite(in1, HIGH);
  delay(500);

  printResult("ClockStrech Mode",
sht3xd.readTempAndHumidity(SHT3XD_REPEATABILITY_HIGH,
SHT3XD_MODE_CLOCK_STRETCH, 50));

  digitalWrite(in1, HIGH);
  delay(500);

  printResult("ClockStrech Mode",
sht3xd.readTempAndHumidity(SHT3XD_REPEATABILITY_HIGH,
SHT3XD_MODE_CLOCK_STRETCH, 50));

  digitalWrite(in1, HIGH);
```

```
  delay(500);
}
void printResult(String text, SHT31D result) {
  Serial.print("Time: ");
  time = millis();
  //prints time since program started
  Serial.print(time);
  Serial.print(" ms  ");

  Serial.print(text);
  Serial.print(": T ");
  Serial.print(result.t);
  Serial.print(" C, RH ");
  Serial.print(result.rh);
  Serial.println(" %");
}
```